UNIVERSITÀ DEGLI STUDI DI PALERMO

Dottorato di Ricerca in Ingegneria Chimica, Gestionale, Informatica, Meccanica
Indirizzo "Ingegneria dell'Innovazione Tecnologica"
Dipartimento dell'Innovazione Industriale e Digitale (DIID)
Settore Scientifico Disciplinare ING-IND 25

DESIGN AND DEVELOPMENT OF A PILOT PLANT FOR MICROALGAE CULTIVATION AND POST-TREATMENT IN SUPERCRITICAL WATER

IL DOTTORE
Ing. GASPARE MAROTTA

IL COORDINATORE
Prof. Ing. SALVATORE GAGLIO

IL TUTOR
Prof. Ing. ALBERTO BRUCATO

I CO TUTORS
Prof. Ing. FRANCESCA SCARGIALI
Prof. Ing. FRANCO GRISAFI
Prof. Ing. GIUSEPPE CAPUTO

CICLO XXIX
ANNO CONSEGUIMENTO TITOLO 2017

DESIGN AND DEVELOPMENT OF A PILOT PLANT FOR MICROALGAE CULTIVATION AND POST-TREATMENT IN SUPERCRITICAL WATER

IL DOTTORE

Ing. GASPARE MAROTTA

IL COORDINATORE

Prof. Ing. SALVATORE GAGLIO

IL TUTOR

Prof. Ing. ALBERTO BRUCATO

I CO TUTORS

Prof. Ing. FRANCESCA SCARGIALI
Prof. Ing. FRANCO GRISAFI
Prof. Ing. GIUSEPPE CAPUTO

CICLO XXIX

ANNO CONSEGUIMENTO TITOLO 2017

To my love Concetta, who has always supported me and made this enterprise possible.

Gaspare Marotta

CONTENTS

LIST OF ISI PUBLICATIONS

- G. Caputo, M. Dispenza, P. Rubio, F. Scargiali, G. Marotta, A. Brucato, *Supercritical water gasification of microalgae and their constituents in a continuous reactor*, J. of Supercritical Fluids 118, (2016) 163–170.

- G. Caputo, P. R. Blasquez, F. Scargiali, G. Marotta, A. Brucato, *Experimental and fluid dynamic study of continuous supercritical water gasification of glucose*, J. of Supercritical Fluids 107, (2016) 450–461.

- G. Marotta, M. Di Liberto, M. Ciofalo, *On the influence of curvature and torsion on turbulence in helically coiled pipes*, J. Phys. Conf. Ser. 501, (2014) 012-025.

SUBMITTED PAPERS

- G. Marotta, J. Pruvost, F. Scargiali, G. Caputo, A. Brucato, *Reflection-refraction effects on light distribution inside tubular photobioreactors,* submitted to Canadian Journal Chem. Eng., (2016).

- G. Marotta, F. Scargiali, G. Caputo, F. Grisafi, A. Brucato, *A novel photobioreactor pilot plant: hydrodynamic performances for microalgae cultivation,* submitted to ICheaP13, Milan (2017).

PAPERS IN PREPARATION

- G. Marotta, S. Lima, F. Scargiali, F. Grisafi, A. Brucato, *Operation and perspectives of the first pilot plant for microalgae production with low-cost technology,* in preparation.

PRESENTATIONS AT INTERNATIONAL AND NATIONAL CONFERENCES

- A. Brucato, G. Marotta, F. Scargiali,
  Vacuum temperature control of an Air-Lift photobioreactor,
  European Congress of Chemical Engineering ECCE, September (2015),
  Nice, France.

- G. Marotta, F. Scargiali, G. Caputo, F. Grisafi, A. Brucato,
  Local volumetric rate of photon absorption (LVRPA) in tubular photobioreactors,
  Gricu PhD National School, September (2016), Anacapri, Italy.

SUBMITTED ABSTRACTS FOR ORAL PRESENTATIONS

- G. Marotta, S. Lima, F. Scargiali, F. Grisafi, A. Brucato,
  Novel low cost microalgae technology,
  European Algae Biomass Association EABA, Algae Congress, December (2016), Madrid, Spain.

INTRODUCTION

The World is undergoing a deep energy crisis over the last few decades, associated to the irreversible depletion of traditional fossil fuels sources such as oil, coal and natural gas. As well known, the use of fossil fuels leads to a large greenhouse gases (GHG) formation; for this reason, the interest in new alternative energy resources is greatly increasing.

Among the analysed different typologies, a very promising line is biofuels, i.e. biomass of microalgae origin, which represents the third generation of biofuels and grows much more than classic lignocellulosic biomass (first- and second generation). In addition to biofuel use, microalgae are really interesting to CO_2 reduction [1]; where a single microalgae species presents itself as a sort of *micro-biorefinery*, with an extremely differentiated production also in function of its structural simplicity. However, process development on industrial scale, open or closed systems (photobioreactors), is in the early stage and requires further studies about it [2].

Focus of this PhD was a comprehensive study of microalgae production using an innovative technology, and one possible post-treatment of the same microalgae, both through modeling and experimental activities.

The research activities, strictly associated to the R&D of the BIO4BIO project, as will be discussed in next section 1.1, will conclude with the construction and first experimental tests of a Pilot Plant for microalgae cultivation located within the Palermo University Campus (Italy).

The research activities were primarily concentrated on the development of a suitable mathematical model for microalgae cultivation process considering (i) all necessary parameters for pilot system operation, and also (i) the modeling of all pilot plant units itself. The models were validated by experimental results, and a good comparison was obtained for a microalgae cultivation pilot plant.

Regarding microalgae post-treatment after their cultivation, experimental and numerical activities were carried out for microalgae gasification in supercritical water with an experimental laboratory reactor.

Therefore, the present work, developed during my PhD period with the support of several university students, was prepared to obtain the key parameters and describes the technologies developed for the above-mentioned objectives. In this work:

- Chapter **1** presents a comprehensive introduction on BIO4BIO project, presenting the microalgae state-of-art, with their vital operating parameters and their typical cultivation systems;
- Chapter **2** describes mathematical modeling and results for microalgae cultivation process considering (i) all necessary parameters for pilot system operation, and also (i) the modeling and design of all pilot plant units itself;
- Chapter **3** presents the experimental- and CFD results of a Pilot Plant Unit, in particular a lab-scale Air-Lift;
- Chapter **4** describes a novel modeling and results of radiation transfer effect on microalgae cultivation, and an experimental apparatus developed;
- Chapter **5** presents the design, construction and start-up of the Pilot Plant located within the Palermo University Campus (Italy), with the first experimental results;
- Finally, Chapter **6** shows experimental- and numerical results of microalgae post-treatment in supercritical water.

1 MICROALGAE AND PHOTOBIOREACTOR

1.1 BIO4BIO Project: Photobioreactor (PBR) Pilot Plant

This work is a part of BIO4BIO PON project for bio-molecular energy valorisation of agro-industrial and fish biomass residual (MIUR code: PON02_00451_3362376). This PON project is divided into three targets characterized by agro-industrial waste transformation into a new resource as (i) animal feed products, (ii) pharmaceutical products and/or (iii) renewable energy sources, e.g. bioethanol or biodiesel. Therefore, in this macro-area research program it was inserted this study on the design & development of a Photobioreactor (PBR) Pilot Plant for microalgae production and a feasible post-treatment.

The first studies were based on a lab-scale system in order to obtain the basic experimental results. Following this first results and subsequent thermo-fluid dynamic modeling, the final part of this work has been the installation of a demonstration prototype plant in the South of Italy, located within the Palermo University Campus (Italy), as shown in Figure 1.1. This location is ideal for microalgae growth, as in the south of the Mediterranean area, the climate is warmer, and on average there are no temperature values below 15 °C throughout the year [3].

(a) (b)

Figure 1.1. (a) Location of the PBR pilot plant within the Palermo University Campus; (b) Satellite image of the pilot plant location (space information comes from Google Maps® courtesy).

The development of a microalgae production plant, together with post-treatment, involves the study of many strongly related operating parameters, such as incident light, plant dimensions, temperature, pH, flow rates, O_2 concentrations, etc. Therefore, significant R&D efforts are necessary to achieve a complete and detailed plant design. For this reason, the following R&D activities have been identified and addressed within this PBR Pilot Plant project:

i. Development of new design and low-cost technology components (handling- and stripping system, low-cost photobioreactors, recovery of high-value gas) necessary to the process requirements;
ii. Development of a suitable mathematical model, so as to provide a predictive tool for investigation on microalgae growth, and pilot/large scale units;
iii. Design, construction and testing of a PBR pilot plant and therefore also creating a new laboratory for analysis, inocula production and for pilot plant management;
iv. Experimental and numerical investigation of microalgae post-treatment through laboratory-scale testing;

The research activities presented in this work were entirely performed during the PhD period. In particular, the study of main features for microalgae growth it is described in Chapter 1 below, while the numerical modeling of an entire plant it is presented in Chapter 2. Design phases, construction and testing of the PBR pilot plant are described in Chapter 5. Finally, the experimental and numerical activities on post-treatment are described in Chapter 6.

1.2 Introduction to microalgae

Commonly the word “algae” specifies a heterogeneous set of aquatic photosynthetic organisms. However, this definition is highly generic since it encloses both macro-algae and micro-algae [4]. Microalgae are autotrophic and, in some cases, heterotrophic photosynthetic organisms which were already present on Earth 1.5 billion years ago [4,5]. Indeed, microalgae have a very wide species group [4]. They are differentiated by the different cellular organization: colonial organisms, unicellular and filamentous, by the presence of flagella which allow the movement or

not of the cell and by the different growth habitat as freshwater, saltwater or brackish [6–9]. Microalgae can be both prokaryotes and eukaryotes. Prokaryotic organisms (cyanobacteria or blue-green algae) are unicellular organisms, or at the most in colonial system, with dimensions of a few micrometres (1-10 μm); these have no nuclear membrane and cell bodies. On the contrary, eukaryotes organisms (green algae, red algae and diatoms) have higher dimensions (10-100 μm) and, they owna nuclear membrane and cell bodies. The simplicity of prokaryotes is due not only to their intrinsic mono-cellularity and small size but also by the simple internal organization cell. Indeed, in eukaryotes cells the membranes divide the cell into various compartments (i.e. chloroplasts, mitochondria, nucleus, etc.) and, each of them carries out a certain activity such as cell respiration in mitochondria and photosynthesis activity in the chloroplasts. On the other side in the prokaryotic cells all vital functions are performed within a unique section. However, it is worth noting that prokaryotic organisms are indicated as photosynthetic bacteria in applied algology and, micro-algae term indicates the microscopic algae per se [4]. Currently, microalgae are of high interest due to their ability to accumulate high amounts of biomass; this is mainly made up of essential elements such as carbohydrates, proteins and lipids through photosynthesis process [5]. These microalgae have a different set of pigments, in particular *carotenoids* and *chlorophyll type a*, and their structure is functional to the biochemical process photosynthesis essentially [10]. The photosynthesis process is the own growth mechanism of autotrophic microalgae which it can take place during the day through biochemical conversion of sunlight and carbon dioxide only; this process produces sugars needed for energy metabolism, biosynthetic and oxygen, which it is used in cellular respiration in part and the remaining it is released into external environment.

Microalgae are the primary producers of these elements in aquatic environments and, they are an essential link in the food chain of marine ecosystems ensuring the necessary mass and energy flow to maintenance of heterotrophic organisms. In fact these latter are microalgae species that can grow even overnight if there are present the organic nutrients outside [7].

Microalgal biodiversity is extensive and it is estimated there are over 10 millions of species; these are classified into reigns, divisions and classes generally [5].

1.3 Microalgae applications: nutraceutical and biofuel

In the '50s in several world areas microalgae cultivation practice has become widespread. The oldest cultivation practice dates back on the Kossorom lake shore (Africa), where microalgae were cultivated in small water pools. Initially, the scientific community was attracted to these aquatic microorganisms especially for the beneficial properties of compounds obtained and the high cell reproduction speed.

In general, algae are able to synthesize in a short time high amounts of biomass which contains mainly carbohydrates, proteins and lipids, natural antioxidants, vitamins, essential amino acids, pigments, etc. Table 1.1 and Table 1.2 show components of primary interest in food industry for several microalgae species [10] and some traditional foods [5].

Table 1.1 Comparison of chemical composition of dry biomass between traditional food and microalgae. Adapted from [5].

Commodity	Protein	Carbohydrates	Lipids
Baker's yeast	39	38	1
Meat	43	1	34
Milk	26	38	28
Rice	8	77	2
Soybean	37	30	20
Anabaena cylindrica	43-56	25-30	4-7
Chlamydomonas rheinhardii	48	17	21
Chlorella vulgaris	51-58	12-17	14-22
Dunaliella salina	57	32	6
Porphyridium cruentum	28-39	40-57	9-14
Scenedesmus obliquus	50-56	10-17	12-14
Spirulina maxima	60-71	13-16	6-7

Table 1.2 Dry biomass composition of some microalgae species. Adapted from [10].

Species	Protein	Carbohydrates	Lipids
Chlorella vulgaris	55	15	25

Chlorella pyr.	54	26	16
Dunaliella s.	52	32	12
Nannochloropsis	40	25	31
Nannochloropsis s.	44	26	27
Neochloris ol.	44	24	28
Ettlia ol.	36	24	36
Phaedactylum tric.	53	18	21
Spirulina pl	60	12	13
STANDARD micro	50	25	20
OPTIMAL micro	40	15	40

Below some information about the main components:

- Carbohydrates: they come in cellulose form, sugars and starch. The available carbohydrate amount is of fundamental importance as it greatly affects food digestibility, avoiding to cause gastro-intestinal issues;
- Protein: generally, microalgae protein content is greater than 50% by weight, i.e. a double content compared with milk food;
- Lipids: lipids and fatty acids are present in all crops by metabolites form and membrane components, having an energy resource function. Most polar lipids are constituted by glycerides, while triglycerides and free fatty acids constitute almost the entire of non-polar lipids. In microalgae biomass, the average lipid content varies between 1 and 40%; however, it is an approximate range, since oil content can vary widely depending on microalgae species. Table 1.3 shows lipid content of several species by reference to the dried biomass. It shows that the percentages vary within 16-77% [11].

Table 1.3 Oil content of several microalgae species (% dry wt). Adapted from [11].

Microalga	**Oil content (% dry wt)**
Chlorella sp	28-32
Botryococcus braunii	25-75
Dunaliella p.	23
Nannochloropsis sp.	31-68
Nannochloris sp.	20-35
Neochloris ol.	35-54
Nitzschia sp.	45-47
Phaedactylum tric.	20-30
Schizochytrium sp.	50-77
Tetraselmis sueica	15-23
Isochrysis sp.	25-33

In the commercial sector, the most important fatty acids from microalgae species are polyunsaturated acids, i.e. oleic acid, arachidonic acid, eicosapentaenoic acid, linolenic acid, etc.; however, from research study it emerged that microalgal lipids cannot replace the classical sources in human alimentation [4].

Microalgae present different vitamins and pigments also. The latter have several commercial applications; for example, *β-carotene* is used as colorant in food industry to improve meat and fish colour, moreover thanks to its antioxidant properties it is used as food additive to prevent some cancer forms.

Eventually, unconventional foods such as microalgae must overcome a series of toxicology tests before being marketed. These tests are aimed to investigate the presence of toxic substances, which can be distinguished in:

- biogenetics toxicity synthesized by microalgae in the growth process or decaying of the same;
- non-biogenetics toxicity accumulated outside, which can be disposed by controlling crop contamination.

This kind of culture has achieved a growing interest by scientific community, not only for food applications but also for medical, cosmetic and, more recently energy applications [12]. In the medical field for example, microalgae assume the role of promising sources for substances with antiviral, antibacterial and anti-cancer properties [13].

Nowadays microalgae are marketed as capsules, liquids, bars, which are used together with conventional foods such as pasta, snack, drinks, sweets and in addiction as food additives. However, there are still concerns regarding algae-based food consumption, due to the lack of a normative reference based on assured toxicological data. Consequently, several companies involved on microalgae production in the food industry shall comply with the guidelines imposed by the same industrial sector [4].

Since a few years, new processes to produce energy have been studied from microalgae biomass. Figure 1.2 [14] shows some of these conversion processes.

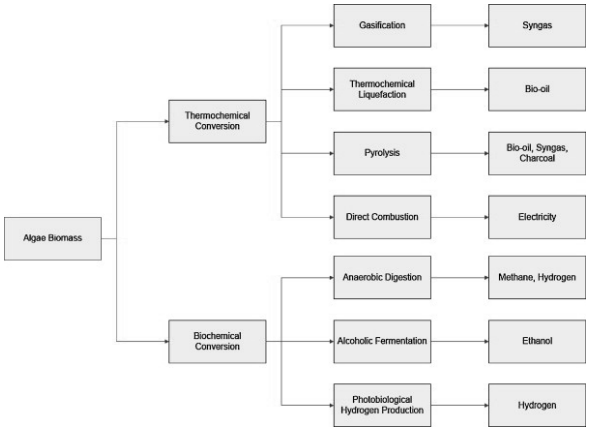

Figure 1.2 Potential algal biomass conversion processes [14].

Despite these various conversion processes, the greatest development potential is linked to biofuels production, as an alternative to fossil fuels; indeed from microalgae can be extract the necessary oil to produce biofuels fully compatible with the present technologies [14]. In the *National Algal Biofuel Roadmap* [15] report of USA Department of Energy (DoE), several factors that have stimulated the curiosity of many researchers towards these microalgae species as renewable source energy for the future are reported . They are competitive [11] compared to conventional sources and can be identified by:

- *high productivity per unit of cultivated area*: the ability to use solar energy for the production of organic substances is five times higher than other crops. This means a greater lipids quantity in the equal occupied ground. Furthermore, microalgae are growing very quickly since they can double their biomass in a period between 3 and 24h, unlike other crops with a doubling time one day at least. Regarding the photosynthetic efficiency of sunlight is slightly less than 1% in common crops; indeed, in microalgae species is possible to estimate experimental values up to 5%, with peaks of about 7% in the photobioreactors, in which it is possible to control the growth inhibitory phenomena such as, for example, photorespiration. In large scale photobioreactors the photosynthetic efficiency is much lower than 12% [16]. Table 1.4 shows a comparison between microalgae and traditional oilseed crops in terms of oil productivity and land

required [11]. It is estimated that if a percentage between 1% to 3% of land of the United State was cultivated with microalgae, the biofuel produced is sufficient to cover 50% of fuel required for the transport; indeed, it would be about 24% of land with palm oil cultivation to produce the same quantity of biofuel [11,17];

- *no-competitive with agricultural crops and possibility to use non-productive land*: recently the intensified use of traditional crops for bioethanol conversion has caused a rise in costs of raw materials for human consumption, making these techniques unsustainable and, without taking into account environmental impacts on ecosystems due to conversion of large arears for energy purposes [15]. This negative aspect does not concern microalgae, since its cultivation is open to different environment conditions: sea, desert land or otherwise non-productive. This is a great advantage both economically since large plant size (hundreds of hectares) imply a tolerable investment if made only in unusable land, and also because microalgae cultures are not in competition with agricultural crops;
- *wide growth medium range*: the great variability of algal species makes their cultivation possible in many aquatic environments, fresh water, brackish, waste water and livestock waste. This feature simplifies water management with a recycling less complex, to reduce the impact on aquatic systems and the availability of water resources;
- *combination of energy production & co-products with high added value:* during microalgae biomass synthesis for biofuels production, it is possible to obtain co-products as well, with high added value up to 10,000 $/kg for sectors as food, pharmaceutical, aquaculture etc. This allows to reduce the costs for the production of the same in the initial phase at least;
- *carbon dioxide emission reduction & integration with other processes:* microalgae use carbon dioxide for biochemical processes, which is stored and converted in organic macromolecules; these ensure a cycle with zero emissions virtually. Therefore, microalgae cultivation can be a reasonable solution to reduce emission from fossil fuel plants. In this aspect, they can easily become integrated processes with other existing such as wastewater treatment, power plants, etc.

Table 1.4 Comparison between microalgae and traditional oilseed crops in terms of oil productivity and land required. Adapted from [11].

Commodity	Oil Productivity (L/ha)	Cultivable area required (M ha)	% of currently farmland (USA)
Corn	172	1,540	846
Soy	446	594	326
Canola	1,190	223	122
Jatropha	1,892	140	77
Palm Oil	5,950	45	24
Microalgae 30% oil	58,700	4.5	2.5
Microalgae 70% oil	136,900	2	1.1

1.4 CO_2 Capture

The use of fossil fuels leads, as is well known, greenhouse gases (GHG) release in the atmosphere, which determine a serious of negative effects for human and environment. Due to anthropogenic activities, the release of these GHG has resulted an increase of atmospheric carbon dioxide concentration, approximately 280 ppm from the year 1750 to 390 ppm in 2010 and 50% of this increase occurred in the last thirty years [18].

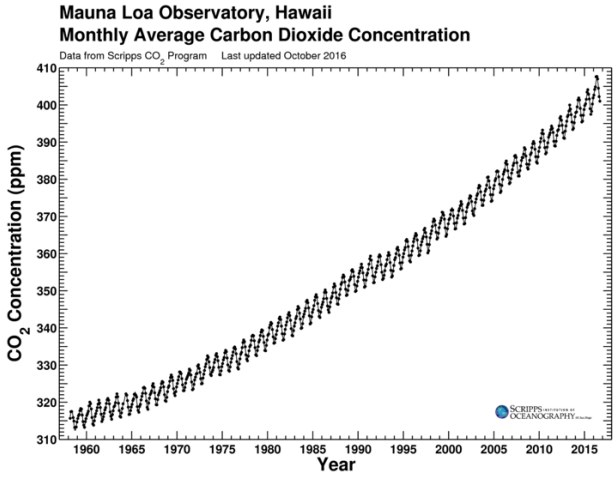

Figure 1.3 Monthly average atmospheric carbon dioxide concentration versus time at Mauna Loa Observatory, Hawaii (20 °N, 156 °W) [18].

Figure 1.3 shows the concentration of CO_2 in parts per million in the molar fraction (p.p.m.) from the 60s until today. This graph was produced by the Institute of Oceanography in San Diego by Ralph Keeling et al. [18]. However, the factor of major concern is not the same CO_2 concentration but growth velocity; this latter is more visible in Figure 1.4 that shows the concentration values of CO_2 in petagram (Pg) of Carbon and the cumulative production of industrial CO_2 from fossil fuel and cement versus time in units of PgC.

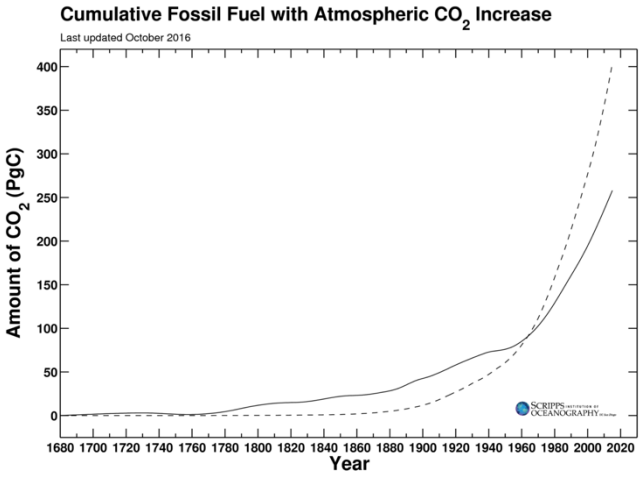

Figure 1.4 Solid Curve: Observed increase in atmospheric CO_2 in units of PgC. Dashed Curve: Cumulative production of industrial CO_2 from fossil fuel and cement versus time in units of PgC. [18].

Then, to reduce the greenhouse effect correlated with the temperature rise, the main target is to decrease the gas amount that caused this effect. One of geo-engineering technique considered is *Carbon Capture Utilization and Storage (CCUS)*, which requires CO_2 capture systems to the emission source directly. After capture, post-treatment and storage in liquid state, for example it can be used in chemical industry directly or geological storage by underground injection. Despite this latter technology is of high interest, geological conditions to be observed are complicated to manage: (i) depth greater than 800 meters such as to maintain CO_2 at supercritical state, (ii) sufficient porosity and permeability for CO_2 absorption, (iii) water absence

and (iv) impermeable material above the geological site. Currently there are three experimental site for this geological sequestration only and they related on oil industry: *Weyburn* (Canada), *Salah* (Algeria) and *Sleipner* (Norwegian off-shore). The amount of CO_2 captured is rather small, around one million tonnes per year and therefore this technology is not efficient economically [19,20].

However, to disposal large quantities of carbon dioxide the primary method is photosynthesis carried out by natural plants. It is the simplest, economic and spontaneous method that occurs naturally in the earth. Then, microalgae are part of this context. As already mentioned in presence ofall needed nutrients such as minerals, light and carbon dioxide, microalgae present high growth velocity compared to common natural crops [4]. Recent years have seen an increase of the interest on microalgae culture, in particular for CO_2 capture for these reasons [21]:

- growth rate and carbon dioxide fixation much higher than other natural crops;
- photosynthetic efficiency ten times circa higher than natural terrestrial crops;
- maximum carbon dioxide concentration. However, this must not be too high to inhibit the growth microalgae reaction.

Considering the high growth and productivity rates of microalgae through photosynthesis, it appeared clear that just the atmospheric carbon dioxide may not support the reproduction process. One possible solution could be employing the spent industrial gas steams coming from fossil fuels combustion, which contains on average 15% of CO_2 in volume Two important advantages could be in this way obtained: (i) water saving resulting from the employment of waste water and elimination of CO_2 removal unit thanks to the recycling of exhausted gas steams [21].

1.5 General selection criteria and microalgae species under consideration: *Phaeodactylum Tricornutum*

The selection of a particular microalgae species is a very complex process to manage considering that there are more than 10 million of species in the world. Every microalgae species has its own characteristics that strongly depend on cultivation system, operating conditions and so on. Consequently, there is no an absolute

parameter to prefer one species over another. Nevertheless, it may be worth analysing microalgae species in relative terms, focusing attention on the most important aspects.

Since the '90s were intensified the studies on various microalgae species, indicating for each species the natural characteristics depending on the use which they are intended [10]. In Table 1.5 are reported some characteristics to look on for microalgae choice and, for each characteristic is shown the benefit that may ensue.

Table 1.5 Desirable characteristics for microalgae cultivation. Adapted from [10].

Characteristic	**Benefits**
Growth velocity	competitive advantage; reduction of the required cultivation
Product contained	higher biomass value
Big cells/filaments	reducing costs of down-processing;
Wide tolerance of environmental conditions	small cultivation control;
CO_2 tolerance	high potential for CO_2 capture;
Shear stress tolerance	pumping and mixing less expensive;
Contaminants tolerance	growth in polluted water;
No self-inhibitors excretion	reducing of self-inhibition at high concentrations;

1.5.1 *Phaeodactylum tricornutum* microalgae species

In this work *Phaeodactylum tricornutum* is the microalgae species considered for the first mathematical modeling. Figure 1.5 shows various morphologies of this species selected. Biologically it is defined as a diatom, therefore it is a brown microalga, unicellular, eukaryotic and autotrophic which can live in fresh, salt or brackish water. It can be isolated live in colony, although the latter is much rarer to find; it can be found in coastal waters, rock pools, temperature climates and in habitats with large salinity fluctuations. It is mainly distributed in Europe and North America [22].

Generally, diatoms are divided into pinnate and centric basis according of their internal structure; *Phaeodactylum tricornutum* has a pinnate structure. During the life cycle it can have three different morpho-types dependent on environmental

conditions: oval cells, fusiform and triradiate rarely; the most common is the rod-fusiform of 25-35 µm in length and 3 µm of diameter [23].

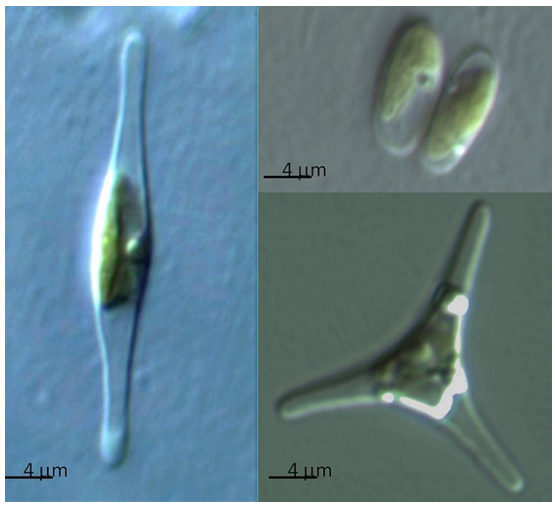

Figure 1.5 Micrographs of (clockwise from top right) oval, triradiate and fusiform *P. tricornutum* morpho-types [24].

Furthermore, depending on medium culture conditions *Phaeodactylum tricornutum* is capable to change its shape [25].

The characteristics that make this microalgae species one of the most studied are the following:

- It is a freshwater but it can tolerate high salinity; this it helps to avoid frequent bacterial contamination in large-scale production;
- High amounts of ω-3 fatty acids, particularly EPA (good for fish farming and for cardio-vascular diseases);
- pH and Temperatures conditions are reasonable for growing at our latitudes;
- High CO_2 affinity;
- Photo-adaptation strategy developing an increase of chlorophyll cellular content under light limit conditions. It means an almost constant photosynthetic efficiency and growth rate over a wide range of irradiance;
- Shortly biological age influence on lipid content.

1.6 Microalgae photosynthesis system

The biochemical process with which green plants and other organism produce macromolecules is the photosynthesis. Chemically, chlorophyll photosynthesis can be defined as a redox endothermic reaction in which atmospheric carbon dioxide and the metabolic water are converted into organic substances (carbohydrates, proteins, lipids mainly) and oxygen by means of solar energy. The chemical reactions series that constitute the photosynthesis falls within anabolic processes of organic macromolecules synthesis and it is completely opposite to reverse catabolism processes (i.e. oxidation). Photo-autotrophic microalgae exploit their photosynthesis to produce necessary sugars for its biosynthetic and energy metabolism [26]. This process takes place within chloroplasts that they are cellular organs present in the plants leaves and in microalgae cells; these contain specific photosynthetic pigments, i.e. molecular capable of light absorbing in a certain band of light visible. In the photosynthesis process chlorophyll plays the fundamental role between all other internal molecules [4].

1.6.1 Light-and Dark-phase reactions

Solar radiation ($E=h\nu$), is the primary energy source for biological reaction, but it must be provided in the appropriate range of wavelengths λ; photosynthetic organisms possess a limited absorption spectrum ranging from 400 nm to 700 nm, defined as PAR (photosynthetically active radiation). The overall reaction is the following [26]:

$$6CO_2 + 6H_2O + solar\ energy \rightarrow C_6H_{12}O_6 + 6O_2 \quad (1.1)$$

Through chlorophyll molecules, sunlight allows to convert six carbon dioxide molecules and six water molecules into sugars necessary for the plant life. Likewise, it creates also six oxygen molecules which it is a co-produced released into the atmosphere contributing to heterotrophic organisms lives fundamentally. However, the oxygen produced by the biomass it is a problem during microalgae cultivation since it may oxidize and destroy the same biomass. Nevertheless, the above reaction

is the overall process; indeed, photosynthesis involves a complex system of steps and intermediate reactions.

Generally, the chlorophyll photosynthesis is distinguished into two main phases, shown in Figure 1.6, namely:

- light phase, which requires light radiation and it is the phase in which they are synthesized high energy compounds;
- dark phase, which carbon dioxide is fixed for organic substances synthesis with the use of compounds synthesized during light phase [4].

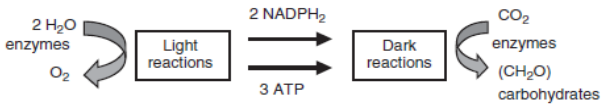

Figure 1.6 Chlorophyll Photosynthesis scheme [4].

During light phase, solar energy is converted into chemical energy and it leads to formation of biochemical reductant, the *nicotinamide adenine dinucleotide phosphate* (NADPH or NADPH2) and a very energetic compound, the *adenosine triphosphate* (ATP) [4]. Reactions of the first phase take place in the thylakoids membrane (lipid membrane within chloroplast), which contains 4 complexes protein: (i) photosystems, (ii) PSI and PSII, (iii) cytochrome and (iv) ATP as shown in Figure 1.7. Photosystem (i) indicates a pigments complex; in fact, it is a molecules cluster (200-300) containing photosynthetic pigments, chlorophylls and carotenoids primarily, which they have the task to capture the sunlight, absorbing incident photons. Figure 1.7 shows the process [27].

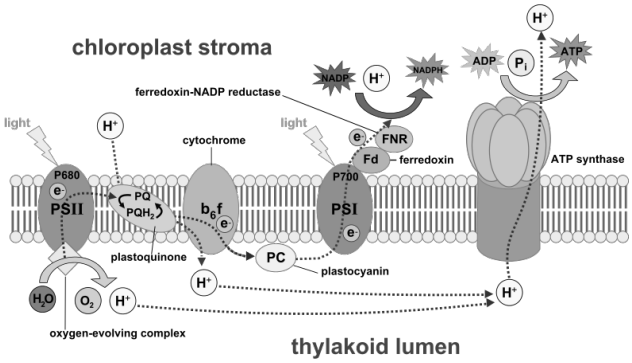

Figure 1.7 Thylakoid membrane photosynthesis: light-dependent reactions [27].

Photosystem take places following three consecutive process: (i) photosynthetic pigments excitation, (ii) photosynthetic electron transport and (iii) photo-phosphorylation [28].

During the first process (i) light photons are absorbed by photosynthetic pigments, which are organized in a complex antenna pigments. The photon absorption, as well as energy absorption $E=hv$, leads to the light energy conversion into electronic energy excitation, which the latter migrates by *inductive resonance*. The latter is a process during the pigment releases accumulated energy to come back to the stable conditions and, it gives the excited electron to another adjacent pigment and then it receives a stable. The second process (ii) relates to energy capture system; this function is performed by the two PSI and PSII transducer. These photosystems differ by wavelength, 680 and 700 nm respectively. These work in series and the electrons disposed from PSII are transported to PSI by redox reactions which take place within cytochrome; these reactions involve an increase of H+ ions concentration into membrane. Finally, in the third process (iii) it occurs that H+ ions accumulation inside the membrane causes the birth of a pH gradient between inside and outside membrane, such as to activate the ATP-asi that transports protons outside the same membrane. This entails ATP-asi structure changes which allow the *phosphorylation* of *adenosine diphosphate* (ADP) to *adenosine triphosphate* (ATP). The overall reaction of light phase, where can be observed water oxidation, it is shown below:

$$H_2O + P_i + NADP^+ + ADP + h\nu \rightarrow \frac{1}{2}O_2 + NADPH + H^+ + ATP \quad (1.2)$$

Regarding dark phase, the biochemical reductant NADPH and the high-energy compound ATP, which are synthesized during light phase, they are used to reduce carbon dioxide into organic compounds, according to the reaction shown below:

$$CO_2 + 4H^+ + 4e^- \xrightarrow{2\,NADPH\;3ATP} (CH_2O) + H_2O \quad (1.3)$$

The dark phase is a very complex mechanism and it was proposed by Calvin and Benson [4]. Carbon dioxide conversion occurs in the chloroplasts stroma and it follows three stages, so-called Calvin-Benson cycle:

- CO_2 fixation on an acceptor;
- ATP use and power reducing of NADPH coming light phase;
- CO_2 acceptor regeneration.

Although the dark phase name may be misleading, this term does not mean a process during the night rather it depends to sunlight since during the process it activates particular enzymes that they regulate the reactions.

1.6.2 Photorespiration

Night cellular respiration R and photorespiration P_r must be taken into account in the photosynthetic system response which it is expressed by following equation:

$$P_n(t) = P_g(t) - R(t) - P_r(t) \quad (1.4)$$

where P_n is the photosynthesis net of losses, while P_g is the gross photosynthesis. The night-time respiration velocity depends on algal species but it is observed that it can also vary by two magnitude orders from 0.01 to 0.6 d^{-1}. For example, diatoms are characterized by low value of R and high growth rates [29]. One of the simplest models that take into account the cellular respiration separates energy consumption in two elements: (i) metabolic rate m maintenance costs, independent from net photosynthesis; (ii) biomass synthesis costs, which depends on the net photosynthesis. This model is given by the following equation:

$$R(t) = m + \gamma P_n \quad (1.5)$$

where R is the metabolic energy consumption rate, m is the metabolic maintenance rate and γ is the dimensionless synthesis cost. Cellular photorespiration is a rival reaction to the chlorophyll photosynthesis dark phase; therefore, it is the opposite oxidation process. During this process, they consume oxygen to produce carbon dioxide, and guaranteeing the microorganisms nutrition. While photosynthesis can take place during day-time only, on the contrary photorespiration takes place both day and night but, during the night carbon dioxide remains within microalgae, while during the day it is consumed by photosynthesis [29].

In order to characterize the photosynthesis, the parameters used are: photosynthetic activity P, i.e. the amount of oxygen produced in time unit and, the photosynthetic efficiency $\alpha=P/I$, i.e. the ratio between photosynthetic activity and light intensity I, as shown in Figure 1.8.

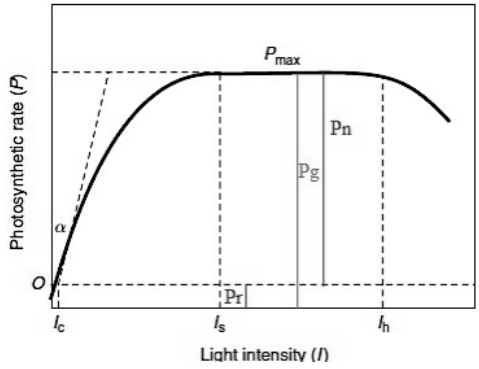

Figure 1.8 Photosynthetic rate as a function of light intensity [29].

Figure 1.8 shows the variation curve of photosynthetic activity to irradiance function, where I_c, I_s and I_h represent compensation intensity, saturation intensity and photo-inhibition intensity, respectively. Values lower than Ic prevails the photorespiration activity, instead for higher values than Ic prevails the photosynthesis. Figure 1.8 also shows the quantity: gross photosynthesis P_g, photorespiration P_r and net photosynthesis P_n. Generally, the respiration rate corresponds to 5-10% of the photosynthesis equivalent rate to the light saturation. At very low light intensities,

$I<I_c$, the respiration rate balance the photosynthesis rate and cells are not able to grow [29].

Then, P-I curve can be divided into three sections:

- *limited radiation section*, where the photosynthetic rate increases with increasing to the irradiance. Then, the absorption photons rate determines the velocity which electrons are transferred from water to carbon dioxide;
- *saturated radiation section*, where photosynthesis is independent from the irradiance. Photosynthetic rate reaches its P_{max} maximum value, therefore the velocity which the electrons are absorbed exceeds the same that they are transferred from the water to carbon dioxide;
- *photo-inhibition section*, where the increase irradiance involves photosynthetic efficiency reduction. Under these conditions it happens a photo-protection process that reduces the photosynthetic PSII activity and it increases energy dissipation to prevent damage of the same [29]. In the PSII section the excess energy is dissipated through alternative reaction for macromolecules synthesis [30].

The P_{max} value indicates the photosynthetic capacity and it depends by the reactions that take place during the dark phase; in fact, very high light intensities are inhibitory for the photosynthetic activity. According to some authors, the temperature parameter is the environmental factor that it most influences the photosynthetic capacity [12,31]. However, the overall balance of O2 and CO_2 from and to the external environments it is in favour to photosynthesis. It occurs because part of absorbed carbon dioxide is fixed as cellulose form and lignin in the wall dead cells. High interfacial gas-liquid exchange area, i.e. small bubbles, high CO_2 concentrations and appropriate mixing they promote CO_2 transport from gas to the medium and the O2 leakage [31]. It is worth remembering that only a fraction (PAR) of the solar spectrum is useful for photosynthesis (400 to 700 nm). Generally, PAR spectrum is measured in *microEinstein* per second per square meter ($\mu Em^{-2}s^{-1}$), where one Einstein is energy per photon mole, where it carried by a monochromatic light beam, regardless of their frequency; then, an Einstein is equal to $6.022 * 10^{23}$ photons [32]. In massive cultivation the trend is to work close to P_{max} value but before I_s value [29].

1.7 Microalgae growth

In the context of biological reactions, it is possible to make a first distinction of the same reactions: (i) aerobic if they require oxygen and (ii) anaerobic in absence of oxygen.

Microalgae growth occurs through the second process, i.e. by aerobic actions that it leads to increase of microalgae cells in the medium culture. When environmental conditions are favourable and there are all nutrients, biomass size of single cell increased. This phenomenon results to DNA increase up to its duplication and, consequently, a cells number increase. The dynamics growth knowledge is a fundamental parameter to be able to choose a specific microalgal species. The higher velocity with which increases algal population, the higher biomass amount produced per time unit. In terms of velocity growth, the *doubling-time* t_d *[s]* is the parameter which indicates biomass development; this it is the time required to obtain the double adult cells number than the original cell number as shown in the following equation:

$$N(t) = N_0 2^{\frac{t}{t_d}} = N_0 2^n \tag{1.6}$$

where N_0 is algal cell number at time zero and n is the cell duplication number. Time t_d is experimentally determined on various algal strains and, if they are known N_0 and n it is possible to obtain the cell number N at a generic instant t [33]. Equation (1.6) can be rearranged by replacing *N(t)* variable with *C(t)*, i.e. cells concentration:

$$C(t) = C_0 2^{\frac{t}{t_d}} = C_0 2^n \tag{1.7}$$

It is easier to control cell concentration compared to the cells number. Regarding the doubling-time, in the case of algal growth, it assumes values in the hours order less than 24 hours.

Another indicator of biomass development it is the *specific growth rate* μ which is express as time inverse [s^{-1}]. This parameter is indicative of the biomass increase per time unit and, it depends on the number of cells present and it is linked to the doubling-time by the following equation:

$$t_d = \frac{l_n(2)}{\mu} = \frac{0.693}{\mu} \tag{1.8}$$

From the specific growth rate μ it is possible to define the volumetric biomass productivity P_{bv} as algal mass produced per time unit and cultivation volume system, as shown in the following equation:

$$P_{bv} = \mu C_{bm} \tag{1.9}$$

where C_{bm} is the biomass concentration [g/L]. The productivity can be expressed on volumetric basis [g/(L d)] or cultivated area basis [g/(m^2 d)], as shown in the following equation:

$$P_{bv} = \frac{(P_a d)}{1000} = \mu C_b \tag{1.10}$$

where d represents the cultivation system depth in meters. Frequently, the information provided for the conversion are not enough and, the typical problems are:

- Surface productivity is provided without indicating the system depth;
- It is provided the specific growth rate in absence of biomass concentration.

In the context of massive microalgae cultivation, the specific growth rate μ and thus, biomass productivity, are two fundamental parameters which however change depending upon the process kinetics [34]. Currently there is no an accurate classification of the properties for each species. The researches of scientific community have indicated from time to time the algal strain to be used in function of culture conditions, operating parameters, etc. [33].

1.7.1 Cultivation system

Generally, algal biomass growth is conducted in two cultivation systems: *indoor* systems when the cultivation system is confined inside a building and *outdoor* systems outside the building. Regardless this type of cultivation system, there are three different operating regimes: *batch*, *fed-batch* and *continuous*.

1.7.1.1 Batch

Batch cultivation is a method used when the aim it is to obtain a small biomass production with well-defined biological characteristics. The process starts with a preparatory phase during they are loaded all necessary nutrients and a small portion of microorganisms; the latter is called *inoculum* which can reach 10% of reaction volume.

During batch cultivation, the microalgae growth follows the trend shown in Figure 1.9.

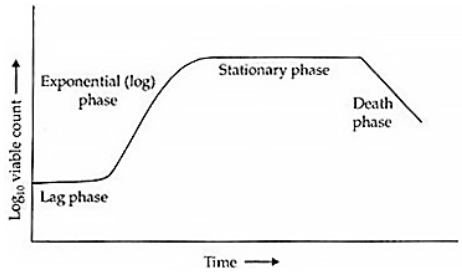

Figure 1.9 Algal growth curve in batch conditions [4].

As shown in Figure 1.9, during this microalgae growth it can distinguish four phases: *lag-phase* or adaptation, *exponential growth phase*, *stationary phase* and *death phase* [4]. It is also noted that the specific growth rate μ corresponds to the curve slope and it remains positive supposing high values. This trend continues until it has the nutrient exhaustion or toxic substances accumulation into the cultivation system. Regarding the extensive microalgae cultivation, it is convenient to operate along the stationary phase, i.e. at constant slope, by adjusting microalgae concentration, nutrient, oxygen and ensuring sufficient light to the metabolically active cells.

In these conditions, the specific growth rate depends to the external light flux solely, according to the following relation:

$$\mu = \mu_{max} \frac{I}{I + K_I} \tag{1.11}$$

where K_I is the semi-saturation light constant, i.e. the photon flux density necessary to obtain $\mu=\mu_{max}/2$ (same irradiance dimension). Furthermore, with fixed light conditions and system geometry, it holds the following equation [34]:

$$IA = \mu X \frac{V}{Y} \tag{1.12}$$

where I is the irradiance [$Jm^{-2}h^{-1}$]; A is the irradiated surface [m^2]; V is the culture volume [m^3]; X is the biomass concentration [kg/m^3] and Y is the biomass growth yield [kg/J]. The Y yield is typical of algal species and it is assumable as a constant in the equation. In the equation (1.12) it is noted that varying X it also varies the specific growth rate μ. Combining equation (1.11) and (1.12) and by solving for I, it is possible to calculate the light energy necessary to obtain the desired concentration X [34].

1.7.1.2 Continuous

Continuous cultivation is used to obtain high biomass production. In this case, during biomass growth, the medium is supplied to the system continuously, while the harvest can be performed continuously or intermittently when the biomass reaches a certain threshold value.

Regarding the case of continuous biomass harvest it is possible to make a mass balance in order to determine the parameters on which depends the specific growth rate:

$$\frac{d(VX)}{dt} = FXi + FX + \mu XV - K_d XV \tag{1.13}$$

where F is the volumetric flow rate of medium culture and K_d is the cell decay constant. The various terms of equation (1.13) are: the variation of active mass cells present in each instant to time, biomass flow rate input and output, generation velocity and biomass disappearance.

It defines *broth residence time* inside the system by the following equation:

$$\tau = \frac{V}{F} \tag{1.14}$$

However, it is its inverse relation which it is taken into account, i.e. the *dilution velocity* or *dilution rate* given by the inverse of residence time:

$$D = \frac{1}{\tau} = \frac{F}{V} \tag{1.15}$$

Assuming that the culture system is agitated perfectly, no volume effects and assuming steady-state condition, the input-flow will be the same of output-flow, obtaining at the end:

$$\frac{dX}{dt} = 0 \tag{1.16}$$

$$\mu = D \tag{1.17}$$

Richmond et al. claim that the achievement of steady-state it is independent of culture initial conditions and, once achieved, it tends to be self-regulating. Moreover, they claim that it is theoretically possible to fix any reasonable specific growth rate different to zero, by varying the dilution rate *D* [4].

1.7.1.3 Fed-batch

Fed-batch cultivation consists in an intermediate cultivation between the continuous and discontinuous culture. In this case the volume is changing over time because there is an input but not output of mass, thus the design will have to be very accurate. However, the feed flow rate is such ensures the progressive filling in order to adapt the volume to the biomass growth. The fed-batch cultivation is widely used for the mass production of microalgae on industrial-scale and it operates in a quasi-steady state condition. The medium culture is maintained for long periods, by taking a sample of about 20-30% from time to time, and by restoring the volume with enriched aqueous medium. In fact, the harvest does not take place continuously but only when the concentration reaches a prefixed value at the end of process, according to the microalgal species. The main advantage of the fed-batch cultivation is the simplicity of operation that it allows the application to bioreactor with high volume [4].

1.7.2 Cell kinetics

Regarding the biological reactions of microalgae cultivation, it is important to investigate the process kinetics, in order to predict the behaviour of the cultivation system during its evolution. The cell kinetics is formed by three processes: (i) active cellular generation, (ii) cellular decay and (iii) substrate disappearance.

In the first process (i), the kinetic equation that describes the active biomass generation it is the following:

$$r_x = \mu X \tag{1.18}$$

where r_x is biomass generation velocity per time unit volume [kg/(m3*s)]. The specific growth rate depends on the conditions in which the environment is located, i.e. temperature, pressure, nutrients concentration, etc. Fixing the temperature, the dependence of μ from each substrate it is provided by Monod:

$$\mu = \frac{\mu_{max}}{K_s + s} s \tag{1.19}$$

where s is the substrate concentration [kg/m^3], μ_{max} is the specific maximum growth rate [s^{-1}] and K_s is the substrate concentration that it provides $\mu_{max}/2$ value [kg/m^3]. Figure 1.10 shows the Monod equation. In this equation, it is possible to identify two extreme sections: if s is equal to zero then μ is equal to zero and r_x is equal to zero consequently. In the absence of biomass substrate, the generation reaction cannot take place.

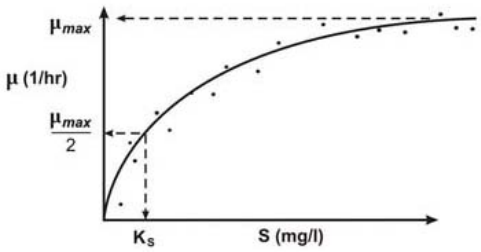

Figure 1.10 Monod equation diagram [4].

Increasing the substrate concentration, the specific growth rate μ increases initially with a linear trend up to tend to an asymptotic value of μ_{max}. This second

condition is due to the existence of a limiting substrate for each cell, typically carbon dioxide, but also nitrogen, phosphorus, oxygen etc.

The parameters, K_s and μ_{max}, are obtained experimentally, through different measures; indeed, reporting the values measured on the Monod diagram, it is obtained K_s as slope of the linear trend, while μ_{max} is obtained from the asymptote. Substituting Monod equation (1.19) to the kinetic equation (1.18) it is obtained:

$$r_x = \frac{\mu_{max}}{K_s + s} sX \tag{1.20}$$

It is worthwhile to note that this criterion is quite general. For example, after saturation phase during the microalgal cultivation it will have a starving phase until the operation will be interrupted. *Fed-batch cultivation* are always operating in this condition by controlling the limiting substrate concentration.

Regarding the cellular decay (ii), its kinetic equation it is the following:

$$r_d = K_d X \tag{1.21}$$

where r_d is the cell decay rate per volume unit and time [kg/(m3*s)], and K_d is specific rate of decay [s^{-1}]. The latter parameter can be determined by the *half-time* t_h that it is opposite of the doubling-time, which represents the period necessary to halve cells number:

$$K_d = \frac{\ln(2)}{t_h} \tag{1.22}$$

Finally, it should be considered the third process (iii), namely *substrate disappearance* and its kinetic equation it is shown below:

$$r_s = q_s X \tag{1.23}$$

where q_s is the disappearance substrate rate per time unit and active biomass [kg/(kg*s)]. In the latter case, q_s is not a specific rate and it does not have the dimensions of s^{-1}. To obtain qs it is necessary to consider all the mechanisms that they lead to substrate consumption, which they are listed below:

- *Biomass growth*. Substrate becomes a biomass part and it is consumed to generate new cells, then it is introduced the quantity:

$$Y_{XS} = \frac{kg\ of\ new\ biomass\ generated}{kg\ of\ substrate\ consumed\ to\ generate\ biomass} \tag{1.24}$$

then, the substrate consumption rate will be:

$$r_s = \frac{r_x}{Y_{XS}} = \frac{\mu X}{Y_{XS}} \tag{1.25}$$

- *Biomass maintenance*. One substrate portion is used to keep alive existing biomass, then it introduces the quantity:

$$m_s = \frac{kg\ of\ necessary\ substrate\ maintenance}{kg\ of\ living\ biomass\ per\ time\ unit} \tag{1.26}$$

then, the substrate consumption rate will be:

$$r_s = m_s * X \tag{1.27}$$

- *Biomass creation*. One substrate part reacts directly to provide a different product from biomass, without contributing to the growth or maintenance of the same, then it introduces the quantities:

$$Y_{PS} = \frac{kg\ of\ secondary\ product\ generated}{kg\ of\ substrate\ consumed} \tag{1.28}$$

$$r_p = \frac{kg\ of\ secondary\ product\ generated\ obtained}{time\ and\ volume\ unit} \tag{1.29}$$

then, the substrate consumption rate will be:

$$r_s = \frac{r_p}{Y_{PS}} = \frac{q_p X}{Y_{PS}} \tag{1.30}$$

Eventually, the global substrate consumption rate is provided by the following kinetic equation:

$$r_s = \left(\frac{\mu}{Y_{XS}} + m_s + \frac{q_p}{Y_{PS}}\right) X \tag{1.31}$$

In the equation (1.31) the brackets term represents q_s quantity. It is worth noting that without obtaining extracellular products, last term q_p/Y_{PS} will be zero in the q_s definition.

1.7.3 Operating parameters

Every natural environment is the result of various physical and chemical factors, such as abiotic factors, which create the existence conditions of a given environment and then, influencing organisms can establish themselves, as well as the mutual

relations to be established. In a general environment for each factor present there are two values, maximum and minimum value, in which life is possible. The environmental conditions, which in any way they slow down the growth of one or more groups of organisms, they are known as *limiting factors*. These factors are of fundamental importance, both to understand the reasons of certain phenomena [4].

According to Monod equation (1.19), the specific growth rate μ depends on the limiting factor for the growth, which it varies in relation to the system. Regarding microalgae cultivation, the main factors that influence the growth it can be grouped as:

- *Abiotic*: light, temperature, nutrients concentration, oxygen, carbon dioxide, pH, salinity, presence of toxic chemicals;
- *Biotic*: pathogenic species such as bacteria, fungi and viruses, in competition with other microalgae;
- *Operating*: mixing, depth of the culture medium, harvest frequency and addition of adjuvant substances for microalgae growth.

Then, for microalgae growth the essential elements are light, carbon dioxide, water, and nutrients. It is noted that some of these essential elements they serve to increase the strength of microalgae to contamination, such as bicarbonate [35].

1.7.3.1 Biomass concentration

The productivity expression provided by Monod equation it provides a linear dependence between productivity and biomass concentration, i.e. the *cell density* expressed as microalgae mass per volume culture broth unit. This dependence approximates the real culture behaviour until all microalgae cells are at the same conditions. It happens by the following conditions: (i) low biomass concentrations and (ii) small thickness of reaction section.

However, these conditions cannot occur since the microalgae saturation light intensity corresponds to 1/5-1/10 of incident solar radiation at midday and, even a brief exposure of the culture to this radiation it would damage the same culture [4]. In addition, inside the culture system it is established a phenomenon known as *mutual*

shading, i.e. mutual shading between the various adjacent algal cells. This phenomenon is present at high cell concentrations. For sufficiently high biomass concentrations, the system volume can ideally be divided into two areas, which they are called *photic* and *dark section*, respectively. The mutual shading alters the previous Monod equation but it allows to estimate how cell concentration influences the light field inside the culture. At low biomass concentrations, the mutual shading effects is almost absent, and it is favoured the photo-inhibition; while at high biomass concentrations it is reduced the photons amount available for every single microalgae cell. Therefore, there is an optimum concentration of biomass, *Optimal Cell Density OCD*, so that, for fixed system geometry, light intensity and operating conditions, an optimal light field will be associated and, it is possible to maximize the productivity, as shown in Figure 1.11 [4].

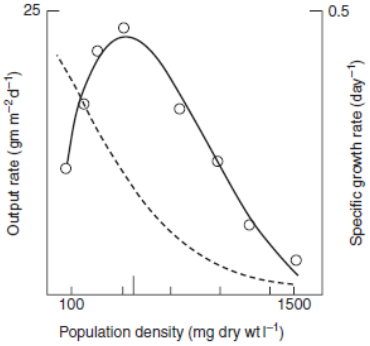

Figure 1.11 biomass concentration influence on specific growth rate (dotted line) and productivity (solid line). The markers identify the values experimentally measured [4].

1.7.3.2 Nutrients

The cultivation of a certain algae species and its stability it depends on the quality culture broth control and all necessary nutrients, which the most important are *carbon*, *nitrogen* and *phosphorus*. During the first cell growth phase, the nutrients balance is

very important, and in particular, these nutrients must be in abundance during the exponential growth phase also [12].

The *carbon* absorption, an essential substrate for organic macromolecules synthesis, it occurs through the carbon dioxide that it is present in the atmosphere; besides, many algae species absorb carbon dioxide at fluid phase with partial pressures of *0.1 - 0.2 kPa* [31]. Considering CO_2 as carbonaceous source, with an intracellular carbonaceous fraction of *0.45*, the minimum amount of CO_2 which must be supplied is *1.65 g* per algae biomass gram. Typically, CO_2 is fixed to *1.8 g* per gram of microalgae. Typically, in the atmosphere the carbon dioxide partial pressure is 0.04 kPa. Therefore, the fresh air is not sufficient to supply the carbonaceous fraction request, and it is required a CO_2 stream enriched [31]. Then, carbon dioxide supply is very important to control pH of the medium as well.

Nitrogen, which constitute 7-10% of the percentage by weight of microalgae, it is an essential element for the protein. They are effective vehicles of nitrogen: ammonium salts, nitrates and urea, while NOx and N2 air they are not bioavailable generally. Overall, microalgae have a limited capacity to produce nitrogen compounds, where the culture is characterized by a high amount of nitrogen. An alternative cultivation technique could be the so-called *nutritional stress*; for example, working under nitrogen nutrients deficiency. In these conditions, due to the degradative phenomena, in photosynthesis the fixed carbon is not used for proteins synthesis but for lipids or carbohydrates production. This stress condition results in a protection mechanism that it stimulates oil synthesis production by inhibiting the further biomass growth [31,36]. The lipid content increase may be up to 50% by weight and, alternatively it can work in phosphorus deficiency, despite the effects are less prominent. The latter is provided in the form of phosphates placed in large excess, since in the presence of metal ions they tend to form complexes, making minor the phosphorus bioavailable. The latter usually represents 1% or less of dry biomass [37].

Regarding a high species sample the optimal combination of *nitrogen* and *carbon dioxide* for microalgae cultivation is the following:

- freshwater microalgae present a maximum productivity with nitrogen concentrations between the range of 285-427 mg/L and CO_2 concentration up to 15% and rare cases up to 70%;
- seawater microalgae grow under any nitrogen concentration (from 4 to 20mg/L; best at 4mg/L) and CO_2 concentration (from 400 ppmv to 150.000 ppmv) [38].

Therefore, where there are multiple substrates, it is obtained a generalized Monod equation, as shown by the following relation:

$$\mu = \mu_{max} \prod_{i=1}^{n} \frac{s_i}{K_{si} + s_i} \tag{1.32}$$

Cell composition can be a useful indicator of nutrient limitation. In fact, microalgae cells are constituted by a well-defined atomic ratio between the various fundamental constituents. The minimum nutrient required can be estimated through the following *approximate molecular formula* for microalgae biomass:

$$CO_{0.48}H_{1.83}N_{0.11}P_{0.01} \tag{1.33}$$

In general, the nutrients doses calculation (*carbon dioxide, nitrogen* and *phosphorus*) is conducted using the following equation:

$$Q_{nutrient} = \frac{PM_{substrate}}{PM_{element}} X_{element} \tag{1.34}$$

where $PM_{substrate}$ and $PM_{element}$ they are the molecular weight of the treated substrate from the cells and the molecular weight of the chemical element, respectively. $X_{element}$ represents the fraction by dry basis weight of the specific component into the algal biomass [17].

1.7.3.3 Light

Algal photosynthesis is strongly affected by the incident sunlight, therefore, it also influences the biomass productivity [4,39]. Light is the primary factor that it influences the algae cells growth and reproduction of algal cells since it constitutes the primary energy source [4]. In order to optimize algal biomass growth processes it

is necessary an optimal use of light incident. As already said, photosynthetic organisms have a reduced absorption spectrum called *PAR*, *photosynthetically active radiation* [4].

In the algal photosynthetic system, they are required 8 PAR photons to fix one CO_2 molecule and to convert it into organic macromolecule; it provides about 12% of maximum efficiency [40].

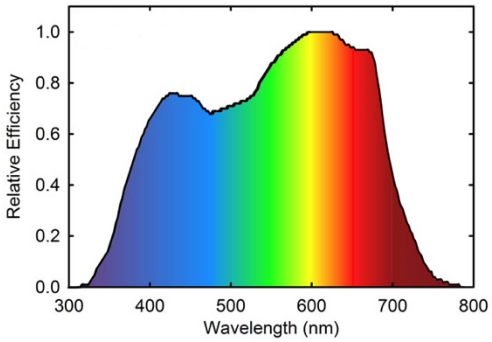

Figure 1.12 Photosynthetically active radiation, PAR, spectrum [4].

PAR spectrum includes an area between *400* to *700 nm*, as shown in Figure 1.12. Within this area, it is possible to distinguish four different bands:

- Blue-violet (*400-490 nm*), it has a medium effect on photosynthesis;
- Green (*490-560 nm*), band less photosynthetically active;
- Yellow (*560-590 nm*), similar to previous band;
- Orange-red (*590-700 nm*), it is a very active band. Red is the green complement.

Therefore, photosynthesis behaves differently within PAR spectrum. The main areas of focus are the two extreme bands, violet-blue and orange-red; the latter allows to obtain maximum absorption [26].

Microalgae have a particular mechanism known as *photoacclimation dynamic*, i.e. a mechanism that varies the photosynthetic pigments content to light energy range, both at high light level (*HL, high light*) and low level (*LL, low light*) [26,29]; in these two conditions, *HL* and *LL*, microalgae behaviour is opposite totally:

High Light regime:

- high photosynthetic rate;
- low chlorophyll content per unit biomass;
- high levels of auxiliary pigments;
- low photosynthetic efficiency;

Low Light regime:

- low photosynthetic rate;
- high chlorophyll content per unit biomass;
- low levels of auxiliary pigments;
- high photosynthetic efficiency.

The offsetting between photosynthesis and photorespiration it is recorded in many algal species, with I_c values in the range *10-20* $\mu Em^{-2}s^{-1}$ [41]. When the radiant energy is limiting for the microalgae growth it comes to *photo-limitation*; indeed, at high radiation intensity, above a certain critical value, it comes to *photo-inhibition* or *light-saturation* [1,26]. This phenomenon is due to chloroplasts inability to use the solar light at high intensity.

Typically, microalgae species reach saturation levels for light fluxes oscillating in the range *100-500* $\mu Em^{-2}s^{-1}$, often at values of *200* $\mu Em^{-2}s^{-1}$ (*1* $\mu E = 6.022*10^{17}$ photons). It is worth noted that the maximum solar radiation flux is about *2000* $\mu Em^{-2}s^{-1}$ at the equator. Therefore, it is necessary to avoid high light fluxes, since it damage the photosynthetic mechanism, inhibiting the same biomass life and productivity. To avoid this phenomenon, one of the useful parameters is mixing. This parameter must be such as to maintain microalgae cells in suspension, guaranteeing a continuous microalgae renewal that receive the light; this phenomenon is known as *alternate shading* [12]. Then, light energy abundance may be a limiting phenomenon for the same microalgae growth.

Regarding the microalgal species considered in this work, equation (1.11) which correlates the specific growth rate μ and the irradiance I, it was used for fitting of the data experimentally obtained on the *P. tricornutum* species; in fact, Figure 1.13 shows

the specific growth rate of μ at various value of irradiance I. It is noted that specific growth rate is greater in aerated conditions rather than non-aerated conditions; this is possibly due to the limited extent of CO_2 [12].

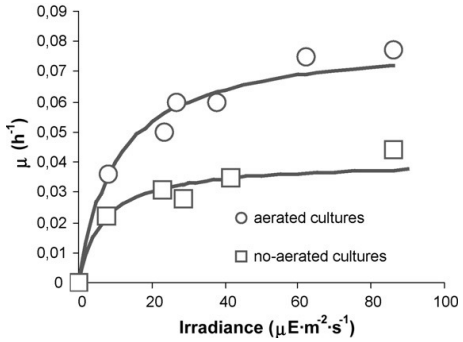

Figure 1.13 Specific growth rate of μ at various value of irradiance I in aerated conditions and non-aerated conditions [12].

1.7.3.4 Light-Dark cycle

Depending on biomass concentration, in the algae system is established the *mutual-shading* phenomenon between microalgae cells; this means that algae cells are submitted to cyclic illumination. For high microalgae cells density, the system volume can be divided into two part: *photic*-and *dark zone*. In the *photic zone*, the lighting conditions are equivalent to those in which light does not restrict microalgae growth and photosynthesis. In the *dark zone*, intensity light ranging from zero to immediately value below to light saturation. Due to the turbulence flow, in a dense culture of microalgae cells, fluid move cyclically between dark-and illuminated zone. These cycles are defined light-dark cycles [30]. Light dark cycle is a sort of *light dilution*, where it is reduced the average light intensity for each microalgae cell. Microalgae have the ability to use high intensity light if they are only subjected to intermittent cycles at high frequency, because light-dark cycles frequency increase increases microalgae cell yield. In fact, lighted microalgae replace dark cells, ensuring that the light-dark cycles frequency increase the number of flashes light for each cell. Thus,

photosystems I and II (PSI and PSII) have the ability to regenerate themselves in the short dark time interval following the light excited state. However, if the dark time interval is too long the beneficial effects are cancelled completely [42].

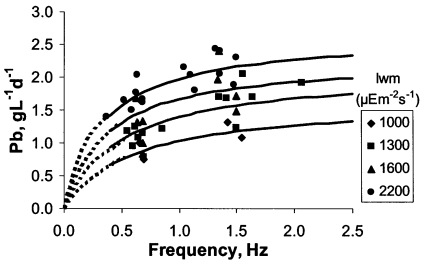

Figure 1.14 Light dark cycles frequency effects to volumetric biomass productivity with different external mean irradiance [39].

Therefore, to increase the biomass amount in unit time, it is necessary to increase microalgae cells exposed to the light in unit time, i.e. to increase light dark cycles frequency. However, considering this frequency-effect an intermittent artificial light source is not economically advantageous compared to using solar light.

Most efficient mean is to increase the turbulence to maintain the micro-algae in suspension, improving gas exchange and nutrients distribution. Likewise, a more effective alternative could be the variation of bioreactor size reducing the diameter in tubular photobioreactors and reducing the depth in the open system to reduce optical path length (OPL) [4].

Regarding *Phaeodactylum Tricornutum* species, in order to obtain high productivity values, some experimental tests have confirmed that the optimum light dark cycles frequency is about *1-2* s^{-1}, as shown in Figure 1.14 [39].

1.7.3.5 Oxygen concentration

During microalgae cultivation, oxygen is a parameter to be monitored and it is a by-product of photosynthesis process. This parameter should be maintained equal to or lower than the saturation value in the air at standard conditions (*P = 1atm, T =*

25°C) *9.1 g/m*^{3}, such as to avoid problems and to contribute heterotrophic organism life. Instead, high oxygen concentration, i.e. beyond the saturation level, it becomes a poison for the microalgae cells, inhibiting growth and thus forming the *photo-oxidation* phenomenon [26]. In closed cultivation systems, it becomes difficult to extract the oxygen produced during photosynthetic process; on the contrary, in open systems, oxygen creates problems due to low gas-liquid transfer capacity [43].

Productivity increase in relation to dissolved oxygen reduction was shown in several studies, which show that the excessive oxygen presence causes a drastic reduction of the photosynthetic activity. Figure 1.15 shows the effect of oxygen concentration on photosynthetic activity and biomass concentration, respectively [39].

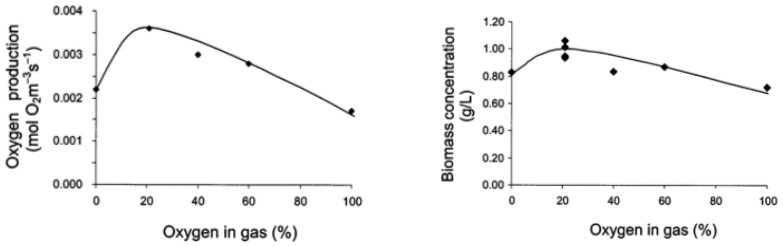

(a) (b)

Figure 1.15 (a) Effect of oxygen concentration on photosynthetic activity and (b) biomass concentration [39].

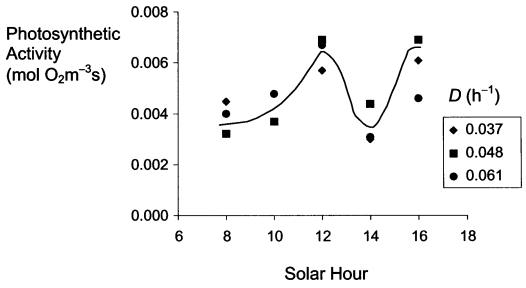

Figure 1.16 Photosynthetic activity variation according to solar time and dilution factor [39].

The dissolved oxygen (DO) is also function of several external parameters, temperature, dilution factor and fluid-dynamic regime [39]. Figure 1.16 shows photosynthetic activity variation according to solar time and dilution factor. Between 8am and 10am, photosynthetic activity increases rapidly, due to light intensity increase, up to reach a maximum value; then, it decreases between 12am and 2pm due to photo-inhibition. The photosynthetic activity grows again until 6pm but with a different slope than the first phase.

Figure 1.17 shows solar irradiance variation as a function of time; it shows a trend similar to that of oxygen. From 6pm the dissolved oxygen concentration is reduced due to the decrease of irradiance. It also notes that there are differences between summer and spring season: the oxygen dissolved reduction in the spring is less marked than in the summer, since the irradiance is less intense and it causes less photo-inhibition.

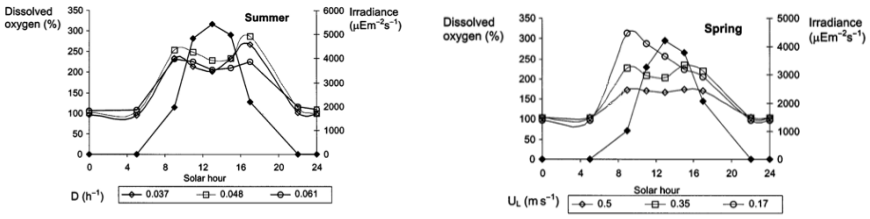

(a) (b)

Figure 1.17 Solar irradiance variation with the dissolved oxygen concentration at different solar hour: (a) data summer and (b) data during spring. [39].

In addition, it was found that liquid surface velocities below *0.17 m/s* cause a lowering of photosynthetic activity on the circadian period. This microalgal cells corruption phenomenon can be attributed to combined effect of high irradiance and high oxygen concentrations [39].

On the photosynthetic efficiency, the oxygen concentration effect was also analysed at irradiance values below the photo-inhibition limit: there is an oxygen

concentration limit, beyond which the photosynthetic efficiency is reduced. Every microalgae species has a characteristic concentration value. Regarding the *Phaeodactylum Tricornutum* the limit value is about *22 - 27 g/m*^{3}. A mathematical model which describes this aspect it is shown in the following equation:

$$\overline{RO_2DO_2} = (1 - \frac{DO_2}{KO_2})^z \tag{1.35}$$

where DO_2 is the oxygen dissolved content, KO_2 is the inhibition constant, i.e. concentration at zero photosynthetic rate, z is the shape factor to obtain experimentally (it is comprised in the range 2-6 and it depends by the species examined) and RO_2DO_2 is the normalized photosynthetic activity [43].

Finally, it is necessary to remove the excess oxygen in the cultivation system. In closed systems one possible method is by stripping with air or CO_2, while in open systems, that they are connected directly with the external environment, oxygen has a slower removal kinetics, obviously.

1.7.3.6 Temperature

Temperature parameter influences algae metabolism and biomass productivity, consequently. Below 0 °C, the ice water crystallization leads to a volume increase, which determines the biological membranes breakage and therefore microalgae cellular death. In theory, temperature parameter is the property that regulates thermal energy transfer from one point to another, but it also influences the biochemical kinetics reactions [31].

Other important aspects, linked to the temperature parameter, they are the condensation-and evaporation cycles of broth culture, and therefore the volume variation also. Regarding *Phaeodactylum Tricornutum* species, *E. Bitaubé Pérez et al.* have carried out several studies on a particular cultivation system by recording temperature influence in two different operating conditions: with-and without aeration. In the aerated system, experimental results have shown experiments have shown condensation of the water present into the air ($T < 10°C$), however at higher temperatures ($T > 20$ °C), the same water is evaporated and it is removed by the

gaseous stream taken. On the contrary, non-aerated systems do not show these evaporation-and condensation cycles.

Regarding temperature influence on the specific growth rate, from the experiment results it showed that in the aerated conditions, the specific growth rate was high, but over *30 °C* it is not detected cell growth for this microalgae species. In general, the link which exists between temperature and specific growth rate it is shown in Figure 1.18:

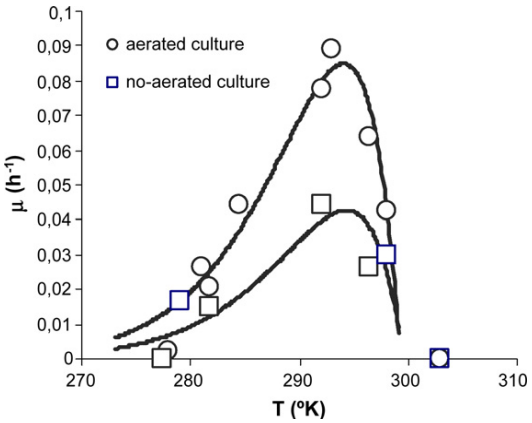

Figure 1.18 Specific growth rates at different temperatures for aerated and non-aerated cultures [44].

Considering the latter aspect, the specific growth rate μ was adapted by the following Arrhenius equation type:

$$\mu = Ae^{-\frac{E_a}{RT}} - Be^{-\frac{E_b}{RT}} \tag{1.36}$$

where E_a and E_b are the activation energy for the growth and cell degradation, respectively [$kcal\ mol^{-1}$]; R is the universal gas constant [$kcal\ mol^{-1}K^{-1}$]; T is the operating incubation temperature [K], A and B are the frequency factors [h^{-1}]. The equation X can be modified in this form:

$$\mu = A_0 e^{-\frac{E_a}{RT}\frac{T-T_0}{T_0}} - B_0 e^{-\frac{E_b}{RT}\frac{T-T_0}{T_0}} \tag{1.37}$$

where A and B were converted into A_0 and B_0, that they are the specific growth velocity and microalgae cell degradation at the reference temperature T_0 [44].

There are two temperature limit values which correspond, (i) the maximum temperature value associated with a high specific growth rate, and (ii) a minimum temperature value below which the metabolism stops or it is not activated (i.e. photo-inhibition). Moreover, the temperature parameter is linked to photosynthetic activity since as temperature increase the PSII is turned, and consequently it is increases saturation light value, and then the maximum photosynthetic rate. In conclusion, with a fixed irradiance value, there is an optimal temperature that maximizes the photosynthetic activity. In conclusion, with a fixed irradiance value, there is an optimal temperature that maximizes the photosynthetic activity.

Every microalgal species has an optimum temperature range. There are three categories of microalgae as a function of temperature: (i) *mesophilic* species, with temperature range between *20 and 30 °C*; (Ii) species *psychrophiles*, with an active metabolism in a range between *0 and 15 °C*; (Iii) *thermophilic* species, with the optimal temperature range between *35 and 60 °C* [4]. Therefore, to control the temperature parameter, there are different possibility: water evaporate by exploiting the natural temperature lowering; a thermostatic bath via a secondary circuit to control the microalgae culture temperature; simple external shading (with a possible heat exchanger) etc. [1,31,40].

1.7.3.7 pH

Every microalgae species owns a pH range for the maintenance of its life cycle. For the most algae species the optimal pH range is between 7 and 9. However, there are some exceptions such as the cyanobacterium Spirulina platensis with an optimal pH value between 8 and 10. The variation of pH growth range, out of the optimal range, it can result in a complete culture collapse due to the destruction of the cellular processes [1]. This parameter determines the balance between carbonaceous species in solution and the total inorganic carbon in the medium consumed by microalgae cells [1]. In this sense, the pH can be viewed as the direct expression of CO_2 concentration dissolved in solution, and then one of the photosynthetic reaction reagents. In fact, into the water carbon dioxide forms carbonic acid and it contributes

to the acidification of algal solution. CO_2 balance without water solution are shown below:

$$H_2O + CO_2 = H_2CO_3 \quad (1.38)$$

$$H_2CO_3 = H^+ + HCO_3^- \quad (1.39)$$

$$HCO_3^- = H^+ + CO_3^{2-} \quad (1.40)$$

On-demand CO_2 injection could avoid the problems about the optimal pH range, however the excessive variation of the same pH value can reduce microorganism productivity [43].

The pH control can be made in two ways: (i) air-CO_2 mixture injection on-demand that it is integrated with a basic solution, NaOH typically. The first to acidify the solution and the second to increase the pH value; (ii) utilization of biological buffers substances as so-called TAPS and TAPSO. However, their composition could induce bacterial growth such as to affect the metabolism of microalgae. Normally, it is adopted the first pH system control [1].

Referring to *P. tricornutum* species, E. Bitaubé Pérez et al. [44] have studied the specific growth rate variation as a function of the pH parameter. Then, different experimental tests were carried out by changing pH from time to time; These results are shown in Figure 1.19.

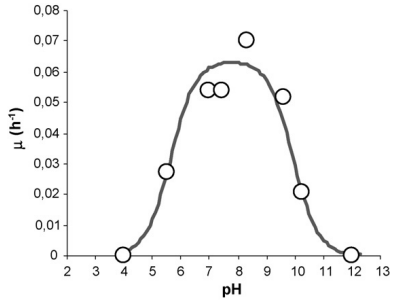

Figure 1.19 Specific growth rate as a function of pH parameter and the mathematical model proposed for these variations [44].

The experimental data show a maximum optimal μ value with a pH value of about 8 for this microalgae species, and a typical bell-shaped trend in reference to pH

variation of the same microalgae growth. Therefore, the mathematical model proposed with the experimental data obtained it is the following [44]:

$$\mu = \frac{\mu_{max}}{1 + (\frac{[H^+]}{K_1} + \frac{K_2}{[H^+]})} \tag{1.41}$$

where *[H+]* is the proton concentration (*mol/l*) and K_1, K_2 are the kinetic constants (*mol/l*).

It was observed a reduced of almost *75%* of the photosynthetic activity with pH values higher than *9* and less than *5.5* for the *Phaeodactylum tricornutum* species [44].

1.7.3.8 Mixing

Normally, the microalgae living in their natural habitat with a cell density of about 10^3 *cells/ml* and with distance between cells to cells of *1000 µm*. However, in algal cultures at high concentration, the cell density can reach 10^9 *cells/ml* that it may result in: (i) a drastic reduction of light transmission, (ii) an increase of CO_2 consumption rates, (iii) an increase of dissolved oxygen and (iv) a rapid increase of temperature. Therefore, mixing parameter is an important characteristic to consider in the microalgae culture for:

- preventing algal cells sedimentation;
- ensure uniform average exposure to the light and an uniform distribution of all nutrients;
- improve heat transfer to avoid thermal stratification;
- improve gas exchange between air and medium;
- promote pH control.

According to cultivation system size and typology, the mixing can be achieved by pumping, aeration, mechanical stirring or combination among the latter. However, it is noted that mixing too high, where the mechanical stirring and gas bubble disruptions may cause high hydrodynamic stress, that it can inhibit microalgae metabolic and growth [1].

Then, the best mixing adopted it is the insufflation of air-CO_2 gas mixture, and its value it is measured through mixing index D_z. The latter is defined as the reciprocal of Peclet dimensionless number *Pe*:

$$Pe = u\frac{L}{D_z} \tag{1.42}$$

where *u* is the linear average fluid velocity and *L* is the characteristic system size. The Peclet number is obtained through the use of known graphic *1/Pe-Re*, and if *Pe* is known, it is obtained D_z. A typical value of Peclet number ranging from 3 to 600; in the limit case of piston flow regime D_z is equal to 0 and *Pe* is infinite [12].

1.8 Photobioreactor

Microalgae cultivation can be classified into two main categories: laboratory scale and large-scale or massive cultivation. In lab-scale the microalgae cultivation is employed mainly to preserve algal strain purity and to ensure adequate volumes of inoculum for the scale-up. In addition, it is possible to cultivate microalgae in lab-scale for their own maintenance but also for their characterization.

The cultivation system can be classified according to the location too. (i) Indoor system, if the algal biomass production is conducted within a building. They are expensive systems, such as it is necessary, for example, to ensure different light than solar. (ii) As an alternative, there are the outdoor systems, i.e. cultivation systems carried out outside the building. These systems are appeared cheaper since it is possible to use the sunlight from the energy point of view [45]. Regarding configuration and design criteria for the cultivation system there are another two categories for the industrial cultivations: open systems and closed systems or properly said open-and closed photobioreactors. The latter are less in contact with the external environment with the aim to avoid possible contamination. The photobioreactor choice depends upon a number of factors such as: culture volume, temperature and climatic conditions, energy consumption, maintenance, etc. Therefore, it is necessary to take into account the growing microalgae requirements and economic aspects.

1.8.1 Open system

In these *open photobioreactor*, there is a direct contact between culture and external environment. To date, the algal biomass production is limited to a few species and it is conducted in open ponds mainly, since they represent the most established and mature technology. Generally, these bioreactors are characterized by large areas, but it is noted that there are different types depending on shape, size and agitation system. Therefore, it is possible to classify the open systems: (i) *natural and artificial ponds*, (ii) *circular ponds*, (iii) *inclined systems* and (iv) *raceway ponds*. The natural open ponds are the simplest culture system between the various open systems, since it is simply a large bath in which there is the aqueous medium; mixing and handling are guaranteed by natural phenomena, such as wind. On the contrary, the artificial open ponds are composed of artificial pools, shallow and without an artificial agitation system in order to recreate the natural environment ponds. The technology of these systems is very simple, however, the operating and maintenance costs are onerous due to the high dimensions of the ponds and there is insufficient absorption of atmospheric CO_2. Circular-and inclined open ponds are similar to the artificial open ponds where it changes mainly the handling system.

In its place, the open ponds system that it is better suited to outdoor industrial cultivation is the raceway ponds [46]. Figure 1.20 shows an operating diagram of this system. It is a several circular channels characterized by a sinuous path, where the medium is recirculated and it is mixed by the use of one or more wheels, *paddlewheel*; frequently, they are equipped with special plastic covering to reduce mechanical stress on the biomass culture. During daylight hours, near the paddlewheel the medium is continuously introduced, and then to be harvest upstream the same. During night-time there are no biomass harvest but a small reintegration of evaporated medium. The paddlewheel operates continuously in order to ensure movement and to avoid sedimentation of the microalgae cells on the raceway bottom section. Most of raceway systems are created with plastic material, greatly reducing implementation costs [45].

During the design of raceway ponds one key parameter is the channel depth that it should be between *0.15* to *0.5 m*, in order to ensure an effective penetration of solar radiation. Depths exceeding *0.5 m* it reduces the photosynthetic activity since not all

microalgae are able to come into contact with light source. Depths less than *0.15 m*, the productivity is low as it would not be possible to impose the system an adequate turbulence; in these conditions, the viscous forces are very high, and therefore, it is difficult to obtain an optimal mixing. The limited depth influences the surface/volume ratio and the surface productivity, consequently [4].

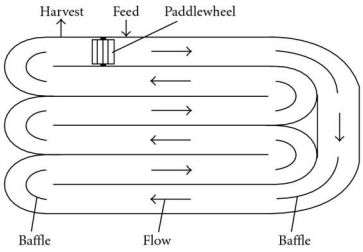

Figure 1.20 Operating diagram of raceway ponds [44].

The necessary powers to the movement of microalgae culture it can be estimated about *6 kW* for plants of about *1000* m^2; if there are an appropriate combination of pumps and slopes it can reduce the previous value to *2 kW*. In addition, the agitation system of the raceway allows the atmosphere gas exchange, through the carbon dioxide absorption and oxygen removal [5].

The main disadvantages of open ponds systems are: inability to ensure adequate illumination to the entire algae culture, inability to maintain uncontaminated culture conditions and the energy costs for medium movement. In addition, there are further problems such as: biomass loss due to medium evaporation, thermal control given to the evaporation and the eventual CO_2 limitation and its absorption for the microalgae culture (H_{CO2}= $1.64 \cdot 10^3$ *atm l/mol*) [46].

Over last years it has grown the interest towards another approach to the intensive cultivation of microalgae that it is towards close photobioreactors, owing to the negative factors that influence microalgae cultivation in the open ponds in terms of product cost and productivity [46].

1.8.2 Closed Photobioreactor

This type of photobioreactors can be both indoor and outdoor. The latter uses sunlight as primary energy source for the photosynthesis, and it can be defined as a culture system in which a large light portion, greater than 90%, it not directly hits culture surface, but it must pass through the transparent walls that surround it. Therefore, in some cases, indoor closed photobioreactors are used with artificial light (lamps, fiber optics, etc.), however, with the disadvantage to increase equipment cost greatly. These closed photobioreactors have a volumetric productivity even three times higher than to the open ponds. However, the industrial diffusion of this microalgae production technique is limited due of the high operating-and investment costs. Therefore, the aim of current research is to study different construction design of these close photobioreactors and to analyze all necessary parameter to optimize costs. These latter parameters are listed below:

- *Lighted surface to reaction volume ratio (S/V)*: this ratio influences light penetration depth and it is crucial to improve photobioreactor photosynthetic efficiency. Higher this ratio, greater biomass productivity since it is bigger algae amount exposed to light source respect to the total microalgae present. In this case, the biomass concentrations will be higher, and then the costs are lowered for the separation treatments at end cycle. However, high S/V ratio involves a very inefficient system at industrial scale: oxygen production, carbon dioxide absorption and nutrients consumption they are increased significantly, and then this may lead to negative effects on the culture stability [4].
- *Inclination and orientation:* these closed photobioreactors may be oriented and inclined in such a manner to maximize the irradiance on the bioreactor surface [40].
- *oxygen accumulation:* it is one parameter that it limits the photobioreactors scale-up primarily. Oxygen production is correlated with the volumetric productivity. Therefore, at high productivity it corresponds the danger to reach toxic oxygen concentrations dissolved due to the algal species.

- *mixing parameter:* it is necessary a good mixing to prevent microalgae sedimentation, to avoid thermal stratification, to ensure nutrients homogeneous distribution and to avoid oxygen accumulation. This biomass handling may be effected by centrifugal pumps, mechanical stirrers immersed in the culture; however, the latter ensure high mixing levels but they can damage microalgae cells due to mechanical stress. A viable alternative is the Air-Lift pump, since it does not have mechanical parts such as to stress microalgae cells mechanically. The culture fluid dynamics also influences average irradiance absorbed by microalgae and light-dark cycles alternation, then it affects the productivity directly [1].
- *temperature parameter:* optimal temperatures ensure high biomass productivity. Whereas open ponds are limited to the low temperatures during early morning hours, closed photobioreactors are limited by the high temperatures that it can be reached during the hottest hours. Then, it is necessary to provide a cooling unit, since the simple water evaporation may not be enough. The most used thermal unit are water sprayers and cooling tanks. A low heat exchange coefficient of the photobioreactor construction material may be useful to perform a heat exchange without direct contact to the microalgae culture [31].
- *carbon dioxide supply:* carbon dioxide is the main nutrient for microalgae production. As acid gas, the carbon dioxide reduces the pH into the culture. This parameter must be maintained under neutral conditions with microalgae vital conditions; it limits the maximum amount of carbon dioxide to be used in these reactors. In order to ensure an adequate carbon dioxide supply in the photobioreactor one way is to maintaining high the CO_2 residence time. However due to high velocity in the photobioreactor, the carbon dioxide residence time is insufficient for absorption and a high amount of carbon dioxide is wasted.
- *photobioreactor construction material:* photobioreactor materials must be transparent, sterile, with high mechanical strength, resistant to weather conditions, stable chemically and low-cost. Material cleaning is another important criterion for choice of the photobioreactor. Then, in the materials

to be selected the main parameters observed are refractive index, transparency, density and heat transmission coefficient. Usually, the most used materials are polymethylmethacrylate (PMMA), polyvinyl chloride (PVC), low density polyethylene (LDPE) and polycarbonate (PC) [12].

Here below are described some of the closed photobioreactors used.

1.8.2.1 Flat-plate Photobioreactor

These photobioreactor are designed to achieve an efficient solar radiation use conceptually. These photobioreactors are made of transparent plastic material panels placed in parallel or in series to obtain a very high S/V ratio [1]. The productivity values reached are rather high, up to *1.7* times greater than bubble column, which it will be described further below [47]. In addition to series- and parallel arrangement, these photobioreactors can be oriented vertically or horizontally respect to the solar radiation. The dimensions are quite different, and they have heights less than *1.5 m* and widths smaller than *0.1 m*, typically. The handling is provided by air-injection and, for the thermal control it is possible to insert a cooling jacket on the reactor sides [35]. The combination of small reactor size and high photosynthetic activity giving rise to some problems of oxygen accumulation and nutrient supply. This is the main disadvantage of flat-plate photobioreactors, despite oxygen accumulation is lower than in a tubular photobioreactor [48].

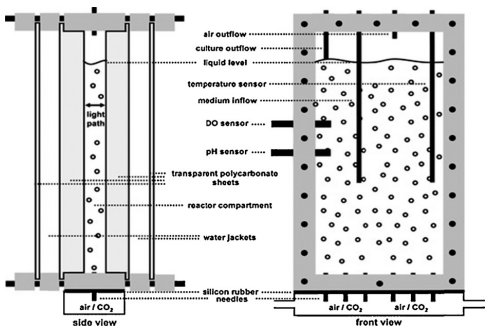

Figure 1.21 Schematic diagram of flat-plate photobioreactor [48].

Due to the high consumption rate of CO_2 it is difficult also to supply the same. Then, the industrial interest towards these photobioreactors is reduced since in terms of cost and flow control they are less competitive compared to the other photobioreactors. Figure 1.21 shows a schematic diagram of flat-plate photobioreactor.

1.8.2.2 Plastic bag Photobioreactor

These plastic bag photobioreactors operate in batch, generally. Each plastic bag is filled with a given culture amount and carbon dioxide; it is measured gas content inside the bag, and after a certain period, biomass is picked up and this bag is reused [1]. When they occur fouling and contamination problems, bag replacement operations are provided [35]. Figure X shows a typical flat-plate photobioreactor plant (picture from *Algenol's photobioreactors* -Florida).

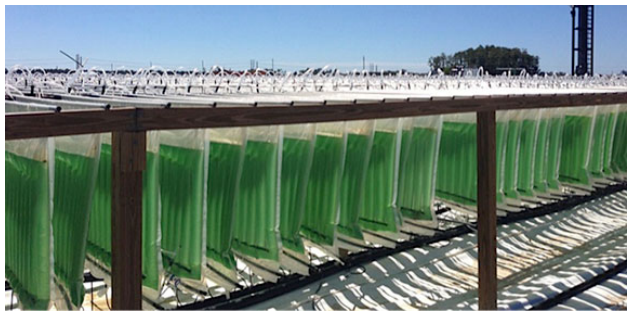

Figure 1.22 Typical flat-plate photobioreactor plant (picture from *Algenol's photobioreactors* -Florida) [48].

These bioreactors have the same versatility of flat-plate photobioreactors and they are characterized by a more simple and economical technology. One of main advantages it is the low oxygen accumulation since biomass productivity is lower than to flat-plate photobioreactor. However, one the main defects is related to mechanical strength of plastic bags; it is foreseeable that stress accumulation involves their breakage in the bottom section. Other disadvantages are the inadequate mixing and the large-scale disposal of these plastic used materials [1].

1.8.2.3 Tubular Photobioreactor

Tubular photobioreactors are better suited to mass cultivation of microalgae, probably. Generally, they are made of glass or transparent plastic materials and according to the geometry and handling system there are three main groups: vertical- horizontal- and helical photobioreactor, where the latter technology is a combination of the first two. These closed photobioreactors provide high lighting surface and biomass volumetric productivity reaches high values, even higher than $2.76\ gl^{-1}day^{-1}$, typically [48]. However, the main limits are: (i) mass transport of oxygen within system; (ii) thermal control since it is not enough the simple water evaporation; (iii) pH to control with frequent cycles of CO_2 release, which it involves costs increase; (iv) geometric parameters for the scale-up: by increasing the diameter decreases the interfacial area, and hence the illuminated surface, while a length increase exalts oxygen accumulation. Then, it is necessary to find a compromise [48].

1.8.2.4 Bubble column and Air-Lift Photobioreactor

Essentially, vertical tubular photobioreactors are constituted by transparent cylindrical vessels in which the carbon dioxide, which is bubbled from below into the medium by appropriate nozzles, perforated tubes or sparger, it carries out a double function: (i) to create the required turbulence to ensure the correct light-dark cycles and (ii) to provide the gas necessary for microalgae growth. There are two types of these vertical photobioreactor: bubble column and Air-Lift Reactor (ALR) [1]. Figure 1.23 shows a schematic diagram of these two types of photobioreactors. These two bioreactors are differentiated for the fluid flow; bubble column is a simple vessel in which gas injected generates a mixing and it comes into contact with the medium. Instead, due to a density gradient that generates a natural recirculation, ALR is divided into two channels, and the fluid-path is determined by (i) an ascent channel design, named *riser*, and (ii) a downward channel, named *downcomer*. In addition, ALR have three different configurations as may be noted in Figure 1.23 (2.A-B-C); case A is

called *internal-loop concentric Air-Lift*, where gas is injected by central tube, which represents the riser where it ascends gas-liquid mixture. Consequently, liquid phase descends in the annular section, i.e. the downcomer, free-gas hopefully; case B is called *internal-loop split Air-Lift*, where gas is injected by one vessel side and the liquid phase descends in the opposite side thanks to a central baffle; case C is called *external loop Air-Lift* where riser and downcomer are two separate pipes, and they are connected at the top and bottom section. In the top section there is a degaser zone which allows gas-liquid separation phase [1]. Definitely, *Air-Lift systems* are a very promising multiphase reactor for industrial applications.

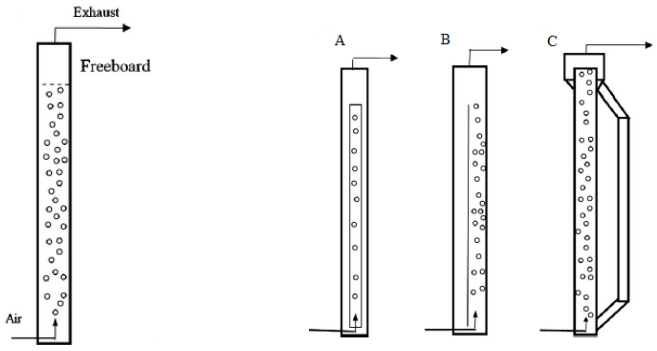

Figure 1.23 Schematic diagram of (1.) bubble column and (2.) Air-Lift Reactor ALR: *(A) internal-loop concentric Air-Lift; (B) internal-loop split Air-Lift; (C) external loop Air-Lift* [1].

In general, the main advantages of using these vertical reactors for microalgae cultivation listed below:

- good mixing of the gas-liquid phase;
- no issue by oxygen accumulation due to degaser section;
- no cells damage. In fact, the shear stress is not focused in one point but it varies uniformly into the photobioreactor.

The main disadvantage of this type of equipment is the scale-up; to process high flow rates and to ensure efficient gas-liquid mass exchange, the photobioreactor diameter should be very large and this would result in a low S/V ratio [1].

1.8.2.5 Horizontal Tubular Photobioreactor

These photobioreactors represent the culture system characterized by high productivity and high *S/V* ratios, and they can treat large culture flow, and thus obtaining high cell concentrations [1]. These photobioreactors are constituted by transparent horizontal pipes arranged in order to maximize sunlight absorption. That provision allows to exploit a larger volume than other culture techniques at equal occupied land. A schematic diagram of a typical horizontal tubular photobioreactor it is shown in Figure 1.24.

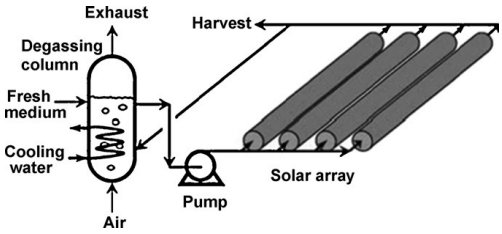

Figure 1.24 Schematic diagram of a typical horizontal tubular photobioreactor [47].

In general, diameter pipe is lower than *0.1 m* and, this involves high turbulence values [46]. A key element for the design of these photobioreactors is handling system: normally, it is a mechanical pump or an Air-Lift system and it is placed in a separate section than the photobioreactor section [1].

Compared to the use of a common pump, an Air-Lift pumping system for the horizontal tubular photobioreactors ensures: (i) culture isolation from outside environment; (ii) low microalgae cell damage due to handling system without mechanical parts and (iii) excess oxygen removal from the photosynthesis [1].

1.8.3 Comparison between open and closed systems

Table 1.6 shows a qualitative comparison between open and closed systems. Open ponds systems are less expensive to construct than closed systems and they have a higher lifetime and they do not present scale-up problems. However, (i) they need a very large free-surface; (ii) it is impossible to maintain the pristine algal species; (iii) it has low values of productivity and (iv) gas-liquid mass transport is very low. These latter factors result in high cost in the biomass post-processing.

Table 1.6 Comparison between open and closed systems.

Parameter	Open System	Closed System
S/V ratio	High	Low
Algae species	Low	Flexible
Criteria of species selections	Competition	Resistance
Resistance	Contained	Concentrated
Harvest efficiency	Low	Facilitated
Cultivation period	Limited	Extended
Contamination	Possible	Unlikely
Water losses	Constant evaporation	Prevented
Light use	Low	Optimizable
Gas transfer	Low	Controllable
Temperature control	Evaporation	To implement
Significant costs	Mixing and O2 control	Temperature control
Scalability	Easy	Onerous
Investment	Low	Very high

Regarding the closed systems, the main advantages are listed below: (i) high photosynthetic efficiency; (ii) small system size; (iii) possibility to maintain the environment culture uncontaminated, and (iv) to work in sterile conditions. Also, it is possible to prevent CO_2 losses, biomass and to ensure a more accurate parameter control. This results in high biomass productivity. The main disadvantages are due to the oxygen accumulation into the system, pumping- and temperature control costs [1,47,48].

Considering all these aspects, the closed systems seem to be the most effective cultivation technique for intensive microalgae production, although the open ponds technology cost is lower than closed photobioreactors, significantly.

1.8.4 General criteria of microalgae culture pre- and post-treatment

Usually, in microalgae cultivation it is performed a specific procedure:

- inoculum preparation from small microalgae samples;
- vitro cultivation with increasing volume in the first growth period;
- reactor filling with inoculum;
- condition maintenance to obtain optimal concentration;
- reduce of humidity by drying;
- biomass preservation and regular system cleaning;

After these processes in series, the algae biomass is preserved according to the final objective to achieve:

- oil fraction extraction to obtain bio-diesel;
- exhausted biomass for bio-gas or electricity;
- downstream treatments to obtain carbohydrates or proteins;

and so on.

2 MATHEMATICAL MODELING OF MICROALGAE CULTIVATION IN A CLOSED PHOTOBIOREACTOR

As previously introduced in Chapter 1, the main work purpose is to design a pilot plant for microalgae production. This chapter presents the conceptual plant scheme and its block flow diagram (BFD) necessary to the mathematical modelling of the cultivation process. Taking into account the cultivation choice of the *Phaeodactylum tricornutum* microalgae species, and then to obtain microalgae productivity for tubular photobioreactors principally, mathematical models will be implemented on the basis of all parameters introduced in previous Chapter 1.

2.1 BFD & Pilot Plant Concept Design

Figure 2.1 shows the conceptual pilot plant scheme developed for this BIO4BIO research project that it focuses on microalgae cultivation.

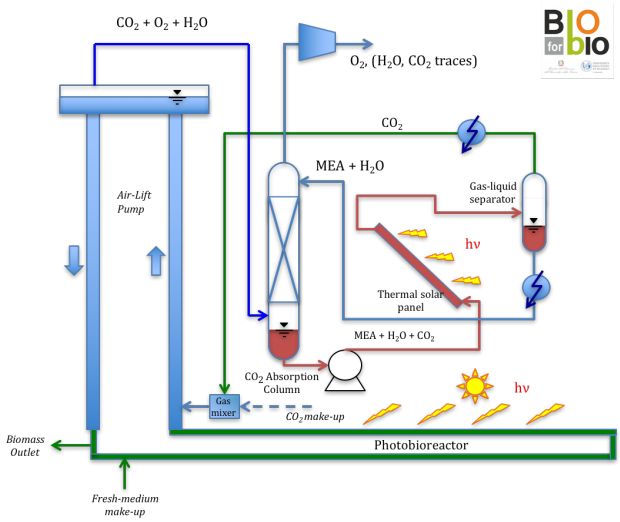

Figure 2.1 BIO4BIO Project - Conceptual pilot plant scheme for microalgae cultivation.

As can be seen, compared to a typical microalgae cultivation plant, in this new plant the innovative sections are the handling system by Air-Lift pump and the CO_2 recovery section by mono-ethanolamine (MEA) by absorption/desorption. In summary, the several plant sections are described as follows:

- *Photobioreactor section*: in this pilot plant, photobioreactor pipes are of horizontal type exposed to sunlight (outdoor system). Pipe construction material must be low-cost and characterized by high solar radiation transparency for the photosynthesis biomass process; therefore, low density polyethylene LDPE was chosen. PBR pipes are suitably connected by two collectors in such a way to connect inlet and outlet section.
- *External loop Air-Lift section:* the main components are riser, downcomer and degaser. In the riser section, it ascends the medium coming from the photobioreactor section with an air-CO_2 gas mix stream via a sparger. The separation between gas and liquid phase it takes place in the degaser section. Instead, liquid phase descends in the downcomer which it can contain small gas bubbles that have left no the liquid phase.
- *Make-Up section:* from downcomer, the liquid phase enters in this section, where it comes out one portion of the same at high microalgae concentration and it enters a fresh medium current in order to respect mass balances; final output liquid stream will be sent to the photobioreactor in order to continue the production cycle.
- *Chemical separation section:* this section comprises two chemical absorption and desorption columns where the input flow is the gas phase coming from the degaser section and the mono-ethanolamine (MEA) water solution. Pure oxygen stream and CO_2 gas stream are the outputs from the first and second column, respectively. This latter will be re-circulated in the riser. In addition, a solar thermal panel is inserted to the heating of the *MEA-H_2O-CO_2* mixture.

Then, a *block flow diagram* (BFD) of the pilot plant is shown in Figure 2.2. Hereinafter, a detailed description of the patch followed by microalgal culture.

By selecting photobioreactor inlet as starting point, it can observe that the medium containing microalgae and all necessary nutrients for their growth, they enter photobioreaction zone, where the photosynthesis process takes place by solar radiation and it has biomass cell growth, oxygen production as co-product and carbon dioxide consumption.

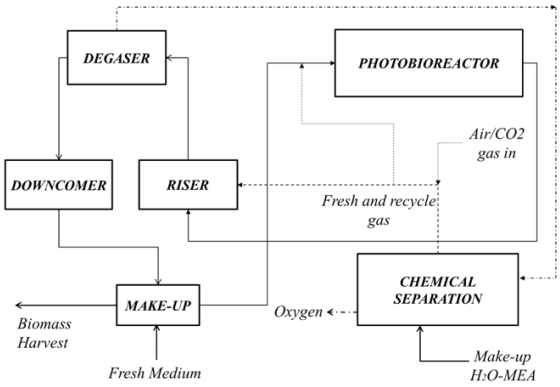

Figure 2.2 Block flow diagram (BFD) of the pilot plant for microalgae cultivation (solid and dashed lines for liquid- and gas phase, respectively).

The photobioreactor output flow is sent to the riser which it ensures to send gas stream (*air*-CO_2 mix) also. Then, a multiphase system it is generated where liquid flow is the continuous phase, and gas flow is the dispersed phase. The oxygen gas stripping takes place along the riser height from the liquid phase together with the presence of CO_2, and a partial water evaporation that it will allow a lowering of temperature, simultaneously.

The output riser flow is sent into the degaser section, where it takes place the gas-liquid phase separation. The output liquid flow from this degaser, it descends along the downcomer without gas phase. The density difference between liquid phase in the downcomer and the two-phase in the riser section, it represents the force for the fluid recirculation, i.e. it is established a natural circulation in the system.

The output liquid flow from the downcomer is sent to the make-up section; in this last section, it occurs the biomass recovery and the fresh medium culture reintegration, in order to maintain constant conditions in the photobioreaction environment.

Finally, the gas stream from the degaser section, containing oxygen, carbon dioxide and water vapour essentially, it is removed and it is sent to the CO_2 Recovery Unit. This last section, which will be analysed in section 2.5 extensively, it has a mono-ethanolamine (MEA) aqueous solution input current and at the output it is obtained a pure oxygen stream and a MEA-CO_2 mix stream that it is recycled in the system.

Definitely, a mathematical modeling of that system is complex for these reasons: (i) it is a biological complex system where the phenomena depend on a high variables number, and they vary from case to case within biological species; (ii) instantaneous mass balance resolution is required together with momentum and energy balance equation; (iii) the closed system includes a recirculation and (iv) the solar radiation intervenes in the photosynthesis reaction drastically.

Mass balance, momentum, energy equation and the productivity mathematical models are shown in the following section according to the different parameters for the various pilot plant units.

2.2 PBR Unit

The photobioreactor is the main section of the entire pilot plant. In this phase, although it is the new twisted helical system, the horizontal tubular photobioreactor type was chosen for the purposes of mathematical modeling of microalgae biomass production. Therefore, this photobioreactor choice will lead to (i) light-dark cycles frequency decrease, (ii) turbulence decrease respect to a helical configuration and (iii) a decrease of the heat transfer coefficients, consequently.

Consider an infinitesimal control volume as shown in Figure 2.3.

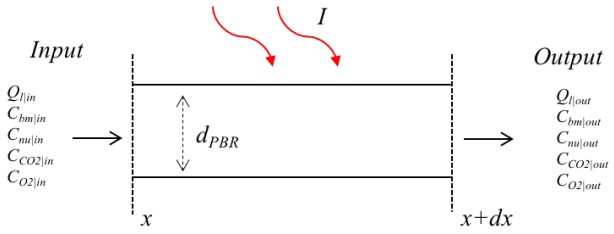

Figure 2.3 Infinitesimal photobioreactor control volume.

where Q_l, C_{bm}, C_{nu}, C_{CO2}, C_{O2} are the medium culture, microalgae biomass concentration, nutrients concentration, CO_2 concentration and O_2 concentration at input and output section, respectively. Instead, the external irradiance is I and d_{PBR} is the photobioreactor diameter.

The photobioreactor modeling requires the resolution of mass, momentum and energy balances. A general global balance, both in quantity- or velocity terms, it is given below:

$$I + G = O + A \tag{2.1}$$

where terms I and O are the input and out flow rate, respectively. The term G represents the generation phenomena (positive) or the disappearance phenomena (negative) within control volume. Finally, the last term A represents the accumulation of a generic entity examined. All these terms can be expressed in quantity or velocity terms, as already mentioned.

2.2.1 Mass balance

In quantity terms and dynamic conditions, it is possible to obtain a general mass balance taking into account microalgae biomass, carbon dioxide, oxygen and nutrients. Then, considering a continuous system regime and by setting a Δt time interval, they take into account two preliminary hypotheses: (i) negligible radial concentration gradients due to a high radial diffusion velocity, as to assume a constant concentration along each section, and (ii) axial dispersion due to negligible mass transport. Therefore, this system is considered as a *Plug Flow model*.

$$(VC_{bm})|_{t+\Delta t} - (VC_{bm})|_t = (VC_{bm})|_x - (VC_{bm})|_{x+\Delta x} + P_{bmv}\Delta t S \Delta x \quad (2.2)$$

$$(VC_{CO_2})|_{t+\Delta t} - (VC_{CO_2})|_t = (VC_{CO_2})|_x - (VC_{CO_2})|_{x+\Delta x} - r_{CO_2}\Delta t S \Delta x \quad (2.3)$$

$$(VC_{O_2})|_{t+\Delta t} - (VC_{O_2})|_t = (VC_{O_2})|_x - (VC_{O_2})|_{x+\Delta x} + r_{O_2}\Delta t S \Delta x \quad (2.4)$$

$$(VC_N)|_{t+\Delta t} - (VC_N)|_t = (VC_N)|_x - (VC_N)|_{x+\Delta x} - r_N \Delta t S \Delta x \quad (2.5)$$

where V is the volume culture (m^3), C_i is the mass concentration (g/m^3), r_{O2} is the O_2 production velocity ($g/m^3 s$), P_{bmv} is the volumetric productivity ($g/m^3 s$), S is the lateral surface of the tubular photobioreactor (m^2), L is the pipes length (m) and r_{CO2} is the CO_2 consumption velocity rate ($g/m^3 s$).

Regarding oxygen production and carbon dioxide consumption were found the kinetic equations for the two phenomena in the literature, while for the nutrients equation it is not obtained the kinetic equations that describe their consumption inside photobioreactor. Therefore, it is assumed a large nutrients excess compared to the biomass concentration in the input flow, so as to neglect their consumption dynamics within the system.

Despite this system is complex due to all biochemical processes and, strictly speaking, to be at least a two-phase system, it can be introduced two further assumptions: (i) mono-phase system assuming that the chemical-physical properties of all culture they are attributable to the water properties, and (ii) slow biological kinetic reactions compared to the residence time. Therefore, moving within the photobioreactor, the biomass concentration, carbon dioxide and oxygen concentrations they are subject to small variation.

Then, the instantaneous phenomena are not analysed, remaining the same conditions inside the photobioreactor, and a differential equation is obtained in x and t independent variables by dividing both equation sides for Δt and Δx and making the difference quotient. Then, considering a steady-state system and neglecting any volume effects, i.e. constant volume, it is deduced that the input flow rate is equal to the output flow rate, Q_l (m^3/s); otherwise there would be an accumulation inside the photobioreactor. Hereinafter, they are reported the local mass balances at steady-state for the microalgae biomass, carbon dioxide, oxygen and neglecting nutrients concentration.

$$-Q_l \frac{dC_{bm}}{dx} + P_{bv} S = 0 \tag{2.6}$$

$$-Q_l \frac{dC_{CO_2}}{dx} - r_{CO_2} S = 0 \tag{2.7}$$

$$-Q_l \frac{dC_{O_2}}{dx} + r_{O_2} S = 0 \tag{2.8}$$

Regarding the kinetic equations for CO_2 consumption and O_2 generation, they are reported below:

$$r_{CO_2} = \nu_{CO_2} C_{bm} \tag{2.9}$$

$$r_{O_2} = \nu_{O_2} C_{bm} \tag{2.10}$$

Thus, the equations (2.9) and (2.10) provide the O_2 production velocity rate and CO_2 consumption velocity rate and considering an average biomass concentration value between input and output section that they will be constant, approximately. Therefore, another simplifying assumption was considered, and it regards the constant conditions of irradiance, biomass growth, carbon dioxide consumption and oxygen production within the photobioreactor.

The differential equations resolution that provide the biomass concentration profiles, carbon dioxide and oxygen they are shown below:

$$C_{bm}|_x = C_{bm}|_0 \, e^{\frac{\mu S}{Q_l} x} \tag{2.11}$$

$$C_{CO_2}|_x = C_{CO_2}|_0 - \left(\frac{\nu_{CO_2} C_{bm} S}{Q_l} x \right) \tag{2.12}$$

$$C_{O_2}|_x = C_{O_2}|_0 + \left(\frac{\nu_{O_2} C_{bm} S}{Q_l} x \right) \tag{2.13}$$

where $C_{bm|0}$, $C_{CO2|0}$, and $C_{O2|0}$ are the input photobioreactor concentrations, i.e. at x equal to zero.

According to Monod equation (1.9), biomass productivity depends by the concentration, linearly. This dependence approximates the real culture behaviour when all cells are at the same conditions. However, due to the mutual self- shading, it is necessary to use more accurate mathematical models to obtain the biomass productivity; then, these models are described in the next paragraph 2.2.4.

2.2.2 Energy balance

A thermal profile inside the photobioreactor is determined by the energy balance within it. In this energy balance, due to the solar radiation the irradiance is the term that most influence the temperature inside the photobioreactor; then the latter must be less than the maximum tolerable temperature by microalgae cells.

Considering the medium culture as volume control, and the energy balance in quantity terms, all the various contributions will be in thermal energy dimension terms.

$$\left(m\widehat{H}\right)|_{t+\Delta t} - \left(m\widehat{H}\right)|_t = (m\widehat{H})|_x - \left(m\widehat{H}\right)|_{x+\Delta x} + \pi d_f \Delta x \Delta t I - rV\Delta t \Delta H_r \tag{2.14}$$

The enthalpy difference in time represents the quantity in the LHS equation; instead in the RHS equation they are present the enthalpy difference due to convective flows, energy irradiance and the heat quantity absorbed by the medium. In fact, the photosynthesis reaction is an endothermic reaction, and then it is express as an output term. By dividing both equation sides for Δt and Δx and making the difference quotient equal to zero it is obtained a differential equation in two independent variables x and t.

Then, some simplifying assumptions can be introduced: (i) chlorophyll photosynthesis is an endothermic process, i.e. $\Delta H_r > 0$, and it absorbs heat from the system; however, this contribution is negligible compared to the thermal flow associated with convective- and radiant terms; (ii) steady-state system; (iii) at steady-state condition temperature and pressure settle to constant values; (iv) constant mass- and volumetric flow rate, and then constant density. Therefore, the energy balance is as follows:

$$\dot{m}\frac{d\widehat{H}}{dx} + \pi d_f I = 0 \tag{2.15}$$

where $\widehat{H}$ is the specific enthalpy (kJ/kg), $\dot{m}$ is the mass flow (kg/s) and I is the irradiance (W/m^2). The specific enthalpy can be expressed by selecting a reference temperature and then obtain:

$$\widehat{H} = c_p\left(T - T_{rif}\right) \tag{2.16}$$

The resolution of equation (2.15) by integral between the photobioreactor input ($x = 0$) and output ($x = L_f$) it allows to obtain:

$$Q_l \rho c_p \left(T_{in} - T_{rif}\right) + \pi d_f L_f I = Q_l \rho c_p \left(T_{out} - T_{rif}\right) \tag{2.17}$$

Then, the outlet photobioreactor temperature can be expressed as:

$$T_{out} = T_{in} + \frac{S_{irr} I}{\rho c_p Q_l} \tag{2.18}$$

where average values are considered for the specific heat c_p and density ρ and the irradiate surface S_{irr} is indicated as the product $\pi d_f L_f$.

Then, this last obtained temperature is compared with the microalgae limit temperature and the following condition has to be respected:

$$T_{out} < T_{lim} \tag{2.19}$$

In conclusion, the medium microalgae culture absorbs the thermal input flow due to solar radiation that can be expressed by the following equation:

$$\dot{Q}_1 = \dot{m} c_p \Delta T = S_{irr} I \tag{2.20}$$

The Air-Lift system allows not only medium culture movement inside the photobioreactor, but there is a partial evaporation of the medium culture along the riser column due to vacuum pressure applied within degaser section, i.e. $P < P_0$ where P_0 is the atmospheric pressure. Since the evaporation is an endothermic process, the vacuum pressure involves a temperature lowering and by water evaporating, it removes latent evaporation heat. Then, this thermal flow is expressed by the following equation:

$$\dot{Q}_2 = \dot{m} \lambda_{ev} \tag{2.21}$$

Therefore, in the case $\dot{Q}_1 \gg \dot{Q}_2$ will be appropriate to assess a suitable heat exchange system.

2.2.3 Momentum balance

Volumetric flow rate can be defined as momentum in the time unit:

$$\dot{q} = \frac{q}{t} = \frac{mv}{t} = \frac{\rho V v}{t} = \frac{\rho S L_f v}{t} = \rho S v^2 \tag{2.22}$$

It is noted that flow rate is developed along the photobioreactor axial direction. Considering an infinitesimal control volume, the momentum balance can be expressed by the following equation:

$$\frac{dq}{dt} = \dot{q}_{in} - \dot{q}_{out} + \sum_{i=1}^{n} F_{ext_i} \tag{2.23}$$

Figure 2.4 shows the infinitesimal photobioreactor control volume for momentum balance. The latter is a vector balance, however, due to the flow rate being oriented along the axial direction, it is possible to consider the projection of the same along the horizontal direction.

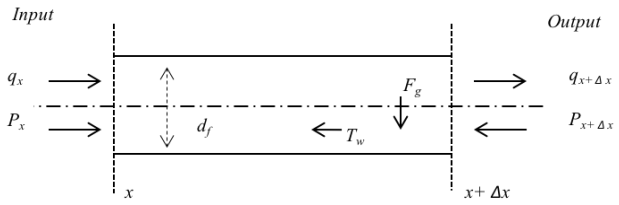

Figure 2.4 Infinitesimal photobioreactor control volume for momentum balance.

The last term on the RHS equation (2.23) is the external forces due to:

$$\sum F_{ext} = \Delta F_P + \Delta F_w + F_g + F_s \tag{2.24}$$

where ΔF_p is the pressure force applied by the external flow rate on the internal flow in the control volume. This pressure force is expressed as:

$$\Delta F_P = (P_x - P_{x+\Delta x})S \tag{2.25}$$

The gravity force F_g is negligible considering the horizontal flow rate direction; the mechanical forces F_s are zero because there are no mechanical moving parts; the frictional forces F_w on the walls, related to the tangential stress, are expressed as:

$$\Delta F_w = \tau_w \pi d_f \Delta x \tag{2.26}$$

Considering the steady-state system, the variation of momentum in time is zero; therefore, the momentum balance is expressed as:

$$\rho S v^2|_x - \rho S v^2|_{x+\Delta x} - \tau_w \pi d_f \Delta x + (P_x - P_{x+\Delta x})S = 0 \tag{2.27}$$

each term has force dimensions. The shear stress τ_w is related to Darcy friction coefficient f_c according to the following equation:

$$f_c = \frac{8\tau_w}{\rho v^2} \tag{2.28}$$

2.2.4 Productivity models

As previously mentioned in section 1.7.3, the productivity depends on several factors such as biomass concentration, nutrients, light, temperature, etc. Obtaining a mathematical model that describes the relative weight of each factor is an hard; taking into consideration various operating parameters groups it is possible to obtain the influence of these last on biomass productivity. However, the irradiance is the key factor in the photosynthetic process, then it is necessary to use the most appropriate models for such biological systems.

Hence, for the biomass productivity the most important mathematical models are two and they were proposed by *Molina and Grima et al., Cornet et al.* and *Acién Fernández et al.* The first productivity model only depends to the average irradiance available and neglecting photobioreactor internal fluid dynamics; this is the *simplified model* [39,49]. Instead, the second productivity model depends to the average irradiance available and to the photobioreactor internal fluid dynamics, and then to light-dark cycles influence; this is the *full fluid dynamic model* which it has a more complex form [22].

2.2.4.1 Simplified model

According to this simplified model the microalgae cells inside the photobioreactor they are subject to same average irradiance I_{av}; therefore, it is possible to use suitably modified Monod equation for the estimation of biomass productivity. The average irradiance is the light received by microalgae cells that randomly move inside the culture broth [49] and it is expressed in the following equation:

$$I_{av} = \int_V I \, dV \tag{2.29}$$

where I is the irradiance field within the photobioreactor. On the basis of this approach there are three different formulations of the irradiance field within the simplified model: (i) *Molina-Grima* formulation, (ii) *Cornet* formulation and (iii) *Acién Fernández* formulation.

The first formulation (i) by *Molina and Grima et al.*, involves the Lambert-Beer law for the irradiance estimation; this empirical relation correlates light absorbed by the medium to the concentration, medium thickness and chemical nature, as shown in the following equation:

$$I_{(\lambda)} = I_{0\,(\lambda)} e^{-K_{a(\lambda)} \xi C_{bm}} \tag{2.30}$$

where ξ is the optical path, Cbm is the microalgae biomass concentration, $I_{(\lambda)}$ is the irradiance to the λ wavelength, $I_{0(\lambda)}$ is the irradiance to the λ incident wavelength (to the surface) and $K_{a(\lambda)}$ is the biomass extinction coefficient to the λ wavelength. The light attenuation phenomenon depends by this last extinction parameter, mainly. This parameter depends to the pigment contained inside the culture, linearly. Then, the following equation:

$$K_a = Y_b + X_p Y_p \tag{2.31}$$

which shows an experimental relation between the extinction coefficient and the pigments content, where Y_b is biomass without pigments (m^2/g), Y_p is the normalized absorption coefficient to the total pigment content (m^2/g) and X_p is the total pigment fraction.

Substituting the irradiance estimation given by the equation (2.30) into the equation (2.29) and by integrating it the following equation is obtained:

$$I_{av} = \frac{I_0}{K_a \xi C_{bm}} \left(1 - e^{-K_{a(\lambda)} \xi C_{bm}}\right) \tag{2.32}$$

The model limitation is the Lambert-Beer law, which is valid if the following assumptions are respected: (i) no light direction change when crossing the microalgae species; (ii) no selective absorption; (iii) negligible photon scattering effects.

However, microalgae cells absorb a fraction of the incident radiation spectrum only (PAR), and then the absorption is selective. Furthermore, photon scattering

phenomena are not negligible in the case of high-concentration cells. In conclusion, Lambert-Beer law loses validity for high concentrations microalgae cultivation and it is rather approximate [49]. There are many mathematical correlations that link the average irradiance of equation (2.29) to the specific growth rate μ, and then to the biomass productivity [46]. In this work this correlation *I*-μ used is reported by the following equation:

$$\mu = \frac{\mu_{max} I^n}{I^n + I_k^n} \tag{2.33}$$

where I_k^n is a constant dependent from the microalgae species considered and *n* is an experimental exponent.

The second formulation (ii) by *Cornet et al.*, involves the Lambert-Beer law for the irradiance estimation by taking into account photon scattering phenomena and the selective microalgae absorption [50]. In the case of high biomass concentration, the average irradiance is expressed as

$$I = \frac{4 I_0 \alpha_1}{e^{-\alpha_2}(1+\alpha_1)^2 - e^{-\alpha_2}(1-\alpha_1)^2} \tag{2.34}$$

where the coefficients α_1 and α_2 are expressed as:

$$\alpha_1 = \sqrt{\frac{E_a}{E_a + E_s}} \tag{2.35}$$

$$\alpha_2 = (E_a + E_s)\alpha_1 \xi C_{bm} \tag{2.36}$$

This model is valid if the following assumptions are observed: (i) isotropic radiation field and (ii) independent light absorption and scattering factors E_a and E_s.

Both the preceding two formulas have the main limit of Ka, E_a and E_s parameter obtained experimentally; these last parameters are strongly influenced by the radiation nature. Therefore, there is the necessity of a correct model that reproduces the experimental data for any biomass concentration value, wavelength and independently from the nature of the radiation [49].

Finally, the third formula (iii) by *Acién Fernández et al.* is depicted by the following equation:

$$I_{(\lambda)} = I_{0\,(\lambda)} e^{-K'_{a(\lambda)} \xi C_{bm}} \tag{2.37}$$

In this last equation, the biomass extinction coefficient $K'_{a(\lambda)}$ is expressed as:

$$K'_a = \frac{1}{\xi_{av}} \frac{At_{max}}{K_{at} + C} \tag{2.38}$$

where ξ_{av} is the average optical path, K_{at} is a constant, At_{max} is the maximum attenuation of light on all wavelengths and C is the biomass concentration. This last equation reproduces the experimental tests well, deviating for low concentration value only, i.e. $C < 0.2\ g/L$ [51].

2.2.4.2 Full Fluid Dynamic model

In the previous section, the productivity is function of the average irradiance parameter. However identical average irradiance values do not involve identical productivity values [46]. In fact, the biomass productivity also depends on fluid dynamic parameters that are not present in the simplified model; in particular, it is neglected the light dark cycles frequency [46]. A more accurate model that takes into account this last parameter it is proposed by *Molina Grima et al.* [39], where the productivity is given by the following equation:

$$P_{bv} = \frac{\nu(a + bI_{wm})}{\nu + c + dI_{wm}} \tag{2.39}$$

where *a, b, c, d* are the characteristic algae coefficients, I_{wm} is daily average incident irradiance and ν is the light dark cycles frequency. This last parameter is defined as the inverse of the sum of residence time in dark- and photic zone, t_k and t_l, respectively. This residence time t_k is proportional to the dark zone volume V_k, as well as the residence time t_l is related to the photic volume V_l. On the basis of these analogies, it can be expressed the frequency ν as a function of the illuminated volume fraction φ:

$$\nu = \frac{1}{t_k + t_l} = \frac{1 - \varphi}{t_k} \tag{2.40}$$

where φ is equal to:

$$\varphi = \frac{V_l}{V_l + V_k} \tag{2.41}$$

The residence time t_k indicates the average time of one microalgae cell to switch from dark- to photic zone; therefore, it can determine the residence time t_k by the photobioreactor geometry and the velocity U_r, i.e. the dark- to photic zone cell velocity. This last parameter U_r is a radial velocity and takes into account the radial cells velocity within the photobioreactor due to momentum transport between turbulent zone and the boundary-layer to the walls. The radial velocity U_r is given by the following equation [30]:

$$U_r = 0.2\left(\frac{U_s^7 \zeta}{\rho d_f}\right)^{1/8} \tag{2.42}$$

where U_s is the superficial velocity inside the tubular photobioreactor, and ζ is the dynamic viscosity of medium culture. Concurrently, radial velocity is defined as volumetric flow rate per unit length that it crosses the dark area Q_r, to the arc length s which marks the boundary between the photic- and dark zone [30]:

$$U_r = \frac{Q_r}{s} = \frac{d_f(\vartheta - sin\vartheta)}{4t_k\vartheta} \tag{2.43}$$

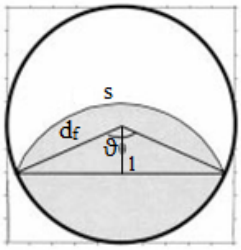

Figure 2.5 Light profiles inside a tubular photobioreactor by Molina Grima et al. [30] and the geometric parameters that characterize photic- and dark zone boundary.

Taking into account the irradiance profiles inside a tubular photobioreactor developed by *Molina Grima et al.* as shown in Figure 2.5, the angle ϑ is obtained by the following equation [30]:

$$\vartheta = 2\arccos\left(\frac{l}{d_f}\right) \tag{2.44}$$

Getting the angle ϑ by the equation (2.44) or experimental spectroscopic measurements it can be achieved the residence time t_k by the equation (2.43):

$$t_k = \frac{d_f(\vartheta - sin\vartheta)}{4U_r\vartheta} \tag{2.45}$$

Alternatively, it can be achieved through the volumetric flow rate by the following equation:

$$t_k = \frac{V_k}{S_k U_r} \tag{2.46}$$

Having obtained the illuminated volume fraction φ by the equation (2.41), light dark cycles frequency can be determined, and then the average daily irradiance I_{wm} and the characteristic microalgae coefficients can be calculated [39]. Compared to this full model proposed by *Molina Grima et al.*, where they use equations and experimental measurements, an alternative way could be to set light-dark cycles frequency to obtain the geometric parameters or the biomass productivity [30].

2.2.4.3 Superficial Productivity

The previous illustrated models typically provide the volumetric productivity. However, it is useful to obtain these parameters in terms of superficial productivity, in order compare photobioreactors with different geometry containing the same culture volume. Considering the horizontal tubular photobioreactors one can define two areas: (i) *useful area*, i.e. the area exploited for the photobioreaction purpose (single tubular pipe area to the same number of pipes); (ii) *occupied area*, i.e. all the physical space occupied by the photobioreactor, taking into account the existing gaps between the various pipes. Therefore, to obtain the superficial productivity, one takes into account the useful area through the following equation:

$$P_{bs} = P_{bv}\frac{V_{PBR}}{A_u} = P_{bv}\frac{\pi d_f^2}{4}L_f n_T \frac{1}{d_f L_f n_T} = P_{bv}\frac{\pi d_f}{4} \tag{2.47}$$

where A_u is the useful area and n_T is the number of pipes. An error coefficient ψ was introduced and linked to the gap between the various pipes in the two different areas, by the following simple relation:

$$\Psi = \frac{A_u}{A_o} \tag{2.48}$$

This coefficient has values between 0 and 1. In particular the value 1 refers to the situation in which pipes occupy all the space without gaps. Then, the superficial productivity was defined by reference to the useful area.

2.2.5 Photobioreactor Pressure Drop

The distributed pressure drops inside the photobioreactor they can be expressed by the Bernoulli equation:

$$\Delta P_d = 2\frac{L_f}{d_f} f_c \rho v^2 \tag{2.49}$$

where L_f e d_f are the length- and diameter of the photobioreactor, respectively; v is the liquid velocity and f_c is the friction factor that it is calculated by *Churchill* equation for both laminar and turbulent flow. This last parameter is express by the following equation:

$$f_c = \frac{1}{\left(-4 \cdot log\left(0.27\frac{\epsilon}{d_f} + \left(\frac{7}{Re}\right)^{0.9}\right)\right)^2} \tag{2.50}$$

where ϵ is the roughness of the inner pipe surface.

Finally, the concentrated pressure drops were calculated by the following equation:

$$\Delta P_{conc} = 2\,\rho\, k_c v^2 \tag{2.51}$$

where k_c is the friction factor for concentrated pressure drops. Then in the system referred, the fluid flow disperses its energy in the inlets and outlets section, mainly.

2.3 Air-Lift Unit

This section describes modeling of the entire Air-Lift system. Then, mass- energy- and momentum balances are solved for each system section: riser, downcomer and degaser.

2.3.1 Riser modeling

Riser section can be described as a vertical tube in which gas phase is injected by a sparger system, and liquid phase move upward. In Figure 2.6 a schematization of the riser is represented with inlet and outlet flows. The complexity of the modeling is due to mass flows since they are influenced by exposed interfacial area and transport coefficients: the latter parameters are variable because they are strongly influenced by pressure and temperature. In order to know all the variables characterizing the system, all the input parameters should be known and all necessary balances have to be solved.

2.3.1.1 Mass balance

With reference at Figure 2.6, W_l and W_g are, respectively, molar flow rate of liquid and gas (*kmol/s*), x_g and y_g molar fractions in liquid and gas phase of the gas component and Δm the amount of substance which is transferred from one phase to another (*kmol/s*). Note that, the system is considered in steady state conditions and no generation phenomena occur.

Therefore, mass balance equations in liquid phase are expressed as:

$$W_{l|_{out}} = W_{l|_{in}} - \Delta m_{tot} \tag{2.52}$$

$$W_l x_g\,|_{out} = W_l x_g\,|_{in} - \Delta m_g \tag{2.53}$$

Consequently, mass balance equations in gas phase are expressed as:

$$W_{g|_{out}} = W_{g|_{in}} + \Delta m_{tot} \tag{2.54}$$

$$W_g y_g\,|_{out} = W_g y_g\,|_{in} + \Delta m_g \tag{2.55}$$

In order to solve these equations is necessary to determine the amount of mass transferred among the two phases, per each component. Mass transport varies, from one component to the another, in relation to volumetric fractions and available interfacial area of exchange between liquid and gas phases. Interfacial area, in a system like this, corresponds to the surface of bubbles. This surface depends, through the state equation of gas, on temperature and pressure conditions. Temperature, in

turn, is linked to mass fluxes due to the evaporation phenomena; while, pressure, varies along the riser due to the hydrostatic pressure drops.

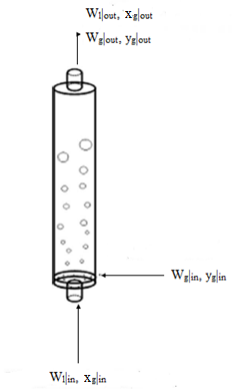

Figure 2.6 Schematization of riser section.

Therefore, the system is particularly complex and cannot be solved exclusively with global balance equations. It's clear that it is necessary to resort to differential balance equations in order to study the behavior of the system. For this purpose, infinitesimal control volume may be chosen expressed as $\Delta V = S_r \Delta z$, where S_r is the transversal section of the riser while Δz the thickness of the control volume. The latter one is shown in Figure 2.7, in which are also indicated mass and energy fluxes that take place among liquid- and gas phases.

Notably, it's important to underline that the presence of bubbles further complicates the modelization of the riser. This is because it would be necessary to estimate the variation in form, dimension and number of bubbles; which, inevitably, influences fluid dynamic and mass transfer. Then, a series of considered assumptions is reported: (i) all bubbles are considered spherical; (ii) absence of coalescence and breakage phenomena; (iii) perfect mixing inside the bubbles and, then, no concentration gradients; (iv) thermal equilibrium between liquid and gas; (v) bubbles volume depends only on gas content and pressure.

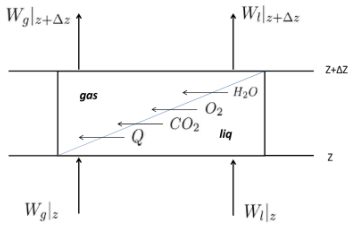

Figure 2.7 Riser control volume for mass balance equations.

From these hypothesis, two important consequences emerge: (i) the number of bubbles which crosses the generic transversal section is constant and (ii) their diameter varies with the height of riser only. Nevertheless, it is noted that the assumptions made are very simplifying.

Looking at Figure 2.7 mass balance equations can be rewritten as:

$$W_{l|_{z+\Delta z}} = W_{l|_z} - \dot{n_b}\Delta mol_{tot} \tag{2.56}$$

$$W_l x_g|_{z+\Delta z} = W_l x_g|_z - \dot{n}_b \Delta mol_g \tag{2.57}$$

$$W_{g|_{z+\Delta z}} = W_{g|_z} + \dot{n}_b \Delta mol_{tot} \tag{2.58}$$

$$W_g y_g|_{z+\Delta z} = W_g y_g|_z + \dot{n}_b \Delta mol_g \tag{2.59}$$

In these new equations $\dot{n_b}$ is the bubbles frequency (s^{-1}) which crosses the generic section of the riser and it is constant, while *Δmol* is the number of moles which crosses the generic section of the bubbles (*kmol*). It's given by the ratio between volumetric gas flow rate and volume of bubbles.

Thus, by indicating with d_{b0} the initial diameter of bubbles and Q_g the volumetric gas flow rate exiting from the sparger, we have:

$$\dot{n}_b = \frac{Q_g}{V_b} = \frac{6Q_g}{\pi d_{b0}^3} \tag{2.60}$$

Inside the riser a biphasic system is present, constituted by a liquid phase together with the gas phase in form of bubbles. Hereinafter, it shows void fraction calculation and further considerations about the number of moles *Δmol.*

The volumetric gas flow rate can be related to the superficial gas velocity U_g inside the riser by the following equation:

$$Q_g = U_g S_R \tag{2.61}$$

where S_R is the riser cross section. Then, gas velocity U_g may also be expressed as a bubble velocity function u_b according to the following equation:

$$U_g = u_b \varepsilon \tag{2.62}$$

Where ε is the void fraction which can be defined as

$$\varepsilon = \frac{V_g}{V_g + V_l} = \frac{V_g}{S_R \Delta z} \tag{2.63}$$

Bubble velocity u_b, after a short transient acceleration phase, it will be constant and it will be the sum of two contributions: (i) terminal bubble velocity u_t and (ii) liquid drag force, as shown in the following equations

$$u_b = u_t + \frac{u_l}{1 - \varepsilon} \tag{2.64}$$

$$u_l = \frac{Q_l}{S_R} \tag{2.65}$$

Bubble volume inside the control volume, V_g, can be obtained by the following equation:

$$V_g = n_b \frac{\pi d_b^3}{6} S_R \Delta z \tag{2.66}$$

that is the product of the number of bubbles per unit volume, n_b (m^{-3}), for single bubble volume and for control volume. Then, by combining equations (2.64) and (2.66), void fraction is given as:

$$\varepsilon = n_b \frac{\pi d_b^3}{6} \tag{2.67}$$

Consequently:

$$n_b = \frac{6\varepsilon}{\pi d_b^3} \tag{2.68}$$

$$\dot{n_b} = n_b u_b S_R \tag{2.69}$$

Considering the equations (2.61), (2.63) and (2.64), void fraction can be expressed as

$$\varepsilon = \frac{U_g}{u_b} = \frac{U_g}{u_t + \frac{u_l}{1 - \varepsilon}} \tag{2.70}$$

The latter equation (2.70) can be rearranged to form where actual void fraction in z is function of superficial velocities of gas and liquid phase and terminal bubble velocity

$$\varepsilon|_z = \frac{u_l + u_g + u_t \pm \sqrt{-4u_g u_t + \left(u_l + u_g + u_t\right)^2}}{2u_t} \tag{2.71}$$

Estimating molar fluxes inside the control volume is very important. The bubble residence time inside control volume is given as

$$\Delta t = \frac{\Delta z}{u_b} \tag{2.72}$$

As concerns mass transport, two species may be considered: air or oxygen subjected to stripping and water molecules which evaporate. Otherwise, these phenomena are based on different mechanisms and, then, described by different equations. For determining the amount of air moles, the following equation can be used:

$$\Delta mol_g = K_g C_{tot}\left(x_g^{bulk} - x_g^*\right)\pi d_b^2 \Delta t \tag{2.73}$$

where:

- K_g is the global mass transport coefficient. Thanks to the previous hypothesis of perfect mixing, this coefficient coincides with the liquid phase side coefficient, calculable by using the Penetration's Theory:

$$K_i = \sqrt{\frac{4D_i u_t}{\pi d_b}} \tag{2.74}$$

- x_g^* is the molar fraction of gas species in liquid side which would do equilibrium at the gas phase (y^{bulk}), expressed by Henry's Law regarding the equilibrium at the interface

$$x_g^* = y_g^{bulk} \frac{P}{H_g^{Liq}} \tag{2.75}$$

where y is the gas phase molar fraction expressed as:

$$y = \frac{mol_{\,g}}{mol_{\,tot}} \tag{2.76}$$

For estimating evaporated water moles per unit of time the same previous equations, used for air, cannot be used because of different mechanisms involved

during mass transport. Notably, in liquid phase molecules continuously evaporate in order to pass in gas phase, in which a perfect mixing assumption is valid. Hence, water flux may be expressed as the difference between water moles that exiting from the control volume, decreased by inlet water moles:

$$\Delta mol_{H_2O} = mol_{H_2O}|_{z+\Delta z} - mol_{H_2O}|_z \tag{2.77}$$

By supposing gas-condensate liquid physic equilibrium is verified at the interface, then

$$y_{H_2O} = \frac{mol_{H_2O}}{mol_{tot}}|_z = \frac{P^0_{H_2O}}{P}|_z \tag{2.78}$$

$$y_{H_2O} = \frac{mol_{H_2O}}{mol_{tot}}|_{z+\Delta z} = \frac{P^0_{H_2O}}{P}|_{z+\Delta z} \tag{2.79}$$

Consequently:

$$mol_{H_2O}|_z = mol_g|_z \frac{P^0_{H_2O}}{P - P^0_{H_2O}}|_z \tag{2.80}$$

$$mol_{H_2O}|_{z+\Delta z} = mol_g|_{z+\Delta z} \frac{P^0_{H_2O}}{P - P^0_{H_2O}}|_{z+\Delta z} \tag{2.81}$$

where P^0 is the water vapour pressure, that depends on temperature only.

2.3.1.2 Energy balance

Temperature profile inside the riser section it is achieved by energy balance along the same column. This can be studied by using energy balance applied on the selected control volume, as reported in the following equations:

$$W_l h_l|_{z+\Delta z} = W_l h_l|_z - \dot{n}_b \Delta n_{H_2O} \lambda_{H_2O} \tag{2.82}$$

$$W_g H_g|_{z+\Delta z} = W_g H_g|_z + \dot{n}_b \Delta n_{H_2O} \lambda_{H_2O} \tag{2.83}$$

where the parameters h_l and H_g are enthalpies of liquid- and gas phases, respectively and λ latent evaporation heat (*kJ/kmol*).

Regarding liquid temperature variation due to heat evaporation capacity, and thus through the variation of number of water moles of water in the gas phase, a preliminary study was carried out. Then, one calculates the derivative of the number of moles with respect to time:

$$\frac{dn_{H_2O}}{dt} = \frac{d}{dt}\left(\frac{n_g P^0_{H_2O}}{P - P^0_{H_2O}}\right) = \frac{d}{dP}\left(\frac{n_g P^0_{H_2O}}{P - P^0_{H_2O}}\right)\frac{dP}{dt} = \frac{-n_g P^0_{H_2O}}{\left(P - P^0_{H_2O}\right)^2}\frac{dP}{dt} \tag{2.84}$$

Pressure varies due to hydrostatic head from bottom to the top of riser; by setting pressure head, P_{top}, and the riser height, z, it is possible to determine pressure P

$$P = P_{top} + \rho g z \tag{2.85}$$

Then the derivative with respect to time would be equal to

$$\frac{dP}{dt} = \rho g \frac{dz}{dt} = -\rho g u_b \tag{2.86}$$

The negative sign is due to opposite z-axis direction respect to the ascent velocity, merely.

By replacing equation (2.86) to the equation (2.84), one obtaines

$$\frac{dn_{H_2O}}{dt} = \frac{-n_g P^0_{H_2O}}{\left(P - P^0_{H_2O}\right)^2}(-\rho g u_b) = \frac{n_g P^0_{H_2O}\,\rho\, g\, u_b}{\left(P - P^0_{H_2O}\right)^2} \tag{2.87}$$

Taking into account the control volume, global energy balance is equal to:

$$\lambda \frac{dn_{H_2O}}{dt} = h\,\pi\, d_b^2\,\Delta T \tag{2.88}$$

where h is the heat transport coefficient by *Frössling* correlation and d_b bubble diameter to generic quota.

Then, liquid temperature variation is given as

$$\Delta T = \frac{\lambda\, n_g P^0_{H_2O} \rho\, g\, u_b}{h\,\pi\; d_b^2\left(P - P^0_{H_2O}\right)^2} \tag{2.89}$$

Bubble diameter is a system variable and its value varies along the quota. So, it is necessary to find the dependencies of this variable from other system parameters. By the ideal gas law state, bubble volume may be expressed as

$$V_b = \left(n_g + n_{H_2O}\right)\frac{R\,T}{P} \tag{2.90}$$

Consequently:

$$V_b = \left(n_g + \frac{n_g}{\frac{P}{P^0_{H_2O}} - 1}\right)\frac{R\,T}{P} \tag{2.91}$$

$$V_b = \frac{R\ T\ n_g}{P}\left(1 + \frac{P^0_{H_2O}}{P - P^0_{H_2O}}\right) \tag{2.92}$$

The initial bubble volume, i.e. to input conditions, is expressed as

$$V_b^0 = \frac{n_g R\ T}{P_{bottom}} \tag{2.93}$$

Then, dividing and multiplying equation (2.92) for pressure P_{bottom} is obtained

$$V_b = \frac{n_g\ R\ \ T}{P_{bottom}}\left(1 + \frac{P^0_{H_2O}}{P - P^0_{H_2O}}\right)\frac{P_{bottom}}{P} \tag{2.94}$$

Substituting equation (2.93) to equation (2.94), a relationship between the current bubble volume and the initial bubble volume is obtained, and then a relationship between the actual diameter and the initial diameter

$$d_b = d_b^0\left(\frac{P_{bottom}}{P - P^0_{H_2O}}\right)^{1/3} \tag{2.95}$$

Finally, substituting equation (2.95) to equation (2.89) and simplifying, the temperature variation: is obtained

$$\Delta T = \frac{\lambda\ n_g P^0_{H_2O}\rho\ g\ u_b}{h\ \pi (d_b^0)^2\left({P_{bottom}}^2\left(P - P^0_{H_2O}\right)\right)^{1/3}\left(P - P^0_{H_2O}\right)} \tag{2.96}$$

From the latter equation (2.96) one can observe that temperature variation is influenced by numerous parameters such as the vapour pressure, the latent evaporation heat and ascent bubble velocity.

However, by developing a simplified case, it was shown that the thermal effect due to the latent evaporation heat it is negligible compared to the thermal contribution provided by (i) solar radiation and (ii) convective effect with the external environment. In conclusion, merely these last two parameters are taken into account on the energy balance equation in the riser section.

2.3.1.3 Momentum balance

Modelization of the riser ends up with momentum balance equation used to determine pressure drops on the system. This is based on momentum conservation principle, mathematically expressed as:

$$\frac{dQ}{dt} = \dot{Q}_{|z} - \dot{Q}_{|z+\Delta z} + \sum F_{ext} \tag{2.97}$$

Looking at Figure 2.8 is possible to identify the terms in the above equation. Note that momentum balance is a vector balance, so it becomes important the assignment of vectors direction.

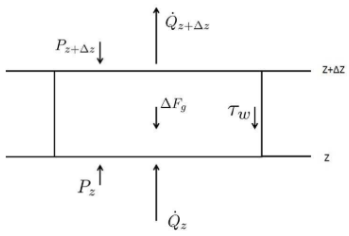

Figure 2.8 Riser control volume for momentum balance equation.

Under steady state conditions time derivative of momentum is void, and, therefore, the equation becomes:

$$\sum F_{ext} = \dot{Q}_{|z+\Delta z} - \dot{Q}_{|z} \tag{2.98}$$

Then, the momentum flow rate can be written as:

$$\dot{Q} = \left[\rho_l \left(\frac{u_l}{1-\varepsilon}\right)^2 + \rho_g u_b^2\right] S_{R_{|z}} \tag{2.99}$$

While the summation of external forces is given by the contribution of different factors:

$$\sum F_{ext} = \Delta F_P + \Delta F_w + \Delta F_g + \Delta F_s \tag{2.100}$$

where:

- ΔF_P, pressure forces execute by external fluid to the fluid inside the control volume:

$$\Delta F_P = \left(P_{|z} - P_{|z+\Delta z}\right) S_R \tag{2.101}$$

- ΔF_g, gravity force:

$$\Delta F_g = \left[\rho_l(1-\varepsilon) + \rho_g \varepsilon\right] \frac{\pi d_R^2}{4} \Delta z g \tag{2.102}$$

- ΔF_s, shaft force inherent the presence of active mechanical elements, in this case zero;
- ΔF_w, friction forces to the wall:

$$\Delta F_w = \tau_w \pi d_R \Delta z \tag{2.103}$$

where τ_w is the shear stress, related to Darcy friction coefficient by the following relation:

$$f_c = \frac{8\tau_w}{\rho u^2} \tag{2.104}$$

This Darcy friction coefficient may be estimated through the following Shannak's correlation [52], valid in the case of biphasic gas-liquid fluid, where gas phase is the disperse phase in form of bubbles and liquid phase is the continuous phase:

$$f_c = \left[-2\log\left(\frac{\xi}{3.7065} - \frac{5.0452}{Re_b}\log\left(\frac{\xi^{1.1098}}{2.8257} + \frac{5.8506}{Re_b^{0.8981}}\right)\right)\right]^{-2} \tag{2.105}$$

where ξ is the inner wall roughness; and then

- Re_b, the Reynolds Number for biphasic systems, that it is given as:

$$Re_b = \frac{\rho_b u_g^2 d_R^2 + \rho_l u_l^2 d_R^2}{\mu_g u_g d_R + \mu_l u_l d_R} \tag{2.106}$$

- ρ_b, biphasic system density, calculated as:

$$\rho_b = \left(\frac{\gamma}{\rho_{g\,mix}} + \frac{1-\gamma}{\rho_l}\right)^{-1} \tag{2.107}$$

- γ, vapour content, expressed as:

$$\gamma = \frac{W_g}{W_g + W_l} \tag{2.108}$$

Eventually, by developing these last equations and correlations, pressure drops can be written as:

$$\Delta P = f_c \frac{\Delta z}{d_R} \frac{W_{tot}^2}{2\rho_b} \tag{2.109}$$

2.3.2 Downcomer modeling

Downcomer section has exactly the same dimensions of the riser. The only necessary analysis is associated to the pressure drops, since no energy or mass exchanges and state transitions occur inside it. Pressure drops astride the downcomer depend on two contributions:

$$\Delta P_{tot} = \Delta P_{hydr} - \Delta P_{distr} \tag{2.110}$$

where

- Hydrostatic pressure drops are given as

$$\Delta P_{hydr} = \rho g h_{dc} \tag{2.111}$$

- Distributed pressure drops are given as

$$\Delta P_{distr} = 2\frac{h_{dc}}{d_{dc}} f_c \rho_l u_l^2 \tag{2.112}$$

The contribution of these two terms is opposite because hydrostatic pressure drops decrease from bottom to top, while, distributed pressure drops increase from top to bottom of the downcomer. But, being inside the system $\Delta P_{hydr.} \gg \Delta P_{distr.}$, it's clear that, overall, bottom pressure is greater than top pressure.

2.3.3 Degaser modeling

Outlet biphasic current, from the riser, enters into the degaser, which has to separate gas phase and liquid phase. The schematization of the degaser is shown in Figure 2.9 and provides a tube slightly inclined with respect to the horizontal plane. The development of the model has predicted to consider the efficiency of disengagement equal to 100%. This means that, this unity is able to separate completely the gas phase that is withdrawn by using vacuum pump from liquid phase and sent to downcomer. Note that gas phase once going out from the degaser, may be recirculated in the riser by the sparger. As regards design criteria of degaser, different methods exist, and according to the simplified Chisti model [53], in order to ensure the maximum efficiency of separation, residence time inside the degaser must be

larger than the time spent by the bubbles to get on the liquid surface. Hence, mathematically, this can be expressed as:

$$\frac{L_d}{u_d} > \frac{h_d}{u_b} \tag{2.113}$$

where

- u_d, liquid superficial average velocity into the degaser *(m/s)*;
- u_b, superficial average velocity of gas bubbles *(m/s)*;
- L_d, length of the degaser *(m)*;
- h_d, average height of liquid inside the degaser *(m)*.

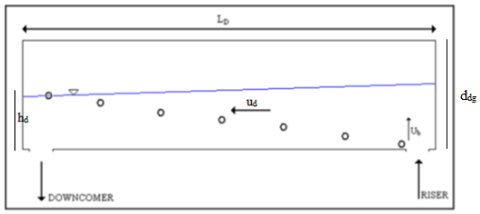

Figure 2.9 Degaser scheme with water level (blue line).

Considering that outlet fluid from the riser crosses the section of the degaser, it is possible to assay:

$$u_R A_R = u_d A_d \tag{2.114}$$

where

- u_R, liquid superficial average velocity along the riser *(m/s)*;
- u_d, liquid superficial average velocity into the degaser *(m/s)*;
- A_R, riser cross section *(m^2)*;
- $A_d = h_d d_{dg}$, degaser cross section *(m^2)*.

Finally, by combining equations (2.114) and (2.113), one obtains:

$$L_d = \frac{h_d u_d}{u_b} = \frac{h_d u_d d_{dg}}{u_b d_{dg}} = \frac{u_d A_d}{u_b d_{dg}} = \frac{u_R A_R}{u_b d_{dg}} \tag{2.115}$$

Notably, considering in equations (2.113) the equality of both members, then a limit condition will be obtained in terms of degaser length. Therefore, degaser choice will provide a length higher than the design limiting value L_d.

2.4 Make-up & Biomass Removal Unit

In this section nutrients reintegration and biomass removal are discussed. Furthermore, it is worth noting that it is a section to consider for a possible external thermal system control.

2.4.1 Mass balance

The mass balance that describes this section is the following:

$$W_m = W_p + W_e \tag{2.116}$$

Taking into account the entire system as control volume, this last equation is the overall mass balance; W_p and W_m are recovery- and make-up molar flow rate. Instead, W_e is the outlet molar flow rate from degaser section. Therefore, mass balance in the make-up section is given only by the following equation:

$$W_d + W_m = W_p + W_n \tag{2.117}$$

where W_d is the outlet molar flow rate from downcomer, and W_n is the outlet molar flow rate from this make-up & biomass removal unit.

By W_p molar flow rate the biomass produced is removed and it is restored with the steady state biomass concentration value. However, this molar flow rate is unknown and it is necessary a mass biomass balance to determine it; therefore, considering a constant density it is obtained:

$$Q_p c_{b,p} + Q_d c_{b,d} = Q_n c_{b,p}^0 \tag{2.118}$$

where Q_i are the volumetric flow rates, c_i the biomass concentrations and $c_{b,p}^0$ is the steady state biomass concentration. Obviously, $c_{b,\,p}$ is equal to $c_{b,\,d}$.

2.4.2 Energy balance

From a modeling point of view, energy balance is critical to close all necessary balances and to obtain inlet riser temperature. Considering density- and specific heat capacity as constant values, in order to obtain the output unit temperature, the energy balance is given by the following equation:

$$Q_n T_n + Q_p T_d = Q_d T_d + Q_m T_m \tag{2.119}$$

2.5 CO_2 Recovery Unit

As already discussed in section 2.1, this unit comprises two chemical absorption and desorption columns where the input flow is the gas phase coming from the degaser section and the mono-ethanolamine (MEA) water solution to produce pure oxygen and to recovery CO_2 gas stream. Therefore, in this section the estimation of process unit's dimensions for the MEA absorption of CO_2 is carried out together with the regeneration process unit's dimensions for the output solution from the first absorption column.

2.5.1 Chemical Absorption Unit

In the chemical absorption column at low temperatures, CO_2 is absorbed and it reacts in the aqueous solution of MEA chemically due to the high solubility; this leads to salt formation, carbamate, and simultaneously it is recovered a gas oxygen stream without CO_2 and water vapour. Then, this salt solution is sent to a second column, desorption tower, where by operating at high temperatures it reduces the CO_2 solubility and by the reverse reaction it is released the same in gas phase, while MEA solution is recycled into the first column. This absorption-desorption system is chosen due to (i) cheap MEA compound with high CO_2 affinity, (ii) high absorbent capacity and (iii) high absorption velocity. However, monoethanolamine presents problems as toxicity, corrosivity and foams formation; therefore, it will be necessary to take appropriate precautionary measures.

Hereinafter the main chemical reactions involved in absorption-desorption process of CO_2-MEA-H_2O solution:

$$CO_2 + HO(CH_2)_2NH_{2(aq)} \leftrightarrow HO(CH_2)_2NHCOO^- + HO(CH_2)_2NH_3^+ \quad (2.120)$$

$$CO_2 + HO(CH_2)_2NH_{2(aq)} \leftrightarrow HO(CH_2)_2NHCOO^- + H_3O^+ \quad (2.121)$$

$$H_2O + HO(CH_2)_2NHCOO^- \leftrightarrow HO(CH_2)_2NH_{2(aq)} + HCO_3^- \quad (2.122)$$

$$HO(CH_2)_2NH_{2(aq)} + H_3O^+ \leftrightarrow HO(CH_2)_2NH_3^+ + H_2O \quad (2.123)$$

$$CO_2 + OH^- \leftrightarrow HCO_3^- \quad (2.124)$$

$$HCO_3^- + H_2O \leftrightarrow CO_3^{2-} + H_3O^+ \quad (2.125)$$

$$2H_2O \leftrightarrow H_3O^+ + OH^- \quad (2.126)$$

Carbon dioxide balance in water solution with bicarbonate ions and carbonate formation they concern reaction (2.124) and (2.125). Reaction (2.126) is water self-protonation.

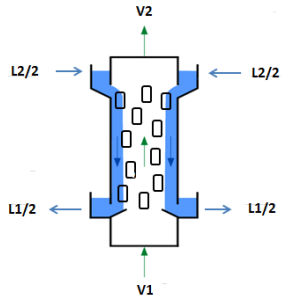

Figure 2.10 Conceptual apparatus diagram of wet walls column with filling bodies.

To design this CO_2 recovery unit, the procedure present in literature was followed [54,55], with appropriate assumptions and simplifications. As absorbent solution a water vapour with 30% w/w monoethanolamine is chosen and sent in counter-current

to the gas phase to treat. Regarding gas-liquid contactor a wet walls column with filling bodies was used in order to enhance mass transfer. Figure 2.10 shows the conceptual apparatus diagram, where L1 is the saline solution to be regenerated; L2 is the absorbent water solution with monoethanolamine 30% w/w; V1 is the steam gas to treat and V2 is the steam gas without CO_2.

An operating temperature process of 25°C was chosen and a pressure of 1.1 bar, slightly higher than atmospheric pressure. Since it is an exothermic process, it is appropriate to work at low temperature under the thermodynamic point of view. So, in order to sizing the several factors were ignored: (i) solution evaporation, (ii) oxygen absorption in the aqueous solvent, (iii) chemical absorption surface process, (iv) water effect as a base during the de-protonation step. Table 2.1 and Table 2.2 show all known data for the two vapour: components, flow rates, molecular weights and compositions. Moreover, the MEA quantity is fixed and the amount of CO_2 to achieve it is equal to 99.99%.

Table 2.1 Input data of stream V1.

S	$y1_{CO2}$	$y1_{O2}$	PM_{CO2} [g/mol]	PM_{O2} [g/mol]	PM_{V1} [g/mol]	$V1_{mol}$ [mol/s]	$V1_{w}$ [kg/s]
V1	0.8	0.2	44	32	41.6	1.86E-3	7.74E-5

Table 2.2 Input data of stream L2.

S	$x1_{MEA}$	$x1_{H2O}$	$x1_{salt}$	PM_{H2O} [g/mol]	PM_{MEA} [g/mol]	PM_{salt} [g/mol]	PM_{L1} [g/mol]	$L1_{mol}$ [mol/s]	$L1_{w}$ [kg/s]
L2	0.112	0.118	61.08	18	22.83	4.95E-2	5.55E-3	4.4E-2	1.13E-3

Finally, Table 2.3 and Table 2.4 show data of V2 and L1 obtained through the mass balance.

Table 2.3 Input data of stream V2.

S	$y2_{CO2}$	$y2_{O2}$	PM_{CO2} [g/mol]	PM_{O2} [g/mol]	PM_{V2} [g/mol]	$V2_{mol}$ [mol/s]	$V2_{w}$ [kg/s]
V2	3.99E-4	0.9996	44	32	32	3.72E-4	1.19E-5

Table 2.4 Input data of stream L1.

S	$x1_{MEA}$	$x1_{H2O}$	$x1_{salt}$	PM_{H2O} [g/mol]	PM_{MEA} [g/mol]	PM_{salt} [g/mol]	PM_{L1} [g/mol]	$L1_{mol}$ [mol/s]	$L1_{w}$ [kg/s]
L1	0.053	0.92	0.031	18	61.08	104.08	22.98	4.80E-2	1.10E-3

After calculating the mass balance from previous considerations, it was carried out the column design and all the necessary fluid-dynamics checks to obtain diameter and height dimensions: (i) flooding checks less than 80%; (ii) a minimum flow rate to ensure walls wettability; (iii) transfer height HTU with reference to the gas phase and (iv) number of transfer units NTU. Finally, as shown in Table 2.5, a chemical absorption dimensioning was done by designing a column containing MEA inside a packed tower with wet walls. The dimensions were determined as 1.26 m height and 1.3 cm as internal diameter.

Table 2.5 Design criteria of the absorption column.

Column	Walls	H [m]	D [m]	T_{op} [°C]	P [bar]
Packed	Wet	1.26	0.013	25	1.1

2.5.2 Solar Thermal Regeneration Unit

For what concerns the chemical absorption unit from the column head, a gas stream containing essentially pure oxygen with negligible CO_2 traces will be released; otherwise, the solution of water together with the unreacted monoethanolamine and the formed salts will be picked up from the column bottom. More precisely, this last liquid stream must be regenerated in order to release the solubilized and reacted CO_2 and to restore the MEA absorbent alkaline aqueous solution. Because of being an opposite process to chemical absorption, it will be facilitated at high temperatures from a thermodynamic point of view.

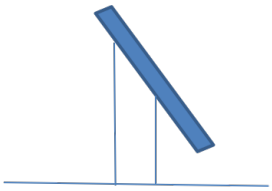

Figure 2.11 Scheme of a solar thermal evacuated pipes for solar thermal regeneration.

Although a similar coupled system would provide two columns, one for chemical absorption and one for chemical regeneration, in this work a solar thermal evacuated pipes was chosen, as shown in Figure 2.11.

Solar thermal system will be crossed by the solution from the chemical absorption column and in the output section will pick up two currents: (i) gas stream containing carbon dioxide and (ii) liquid absorbent solution stream with water and MEA restored. In order to obtain these two gas-liquid streams it is necessary to estimate thermal power required to heat the system from the inlet temperature to the regeneration temperature. Considering temperature range of *80 - 140 °C* for CO_2-ethanolamine-water systems, it was chosen as the operating temperature of *125 °C*. It is noted that by knowing the thermal power transmitted to the fluid by the solar panel, the area required to perform the operation will be determined.

So, the L1 current was characterized in terms of flow rate, composition and molecular weight, as shown in Table 2.6.

Table 2.6 Flow rate, composition and molecular weight of stream L1 to regenerate.

$L1_w$ [kg/s]	$x1_{H2O}$	$x1_{MEA}$	$x1_{SALT}$	PM_{H2O} [g/mol]	PM_{MEA} [g/mol]	PM_{SALT} [g/mol]	PM_{L1} [g/mol]
1.10	0.92	0.0536	0.0310	18	61.08	104.08	22.98

Subsequently, starting from the single specific heats capacity components which constitute the mixture, it was calculated the *cp* of the latter by means of molar average quantities. Then, from molar cp, the mass *cp* was obtained by using the molar weight. Table 2.7 shows the data used.

Table 2.7 Specific heat capacities of components and mixture.

$cp_{mol\ H2O}$ [J/molK]	cp_{H2O} [J/gK]	$cp_{mol\ MEA}$ [J/molK]	cp_{MEA} [J/gK]	$cp_{mol\ SALT}$ [J/molK]	cp_{SALT} [J/gK]	$cp_{mol\ L1}$ [J/molK]	Cp_{L1} [J/gK]
75.348	4.186	147.4	2.41	197.8	1.9	83	3.61

Thermal power required to heat the input stream from 25 °C (i.e. from chemical absorption column) to 125 °C (i.e. operating temperature chosen) it was estimated by the following equation:

$$\dot{Q} = L1_w cp_{L1} \Delta T \tag{2.127}$$

The required power is about *400 Watts* and considering that a single solar panel of one square meter it supplies about *40 Watts*, we can assume that almost *10* m^2 will be required.

2.6 MATLAB Code Structure

In the previous section 2.1 a pilot plant operation system was exhaustively depicted. This section describes instead the numerical operation code of the entire system in steady state and pseudo-steady state condition. Normally, all developed calculations were performed using the steady-state condition. Subsequently, in section 2.6.2, the pseudo-steady state condition will be introduced. In addition, a graphical user interface was developed to improve code management to the end user.

2.6.1 Steady State code

The numerical operation code is divided into logic blocks which represent the main functional units. The calculation is initialized on the basis on some assumed values, and for each of these logic blocks output conditions are calculated; then, the calculation is iterated until convergence.

Figure 2.12 shows a flowchart with all logical function blocks. As it can be seen, the numerical code is started on the basis of some assumed values: inlet temperature and pressure in the downcomer and fluid concentrations in circulation inside the

system. Since these assumptions, output fluid characteristics are calculated from make-up unit, and then from photobioreactor and riser section. The fluid components characteristics in the liquid phase of the output riser section must be identical with circulating fluid in the downcomer; then, from the comparison between hypothesized and obtained pressure an error is calculated, as shown in the following equation:

$$\epsilon_{\%} = 100 \cdot \frac{P_{hy} - P_{ca}}{P_{hy}} \tag{2.128}$$

If this value is less than maximum required error, the calculation can be stopped, otherwise the assumed values are updated with under-relaxed method.

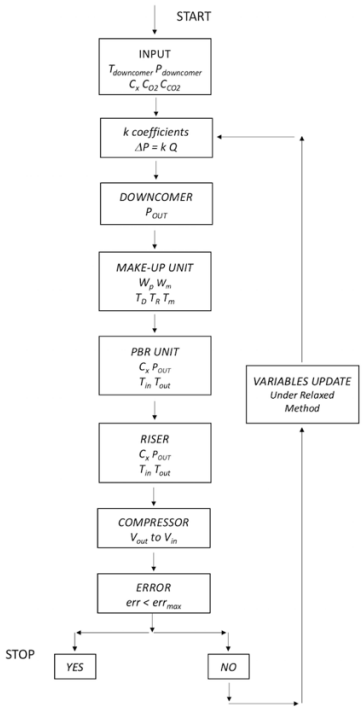

Figure 2.12 Flowchart of the numerical operation code.

The entire computational code was written in MATLAB environment where the presence of functions and structured matrices has simplified the storing and recalling of the various variables from one logic block to another. Figure 2.13 shows a summary diagram of all created functions. In this way, the relationships between different

sections to delineate the physical fluid path between the units and functions order in the loop calculation is more clear.

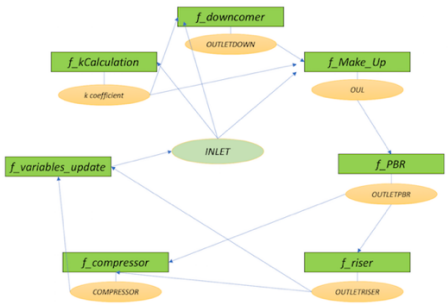

Figure 2.13 Schematic representation of code functions and their connections.

2.6.2 Pseudo-Steady State code

Circadian rhythm of solar radiation leads to a continuous variation of irradiance and the external environmental temperature; this makes necessary a system performance study as a function of these variation values.

This modeling is a pseudo-steady state model, i.e. it has an observation time divided into small intervals such as to consider system variables constant. In every moment, steady-state values are calculated and repeating this procedure for each interval, a points sequence is obtained that describes the dynamic system behaviour.

There are several steps for calculation sequence: (i) observation time period selection, i.e. atmospheric temperature and radiation, in particular; (ii) based on chosen month, irradiance and temperature data at various day hours are inserted in the model; (iii) steady-state iteration for each hour of selected day. Irradiance and temperature values at various day time were obtained by Photovoltaic Geographical Information System (PGIS) site from the Institute for Environment and Sustainability of the European Commission, Joint Research Centre [56].

2.6.3 GUI Interface

A graphical user interface for this plant designing was realized through the graphical interfaces design environment available on Matlab, called *Graphic User Interface Design Environment* (GUIDE). By inserting system geometry and all necessary parameters calculation script can be started to obtain all desired variables in the various plant sections.

Figure 2.14 shows the developed graphic user interface with a plant schematization and all the controls to insert (i) geometric data, (ii) mathematical model and (iii) related parameters to irradiance and external temperature. After executing the code, for example, it is possible to view all necessary variables profile along the riser with the "Riser Graphics" command.

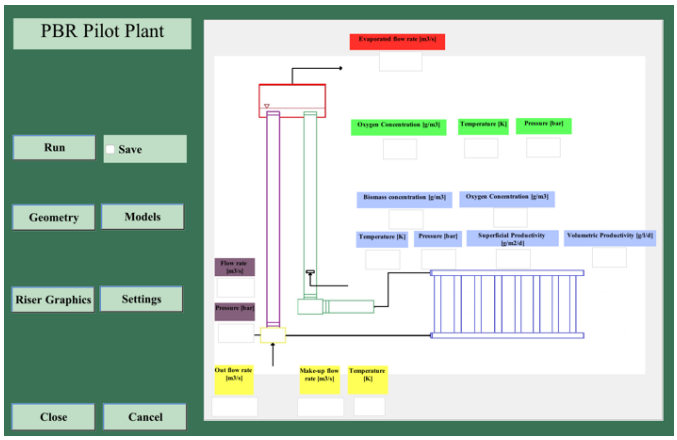

Figure 2.14 PBR Pilot Plant graphic user interface created on Matlab environment.

Therefore, this GUI is really useful to improve code management to the end user by entering the necessary values to model other types of tubular plant geometry and with different mathematical models.

2.7 Results and discussion for *Phaeodactylum Tricornutum*

In this section the studied productivity models were reported, showing the results obtained for *Phaeodactylum tricornutum* microalgae species, regarding the influence of the following parameters: biomass concentration, oxygen concentration, nutrients, temperature, pH and irradiance.

The various models show the relationship between productivity and the generic parameter in question, considering all other parameters fixed. By applying the superposition effect principle, single model data can be combined and it is possible to establish the optimum probable conditions in the biomass culture. More rigorous analysis would require a model that takes into account all simultaneous parameters variation; however, due to extreme complexity of photosynthetic system, this model is still not available.

2.7.1 Biomass Concentration & Productivity Model

Biomass concentration influence on productivity is described by kinetics cell growth equations as shown by the previous equation (1.8) and (1.9) in section 1.7. Normally, in order to obtain the specific growth rate μ and doubling time t_d, the procedure is of an experimental nature where the instantaneous volumetric productivity is measured as biomass concentration on time variation between two consecutive samplings.

In this work, mathematical modeling has started from specific growth rate maximum μ_{max}, that for *Phaeodactylum tricornutum* microalgae species is $0.063\ h^{-1}$ [41]; then, doubling time was calculated by equation (1.8), which results about 11 hours. Subsequently, by setting a concentration range from 0.1 to 5 g/L, volumetric productivity is determined by equation (1.9). Figure 2.15 shows the volumetric productivity trend as a function of biomass concentration.

This model is useful for evaluating biomass concentration influence on productivity; however, it is rather approximate, since it provides a simple linear dependence, and ignores some important effects. Biomass concentration increase results in a cells number increase but also in a mutual shading increase, which will

become more relevant the higher biomass concentration becomes. Therefore, it will result in a deviation from the linear model and a productivity reduction, which is not described by the Monod model.

At the same time, a concentration increase can be seen as cells number increase. Cells can perform photosynthesis, and thus, productivity would tend to increase. Eventually, it is inferred that the two effects are conflicting and it is the biomass concentration range to determine which one will prevail between the two. There is, then, an optimal biomass concentration, the Optical Cell Density (OCD), that, together with fixed geometry, light intensity and operating conditions will be associated to an optimum light field and consequently it will be possible to maximize the productivity, as shown in the previous Figure 1.11. Typically, the OCD takes values comprised between 5 and 20 g/L, and one considers a biomass concentration as excessive when it is 3-4 times OCD value [4].

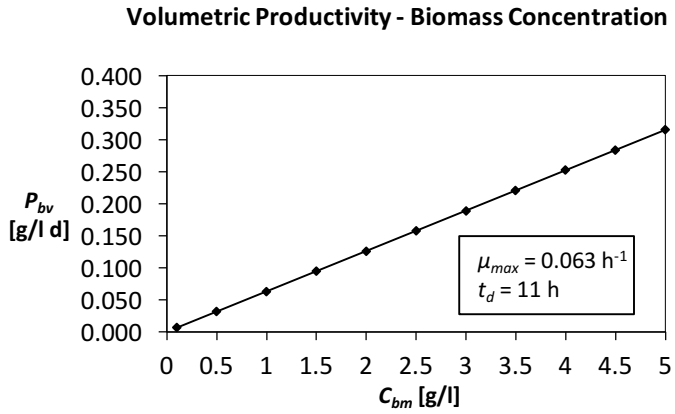

Figure 2.15 Volumetric productivity as a function of biomass concentration.

2.7.2 Nutrients Concentration & Productivity Model

As discussed in Chapter 1, nutrients influence on productivity is described by Monod equation (1.19). This equation describes the specific growth rate hyperbolic

variation on a generic substrate concentration; μ_{max} and K_s are the maximum specific growth rate and the semi-saturation constant, respectively. Usually, these last parameters are obtained experimentally: by fixing the generic nutrient, for each concentration value s, it is measured the specific growth rate, then μ and s pairs values are shown in Monod diagram (Figure 1.10). Finally, from asymptotic line μ_{max} value is obtained and from slope linear part K_s value is obtained

Regarding *Phaeodactylum tricornutum* microalgae species, with μ_{max} known value, three basic nutrients were analyzed: carbon, nitrogen and phosphorus, i.e. the main constituents of carbohydrates, proteins and lipids, respectively.

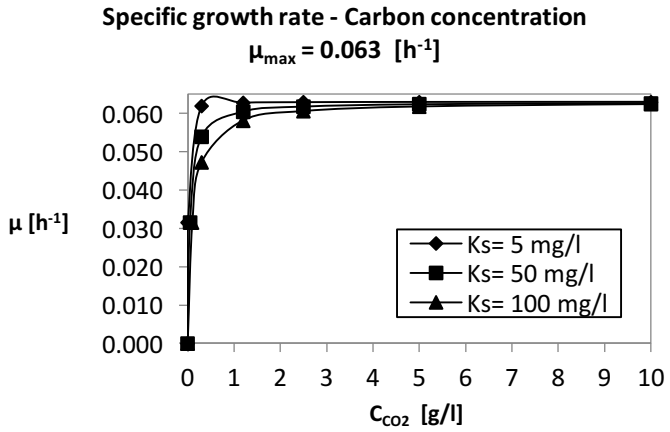

Figure 2.16 Specific growth rate as a function of carbon dioxide concentration at different values of K_s.

Normally, semi-saturation constant K_s is a parameter obtained experimentally that depends on several factors such as: salinity, temperature, density, biomass concentration, medium quality, etc. Having found only a range of K_s values [57], in a first time the main nutrients influence on the specific growth rate was individually studied; then, a sensitivity analysis was performed considering the simultaneous presence of the three nutrients by using a generalized Monod equation (1.32). Carbon, nitrogen and phosphorus nutrients and their simultaneous presence were analyzed, assuming K_s values of 5, 50 e 100 mg/L.

Carbon nutrient. Considering photo-autotrophic microalgae species, carbon dioxide is the carbon source. These biological species synthesize about 2 kg of CO_2 per gram of microalgae. Considering an atmosphere CO_2 concentration of about 0.3 g/L and that some microalgae species are able to tolerate high concentration values up to 150 g/L, a range between 0.3 and 150 g/L was fixed. Therefore, considering three main K_s values 5, 50 and 100 mg/L and a substrate range between 0 and 10 g/L, the specific growth rate was obtained from equation (1.19), as shown in Figure 2.16; it is noted that as K_s increasing, saturation is reached at higher concentrations, gradually. Therefore, with an extremely wide concentration range, the K_s differences are not relevant for this substrate.

Nitrogen nutrient. Ammonium salts, nitrates and urea are the nitrogen source for microalgae cultivation; molecular nitrogen or NOx are not bioavailable for these species. Typically, nitrogen is 7-10% by weight of biomass and with a substrate range between 0 and 80 g/L [57].

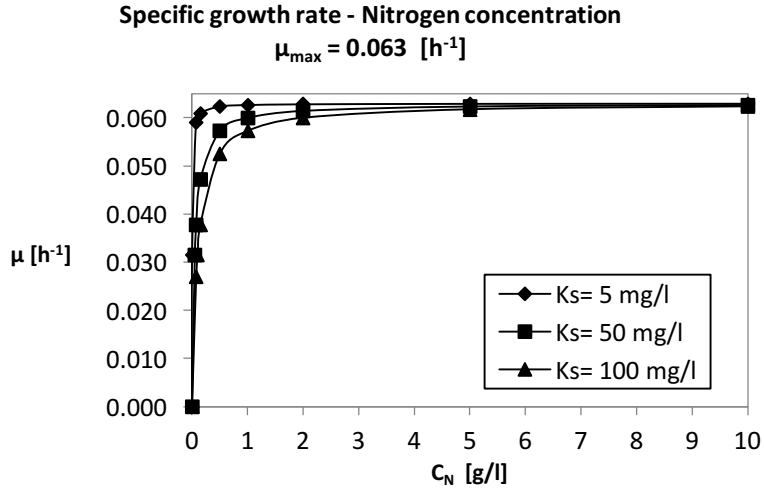

Figure 2.17 Specific growth rate as a function of nitrogen concentration at different values of K_s.

Therefore, considering three main K_s values 5, 50 and 100 mg/L and a substrate range between 0.005 and 10 g/L, the specific growth rate was obtained from equation (1.19), as shown in Figure 2.17.

It is noted that as K_s increasing, the saturation value was reached at higher concentrations. Although this trend is similar to carbon dioxide substrate, the K_s variation makes it more sensitive, since concentration range is more restricted, and also nitrogen content can be an order of magnitude lower than carbon substrate (7-10% for nitrogen and 50% for carbon).

Phosphorus nutrient. Phosphate salts anhydrous and hydrates represent phosphorus source for microalgae cultivation. In microalgae biomass, their content is less than 1% in weight; concentrations are much lower than carbon and nitrogen nutrients and with a more restricted variation range between 0.005 to 1.5 g/L. Therefore, considering three main K_s values 5, 50 and 100 mg/L and a substrate range between 0 and 10 g/L, the specific growth rate was obtained from equation (1.19), as shown in Figure 2.18.

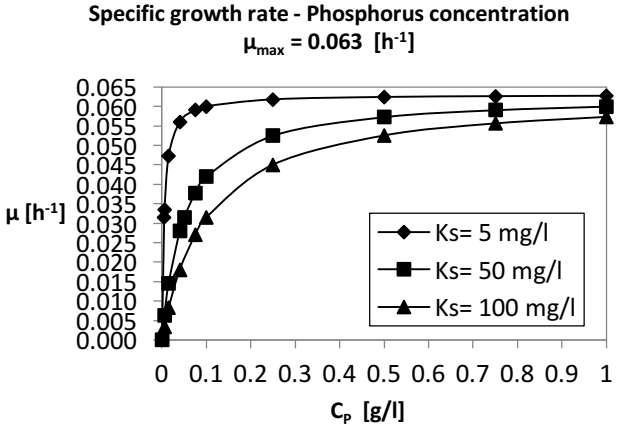

Figure 2.18 Specific growth rate as a function of phosphorus concentration at different values of K_s.

In this case, the semi-saturation variation effect is much more marked because the concentration range is much lower than the previous carbon and nitrogen nutrients; phosphorus content in algae biomass is up to two order of magnitude lower. It can be observed that from 5 to 100 mg/L the saturation value is no longer reached.

Three nutrients simultaneous presence. The previous models analyzed the influence of the individual nutrient independently; however, culture medium has the simultaneous presence of the same nutrients for microalgae cultivation purpose. By the results obtained, it was possible to consider three optimal concentration values for carbon, nitrogen and phosphorus: $K_s|P = 5\ mg/L$, $K_s|N = 50\ mg/L$ and $K_s|C = 100\ ml/L$. By means of equation (1.32), it was possible to obtain the specific growth rate between various concentration pairs. Figure 2.19 shows the graphical representation of these concentration pairs, where ordinate is the specific growth rate, and the two horizontal axes report nitrogen and carbon concentration with a fixed phosphorus concentration, equal to 0.5 g/L.

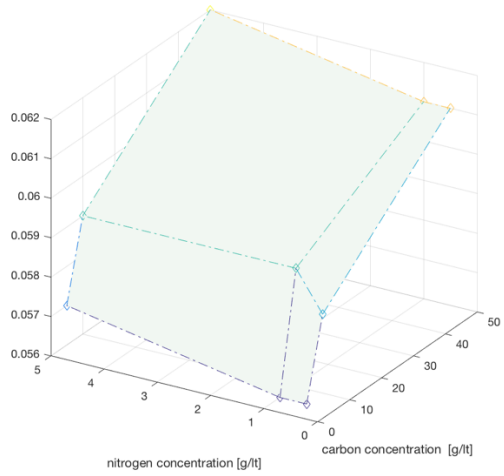

Figure 2.19 Specific growth rate as a function of nitrogen and carbon for a fixed phosphorus concentration of 0.5 g/L.

The aim of this sensitivity analysis is to obtain the best coupling between nitrogen, carbon and phosphorus concentrations; the phosphorus target was set to 0.5 g/L, and as regards nitrogen and carbon concentrations, highest concentration between 50 and 100 mg/L assure the achievement of the saturation.

2.7.3 Oxygen Concentration & Photosynthetic Activity

Considering a generic photosynthetic process for microalgae biomass production, oxygen generation rate is defined by the following equation:

$$RO_2 = \frac{1}{C_{bm}} \frac{d[O_2]}{dt} \tag{2.129}$$

This last equation also provides an experimental methodology to obtain oxygen concentration in the system. By fixing a biomass concentration C_{bm}, at each instant, it will be associated with an oxygen content, and reporting the measurements in a Cartesian diagram it will possible to obtain RO_2 from slope curve [43]. Therefore, considering equation (1.35), which describes the normalized photosynthetic variation rate $RO_2[DO_2]$ as a function of dissolved oxygen DO_2, a range of oxygen concentration between *1e-4* and *3.64e-2* g/L was fixed, considering that*9.1e-3* g/L is the equilibrium concentration, 2.27e-2 g/L is the toxicity concentration equal to 200% and 2.73e-2 g/L is the inhibition constant equal to 300% of saturation.

Figure 2.20 shows the obtained results; it shows the normalized photosynthetic activity as a function of the dissolved oxygen content.

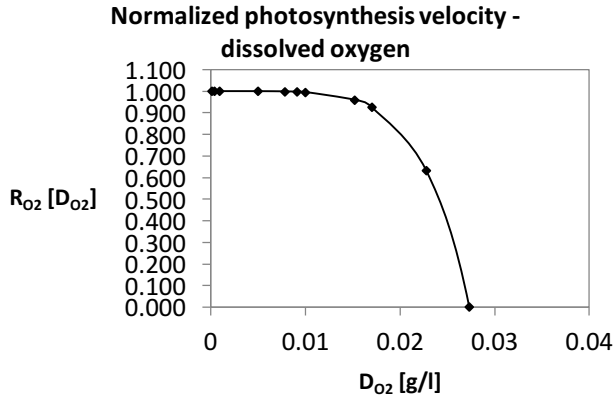

Figure 2.20 Normalized photosynthesis velocity as a function of dissolved oxygen.

Figure 2.20 shows that when dissolved oxygen concentration is less or equal to saturation value of 0.0091 g/L, photosynthetic rate assumes its maximum value. However, photosynthesis rate is quickly reduced when oxygen content increases

according to a power law, equal to zero when $DO_2 = KO_2$, i.e. when dissolved oxygen equals the inhibition constant. The major photosynthetic activity decrease is recorded at 250% saturation, i.e. value which oxygen becomes toxic to microalgae cells; therefore, in phase of plant design it is necessary to avoid this value. Besides KO_2 value, over-saturation of 350 and 400%, photosynthetic rate takes a negative value (not shown in Figure 2.20), which are to indicate that there is no longer photosynthetic activity but cell death, only.

2.7.4 pH & Productivity Model

The influence of pH on microalgae cultivation process is described by the equation (1.41), discussed in section 1.7.3.7. Then, from this equation one obtains a specific growth rate trend in a given pH range. K_1 and K_2 values were taken as reference values obtained for *Phaeodactylum tricornutum* equal to $2.3*10^{-6}$ and $1.2*10^{-10}$ *mol/L*, respectively [44]. Considering a μmax equal to $0.063\ h^{-1}$, the procedure was to fix a pH range variation between 2 and 12 and to derive, for each value, the corresponding H + ions concentration from the pH definition:

$$pH = -log_{10}[H^+] \tag{2.130}$$

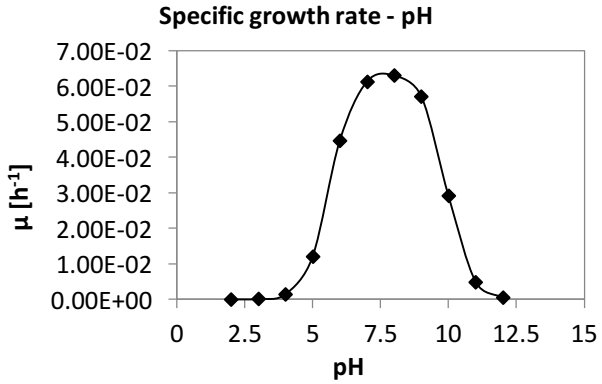

Figure 2.21 Specific growth rate as a function of pH variation.

Therefore, it is possible to obtain the specific growth rate μ trend by equation (1.41) with fixed values of K_1, K_2, μ_{max} values and protons concentration range, as

shown in Figure 2.21, where it can be noted that optimal pH value for *Phaeodactylum tricornutum* species is 7.8.

2.7.5 Temperature & Productivity Model

The influence of temperature on microalgae cultivation process is described by the equation (1.37), discussed in section 1.7.3.6. Then, from this equation it is possible to obtain a specific growth rate trend as a function of temperature. A_0, B_0, E_a and E_b values were taken as reference values obtained for *Phaeodactylum tricornutum* [44]. Considering a reference temperature T_0 equal to *293 K*, the procedure was to fix a temperature range variation between 0 and 40 and to derive, for each temperature value, the corresponding specific growth rate, as shown in Figure 2.22.

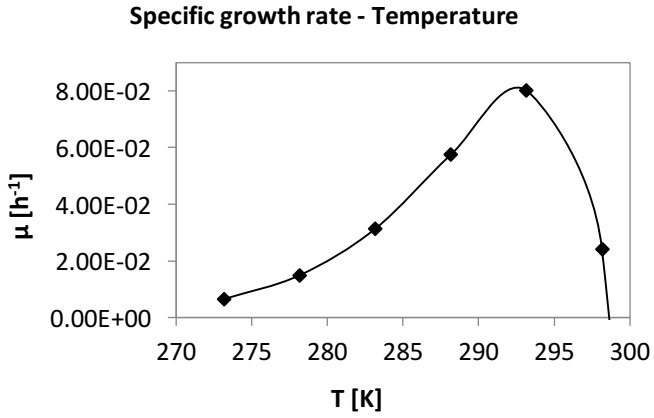

Figure 2.22 Specific growth rate as a function of temperature variation.

In this analyzed range, it was possible to obtain the temperature value where the specific rate reaches the maximum value, equal to $8.04*10^{-2}$. This value is obtained when temperature takes values from 293.35 K (20.2 °C) to 293.75 K (20.6 °C). It is worth noting that with this temperature equation, values above 25.6 °C shows specific growth rate equal to zero.

In conclusion, the optimum temperature for *Phaeodactylum tricornutum* microalgae growth is 20.4 °C, while above 30 °C a growth process isn't observed. Therefore, temperature is one of the most important parameters that influences microalgae growth process.

2.7.6 Irradiance & Productivity Model

As already discussed in the previous Chapters, for the photosynthetic processes not all solar radiation is used but only a fraction, the photosynthetic active radiation (PAR) that it extends from 400 to 700 nm, corresponding to 41% of total radiation. From this irradiance range, one should analyse the light/energy transmitted in the growth medium for microalgae photosynthesis. Taking into consideration a tubular geometry, an optical path ξ, defined as a diameter pipe fraction, is considered:

$$\xi = id_f \tag{2.131}$$

For tubular geometry with a diameter pipe d_f range between 3 and 6 cm, ξ variation is within range of 45-55% of d_f [30].

2.7.6.1 Simplified Model Results

This model requires that microalgae cells within culture system are subject to the same average illumination I_{av} (equation (2.29)) without considering the fluid dynamic aspects. Therefore, in this simplified model three different formulations were considered, according to the model used to express the irradiance. Hereinafter the assumptions and the procedure adopted:

- photobioreactor tubular diameter of 0.04 and 0.06 m, with a optical paths of 0.02 and 0.03 m, respectively;
- fixed characteristic parameters of microalgae species considered;
- three incident irradiance value I_0 of 150, 300 and 500 W/m^2, which correspond approximately to 5 PM (150 W/m^2), 10.30 AM (300 W/m^2) and 12 PM (500 W/m^2), respectively;
- fixed biomass concentration variation range from 50 to 6500 g/m^3;

- specific growth rate calculation through two correlation: (i) Molina Grima et al. [49] provides an increase of the specific growth rate with the irradiance, up to the saturation value; (ii) a modified formulation [58] that taking into account photo-limitation and photo-inhibition phenomena by the following equation (2.133).

$$\mu = \mu_{max} \frac{I_{av}^{n}}{I_{av}^{n} + I_{k}^{n}} \tag{2.132}$$

$$\mu = \mu_{max} \frac{I_{av}^{(b+\frac{c}{I_0})}}{[I_k(1+\frac{I_0}{K_i})^{a}]^{(b+\frac{c}{I_0})} + I_{av}^{(b+\frac{c}{I_0})}} \tag{2.133}$$

Regarding the parameters of equation (2.132), these are expressed below: maximum specific growth rate μ_{max} equal to $0.063\ h^{-1}$; semi-saturation light constant I_k equal to $114.67\ \mu Em^{-2}s^{-1}$ and n is the characteristic microalgae exponent equal to 1.49 [39].

Regarding parameters of equation (2.132), these are listed in the following Table 2.8 [58].

Table 2.8 Characteristics parameters of equation (2.132) for *Phaeodactylum tricornutum* microalgae species [58].

Parameter	Value
$\mu_{max}\ (h^{-1})$	0.063
$I_k\ (\mu Em^{-2}s^{-1})$	94.3
$K_t\ (\mu Em^{-2}s^{-1})$	3426
a	3.04
b	1.209
c	514.6
n	1.49
K_a	0.0369

where K_i is the inhibition constant, and a, b and c are the characteristic microalgae exponents [58].

The three formulations of the simplified model will be discussed below by describing procedure and results obtained.

Beer-Lambert law. This formulation involves Beer-Lamber law using the empirical correlation of equation (2.30): setting a biomass concentration range, for each pipe diameter, i.e. 4 and 6 cm, the optical path was calculated through equation (2.131), assuming a *i* value equal to 0.5; the three irradiance value I_0 were considered for each value of pipe diameter, appropriately converted in $\mu Em^{-2}s^{-1}$ through the following relation:

$$E\left[\frac{\mu E}{m^2 s}\right] = 4.6 \cdot E\left[\frac{W}{m^2}\right] \tag{2.134}$$

Therefore, the specific growth rate was calculated by equations (2.132) and (2.132), as shown in Figure 2.23, Figure 2.24 and Figure 2.25.

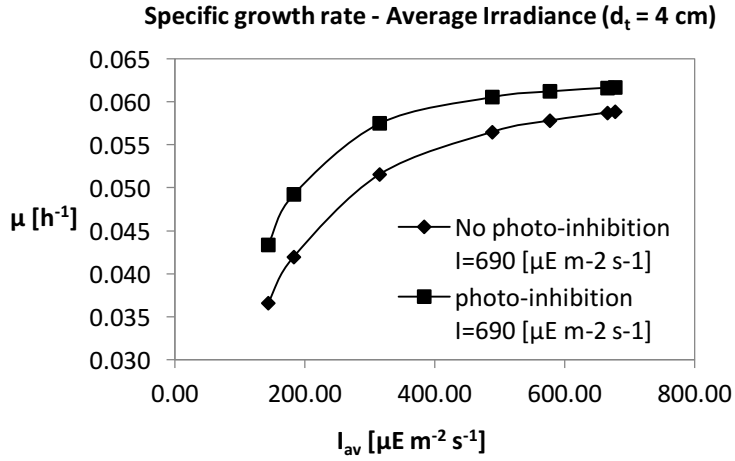

Figure 2.23 Beer-Lambert law: specific growth rate as a function of average irradiance I=690 [μE/m2 s], diameter size dt=4cm and photo-inhibition.

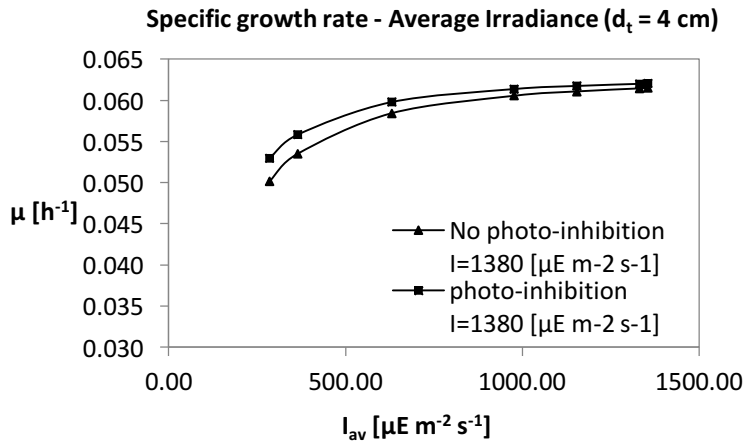

Figure 2.24 Beer-Lambert law: specific growth rate as a function of average irradiance I=1380 [μE/m2 s], diameter size dt=4cm and photo-inhibition.

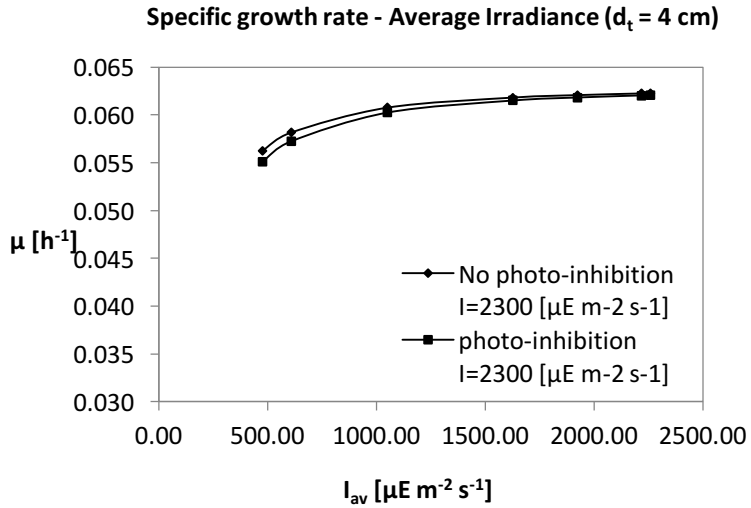

Figure 2.25 Beer-Lambert law: specific growth rate as a function of average irradiance I=2300 [μE/m2 s], diameter size dt=4cm and photo-inhibition.

From these last three figures, Figure 2.23, Figure 2.24 and Figure 2.25, it is observed that at low irradiance, equation (2.133) provides a specific growth rate slightly superior compared to values obtained by equation (2.132); then, at high irradiance value the relative curve to equation (2.132) (no photo-inhibition) exceeds the relative curve to equation (2.133) (photo-inhibition). This could be due to model described by equation (2.132) that refers only to average irradiance and doesn't take into account light gradients inside the system, i.e. a perfect light dilution taking into account photo-limitation but not the photo-inhibition. Instead, the model described by equation (2.133) allows a simultaneous consideration of photo-limitation and photo-inhibition. By increasing the irradiance, equation (2.133) provides a lower specific growth with the same diameter pipe since the reversible deactivation of photosynthetic processes is considered. The same situation occurs in the second case with diameter pipe of 6 cm.

Finally, Figure 2.26 and Figure 2.27 show the specific growth rate with equation (2.133) as a function of average irradiance (690, 1380 and 2300 $\mu Em^{-2}s^{-1}$); it is noted that by increasing pipe diameter the specific growth rate is reduced.

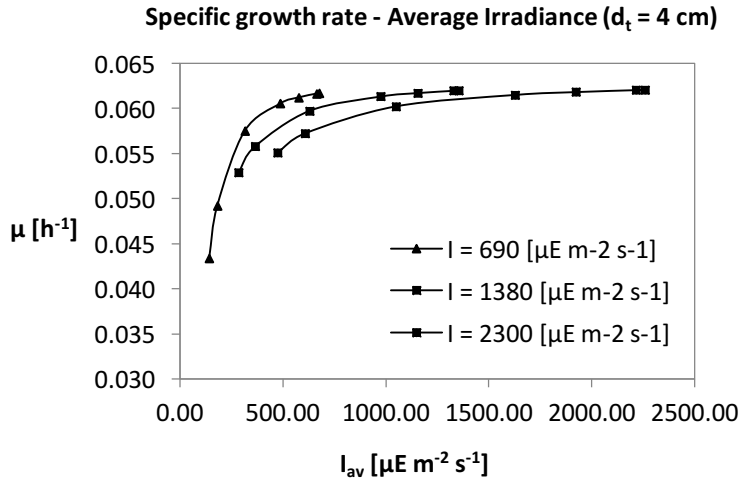

Figure 2.26 Beer-Lambert law: specific growth rate as a function of average irradiance specified and diameter size dt=4cm.

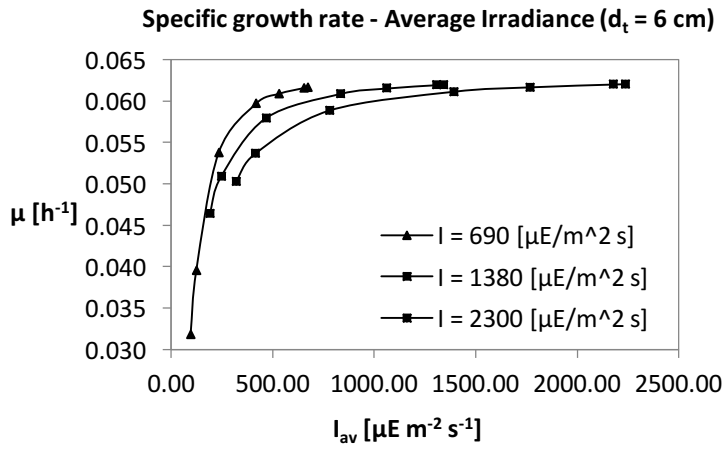

Figure 2.27 Beer-Lambert law: specific growth rate as a function of average irradiance specified and diameter size dt=6cm.

Limit of this model is due to Beer-Lambert law, which is valid with the following assumptions: (i) no selective absorption, (ii) negligible scattering effects and (iii) no deviation of light inside microalgae culture.

Cornet law. The formulation involves the Lambert-Beer law for the irradiance estimation by taking into account also photon scattering phenomena and selective microalgae absorption [50]; then, the average irradiance is expressed by equation (2.34). Following the same procedure of previous model, and taking into account the experimental required parameters by *Acién Fernández et al.* [49], Figure 2.28, Figure 2.29, Figure 2.30, Figure 2.31 and Figure 2.32 show the results obtained for the three external incident irradiance values.

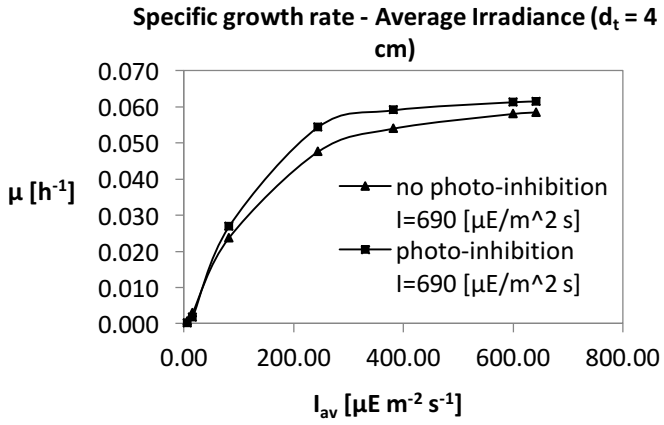

Figure 2.28 Cornet law: specific growth rate as a function of average irradiance I=690 [μE/m2 s], diameter size dt=4cm and photo-inhibition.

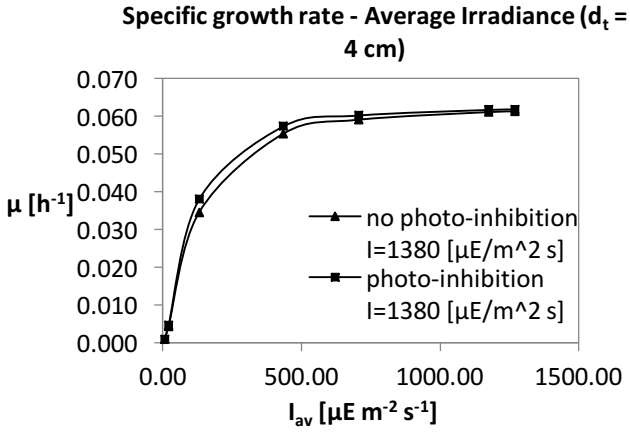

Figure 2.29 Cornet law: specific growth rate as a function of average irradiance I=1380 [μE/m2 s], diameter size dt=4cm and photo-inhibition.

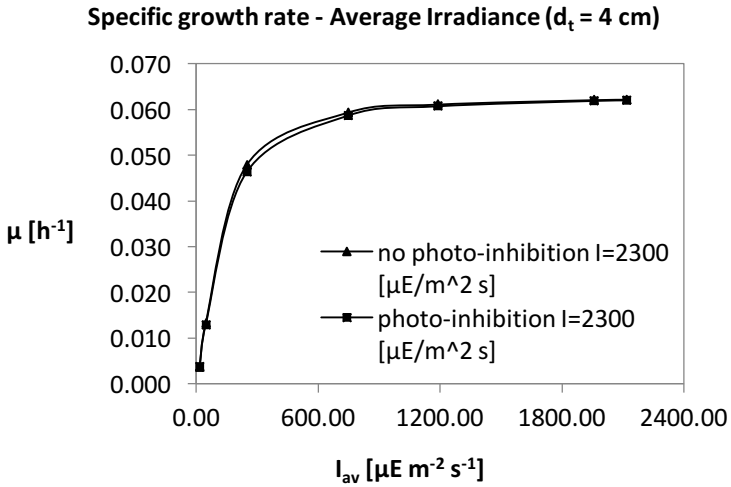

Figure 2.30 Cornet law: specific growth rate as a function of average irradiance I=2300 [μE/m2 s], diameter size dt=4cm and photo-inhibition.

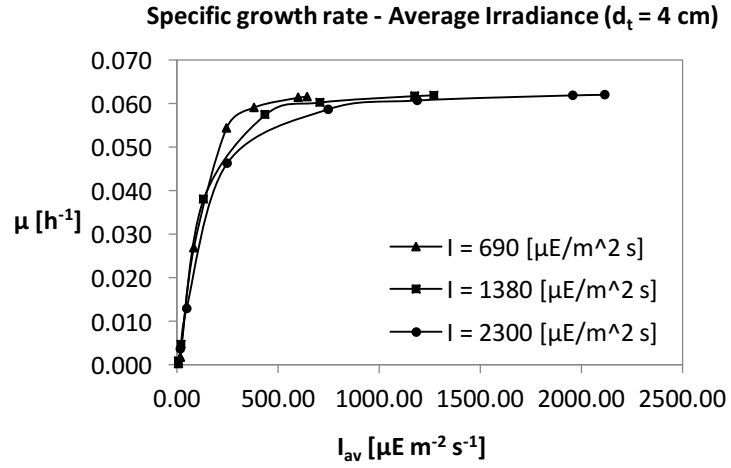

Figure 2.31 Cornet law: specific growth rate as a function of average irradiance specified and diameter size dt=4cm.

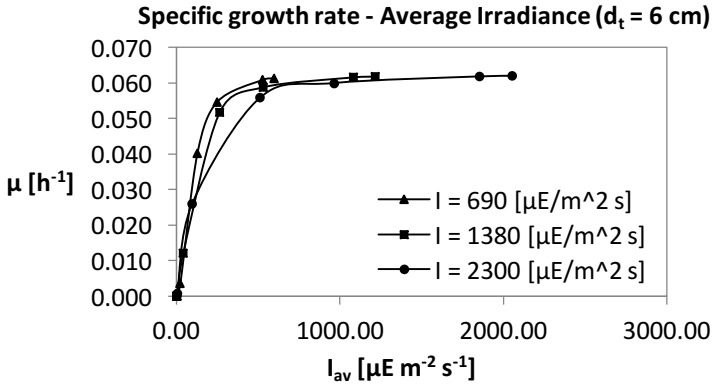

Figure 2.32 Cornet law: specific growth rate as a function of average irradiance specified and diameter size dt=6cm.

The obtained results are similar to the previous model, where by increasing irradiance value and taking into account photo-limitation and photo-inhibition the specific growth rate is reduced. Equally, it occurs in the second case with pipe diameter of 6 cm.

Finally, by comparing the first Beer-Lambert law model and Cornet law modelit was observed that the specific growth rate values obtained with the second model are lower than using first model; this is due to Cornet law which takes into account scattering and photon absorption selectively.

Acién Fernández law. This formulation aims to overcome the limits of the second formulation, i.e. determination of the parameters E_a and E_s, and then considering the two phenomena separately [51]. Therefore, following the same procedure of previous models, and taking into account the experimental parameters required by *Acién Fernández et al.* [51], Figure 2.33, Figure 2.34, Figure 2.35, Figure 2.36 and Figure 2.37 show the results obtained for the three external incident irradiance values.

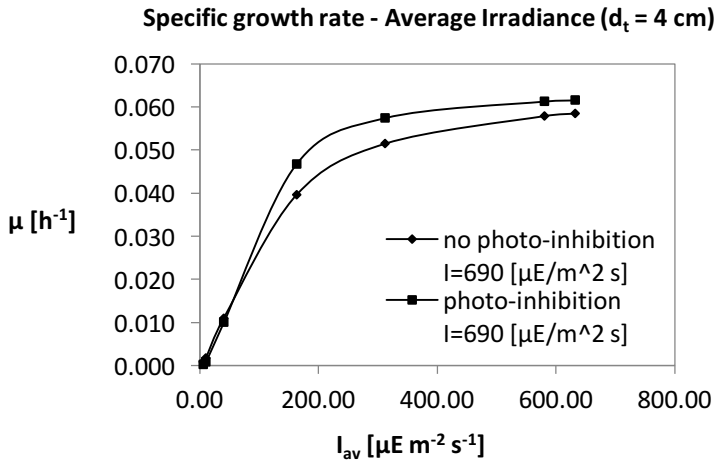

Figure 2.33 Acién Fernández law: specific growth rate as a function of average irradiance I=690 [μE/m2 s], diameter size dt=4cm and photo-inhibition.

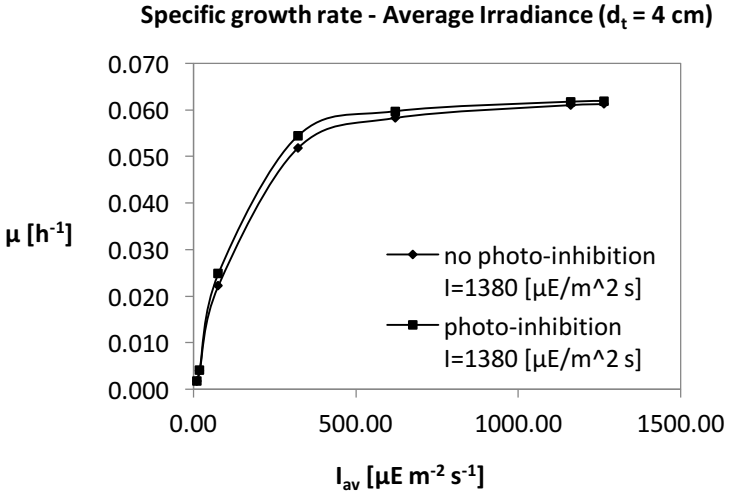

Figure 2.34 Acién Fernández law: specific growth rate as a function of average irradiance I=1380 [μE/m2 s], diameter size dt=4cm and photo-inhibition.

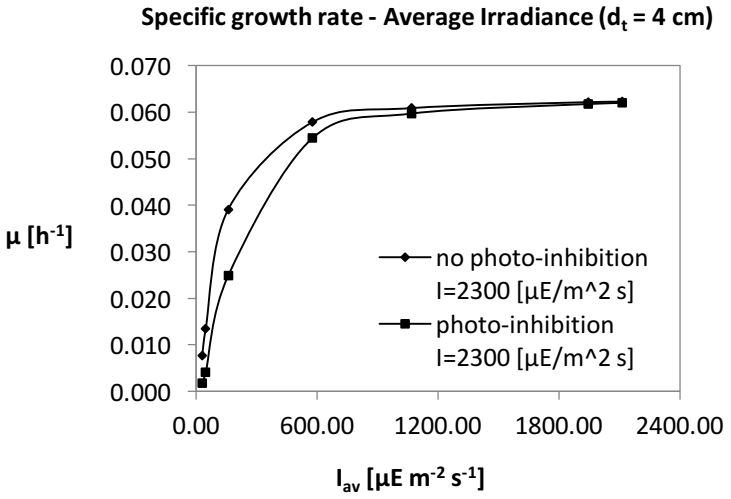

Figure 2.35 Acién Fernández law: specific growth rate as a function of average irradiance I=2300 [μE/m2 s], diameter size dt=4cm and photo-inhibition.

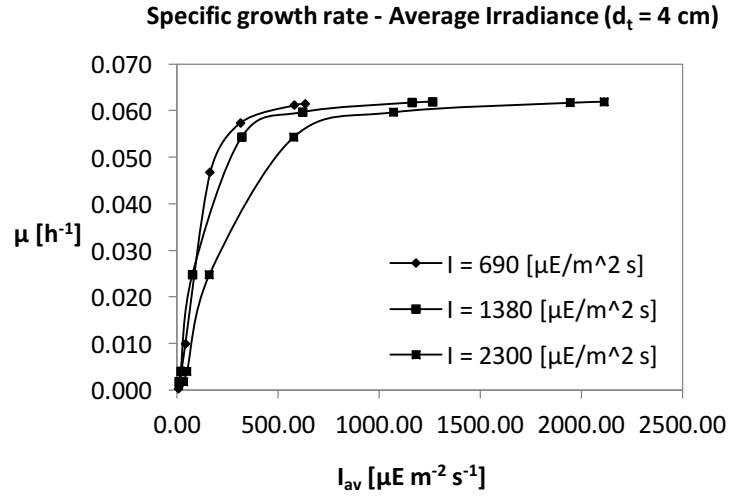

Figure 2.36 Acién Fernández law: specific growth rate as a function of average irradiance specified and diameter size dt=4cm.

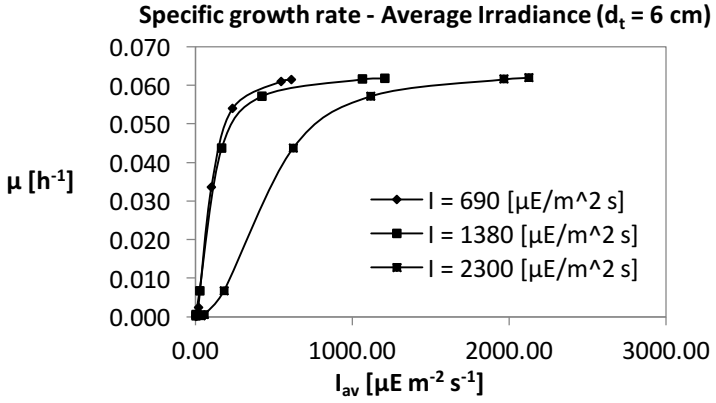

Figure 2.37 Acién Fernández law: specific growth rate as a function of average irradiance specified and diameter size dt=6cm.

The last obtained results are similar to the previous models, and by comparing all models, it was observed that the specific growth rate values obtained with the latter model are lower than other two models; this is because, Acién Fernández law taking into account photon scattering and absorption selective not independently.

Therefore, from simple Beer-Lambert law to Acién Fernández law a more accurate evaluation of specific growth rate was obtained at various irradiance levels.

2.7.6.2 Full Fluid Dynamic Model Results

As already discussed in the previous section 2.2.4.2, a more accurate model that takes into account light dark cycles frequency is proposed by *Molina Grima et al.* [39]. The procedure used in this model included:

- medium culture chemical-physical parameters such as density, viscosity, etc. [30];
- photobioreactor geometry, i.e. 4, 6 and 8 cm;
- average daily irradiance, i.e. 975, 1225, 1625 e 2250 $\mu E\ m^{-2}s^{-1}$;
- average biomass concentration;
- referring to *Phaeodactylum tricornutum* species, a saturation light intensity I_s equal to 200 $\mu E\ m^{-2}s^{-1}$ [35] was taken into account;

- loop calculation implementation to obtain biomass productivity by varying light/dark cycles frequency.

In Figure 2.38 and Figure 2.39 the results of light/dark cycles frequency and volumetric productivity as a function of average daily irradiance for the three pipe diameter values are shown.

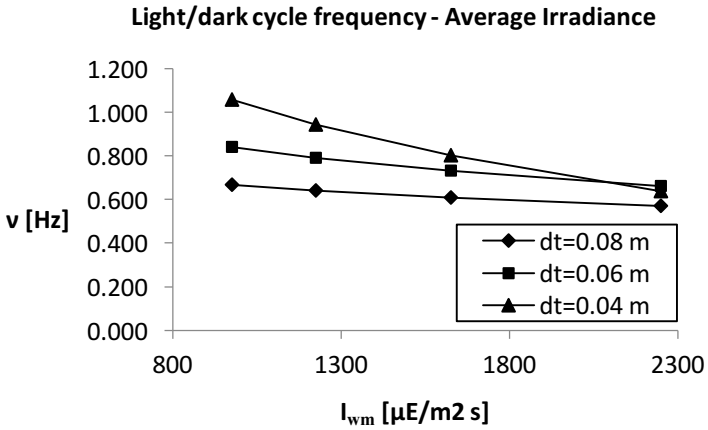

Figure 2.38 Light/dark cycles frequency variation as a function of average daily irradiance.

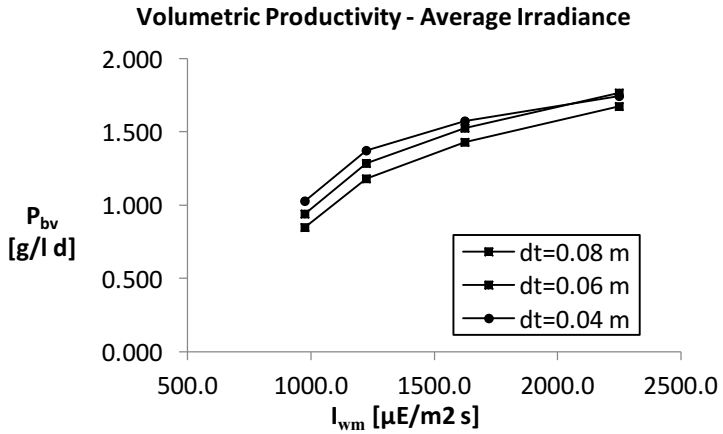

Figure 2.39 Volumetric productivity as a function of average daily irradiance.

Since optimal light/dark cycles frequency must be at least *1 Hz*, as suggested by Molina Grima et al. [35] for *Phaeodactylum tricornutum* cultivation, a sensitivity analysis was carried out by changing the input parameter, i.e. the superficial fluid velocity u_L. In particular, the superficial velocity u_L was investigated at different pipe diameter, that it would make the minimum value of light/dark cycles frequency, as shown in Table 2.9.

Table 2.9 Superficial velocity u_L for minimum value of light/dark cycles frequency.

Superficial Velocity u_L [m/s]	*Pipe diameter d_t [m]*
0.5	0.04
0.48	0.06
0.57	0.08

Then, on the basis of the four average daily irradiance values chosen, the next step was to fix a light/dark cycles frequency range, i.e. *0, 0.5, 1, 1.5, 2* and *2.5 Hz*, in order to obtain volumetric productivity by equation (2.39). Figure 2.40 shows the results obtained with a pipe diameter of 0.04 m.

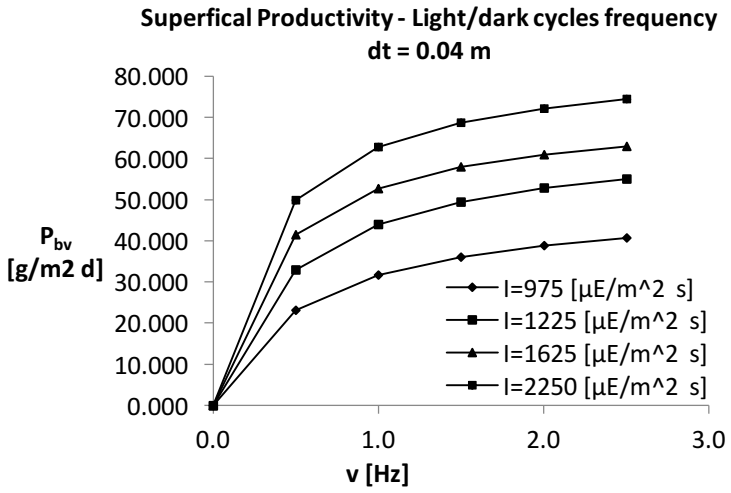

Figure 2.40 Superficial productivity as a function of light/dark cycles frequency with dt=0.04m.

However, it is noted that volumetric productivity is not sensitive to pipe diameter variation; this productivity increases with increasing of light/dark cycles frequency until reaching saturation level, and it increases with increasing average daily irradiance.

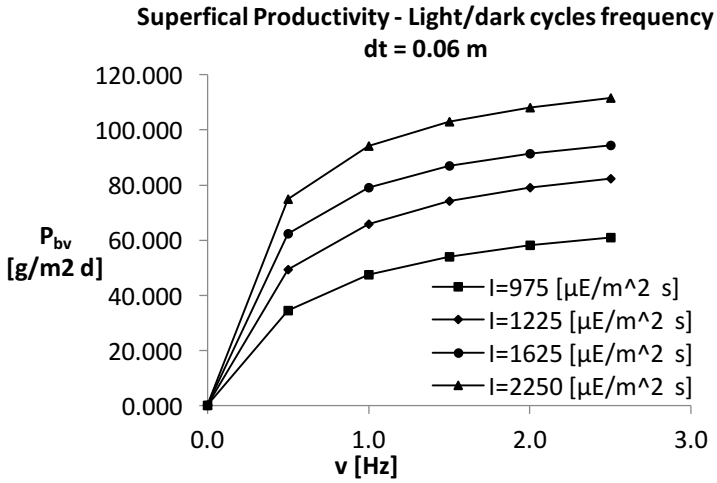

Figure 2.41 Superficial productivity as a function of light/dark cycles frequency with dt=0.06m.

Now, one considers the superficial biomass productivity as a function of pipe diameter, as shown in Figure 2.41 and Figure 2.42. It is noted that increasing pipe diameter results in an increase of superficial productivity, but also a light/dark cycles frequency reduction is obtained; then, it is necessary to find a compromise in the choice of pipe diameter to obtain the optimal productivity.

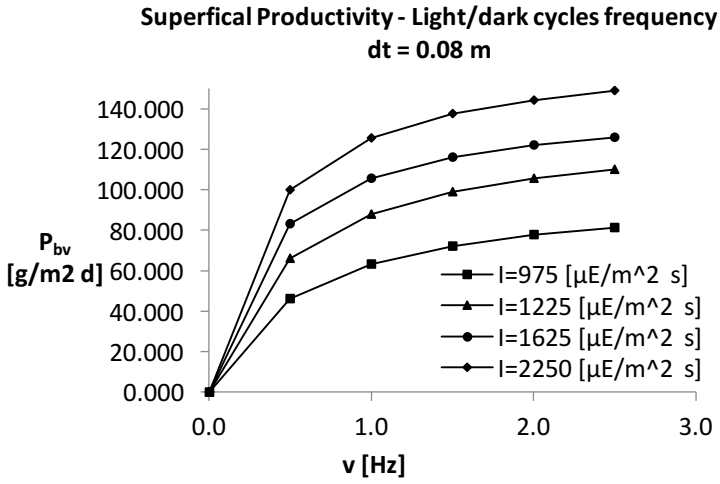

Figure 2.42 Superficial productivity as a function of light/dark cycles frequency with dt=0.08m.

In conclusion, for *Phaeodactylum tricornutum* microalgae species there are some reference values which it is possible to conduct the process in ideally optimal conditions:

- an optimal biomass concentration range between 5 and 15 g/L, within which the optical cell density is located, while beyond it the biomass productivity decreases;
- the three main nutrients are assimilated by the microalgae species in different concentration ranges, on a gradually decreasing from carbon, nitrogen to phosphorus;
- the optimal pH is about 7.8, while the optimal temperature is equal to 20.4 ° C and no growth phenomenon for temperatures higher than 26 °C and in a very aggressive environment (pH less than 2 and greater than 12);
- toxic oxygen with 250% higher values than the saturation equilibrium concentration between the medium and the air at atmospheric pressure;
- influence of growth process due to irradiance: in the simplified model with increasing irradiance, the specific growth rate increases up to saturation, while in the full fluid dynamic model the light/dark cycles frequency decreases with increasing irradiance.

2.8 Results and discussion of PBR Pilot Plant modeling

In this section, the numerical results of the pilot plant in steady state and pseudo-steady state condition are reported. Normally, all developed calculations were performed using the steady-state condition. Subsequently, pseudo-steady state condition results will be shown.

This critical sections of the pilot plant, i.e. photobioreactor and airlift parts, were simulated using Matlab code. Table 2.10 shows the initial modeled conditions.

Table 2.10 Geometric and operational initial parameters.

Initial Configuration		
PBR pipe length	11	*m*
Number of PBR pipes	8	-
PBR diameter	0.06	*m*
Riser height	18	*m*
Riser diameter	0.08	*m*
Biomass Concentration	2000	g/m^3
External temperature	303	*K*
Make-up temperature	293	*K*
Average daily Irradiance	391	W/m^2
Degaser pressure	0.4	*bar*
Gas flow rate	2.05	*L/min*
O2 gas molar fraction	10^{-5}	-
CO2 gas molar fraction	0.84	
H2O gas molar fraction	0.159	
Initial diameter bubbles Riser	1	*mm*

From the previous modeling discussed in previous sections, the flow characteristics were obtained by the resolution of balance equation, as shown in Table 2.11. This last table shows a steady-state results by using the simple model proposed by *Molina-Grima*, as already discussed in section 2.2.4.1.

Table 2.11 Results of flow characteristics from steady-state Matlab simulations for the PBR Pilot Plant with the *Molina-Grima* formulation simplified model.

Steady-State		
Liquid flow rate	1.42	*L/s*
Volumetric Productivity	2.28	$g/l \cdot day$
Superficial Productivity	89.68	$g/m^2 \cdot day$
PBR		

Outlet Biomass concentration	2001.6	g/m^3
O2 Concentration	4.47	*g/l*
CO2 Concentration	7.58	*g/l*
Outlet Temperature	320.77	*K*
Riser		
O2 gas molar fraction	0.04	
CO2 gas molar fraction	0.41	
H2O gas molar fraction	0.53	
Pressure drop	0.02	*bar*
Outlet Temperature	320.66	*K*

It is worth noting that injected gas flow at riser bottom section is mainly composed of carbon dioxide (84% mol), vapour water (15.9 mol%) and it presents a possible oxygen traces. In output riser section, oxygen molar fraction is increased due to flow rate inside the riser column which allows liquid phase degassing, and resulting in dissolved oxygen stripping. Liquid oxygen concentration is about 4.47 g/L, below limit concentration (equal to 9 g/L), and there is not oxygen accumulation beyond the limits of photo-oxidation phenomena. Volumetric productivity is equal to 2.28 g/L day, and it results to be a fairly high value although it is a closed system. Temperature parameters are almost similar even if it is noted a slight liquid cooling at output riser section; this temperature decrease is due to sensible heat exchange between liquid- and gaseous phase.

Table 2.12 Comparison between biomass concentration, volumetric- and superficial productivity numerical obtained at different irradiance models.

Models comparison			
	Biomass concentration g/m^3	Volumetric Productivity $g/l \cdot day$	Superficial Productivity $g/m^2 \cdot day$
Beer-Lambert	2001.7	2.284	89.692
Cornet	2001.6	2.166	85.071
Acién Fernández	2001.4	1.851	72.933
Full-Model	2001.8	2.414	94.814

Table 2.12 shows a comparison between irradiance models used. *Beer-Lambert* model and *Cornet* model not show a significant difference; in fact, the difference between volumetric productivity is about 5%. Instead, *Acién Fernández* model returns

a volumetric productivity of less than 20% compared to *Beer-Lambert* model. Subsequently, Full model allows to take into account fluid dynamics aspects and light-dark cycles frequency; as it can be seen, these values are slightly higher compared to *Acién Fernández* model, with a maximum of 25%.

For an additional model validation, results obtained were compared with other two works [59] and [39], as shown in Table 2.13.

Table 2.13 Comparison between biomass concentration, volumetric- and superficial productivity obtained with numerical models and literature data [59] and [39].

Models comparison			
	Irradiance	Biomass concentration	Volumetric Productivity
	$\mu E/m^2 \cdot s$	*g/l*	*g/ l·day*
Acién Fernández Model	1300	2.40	1.85
Full-Model	1300	2.42	2.41
Ref. 1 [59]	1289	2.38	1.19
Ref. 2 [39]	1126	2.29	1.15

Regarding the biomass productivity higher results were obtained compared to two reference external works with similar irradiance values. Possible explanations are: (i) experimental volumetric productivity values averaged over ten hours while in this work the steady-state results are obtained by balance equation resolution; (ii) different geometry design and then (iii) in this work the liquid velocity is very high, i.e. high turbulence and an increase of light/dark cycles frequency.

Finally, a pseudo-steady state simulation was conducted by using Full model for the irradiance, as shown in Figure 2.43. The aim of this analysis was to estimate the productivity by varying external conditions in terms of temperature and irradiance. As already introduced in section 2.6.2, this analysis was conducted with average daily data for one year (2015) obtained from the Institute for Environment and Sustainability of the European Commission, Joint Research Centre [56].

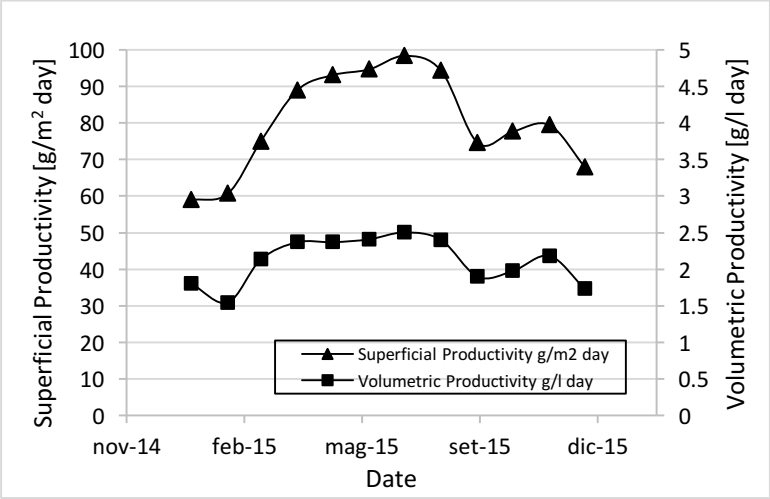

Figure 2.43 Results of pseudo-steady state simulation by using Full Model for the irradiance.

As it can be seen, volumetric- and superficial productivity show the same trend, where there is an increase of productivity during summer months. Therefore, this pseudo-steady state model is useful for a circadian- or annual distribution of biomass productivity.

3 AIR-LIFT LAB SCALE UNIT: EXPERIMENTAL TESTS AND CFD ANALYSIS*

Abstract

In biological cultures, flow regimes and temperature control are particularly important, as the growth rate of the cultivated species. These parameters, in fact, are the major ones which affect metabolism and biomass productivity. This is because they have effects on thermodynamics and kinetics of biochemical reactions.

In most photobioreactors thermal control is operated by suitable external units (heat exchangers) to remove the excess heat developed. However, an attractive and alternative idea is based on water evaporation in the Air-Lift pump system. It is, in fact, a promising device for biomass production, and guarantees two meaningful functions: (i) good handling of the fluid with no moving parts and (ii) suitable gas stripping through the degassing zone in the Air-Lift head. Therefore, as first step, in this work, hydrodynamics experimental laboratory activities were performed using a *20-liters* external loop Air-Lift system *4 meters* high only. Several experimental tests were carried out by varying the air flow rate as well as separator pressure. Liquid circulation flow rates were measured to investigate the effect of imposed head pressure and injected air flow rate on global hydrodynamic parameters. It was found that, in accordance with expectations, liquid velocity circulation decreases while decreasing vacuum level at the top section due to the relevant decreases of average gas fraction in the riser.

Then, computational fluid dynamics simulations were also developed to predict liquid circulation rates within the system. The numerical results were finally compared with experimental data and a good agreement was found.

* Part of this chapter has been published in revised form as:

- A. Brucato, G. Marotta, F. Scargiali,
  Vacuum temperature control of an Air-Lift photobioreactor,
  European Congress of Chemical Engineering ECCE, September (2015), Nice, France.

3.1 Introduction to Air-Lift System

In section 1.8.2.4 Air-Lift Reactors were introduced. These are systems where the gas-liquid density gradient generates a natural recirculation of the continuous liquid phase.

In principle, the so called Air-Lift Systems (ALS) were born as photobioreactor in biological cultivation, belonging to the vertical tubular reactor category [60]. Over the years, thanks to their design and characteristics, they became an innovative handling system. More in details, as regarding gas-liquid mixture with microorganisms, ALS can be used for both biochemical growth and fluid recirculation.

In the second case, they may substitute common mechanical pumps or other types of handling system. From this point of view, Air-Lift pumps are defined as cylindrical vessels with two interconnecting zones. One of these contains gas-liquid mixture which moves upward, while, the second one, contains liquid which goes downward. This recirculation is natural, thanks to a density gradient which establishes between two different fluids: gas-liquid mixture and liquid without or with a very little gas amount. This density gradient generates a pressure difference necessary to create a natural cyclic recirculation.

Regardless of their configuration, these systems are constituted by three characteristic components:

- *Riser*, in which gas-liquid mixture moves upward, pressure decreases and little by little gas bubbles leave the liquid phase (stripping or desorption). The gas phase is introduced at the bottom through a sparger.
- *Downcomer*, that represents the descending zone for liquid phase and imprints the necessary driving force for recirculation (density gradient).
- *Degaser*, the zone that permits the separation between liquid and gas phases and need to be accurately dimensioned.

The introduction of gas phase allows turbulence, mixing and mass transfer between liquid and gas phases. A part of recirculation, which is the priority, other phenomena take place: desorption of gas from gas-liquid mixture and evaporation of the liquid.

As already introduced in section 1.8.2.4, in terms of their design and configuration Air-Lift systems can be classified into three types: Internal-Loop Split (or Outside-Loop), Internal-Loop Concentric Tube and External-Loop, as reported in Figure 1.23 2.A-C. In the Internal-Loop Split configuration (A) the gas phase is introduced, through a sparger, in the annular section (riser) and moves upward with the liquid. Progressively, the mixture loses gas bubbles along the riser and a complete or partial separation occurs on the degaser (head of the Air-Lift). Consequently, liquid phase goes downward along the second tube, the downcomer, generating a natural recirculation thanks to the density gradient and then pressure difference. The so called Internal Loop Concentric Tube (B), is exactly the opposite configuration with respect to the first one. In this case, gas phase is diffused inside a concentric draft tube (riser) and goes up with the liquid. Once the mixture arrives on the top section (degaser) separation occurs. So, liquid phase moves downward along annular section generating a cyclic loop. Finally, the External Loop configuration (C) is completely different, because riser and downcomer are now separated tubes, interconnected only at top and bottom sections. Riser and downcomer are connected at the bottom section with a specific connection pipe, which inevitably influences hold-up of gas and velocity [1]. A correct and accurate degaser sizing will lead to an efficient gas-liquid separation, no transportation of gas along the downcomer and a good recirculation. Inside the riser, gas phase without any agitation, moves upward randomly and haphazardly, reducing the density of the riser with respect to downcomer. The performance of disengagement zone (degaser) also depends on operative conditions.

The circulation of both liquid and gas is facilitated by the difference in gas hold-up between riser and downcomer. This difference, in fact, corresponds to a density gradient among the two fluids, gas-liquid mixture in the riser and liquid in the downcomer, which generates a pressure difference on the Air-Lift System, as shown by the following equation [60]:

$$\Delta P = \rho_m g(\varphi_r - \varphi_d) \tag{3.1}$$

where ΔP is the pressure difference, ρ_m the average density of the fluid, g gravity acceleration, φ_r and φ_d respectively gas hold-up in the riser and downcomer. Gas hold-up is defined as the ratio between gas volume V_g and the total volume of the system

V_t. This pressure difference is generated on the bottom section and represents the driving force to guarantee continuous circulation.

From fluid-dynamic point of view *External Loop Air-Lift* guarantees greater efficiency, major disengagement of gas from liquid with respect to the *Internal Loop* types [61]. This is due to the separator arrangement and sizing in *External Loop* type, which leads to a complete separation of gas and liquid. In *Internal Loop Air-Lift* the shortest path, associated to a single gas bubble, from riser to downcomer, is represented by a straight line across the baffle which separates the two sections. While, in *External Loop* type, there is a minimum horizontal distance that increases the path, and then, the time spent by the fluid in the top section. This, inevitably, leads to a major disengagement of gas from liquid and a greater efficiency of separation. Then, in *External Loop Air-Lift* a total disengagement of gas is reached with maximum efficiency of separation between gas and liquid. In *Internal Loop Air-Lift*, instead, a complete disengagement is very difficult to obtain, only by using the lowest gas flow rate [60].

3.2 Fluid dynamic parameters

The interconnections between design and operating variables are schematically shown in Figure 3.1 proposed by Merchuk et al. [60]. Design variables are: (i) reactor height, (ii) ratio among riser and downcomer areas, (iii) degaser geometric design and (iv) bottom clearance, i.e. the distance between lower extremity of riser and bottom of reactor which is related to the available area to flux and, thereby, represents the resistance to it.

Instead, operating variables are: (i) gas flow rate and (ii) top clearance, i.e. the distance between higher extremity of riser and non-aerated liquid surface. Looking at Figure 3.1, other fluid-dynamic variables that characterize the system are: pressure drops (top, bottom and friction), hold up (riser, downcomer and separator), viscosity and liquid velocity.

Operating independent variables define the conditions which determine the liquid velocity on the ALS by means reciprocal relations of hold-up and pressure drops, as

reported in Figure 3.1. In this case of gas-liquid mixture, viscosity is not an independent variable, because of its dependence from gas hold-up and liquid velocity.

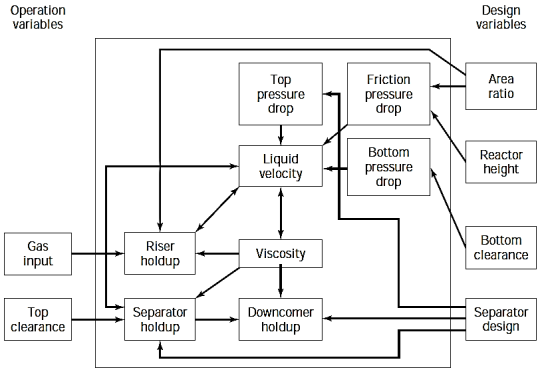

Figure 3.1 Design and Operating Variables of a general Air-Lift System [60].

Riser. As already mentioned, along the riser a pseudo fluid, gas-liquid mixture, is moved upwards, with gas velocity higher than liquid velocity. Generally, three main transport mechanisms are considered: *homogeneous regime* or *bubbly flow*, *heterogeneous regime* or *churn turbulent flow* and *slug flow*, as shown in Figure 3.2.

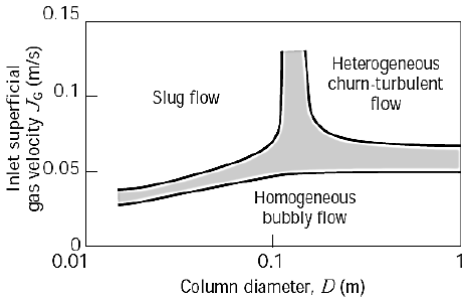

Figure 3.2 Flow regimes in biphasic fluids [60].

In homogeneous regime or bubbly flow gas bubbles have uniform diameter, they are relatively small and turbulence is very low. In this case, liquid velocity and gas velocity are very similar. On the contrary, in heterogeneous regime or churn turbulent

flow, turbulence inside the liquid is high and coexist bubbles with different dimensions. This regime may be generated starting from homogeneous regime by increasing gas flow rate. Alternatively, considering the slug flow as initial regime, by exalting turbulence by means of either higher velocity or greater diameter, it's possible to pass to the heterogeneous regime, as shown in Figure 3.2. Note that, slug flow regime must be avoided because it provides gas bubbles with sizes equal to column dimensions, depressing mass transfer capacity [60].

Downcomer. Here the liquid phase moves downward leading, possibly, gas bubbles that go to the bottom together with the liquid. In order to achieve this, liquid velocity should be superior than ascent velocity of gas bubbles. If input gas flow rate is small, then superficial liquid velocity will be small and, in practice, all gas bubbles would be pushed away from liquid. In other words, along the downcomer only liquid phase will circulate. However, if gas flow rate is incremented therefore liquid velocity will be sufficiently high to trap smallest gas bubbles. So, further increase in liquid velocity, by progressively increasing gas flow rate, will lead to higher gas bubbles trapped. Vice versa, in these conditions, the presence of gas bubbles reduces the available surface to liquid flux, increasing, consequently, the liquid velocity. As a result, gas bubbles are trapped and transported downward, until the number of bubbles inevitably decreases, liquid velocity will also decrease and friction forces won't be able to overcome hydrostatic thrust. This feedback cycle, inside the downcomer, causes bubbles stratification, like a front of bubbles, in which smallest bubbles escape through the bottom while highest bubbles move upward. The front of bubbles goes downward while increasing inlet gas flow rate, until gas bubbles reach the bottom section, ready to be recirculate along the riser. When this point is reached, gas bubble distribution inside the downcomer becomes much more uniform [62]. This is the best configuration in downcomer, unless it's necessary only one gas passage (as happens in microalgae cultivation where gas has to disengage totally the liquid).

Degaser. Gas separator is often ignored in Air-Lift System discussion, despite having significant influence on fluid-dynamic. The geometric configuration of it determines the amount of gas disengaged from liquid. In addition, the sizing of the degaser will influence its performance. If total disengagement of gas is obtained, then

clear liquid will be the only phase that goes down along the downcomer. In more general cases, a certain fraction of gas will be trapped and recirculated. The higher is the turbulence the greater will be the number of bubbles trapped in the top section. This situation inevitably influences the two main parameters: gas hold-up and liquid velocity. A common solution is to enlarge gas-separator dimensions in order to decrease liquid velocity, and therefore, facilitate disengagement of gas [62].

The two principal parameters that describe these systems are (i) gas hold-up and (ii) liquid velocity.

As concerns gas hold-up, it depends on these values:

- *liquid velocity*, the higher liquid velocity the lower gas hold-up;
- *riser and downcomer height*, the higher riser height the lower gas hold-up in the riser and the higher gas hold-up in the downcomer;
- *connection pipe length*, the larger connection pipe length the lower gas hold-up in riser and downcomer;
- *ratio between downcomer and riser areas*, the higher this ratio the larger gas hold-up;
- *liquid level*, the higher liquid level inside the degaser the lower gas hold-up.

Liquid velocity is the most important variable on the design of Air-Lift system because of its influence on gas hold-up, mixing time, resident time of gas phase, interfacial area, mass transport coefficients and heat transfer coefficients. Liquid velocity, like gas hold-up, is not an independent variable but it depends on different values as mentioned above.

As regards liquid velocity, it depends on these quantities:

- *inlet gas flow rate*, the higher inlet gas flow rates the larger liquid velocity;
- *connection pipe length*, the larger this parameter the larger liquid velocity;
- *riser and downcomer height,* the higher riser and downcomer height the higher liquid velocity.

3.2.1 Gas Hold-Up

As already reported in the previous section, gas hold-up is defined as the ratio between gas volume V_g and the total volume of the system V_t., as shown in the following equation:

$$\varphi_G = \frac{V_G}{V_G + V_L} \tag{3.2}$$

This parameter is important for two fundamental aspects: mass transfer and total fluid force. In various correlations [60] for hold up prediction, it can be seen as this parameter depends on system height and it is in agreement with gas bubble expansion moving towards reduced pressures environments. Then, for external loop Air-Lift, these correlations can be summarized by the following formulation:

$$\varphi_R = \alpha\, J_G^{\beta} \tag{3.3}$$

where φ_R is the gas hold up in the riser section, J_G is the superficial gas velocity, α and β are experimental parameters related to pressure drops [60].

In this work, experimental results were compared with a theoretical mathematical model predicted by Bello et al., and it is shown in the following equation:

$$\varphi_R = 0.16 \left(\frac{J_G^2}{J_{1R}}\right)^{0.56} \left(1 + \frac{A_D}{A_R}\right) \tag{3.4}$$

this equation [63] well approximates the real trend for external loop Air-Lift case.

3.2.2 Liquid Velocity

As already reported, liquid velocity is the most important variable on the design of Air-Lift system because of its influence on gas hold-up, mixing time, resident time of gas phase, interfacial area, mass transport coefficients and heat transfer coefficients. Several mathematical models were proposed for the liquid velocity prediction [60,64] but only two are the main models related to energy- and momentum balance equation. Chisti et al. [53] have proposed an approach related to the energy balance of the entire Air-Lift system. In this model, the energy due to bubble expansion is dissipated by (i) friction, (ii) turbulence due to bubble movement along riser- and downcomer section, (iii) fluid recirculation in degaser section and (iv) by

fluid recirculation on the base section. Overall energy balance on entire Air-Lift system is equal to:

$$E_i = E_R + E_D + E_{DG} + E_B + E_F \tag{3.5}$$

where E_i is the energy due to bubble expansion and, E_R, E_D, E_{DG} and E_B, are the energies due to fluid recirculation in riser, downcomer, degaser and base section, respectively. E_F is the energy lost due to the friction. Assuming a Newtonian fluid, it will be possible to ignore friction losses. Then, considering all previous terms, it is explicit the equation (3.5) now.

Regarding the riser energy balance and considering all liquid as control volume, it should be considered its energy contribution by pressure and potential energy gain:

$$E_i = E_R - \rho_l\, g\, h_R(1-\varphi_R)U_{L,R}A_R + \rho_l\, g\, h_R U_{L,R}A_R \tag{3.6}$$

By simplifying:

$$E_i = E_R - \rho_l\, g\, h_R U_{L,R}A_R\varphi_R \tag{3.7}$$

The dissipation energy term due to downcomer is obtained by performing an energy balance on the descending liquid, obtaining:

$$0 = E_D + \rho_l\, g\, h_D(1-\varphi_D)U_{L,D}A_D - \rho_l\, g\, h_D U_{L,D}A_D \tag{3.8}$$

By simplifying:

$$E_D = \rho_l\, g\, h_D U_{L,D}A_D\varphi_D \tag{3.9}$$

Similarly, it can be calculated degaser- and base energy loss as:

$$E_{DG} + E_B = \frac{1}{2}\rho_L\left[V_{L,R}^3 K_{DG}A_R(1-\varphi_R) + V_{L,D}^3 K_B A_D(1-\varphi_D)\right] \tag{3.10}$$

where K_{DG} and K_B are the friction coefficients due to degaser- and base inlet; V_{LR} and V_{LD} are the axial riser- and downcomer velocity, respectively. These last terms are related by the following equation:

$$V_L = \frac{U_L}{1-\varphi} \tag{3.11}$$

Now, one considers continuity equation between riser and downcomer:

$$Q_{L,R} = Q_{L,D} \tag{3.12}$$

that is:

$$U_{L,R}(1-\varphi_R)A_R = U_{L,D}(1-\varphi_D)A_D \tag{3.13}$$

By replacing these into the equation (3.6) and explaining riser liquid superficial velocity the following expression is obtained:

$$U_{L,riser} = \left[\frac{2\ g\ h_D \varepsilon_R}{K_B \left(\frac{1}{(1-\varepsilon_R)^2} + \left(\frac{A_R}{A_D}\right)^2 \frac{1}{(1-\varepsilon_D)^2} \right)} \right]^{0.5} \tag{3.14}$$

The obvious disadvantage of this equation is the not-direct correlation between liquid velocity and gas flow rate. By designing an external-loop Air-Lift, in the downcomer section gas hold-up ε_D can be considered void while in the riser gas hold-up ε_R can be estimated by the correlation [65]:

$$\varepsilon_R = \frac{U_{G,R}}{0.24 + 1.35 \left(U_{G,R} + U_{L,R}\right)^{0.93}} \tag{3.15}$$

this correlation was given by Hills [65] for Air-Lift system in which the superficial velocity of gas- and liquid phase sum is less than *1.5 ms*$^{-1}$.

Regarding friction factor K_B in the equation (3.14) it is calculated by the following correlation [64]:

$$K_B = 11.402 \left(\frac{A_D}{A_B}\right)^{0.789} \tag{3.16}$$

Therefore, in the riser section, gas hold up and liquid velocity have to be calculated simultaneously through a loop calculation. Initially, it is assumed an arbitrary liquid velocity, then it is calculated vacuum level and thus the liquid velocity by two correlations: *Chisti et al.* and *Bello et al.* [53].

3.2.3 Mass transfer coefficient

As already introduced, Air-Lift System is not only efficient as regards circulation of fluids but it is used to exploit mass transfer and evaporation. More in details, in microalgae cultivation oxygen is produced because of the photosynthesis process. High levels of oxygen are toxic for microalgae, so it is necessary to remove it, and one possibility is to take advantage of desorption in Air-Lift system. So, fresh gas spreaded through the sparger in the riser guarantees at the same time the driving force to recirculation (hold-up difference among riser and downcomer) and the achievement

of the stripping. As regards mass transfer, an indicative parameter is the so called Volumetric Mass Transfer Coefficient, k_La: it represents the quantity of gas transferred in correspondence to the gas-liquid interface per driving unit force, namely concentration gradient among gas and liquid. Volumetric mass transfer coefficient may be seen as the product between two terms: (i) mass transfer coefficient k_L, which has dimension of velocity (ms^{-1}) and (ii) specific interfacial area a, which has dimension of a surface per unit volume (m^2m^{-3}).

So, the k_La parameter has dimension like the inverse of time (s^{-1}). Both terms, which make up the k_La parameter, depend on a series of variables that may be gathered into three categories [66]:

- static properties of the fluid, density, diffusivity and surface tension;
- dynamic properties of the fluid, relative to flux, as rheological parameters;
- fluid dynamic parameters.

The methods for defining k_La are several. In general, measurement methods are classified in *steady-state* and *transitory*. Independently of the utilized method, the steps to determine transport coefficient k_La are the same, in the two cases, as illustrated in Figure 3.3. The measured variable, usually species concentration, is compared with the predicted value by using a mathematical model. Note that, the choice of a mathematical model depends on the best value that can be obtained. It is clear that the choice of the model and thehypothesis regarding gas and liquid, are very important and may determine possible deviations from real values.

The various sections of the Air-Lift (riser, downcomer and degaser) have different flux characteristics, and then, volumetric mass transfer coefficient can vary from one region to another. Often, perfect mixing assumption is used to create a generic mathematical model, but it's important to verify if this assumption is close or far to reality. The higher is the height of the Air-Lift the larger is the distance from the perfect mixing assumption. One method to investigate if the assumption is verified or not is that based on species concentration measurements in different zones [66]. If the hypothesis is valid, so the different position of the probes should be irrelevant. Figure 3.4 shows the results of three different probes located, respectively, at the end of riser, at the entrance of downcomer and in the bottom section of an Air-Lift system

[66]. Looking at Figure 3.4, the right side is referred to an Air-Lift apparatus with a very high degaser size and liquid velocity, which ensures the validation of perfect mixing assumption (the same value measured by three different probes).

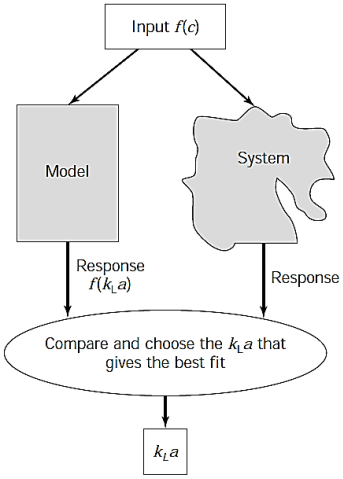

Figure 3.3 Steps for the determination of k_La transport coefficient [60].

Passing to a different gas separator dimension, the values obtained by using three probes are different, as reported on the left graph in Figure 3.4.

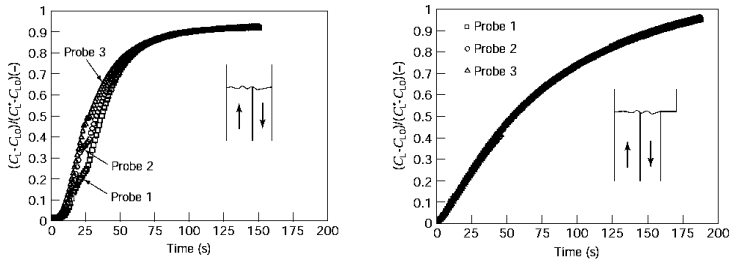

Figure 3.4 Results in k_La measurements [60].

The validation of this criterion is based on the comparison between circulation time on the Air-Lift t_c and the characteristic time of mass transport [60], namely the

inverse of volumetric mass transport coefficient k_La, expressed by the following equation:

$$k_La < \frac{1}{2t_c} \tag{3.17}$$

If this assumption is not validated, then the Air-Lift system cannot be considered as a perfect mixing system, and further sophisticated analysis are necessary.

It has been anticipated that mass transport coefficient is different in correspondence to the various zones of the Air-Lift. This is clearer looking at Figure 3.5.

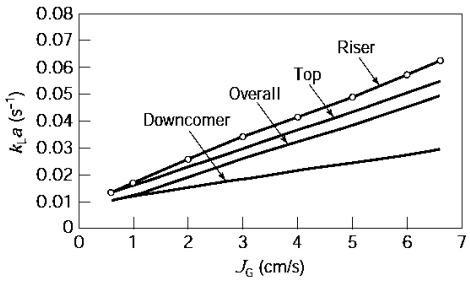

Figure 3.5 k_La measurements in different sections of the Air-Lift, influence of superficial gas velocity [60].

Mass transfer takes place much more along the riser with the highest values. The k_La values, measured on the downcomer, are lower of *50%* than those in the riser. Instead, the measured value on the degaser are intermediate among the previously riser and downcomer values. Finally, the overall k_La values depend on volumes and mass transport in all mentioned sections [60].

3.3 Laboratory investigation in tall Air-Lift Reactor: experimental apparatus and procedures

The external loop Air-Lift system was used in this study. The device consists of four fully transparent pipes in PMMA, each of one referred, respectively, for riser,

downcomer, connection pipe and degaser. The choice of transparent tubes was due to the willing to observe the fluid-dynamic behaviour inside the system. It is shown in Figure 3.6. As discussed previously, the principle of operation provides the injection of gas, by using a porous fritted glass sparger, at the bottom of the riser. It rises up and together with the liquid phase moves upward. Once arrived into the degaser a separation occurs. So, the liquid phase moves downward along the downcomer, while the gas phase is extracted by means a vacuum pump. In the base tube a regulating valve was installed with pressure gauges. The presence of water trap should guarantee no accumulation of water, which might destroy the vacuum pump. Looking at Figure 3.6, additional components are: three pressure gauges by *Rosemount* and two flow meter *Promag 10 – Endress+Hauser*.

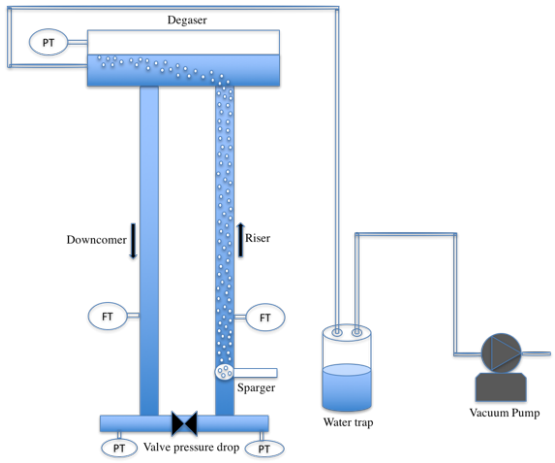

Figure 3.6 Scheme of the external loop Air-Lift apparatus.

After the conceptual design, consecutive steps were construction and the commission of the system. For this purpose, one decided to assemble the various components in order to obtain 4 m head of water and, then, realize a pressure drop of about 0.4 bar at the bottom of the Air-Lift. Overall, Table 3.1 reports the characteristic geometric dimensions of each component of the Air-Lift.

Table 3.1 Characteristic geometric dimensions of riser, downcomer, degaser and connection pipe.

Riser		**Downcomer**		**Degaser**		**Base pipe**	
Height	4 m	Height	4 m	Length	1.33 m	Length	1.33 m
ID	0.04 m	ID	0.04 m	ID	0.096 m	ID	0.04 m
OD	0.05 m	OD	0.05 m	OD	0.1 m	OD	0.05 m

In order to realize the connection among the tubes auxiliary components, compression connectors were necessary. They were: three T joints, four double joints, one elbow fitting and one sphere valve. As concerns, respectively, riser and downcomer, two tubes 2 m long were bought for each one. By using double joints, it was possible connect these tubes and create the Air-Lift 4 m height. Despite the connection pipe has the same diameter of riser and downcomer it is shorter than them, 1.33 m. So, it was necessary to cut the 2 m long tube until the specific dimension, 1.33 m. The same was for degaser, but it had higher diameter for reasons inherent the separation, as discussed previously. Figure 3.7 shows the interconnection between the various parts, their assembling to create the device.

Figure 3.7 Assembling and construction of the external loop Air-Lift apparatus.

Vacuum creation occurs thanks to Venturi effect, by using compressed air as power source. The latter one may be provided with a pressure between *2* and *6 bar*, generating vacuum condition until *-920 mbar*. As seen in Figure 3.8, the compressed air supply (P) crosses the ejection Venturi nozzle causing aspiration (V), creating, then, vacuum conditions at the head of the Air-Lift. At the end, air leaves the system (E). Vacuum level can be regulated by means pressure regulator *FESTO*, situated between vacuum generator and air source tube.

In order to monitor compressed air flow rare, sent to the sparger, a mass flow meter *AALBORG DFM27* was used.

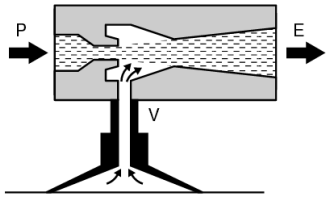

Figure 3.8 Operating principle of the vacuum pump.

Thus, several experimental tests were carried out by varying the inlet sparger flow rate between 0.05 to 0.65 L/min.

3.3.1 Experimental Results

Once fixed the geometrical parameters, manipulation variables are (i) inlet gas flow rate, (ii) degaser liquid level and (iii) vacuum level. Table 3.2 shows the experimental tests carried out by fixing a certain degaser liquid level at different applied vacuum level.

Table 3.2 Lab-Scale Air-Lift experimental tests.

Top Pressure [bar]	0.2 - 0.25 - 0.35				
Q_g [L/min]	0.07	0.17	0.33	0.47	0.63

In order to simulate pressure drops, different tests were carried out by closing ball valve in the bottom section and with a fixed vacuum level (P_{top} = *0.2 bar*), as shown in Figure 3.9. As it can be seen, downcomer liquid flow rate shows the same trend by varying inlet gas flow rate, and increasingly lower values of circulating liquid are obtained by closing ball valve.

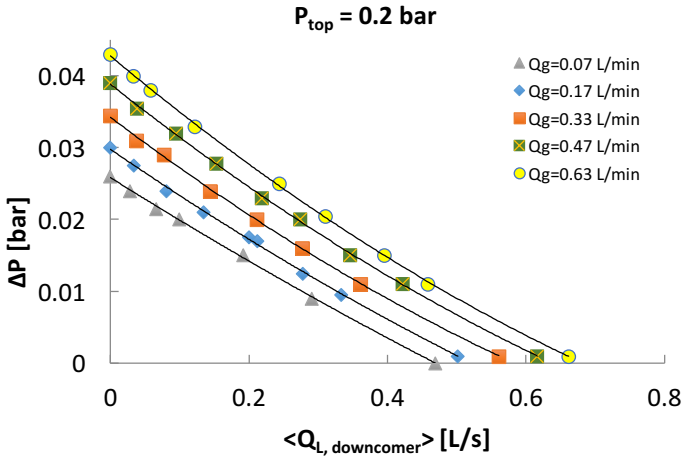

Figure 3.9 Experimental pressure drop tests at fixed vacuum level (P_{top} = *0.2 bar*).

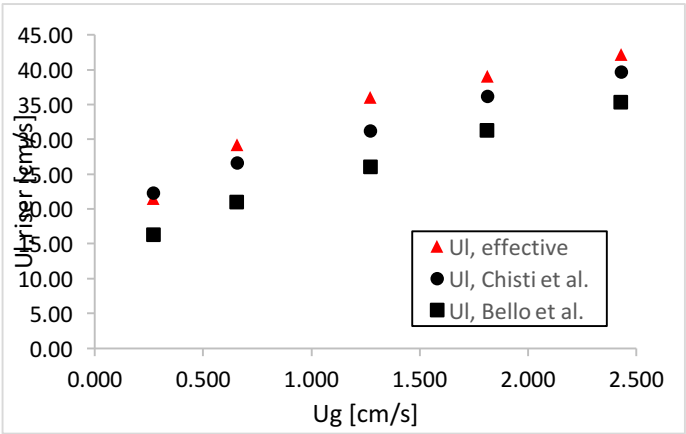

Figure 3.10 Comparison of riser liquid velocity measured and predicted by *Chisti et al.* [53] and *Bello et al.* [63] with head pressure of 0.2 bar.

As already discussed in section 3.2.2, there are various correlations to predict riser liquid velocity; then, Figure 3.10 shows results obtained of liquid riser velocity together *Chisti et al.* and *Bello et al.* correlations with head pressure of 0.2 bar [53].

In Figure 3.10 it's shown that the trend of these results is similar, but these two-present correlation underestimated values compared to experimental results; with *Chisti* correlation this difference is less than 12% and with *Bello* correlation this difference is less than 25%, that it is acceptable considering different geometry and operating conditions.

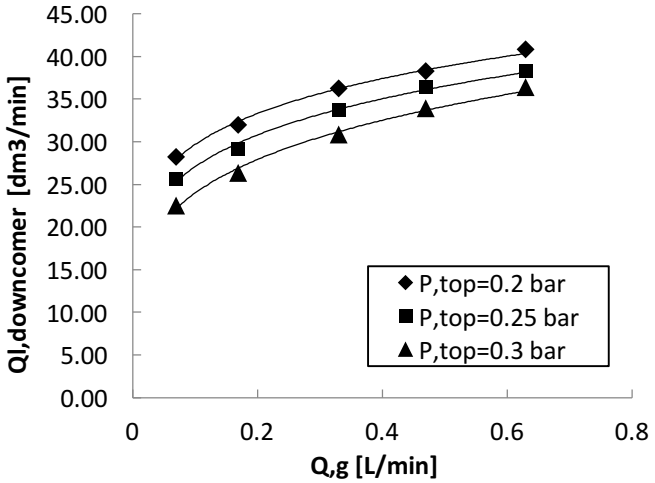

Figure 3.11 Liquid flow rate as a function of inlet gas flow rate at different head pressure.

Figure 3.11 shows the experimental tests by varying head pressure and inlet gas flow rate; these results show the typical performance Air-Lift curve. Therefore, in order to obtain a useful correlation, different functions were obtained by using a power law which connects liquid flow rate with inlet gas flow rate, as shown in Table 3.3.

Table 3.3 Power law functions which express liquid flow rate as function of inlet gas flow rate.

P_{top} [bar]

ΔP [bar]	0.20	0.25	0.30
0	$Q_l = 43.58\ Q_g^{0.167}$	$Q_l = 41.55\ Q_g^{0.186}$	$Q_l = 39.76\ Q_g^{0.221}$
0.01	$Q_l = 31.74\ Q_g^{0.246}$	$Q_l = 29.24\ Q_g^{0.277}$	$Q_l = 26.48\ Q_g^{0.371}$
0.015	$Q_l = 27.09\ Q_g^{0.333}$	$Q_l = 24.75\ Q_g^{0.389}$	$Q_l = 22.97\ Q_g^{0.589}$

Gas hold up measure was carried out using the equation (3.2), in previous section 3.2.1. Gas hold up is not constant in riser section since gas flow rate does not remain constant inside the system but increases: hydrostatic pressure decreases along riser section, and thereby it increases bubble ascent velocity with a consequent hold up increase.

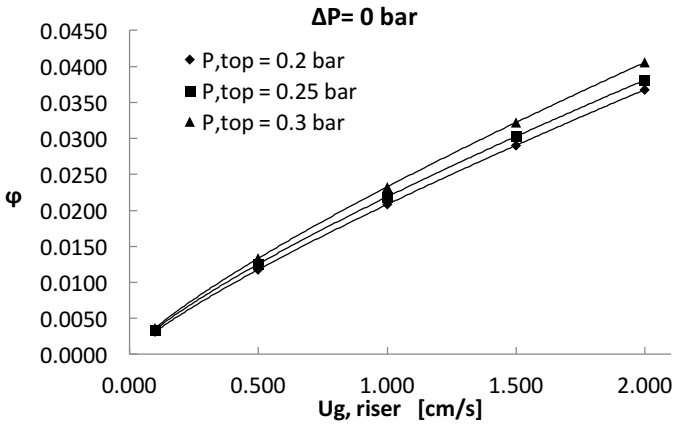

Figure 3.12 Riser gas hold up as a function of gas flow rate in riser section.

Figure 3.12 shows riser gas hold up dependence with superficial gas flow rate; this gas hold-up was calculated by riser discretization and the use of continuity equation for a compressible fluid; the results show a power law correlation which correlates riser gas hold up as a function of superficial gas flow rate in riser section, as shown in Table 3.4.

Table 3.4 Power law functions which express gas hold-up as function of superficial gas flow rate in riser section.

	P_{top} [bar]		
ΔP [bar]	0.20	0.25	0.30

0	$\varphi = 0.021\ U_g^{0.821}$	$\varphi = 0.031\ U_g^{0.731}$	$\varphi = 0.040\ U_g^{0.637}$
0.01	$\varphi = 0.022\ U_g^{0.801}$	$\varphi = 0.033\ U_g^{0.691}$	$\varphi = 0.044\ U_g^{0.570}$
0.015	$\varphi = 0.023\ U_g^{0.802}$	$\varphi = 0.037\ U_g^{0.640}$	$\varphi = 0.052\ U_g^{0.416}$

3.4 CFD modeling of the lab-scale tall Air-Lift Reactor

3.4.1 Model equations and solutions procedure

In order to obtain information about Air-Lift Reactor fluid dynamics, CFD simulations were carried out using the CFX commercial code. Numerical results compared with experimental data may be useful to understand the Air-Lift performances.

As this tall air-lift reactor is a two-phase system, gas-liquid flow numerical simulations were performed in the Eulerian-Eulerian framework with a multi-fluid approach [67]. Numerical resolution of the continuity- and momentum balance equations are solved for each phase. It is noted that liquid flow is the *continuous phase* (incompressible) and gas flow is the *dispersed phase* (compressible) in Air-Lift Reactor. Neglecting thermal effects inside Air-Lift Reactor, isothermal condition was imposed in these first numerical simulations.

3.4.1.1 Transport equations

Simulation runs were performed under transient assumptions; then, unsteady 3-D simulations were performed for all investigated cases. This system equation that characterizes hydrodynamics data may be solved using a direct numerical simulation, DNS, with which it is possible to obtain a complete modeling of the vortices at different length scales, theoretically. However, the velocity fluctuations induced by the smaller vortices require a spatial discretization much denser, and temporal interval much smaller to the time integration. Then, in order to simulate the turbulent flow, the original unsteady N-S equations is modified by the introduction of average and fluctuating quantities to produce the Reynolds Averaged Navier-Stokes (RANS)

equations. This type of equations reduces the computational effort compared to a DNS but the additional unknown terms containing products of the fluctuating quantities, i.e. Reynolds turbulent stresses. Therefore, when Reynolds averaging is used, mass and momentum balance equations can be written for gas and liquid phase as:

$$\frac{\partial}{\partial t}(r_\alpha \rho_\alpha) + \nabla\left(r_\alpha \rho_\alpha \overline{U}_\alpha - \rho_\alpha \frac{\upsilon_T}{\sigma_T}\nabla r_\alpha\right) = 0 \tag{3.18}$$

$$\begin{aligned}&\frac{\partial}{\partial t}(r_\alpha \rho_\alpha \overline{U}_\alpha) + \nabla\left(r_\alpha(\rho_\alpha \overline{U}_\alpha \overline{U}_\alpha)\right) = \\ &+\nabla\left(r_\alpha \mu_{\alpha_{eff}}(\nabla \overline{U}_\alpha + (\overline{\nabla U}_\alpha)^T)\right) + r_\alpha(\bar{F}_\alpha - \nabla p_\alpha) + \overline{M}_\alpha\end{aligned} \tag{3.19}$$

where $\overline{M}_\alpha$ is the interfacial momentum transfer term and $\bar{F}_\alpha$ is body force which is buoyancy term added in the momentum equation as follows:

$$\bar{F}_\alpha = (\rho_\alpha - \rho_{ref})\bar{g} \tag{3.20}$$

where ρ_{ref} is the buoyancy reference density (BRD). In the momentum equation pressure term excludes hydrostatic gradient due to ρ_{ref} and this last variable is related to the absolute pressure as follows:

$$p = p_{abs} - p_{ref} - \rho_{ref}\bar{g}(\bar{r} - \bar{r}_{ref}) \tag{3.21}$$

where $\bar{r}_{ref}$ is a reference location to be the centroid of the domain pressure. Regarding the effective viscosities $\mu_{\alpha_{eff}}$, it represents molecular and turbulent viscosity sum given by the following equation:

$$\mu_{\alpha_{eff}} = \mu_\alpha + \mu_{T\alpha} \tag{3.22}$$

Drag force is function of local slip velocity between dispersed- and continuous phase. It appears when bubbles move with different velocities to surrounded liquid phase. The general form to model interphase drag force, considering spherical particles is formulated by:

$$\overline{M_{l,g}^D} = n_b \overline{D}_b = \frac{3}{4}\frac{C_D}{d_b} r_\beta \rho_\alpha \left|\overline{U}_\beta - \overline{U}_\alpha\right|(\overline{U}_\beta - \overline{U}_\alpha) \tag{3.23}$$

where n_b is the number of bubbles, and C_D is the drag coefficient needed to calculate drag force $\overline{D}_b$ expressed per volume unit. In this work Grace correlation [68]

was used to compute the drag coefficient present within the interfacial momentum transfer term $\overline{M}_{\alpha}$.

The eddy diffusivity hypothesis is used to model the turbulent gas dispersion, characterized by last term at the RHS of continuity equation (3.18), where υ_T is the turbulent cinematic viscosity and σ_T is the Schmidt number. Volume fraction is the r_{α} term, sum of both phases:

$$r_g + r_l = 1 \tag{3.24}$$

To mathematically close the equations system, the *k-ε* turbulence model, developed by Launder and Spalding [69], has been used in various works on Air-Lift Reactors [70–73] obtaining satisfactory predicted results when compared to experiment.

Thus, for turbulence modeling a inhomogeneous model was chosen where a *standard k-ε turbulence model* [69] was used for the continuous- and dispersed phase as frequently used in Air-Lift and bubble column reactors [70–72]. A particle sizing for the dispersed phase was imposed, i.e. for the bubbles formed during operational Air-Lift phase; a fixed diameter of 3 mm for the bubbles was imposed in order to maintain a bubble flow regime as in the experimental apparatus developed.

The *scalable wall function* [74] formulation implemented in the CFX code was used in order to model the viscous-conductive sublayer [75] in the proximity of the walls.

3.4.1.2 Solution domain and boundary conditions

The 3-d fluid domain was created by means of the ANSYS Designer Modeller. The domain was then meshed by means of the Meshing code using a hybrid configuration of hexahedral and tetrahedral cells. In Figure 3.13 the entire meshed domain and an inlet section detail of the mesh are shown.

The operating pressure P_{ref} inside the supercritical reactor was set to atmospheric pressure as in experiments. Inlet conditions with constant mass flow rate was imposed,

while at the reactor outlet an expression was inserted to vary the outlet pressure with an exponential decreasing time-dependent law, as shown in the following equation:

$$P(t) = P_{ref} + \left(P_{ref} - P_{fin}\right)\left(e^{-t/\tau} - 1\right) \quad (3.25)$$

where P_{fin} is the vacuum pressure imposed, i.e. the three experimental cases 0.2-0.25-0.3 bar and τ is an arbitrary time constant. No-slip boundary conditions were imposed at reactor walls.

Thus, three groups of five cases were simulated by varying the inlet sparger flow rate between 0.05 to 0.65 L/min, as shown in Table 3.5.

Table 3.5 Inlet sparger flow rate of all simulated cases.

Case with P_{out} = 0.2 (A) – 0.25 (B) – 0.30 (C) [bar]	**Q_g inlet [L/min]**
1 A-B-C	0.07
2 A-B-C	0.17
3 A-B-C	0.33
4 A-B-C	0.47
5 A-B-C	0.63

In order to create the free surface in the degaser section, fluid domain was initialized with a water volume, i.e. continuous phase, up to a fixed height equal to half of degaser, and the remaining section was initialized with an air volume, i.e. dispersed phase.

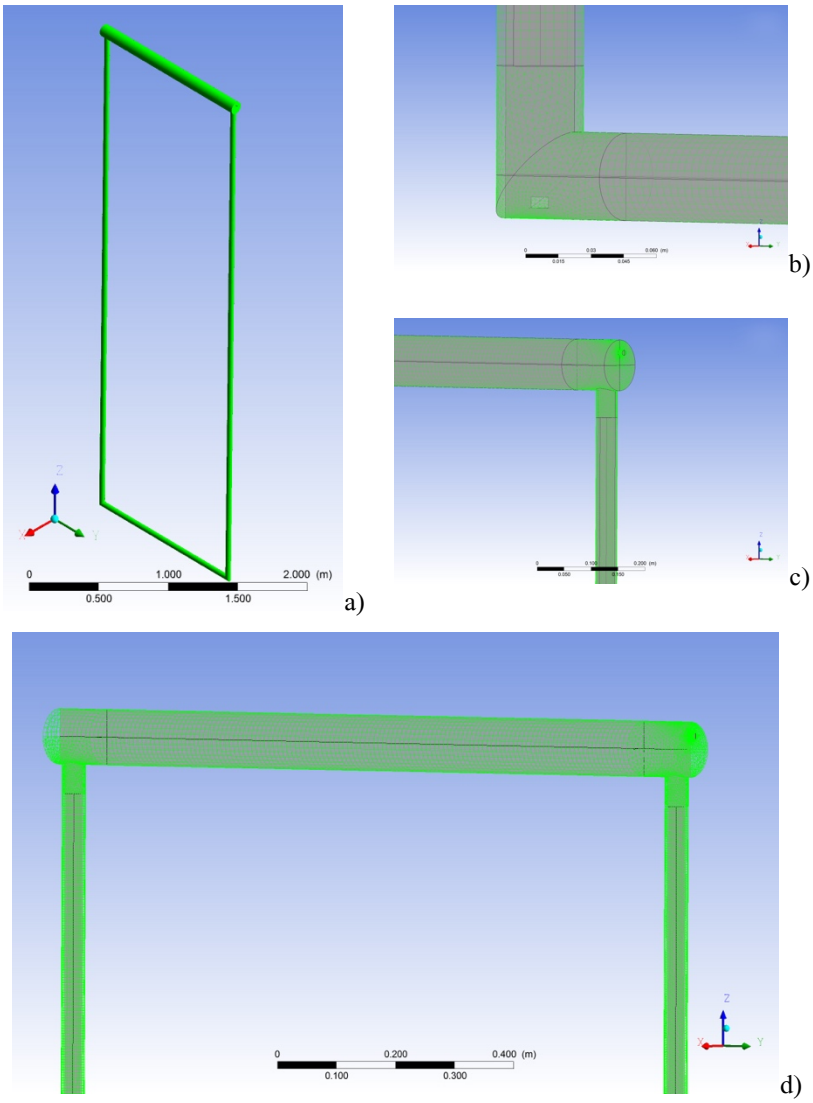

Figure 3.13 (a) Mesh domain and (b) inlet section of the computational tetra- and hexahedral mesh, (c) outlet section and (d) top Air-Lift section.

3.4.1.3 Convergence criteria

Transient simulations were conducted for all the analysed cases. The High-Resolution scheme was selected for spatial discretization of the advective terms and the second order backward Euler was selected as the transient scheme. Convergence

control of max 10 coefficient loops for each time-step was used with a residual target of $1 \cdot 10^{-3}$. Output pressure expressed by the exponential decreasing time-dependent law allowed to impose the desired vacuum level with a rapid convergence. Suitable values for the time-step ranging from $1 \cdot 10^{-3}$ *s* to $5 \cdot 10^{-2}$ *s* were chosen as a good compromise between the need to obtain accurate results (on the basis of Courant-Friedrichs-Lewy, CFL condition) and computational efficiency.

3.4.1.4 Simulation strategy

Satisfactory completion of each simulation run was based on several criteria: (i) sufficient reduction of mass residuals; (ii) accurate balance between the flow rates entering and leaving the reactor and (iii) either practically constant or regularly oscillating local values of all flow quantities. Steady state conditions were considered to be attained when all the above criteria were met.

In this work the density of the lighter fluid was chosen for the reference density. If there is a substantial difference in density between the fluids, round-off errors will be presented [76]; taken in account lighter fluid density, pressure will be constant in the light fluid and hydrostatic in the heavier fluid that simplify pressure boundary and initial conditions. Preliminary simulations were performed inserting the density of the continuous phase in the BRD; no appropriate physical results of the multiphase motion were obtained, and incorrect gravity force was computed for the continuous phase. Hence, after these preliminary numerical results dispersed, phase density was imposed for BRD.

3.4.1.5 Grid refinement and validation

In order to obtain grid-independent results while maintaining acceptable computational effort, a preliminary sensitivity analysis was carried out. Three different computational grids of (1) 110 x 10^3, (2) 350 x 10^3, (3) 550 x 10^3 cells for configuration A (0.2 bar) were set up. To test grid independency, water superficial velocities obtained at different downcomer heights with the various grids were

compared between each other. The fine (3) and medium (2) grids give rise to very similar profiles of water superficial velocity; therefore, since the differences between the numerical results for the medium and fine grid are small and considering the computational time for all examined cases, the 350 x 10^3 elements mesh (2) was chosen for all the simulations carried out in this work.

3.4.2 CFD Results

3.4.2.1 Velocity fields

In Figure 3.14a-b-c-d water superficial velocity vector plots in the critical points of the Air-Lift are shown for configurations 5-A *(P_{top} = 0.2 bar, $Q_{g\,in}$ = 0.63 L/min*).

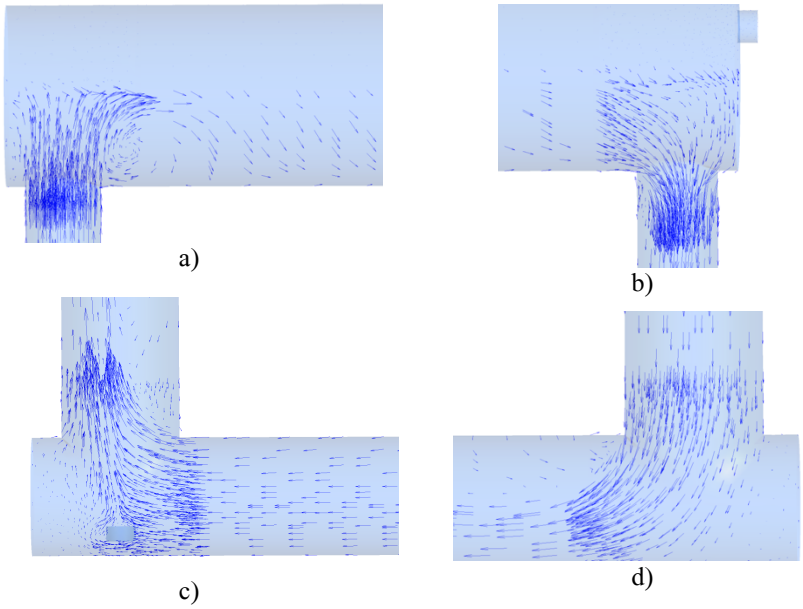

Figure 3.14 Vector plots on the y-z plane of the configuration 5-A *(P_{top} = 0.2 bar, $Q_{g\,in}$ = 0.63 L/min*) at different Air-Lift section (a) downcomer-top, (b) riser-top, (c) riser-inlet section and (d) riser-bottom section.

Inlet gas flow rate from the sparger positioned in the riser bottom section (Figure 3.14-c) establishes an upward liquid handling for dragging effect; then in degaser part

(Figure 3.14-a) this effect will be dampened by gas-liquid gravity separation and by vacuum applied, with gas release from this degaser top section; Finally, in downcomer-top section (Figure 3.14-b) liquid water has a potential energy, due to hydrostatic head, such as to establish a natural downward recirculation.

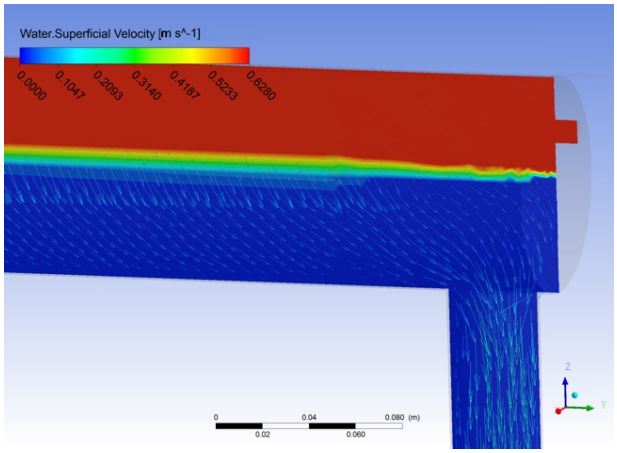

Figure 3.15 Vector plot of water superficial velocity on the y-z plane of the configuration 4-A on volume fraction (P_{top} = *0.2 bar,* $Q_{g\,in}$ = *0.47 L/min*) at riser-top section.

Figure 3.15 shows water superficial velocity vector plots in the crucial degaser point of the Air-Lift on gas volume fraction for configuration 4-A (P_{top} = *0.2 bar,* $Q_{g\,in}$ = *0.47 L/min*). It is worth noting that volume fraction profile is very defined, but it does not show the typical oscillatory trend know experimentally. However, gas-liquid separation is properly simulated, and there is no gas entrainment in the downcomer section.

3.5 Experimental and CFD results comparison

A comparison between experimental- and numerical results of the liquid flow rate in downcomer and riser section was carried out, as shown in Figure 3.16, Figure 3.17 and Figure 3.18 below.

It is noted that Air-Lift performance trends follow the same behavior, however numerical results overestimate experimental data when (i) input gas flow rates increase and (ii) greater head evacuated, especially. In fact, it is noted percentage deviations (figure captions) appear to be smaller by decreasing the head evacuated.

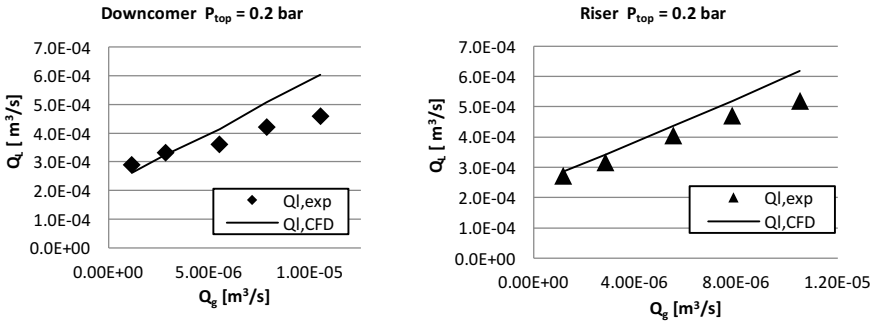

(a) (b)

Figure 3.16 Comparison of downcomer- and riser superficial liquid velocity measured and simulated with head pressure of 0.2 bar. Percentage deviations between -12% and +25%.

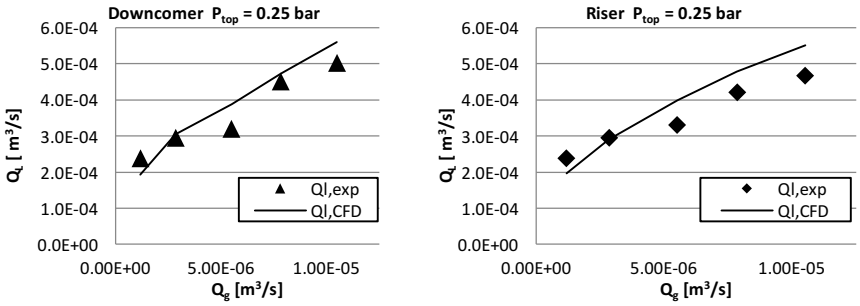

(a) (b)

Figure 3.17 Comparison of downcomer- and riser superficial liquid velocity measured and simulated with head pressure of 0.25 bar. Percentage deviations between -11% to +23%.

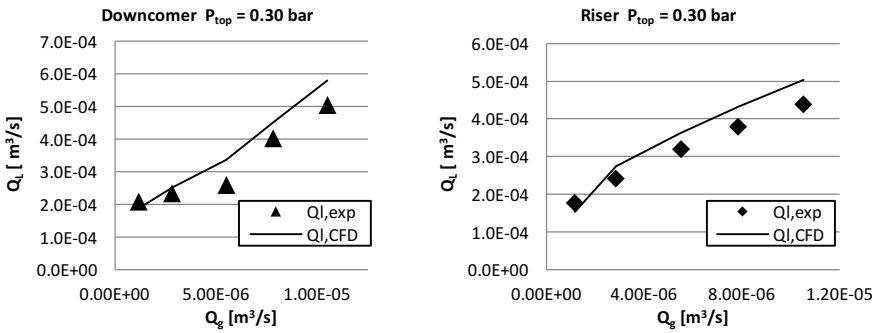

(a) (b)

Figure 3.18 Comparison of downcomer- and riser superficial liquid velocity measured and simulated with head pressure of 0.3 bar. Percentage deviations between -10% to 21%.

Therefore, about these experimental-numerical deviation results, the most accepted hypothesis concerns the simplification of gas-liquid interface forces; e.g. mere implementation of Grace drag model without additional forces such as lift-force or turbulent dispersion forces can report the lack of additional conditions to be considered in the domain system.

4 REFLECTION-REFRACTION EFFECTS ON LIGHT DISTRIBUTION INSIDE TUBULAR PHOTOBIOREACTORS [*]

Abstract

One of the main parameters affecting autotrophic algae cultures is photon absorption distribution inside the photobioreactor. This clearly depends on the geometry of both the radiation source and the photobioreactor, as well as on algae suspension optical properties. In this work the *local volumetric rate of photon absorption* LVRPA in a cross section of a horizontal-pipe photobioreactor was investigated by means of simplified Monte Carlo simulations. In particular, the fate of a number of photons perpendicularly hitting the photobioreactor circular section was simulated in relation to different values of algae concentration. The model takes into account refraction/reflection phenomena at the air/photobioreactor-wall interface. Simulation results show that radiation distribution inside the photobioreactor is quite strongly affected by reflection/refraction at the air-reactor interface. In particular, dark zones (not revealed when neglecting reflection/refraction phenomena) are observed in conjunction with unexpected radiation intensification in other zones. These phenomena are bound to affect photobioreactor performance and should therefore be considered if effective photobioreactor models are sought.

Moreover, in order to experimentally study light intensity effects on microalgae productivity, a thin-slab quasi-isoactinic photobioreactor was realized in laboratory-scale.

[*] Part of this chapter has been published in revised form as:

- G. Marotta, J. Pruvost, F. Scargiali, G. Caputo, A. Brucato *Reflection-refraction effects on light distribution inside tubular photobioreactors*, submitted to Canadian Journal Chem. Eng., (2016).

4.1 Introduction

Nowadays microalgae play an increasingly important role in the pharmaceutical nutraceutical (for the production of food supplements such as PUFA and carotenoids), cosmetics and renewable energy (as third-generation bio-fuels) fields.

Taking advantage of photosynthetic processes, microalgae are able to exploit and to convert in an effective way photons, water, CO_2 and nutrients into valuable products [4]. In order to obtain high amounts of biomass, microalgae cultures are grown in a variety of photo-bioreactors, including open raceway ponds and closed tubular photobioreactors. For reliable photobioreactor design, suitable models need to be developed. This is particularly hard in this case, as to the biological and hydrodynamic complexities shared with other bioreactors, here also the complexities related to light distribution effects need to be accounted for. As a matter of fact, one of the main parameters affecting autotrophic algae culture performance is photon absorption rate distribution inside the photobioreactor.

The importance of radiative field has been demonstrated in a number of investigations on photosynthetic activity relation with the radiation field involved [77–80]. The knowledge of light distribution inside the photobioreactor is essential especially when photobioreactors are operated at high microalgal cell concentrations [81]. This clearly depends on the geometry of both the radiation source and the photobioreactor, as well as on algae suspension optical properties. Considering a uniform cells distribution, in order to properly model the radiation field inside photobioreactors, the relevant balance equation, known as the *Radiation Transfer Equation* (RTE), should be solved. This would allow the computation of the *local volumetric rate of photon absorption* (LVRPA), a quantity strictly related to photosynthetic growth rate and biomass generation [82–84].

Considering that the integro-differential nature of RTE makes it difficult to obtain even numerical solutions, alternative methods have been developed. For instance, Colina et al. [85] used a P1 approach for solving the RTE in solar tubular photoreactors and Machuca et al. [86] used an hybrid approach by fitting model parameters to experimental data. Another interesting approach is the use of Monte Carlo methods, that allow rigorous numerical solutions to be obtained in a much

simpler way than solving the full RTE [87]. Fundamentals of this technique are well-known [88]. For instance, Brucato et al. [89] employed it for validating the simplified "Six Flux" radiation model in slab photo-catalytic reactors while Busciglio et al. [90] employed it to model radiation transfer in "quasi-isoactinic" reactors.

Taking into account this last approach, the purpose of this work is that of studying the *Local Volumetric Rate of Photon Absorption* LVRPA distribution over a cross section of a horizontal-pipe photobioreactor. In particular, a Monte Carlo method was employed to simulate a photobioreactor irradiated by a far-away external radiation source. Tubular closed photobioreactors are commonly used for solar cultures, together with flat panel PBRs. however light distribution simulation is not straightforward in tubular geometries due to complexities related to refraction effects on curved walls. As a difference, flat panel PBRs which respond to the so-called "one-dimensional approximation", are much more amenable to simple simulations [91,92].

4.2 Methodology

4.2.1 Mathematical modeling

The investigated geometry is a tubular photobioreactor with internal radius R and parallel irradiation from the outside, as it would occur with direct sunlight or any other relatively far away source. In Figure 4.1 a schematic diagram of the cross section is reported. It is worth noting that the investigated condition is the specific one encountered at noon for an east-west oriented tube. Also in this case, the irradiation is bound to have a time varying incident angle with respect to solar course. Though the case here investigated may be regarded as a quite singular condition, it was considered sufficiently informative on the peculiar phenomena that take place in these systems. Other tilt angle effects will be the subject of subsequent work.

The tubular reactor simplified mathematical modelling is based on the assumption that photon path is reflected and refracted, according to Fresnel and Snell laws, when passing from one medium to another with different refraction index, as depicted in Figure 4.1. For the sake of simplicity, the deflection effects due to the thin transparent wall of the tubular photobioreactor were neglected, as suggested by

Pruvost et al. [91] and Lee et al. [92]. The history of a statistically meaningful number of photons, N_r, traveling inside a generic photobioreactor cross section was simulated.

It is worth noting that the absorption and scattering properties of the medium affect the mean free path of the photons travelling inside the photobioreactor. Considering the microscopic size of microalgae, these can be modelled as uniformly distributed particles in the culture broth. Therefore, in relation to different values of microalgae concentration, C_x, the fate of a large number of photons was simulated, starting from its entrance into the photobioreactor cross section until they either escaped from the photobioreactor or were absorbed inside the growth medium. A simplified approach was also used as concerns photon-algae interactions, namely scattering and diffraction effects were neglected and all interactions were assumed to result into photon absorption by the microalgae. This assumption was made in view of the strongly forward oriented scattering phase function experimentally measured by Kandilian et al. [93], that results into very small deflection effects when a scattering event takes place, so making acceptable the assumption of no deflection upon scattering. Finally, reflection effects at the inner medium/air interface were also neglected, in view of their negligible extent at sufficient microalgae concentrations [94].

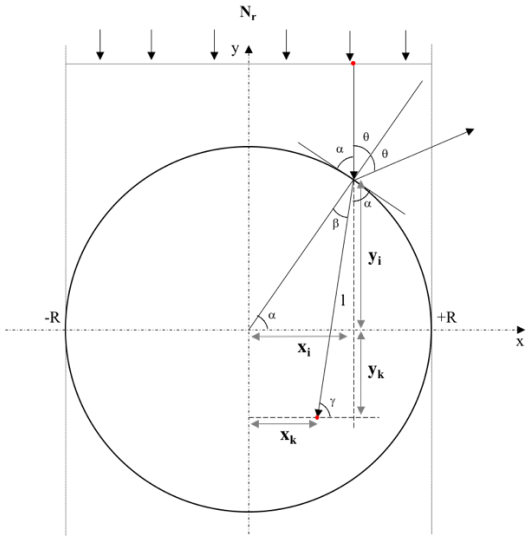

Figure 4.1. Irradiated cross-section by photons taking into account Fresnel and Snell laws.

The procedure was started by randomly selecting the photon offset with respect to tube axis,

$$x_i = R_{n1} \cdot R \tag{4.1}$$

where R_{n1} is a random number between -1 and 1.

Then accordingly, the ordinate is simply derived by the circle equation as

$$y_i = \sqrt{(R^2 - x_i^2)} \tag{4.2}$$

According to Snell's law, which quantifies refraction at the air/wall interface, the deviation angle β of the photon into the photobioreactor is given by

$$\beta = sin^{-1}\left(\sin\theta \cdot \frac{n_1}{n_2}\right) \tag{4.3}$$

where θ is the angle between the direction of photon travel and the normal direction and n_1 and n_2 are the refraction indexes of air and water respectively. As previously stated, it is considered that photobioreactor wall is so thin as to not to affect the optical diffraction phenomena.

Once a photon has entered the photobioreactor space, while travelling it is subject to hitting microalgae cells. As the probability of hitting a cell is uniform, an exponential decay of radiation intensity can be presumed, which is characterized by a characteristic extinction length, λ. This last is inversely proportional to the product of microalgae concentration, C_x, by the radiant energy mass coefficient, E_a [82]:

$$\lambda = \frac{1}{C_x E_a} \tag{4.4}$$

As a consequence, the distance travelled by the photon before hitting a cell and being absorbed was computed as:

$$l_i = -\lambda \ln(R_{n2}) \tag{4.5}$$

where R_{n2} is a new random number between zero and one. The coordinates (x_k, y_k) where the absorption event occurs are therefore given by, this depth is given by:

$$x_k = x_i - l_i \cos\gamma = x_i - \lambda \ln(R_{n2}) \cos\gamma \tag{4.6}$$

$$y_k = y_i - l_i \sin\gamma = x_i - \lambda \ln(R_{n2}) \sin\gamma \tag{4.7}$$

where γ is given by the sum of angles $\alpha=\pi/2-\theta$ and β, as shown in Figure 4.1.

Obviously, when the condition ($x_k^2 + y_k^2 > R^2$) is found to be true, then this implies that the photon has exited the reactor space without being affected by absorption

phenomena. In the other case, photon absorption has occurred inside reactor space and the relevant coordinates are recorded for subsequent processing.

As it is well known, at the air/medium interface the refracted fraction of energy is smaller than one, due to the loss of reflected radiant energy. This might have been accounted for by generating a further random number and deciding whether the photon has been reflected or refracted according to the relevant probabilities. The choice here adopted was instead that of assuming that the refracted photon carries a "weight" smaller than one, and equal to the refracted fraction of energy. This is akin to following the fate of a number of photons, belonging to the same parcel and assuming they all undergo the same absorption events.

In order to compute the refracted energy fraction, if the incident photons are not polarised and medium culture is assumed to be non-magnetic, the Fresnel laws for electromagnetic energy conservation can be employed. According to these, the reflected energy fraction is given by:

$$R_f = \frac{R_s + R_p}{2} = \frac{1}{2}\left\{\left[\frac{(n_1 \cos\theta - n_2 \cos\beta)}{(n_1 \cos\theta + n_2 \cos\beta)}\right]^2 + \left[\frac{(n_1 \cos\beta - n_2 \cos\theta)}{(n_1 \cos\beta + n_2 \cos\theta)}\right]^2\right\} \tag{4.8}$$

where R_s and R_p are the reflectance for s-polarized light and for p-polarized light respectively.

Therefore, the transmitted energy fraction is computed as:

$$T = 1 - R_f \tag{4.9}$$

Each photon entering the reactor space is therefore assumed to carry a weight equal to *T*, and when absorbed inside the reactor, its weight is recorded along with its absorption site coordinates.

A typical computation involved following the fate of a large number of photon parcels, resulting in a smaller number of absorption events inside the reactor space, each one characterized by its coordinates and weight.

4.2.2 LVRPA distribution assessment

In order to obtain the *local volumetric rate of photon absorption* (LVRPA) distribution, the cross section of the photobioreactor was discretized with a 2D

structured mesh of 300*300 (90k) square elements. For each of the photon parcels simulated, the mesh element in which absorption had taken place was identified and the parcel weight was added to the relevant element of a square matrix. The result was finally normalized by dividing it by the total number of photon parcels simulated and multiplying the result by the number of square cells. In this way in each element of the matrix a number proportional to the local rate of photon absorption was obtained.

By exploring several total numbers of photon parcels, it was found that, with the spatial resolution adopted (300*300), a number of fifty million photons was more than sufficient to obtain stable and smooth results.

By using MATLAB as the development environment, even in the most demanding cases, CPU times never exceeded few tens of seconds on the common PC employed for the calculations.

4.3 Results and discussion

All results are reported as normalized LVRPA for convenience of analysis. LVRPA distributions were obtained for different values of the characteristic extinction length λ and then, for different biomass concentrations with fixed value of E_a by means of the developed Monte Carlo code. The results obtained can be compared with the corresponding LVRPA distributions obtained by neglecting the optical refraction/reflection phenomena at the air liquid interface, as it is customarily made in the relevant open literature [30], [92]. Such comparison is shown in Figure 4.2, where the results obtained in relation to four different values of algae biomass concentration C_x (*0.10, 0.20, 0.5, 1.0 kg/m*^{3}) are reported. In particular, on the left side the results obtained while neglecting reflection/refraction phenomena are shown (*Figures 2 a, c, e, g)* and as it can be seen, the distributions obtained are consistent with similar results reported in the open literature. Please note that with the aim of increasing the maps readability, each map is normalized by dividing all values by the maximum LVRPA value observed in the same map. As it can be observed, the smaller the biomass concentration the more spread-out is the LVRPA distribution (though

with smaller absolute values at all points, a feature not revealed by the normalized maps), as it could have been expected.

On the right side of Figure 4.2 the results obtained at the same concentrations are shown, but this time by considering the reflection/refraction phenomena at photobioreactor wall. Reported values are normalized by the same maximum value as the relevant figure at the left. As it can be seen the LVREA distribution is quite strongly affected by reflection/refraction phenomena. In particular, by comparing Figure 4.2a and 2b, both obtained at the same biomass concentration of *0.10 kg/m*^{3}, the existence of completely dark zones in the lower side areas in Figure 4.2b, not present in Figure 4.2a, can be observed.

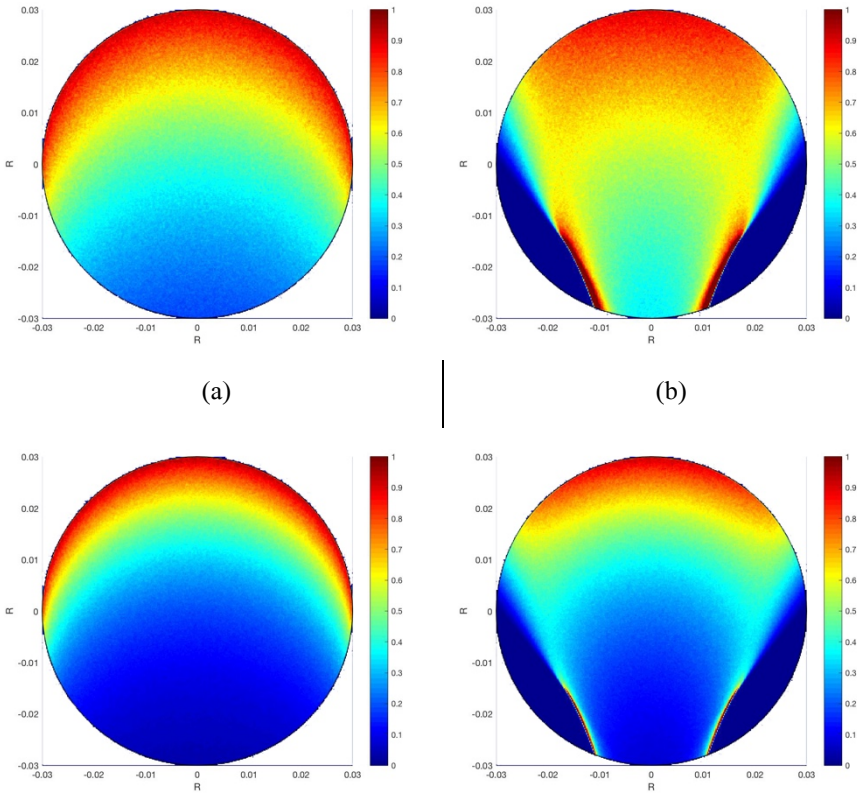

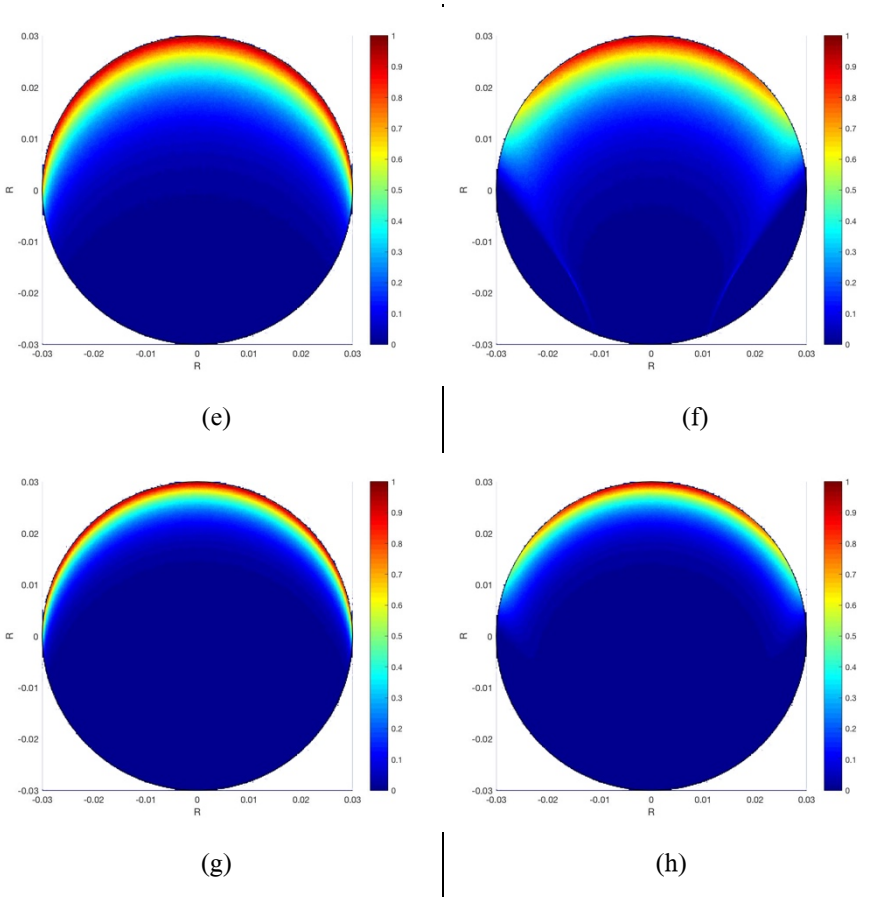

Figure 4.2. Contour maps of normalized LVRPA at different biomass concentration: a-b) C_x 0.10 kg/m^3; c-d) C_x 0.2 kg/m^3; e-f) C_x 0.5 kg/m^3; g-h) C_x 1.0 kg/m^3: left-side (a, c, e, g) refraction/reflection not considered, right-side (b, d, f, h) refraction/reflection at reactor wall included in the model.

This clearly depends on the fact that due to refraction angles directing photons towards the reactor centre, those photobioreactor zones are never reached by any photon. This is a feature not revealed by the simpler, but less realistic, simulation of Figure 4.2a. Due to the sensitivity of algae productivity to passages into dark zones, this may well be an important feature to spot, if accurate simulations of photobioreactor performance are sought. Notably, in Figure 4.2b a strong LVRPA concentration in the close vicinity of the dark zones is also observed, once again due to the photon redirection effects at the photobioreactor walls.

By comparing Figure 4.2 d, f, h with their left side mates, the already described effects are observed, though their importance becomes progressively less important, due to the smaller and smaller photon penetration depths.

On the contrary, going to much smaller microalgae concentrations, such as at *0.02 kg/m^3*, the same effects are further enhanced, as it can be appreciated in Figure 4.3a and Figure 4.3b. A striking feature observable in Figure 4.3b is that the largest LVRPA are observed in the bottom part of the photobioreactor, in the farthest zones from light entrance, due to the focusing lens effect involved in photon redirection by refraction. Obviously, this feature is not captured when neglecting refraction/reflection phenomena, so resulting in Figure 4.3a, where a less realistic, much more uniform, LVRPA distribution is predicted.

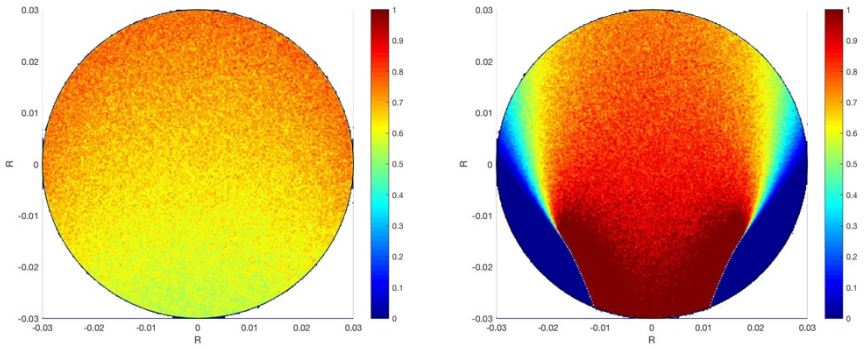

(a) (b)

Figure 4.3. Contour maps of normalized LVRPA at low biomass concentration (C_x 0.02 kg/m^3) a) refraction/reflection not considered, b) refraction/reflection at reactor wall included in the model.

As regards the number of photons lost in the various conditions by both transmission and reflection, this is reported in Table 4.1. As it can be seen, by increasing biomass levels these percentages decrease, implying an increased number of absorbed photons into the photobioreactor. Notably at high algae concentrations the predicted photon loss is higher when considering reflection/refraction phenomena, due to the photons reflected at the air/liquid interface, not accounted for when

neglecting reflection. On the contrary, at low algae concentrations the predicted photon loss is found to be smaller when considering reflection/refraction phenomena than when neglecting them. This is due to the significantly longer path inside the reactor for the refracted photons, especially for those entering the reactor at large *x* values (see Figure 4.1), which makes for a larger absorption probability so offsetting the already quoted reflection effect.

Table 4.1. Percentage of incident photons lost (not absorbed inside the photobioreactor) at various algae concentrations.

	Photon loss %				
C_x **[g/L]**	0.02	0.1	0.2	0.5	1.0
refr. /refl. considered	75.85	26.96	9.89	4.56	4.46
refr. /refl. not considered	77.73	30.19	10.93	1.62	0.39

This is also clearly observable in Figure 4.4, where fractional photon absorption is plotted *versus* microalgae concentration, where it can be seen that the two effects exactly compensate at algae concentration of about *0.20 kg/m*^{3}, while compensation is only partial at all other concentrations. Overall one can state that, due to the partial compensation of increased photon loss due to reflection and decreased photon loss due to longer escape paths, either considering or neglecting the reflection/refraction phenomena has a minor effect on the overall photon absorption inside the reactor. The major effect remains therefore that on the LVRPA distribution, which may be strikingly different in the two cases, especially at relatively low algae concentrations. This effect is especially bound to play a significant role in the resulting photosynthetic growth, as light distribution and especially dark volumes are known to significantly affect resulting light conversion by microalgae and then photobioreactor performances.

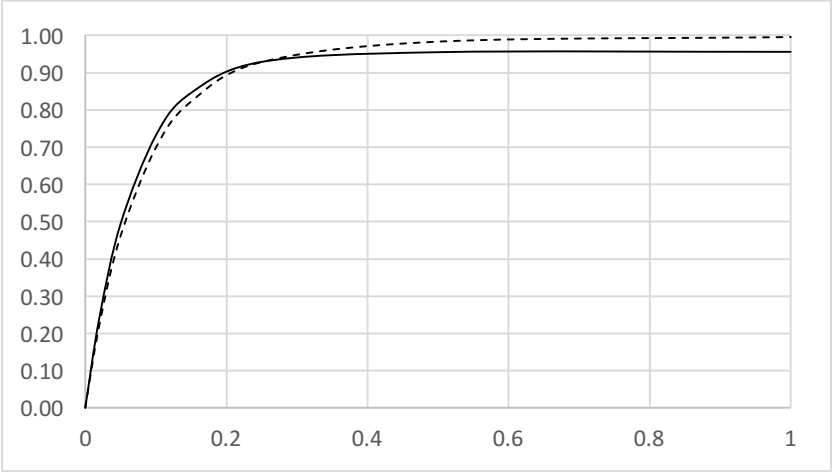

Figure 4.4. Fraction of incident photons absorbed inside the photobioreactor *versus* microalgae biomass concentration, with refraction/reflection at reactor wall considered (solid line) or not (dotted line).

4.4 Conclusion

The *local volumetric rate of photon absorption* (LVRPA) distribution over the cross section of a horizontal-pipe photobioreactor was determined. A uniform orthogonal irradiation was considered for all the cases analysed. A simplified mathematical model based on the Monte Carlo approach was adopted, in order to evaluate the influence on LVRPA of implementing optical reflection/diffraction at photobioreactor walls. Results confirm that tubular photobioreactor is submitted to a strongly heterogeneous light attenuation field as induced by walls curvature, inducing in the culture volume both areas of high LVRPA and dark volumes. The overall photon absorption is only marginally affected by refraction/reflection phenomena, while the same phenomena may quite strongly affect the LVRPA distribution inside the reactor, especially at low algae concentrations. As a consequence, refraction/reflection effects may be neglected in strongly simplified models involving only the average LVRPA while the same effects should be considered in advanced photobioreactor models aimed at predicting photosynthetic conversion, as in such cases LVRPA values and especially dark volumes are bound to significantly affect model results.

4.5

4.6 Experimental Set-Up of a Quasi-Isoactinic Photobioreactor

In order to experimentally study light intensity effects on microalgae productivity, a thin-slab quasi-isoactinic photobioreactor was realized in laboratory-scale. The apparatus consists of glass thin-slab photobioreactor 50 to 50 cm with a useful thickness equal to 1 cm; in this case the slab thickness is assumed to be very small in comparison to the other two dimensions in order to make side end effects small. The photobioreactor were irradiated from two sides, left and right, with two LED panels in order to make the light necessary for the microalgae growth, as shown in Figure 4.5.

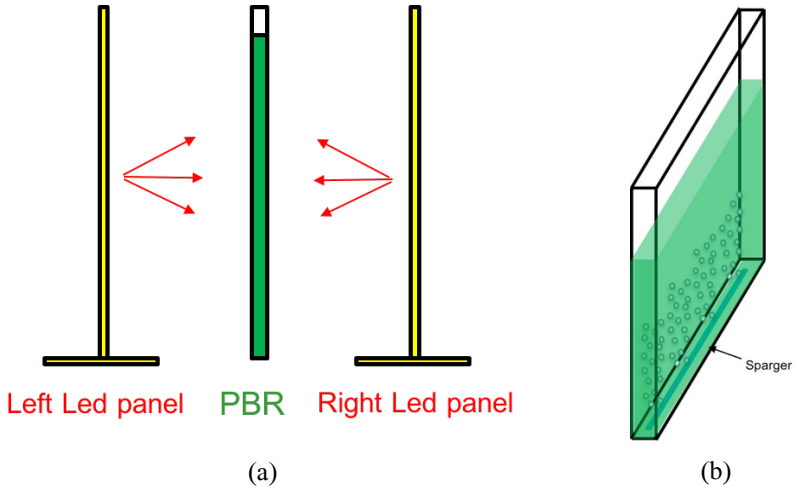

Figure 4.5 (a) Scheme of quasi-isoactinic photobioreactor apparatus with the two LED panels and the thin-slab PBR; (b) scheme of thin-slab photobioreactor with gas sparger in the bottom.

Taking into account the light attenuation by irradiating the photobioreactor from one side only, the irradiation from both sides makes a superposition of the effects such as to create a quasi-perfect irradiation inside the photobioreactor. Then, the LVRPA at each point inside the photobioreactor is given by the sum of the two single

irradiation values. Looking at Figure 4.5-b, in the photobioreactor bottom a gas sparger was inserted for handling growth of the microalgae species.

Regarding LED panels, as shown in Figure 4.6, five meters of light strips were mounted between the two panels; each panel contains 300-SMD 5050 LED Module (surface-mount device light-emitting diode module) with an effective lumen equal to 7200lm, and a power consumption of max 144W. In this work, in order to vary the wavelength of light emission, RGB LEDs were chosen; Table 4.2 shows the characteristics of the adopted LEDs.

Table 4.2 Characteristic of RGB LEDs adopted for the quasi-isoactinic photobioreactor.

Type	**Power [W]**	**Effective lumens [lm]**	**Wavelength [nm]**		
			Red	Blue	Green
SMD 5050 LED	0.24	12	630 ~ 635	475 ~ 480	520 ~ 525

Through an Arduino system a piloting system unit was developed for these two LED panels. This system comprises a hardware part with Arduino UNO R3 with a MEGA328P ATmega16U2 microcontroller, and a software section developed in C++. In the piloting unit (codename Hathor Project) an additional module with display and keys was inserted; using the buttons it is possible to change (i) light intensity, (ii) wavelength and finally (iii) light-dark intermittent level. This latter feature allows to switch ON or OFF light LED panels with a given frequency, in order to carry out microalgae growth analysis at different light-dark intermittent levels.

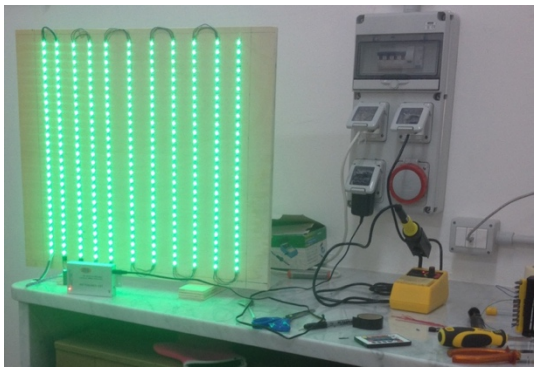

Figure 4.6 Led panels construction with ad-hoc welds.

Figure 4.7 shows the entire lighting system with piloting unit and the two LED panels. In addition, the system was powered with a modified ATX power supply with a 4.7 ohm 10W resistor inserted on the +5V to obtain a constant and max power on the +12V.

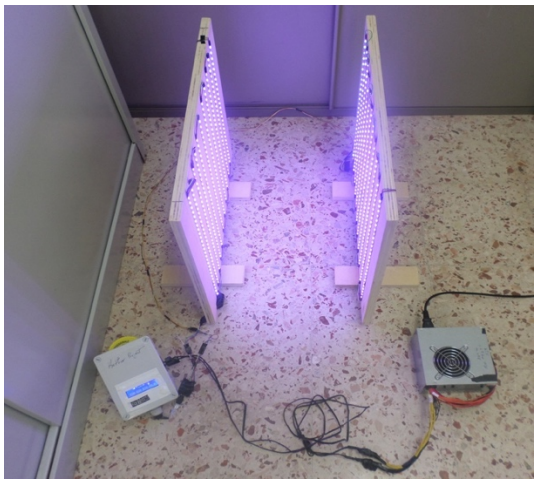

Figure 4.7 (a) Lighting system with piloting unit, LED panels and modified ATX power supply.

In order to make accurate experimental tests of light influence on the microalgae growth, the quasi-isoactinic photobioreactor and lighting system were placed in a laboratory section covered with a thick black tarp to not affect the irradiance from external sources.

Due to overlapping research activities in my PhD program, experimental campaigns of microalgae growth in this quasi-isoactinic photobioreactor have not yet been carried out, and then they were left for future development.

5 PBR PILOT PLANT: DESIGN, CONSTRUCTION AND START UP*

Abstract

This chapter describes the activities carried out during the design, construction and start-up of the innovative PBR pilot plant with low cost technology for microalgae production. The plant is located within the Palermo University Campus (Italy). The main ways through which the goal of costs containment is pursued are the adoption of thin walled transparent tubing for the photobioreactor and an evacuated-head Air-Lift system. To the aim of providing a proof-of-concept of these ideas, a 500-liter pilot plant was built, where this is presently being operated in batch mode under solar irradiation and external climatic conditions. The relevant Air-Lift deployed is about 20 meters high and has an internal diameter of 8 centimetres. A novel double-degaser in the Air-Lift head was found to provide good gas-liquid separation. Air, or an air-CO_2 mixture, is presently sparged at the riser bottom, but pure CO_2 sparging is planned to be tested. This last, in conjunction with the evacuated Air-Lift head should allow the co-production of nearly pure Oxygen from the same plant. Excess CO_2 sparged will be recovered via an absorption-desorption system with monoethanolamine which will also allow sun thermal energy to feed back the recovered CO_2 without the need of resorting to mechanical compression. In this first work phase they are discussed the hydrodynamic performance results of the entire pilot plant. The main pilot plant performances were carried out with the evacuated Air-Lift head and without evacuation, i.e. to atmospheric pressure. The previous mathematical model for the

* Part of this chapter has been revised for publication as:

- G. Marotta, S. Lima, F. Scargiali, F. Grisafi, A. Brucato, *Operation and perspectives of the first pilot plant for microalgae production with low-cost technology,* in preparation.
- G. Marotta, S. Lima, F. Scargiali, F. Grisafi, A. Brucato, *A novel photobioreactor pilot plant: hydrodynamic performances for microalgae cultivation,* submitted to ICheaP13, Milan (2017).

entire pilot plant was used and good results were achieved in the experimental results-mathematical model comparison.

5.1 The installation site: Palermo University Campus

In this work, as already introduced in section 1.1, the innovative PBR pilot plant with low cost technology is located within the Palermo University Campus (Italy), as shown in Figure 5.1. This location is ideal for microalgae growth, as in the south of the Mediterranean area, the climate is warmer, and on average there are no temperature values below 15 °C throughout the year [3].

Figure 5.1. Satellite perspective image of the pilot plant location (space information comes to Apple Maps® courtesy).

The entire available area was about 300 square meters, large enough to start a system on a pilot scale. Through a construction work company, in a few months the area was recovered and prepared for hosting the entire pilot plant, as shown in Figure 5.2.

By the idea of developing a photobioreactor with an evacuated-head Air-Lift system, an Air-Lift of about 20 meters was constructed and mounted on the side of Building 6, in front of pilot area, as shown in Figure 5.3-a. Then, through a trail carved along the street road, as shown in Figure 5.3-b, the evacuated-head Air-Lift was connected to the photobioreaction section.

(a)

(b)

Figure 5.2. Area recovered and prepared for hosting the entire pilot plant; before (a) and after (b).

(a) (b)

Figure 5.3. (a) Evacuated-head Air-Lift mounted on the side of Building 6, in front of pilot area; (b) Trail carved along the street road to connect the evacuated-head Air-Lift to the photobioreaction section.

5.2 Plant design

Figure 5.4 shows the Process and Instrument Diagram (P&ID) of the PBR pilot plant. The Air-Lift unit is installed on the side of Building 6, as already introduced, and the photobioreactor unit is installed in the pilot area recovered. The pilot plant was originally designed taking into account the CO_2 recovery unit; however, in this phase of the pilot plant development, it was not built due to restricted timing.

In the riser bottom a gas sparger, through a compressor air-line, it is inserted for microalgae handling growth. Then, the stripping gas from degaser section (top Air-Lift) it is released to external environment or connected to the vacuum pump. Figure 5.5 and Figure 5.6 show in particular, CAD designs of the two Units.

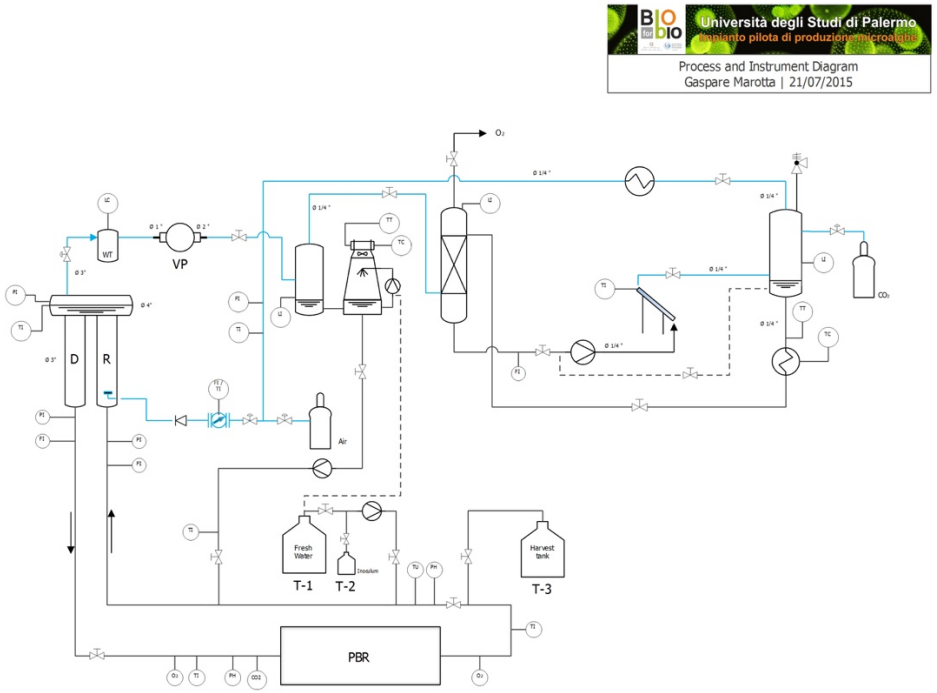

Figure 5.4 Process and Instrument diagram of the PBR pilot plant: black lines for liquid flows and blue lines for gas flows.

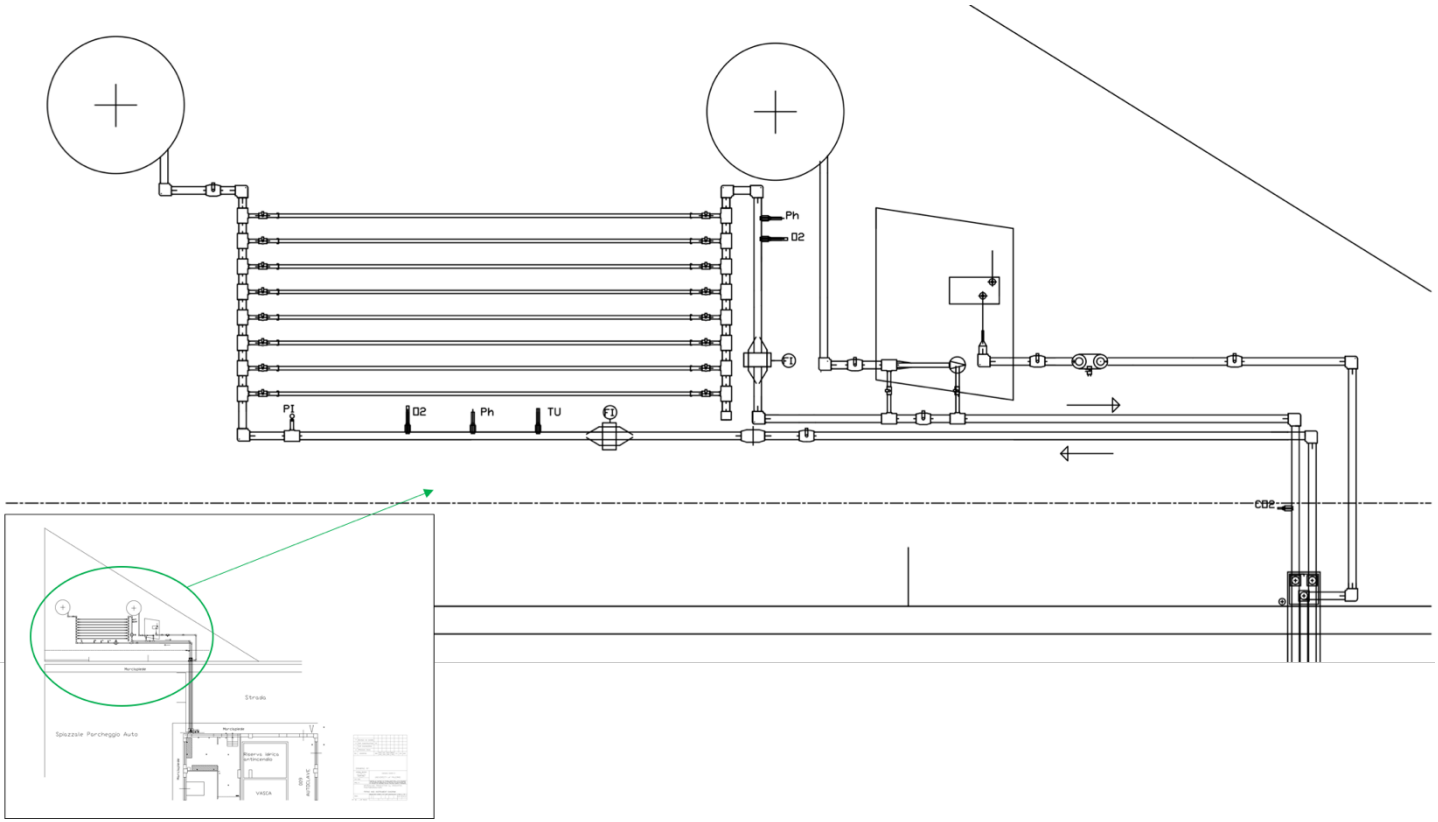

Figure 5.5 PBR pilot plant CAD design: Photobioreactor Unit.

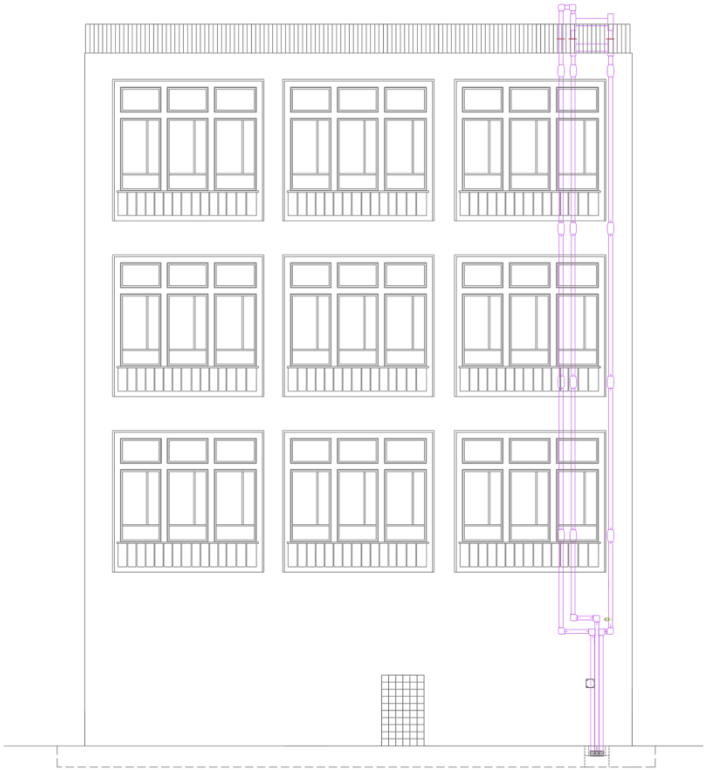

Figure 5.6 PBR pilot plant CAD design: Air-Lift Unit.

5.3 Installation of PBR Pilot Plant units and plant facilities

In order to obtain a complete description of the pilot plant considering CAD design of Figure 5.5 and Figure 5.6. All main pipelines are in polypropylene (PP) of *110 mm* external diameter and of *80 mm* internal diameter, resistant to UV radiation - *PPR FASER UV by Plastica Alfa*. Three small sections, as degaser part and two small vertical section of riser and downcomer they are transparent in PMMA of 110 mm external diameter and of 100 mm internal diameter; these transparent sections make visible the internal fluid dynamics. Photobioreaction section is transparent with thin polyethylene film pipes of *60 mm* internal diameter, such as to be able to capture light radiation for microalgae growth. Table 5.1 shows the main pilot plant size.

Two small tanks of about *500-l* are installed in the pilot area: (i) one for loading fresh water and inoculum, and one (ii) to harvest microalgae biomass at the end of production cycle.

Table 5.1 Characteristics and size of the PBR pilot plant.

Section	ID [m]	Length [m]	Volume [L]
Riser	0.08	18	~ 90
Downcomer	0.08	18	~ 90
PBR line connection	0.08	17	~ 84
Degaser	0.10	0.80	~ 6
PBR	0.06	81	~ 230
		Total Volume [L]	~ 500

A water trap was placed in the outlet section of the degaser before external environment connection or to vacuum pump. This water trap has a dual function: (i) to avoid liquid water presence in the vacuum pump and (ii) to partialize vacuum level via a valve connected with the external environment. This latter feature will be explained in the next section 5.3.3.

5.3.1 Tall External Air-Lift with Dual Degaser

Regarding Air-Lift Unit, as shown in Figure 5.3a and Figure 5.6, this is a really tall handling system. There are three main columns installed on the side of Building 6: downcomer, riser and connection line with external environment or vacuum pump. It is worth noting that degaser section consists of two horizontal sections, one above the other; after preliminary tests with a single degaser, this solution has allowed better gas-liquid separation for preventing bubble entrainment along descending section (downcomer). Typically, degaser section must be much larger than riser or downcomer column; however, PP pipes and fittings used in this pilot plant do not present dimensions greater than 110 mm in the production catalog. Figure 5.7a shows this top Air-Lift section with the dual transparent degaser and an external cam; the latter allows to monitor liquid level, and then free surface inside in the highest degaser.

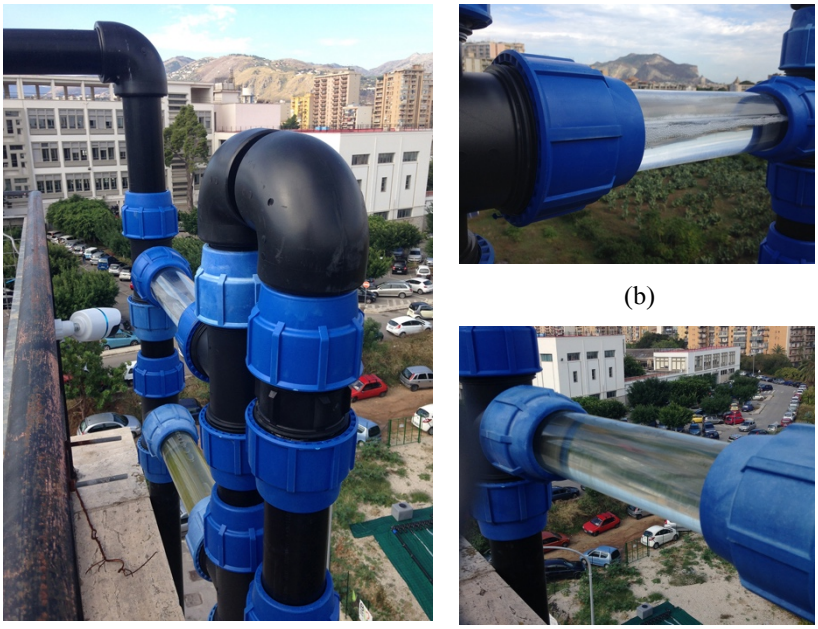

(a) (b) (c)

Figure 5.7 (a) Dual transparent Degaser with (b) free surface in the highest section and (c) lower section completely full.

It is noted that it must be avoided that water level passes the free surface in the highest degaser section, otherwise, pilot plant must be stopped and water excess must be removed by a manual valve mounted in lower section of the plant, i.e. below street level.

Figure 5.8 Bottom section of the Air-Lift with the two-transparent section in PMMA and the gas sparger. Flow direction is indicated by green arrows.

Figure 5.8 shows bottom section of this airlift; two transparent section in PMMA are present to show internal fluid dynamics, which presents the typical bubbles through a gas sparger inserted in the lower part of the riser section. Instead, in the downcomer column there aren't any bubbles and there is a downward flow direction (green arrow in Figure 5.8).

5.3.2 Low-Cost photobioreactor section

As already anticipated, the main ways through which the goal of costs containment is pursued are the adoption of thin walled transparent tubing for the photobioreactor and an evacuated-head Air-Lift system. These thin tubing are in low density polyethylene (LDPE), supplied by *Plastica Alfa*. The internal diameter does not exceed the dimensions of *6 cm* and the material transparency allows microalgae to capture the sunlight necessary for their growth. In this pilot plant, a photobioreactor section with eight horizontal thin tubing connected in parallel was considered, where each of these pipes has a length equal to *10 m*, as shown in Figure 5.9a-b-c.

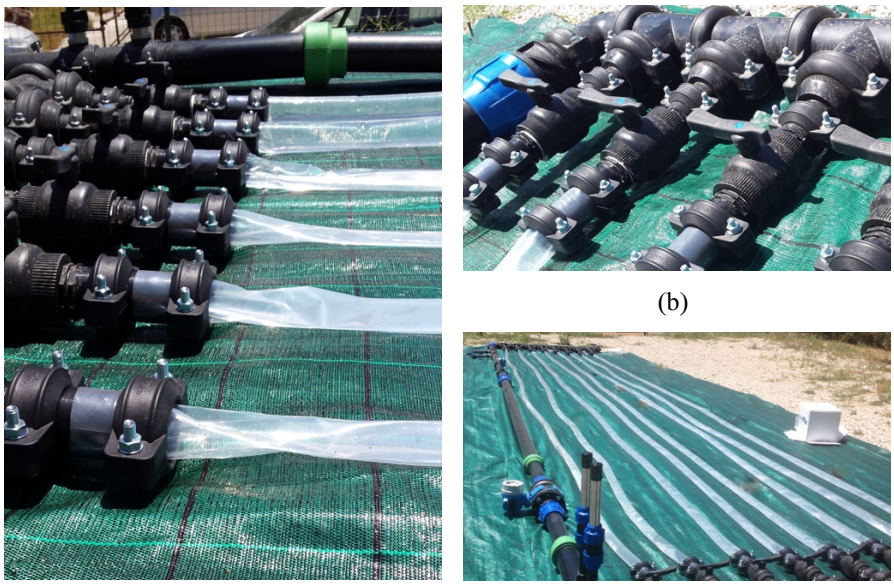

(a) (b) (c)

Figure 5.9. Photobioreactor Unit with LDPE film tubes.

It is worth noting that in this PBR Unit, VICTAULIC® grooved piping, fittings and couplings were chosen, always supplied by *Plastica Alfa*, for easy replacement and modification of the entire section. In order to enable or disable individual parallel photobioreactors, manual PP ball valves were inserted in the inlet and outlet manifold.

5.3.3 Pumps and instrumentation

One centrifugal pump (Calpeda NM40/16B/B) was used to supply fresh water and inoculum to the pilot plant; instead, a vacuum pump (Edwards ES65) was used to perform the gas stripping from the degaser, as shown in Figure 5.10. Centrifugal pump is only activated at the beginning of microalgae growth cycle and it has a prevalence such as to fill up the pilot plant in a few minutes. Since vacuum pump has to treat also condensable vapours from degaser output section, the gas ballast must be activated; in this case, maximum absolute pressure reached it is about *0.40 bar*. In this pilot plant start-up phase, the gas exiting from vacuum pump is released into the atmosphere. Since the two pumps are not waterproof (IP55) a temporary wood box was built to guarantee weatherproofing.

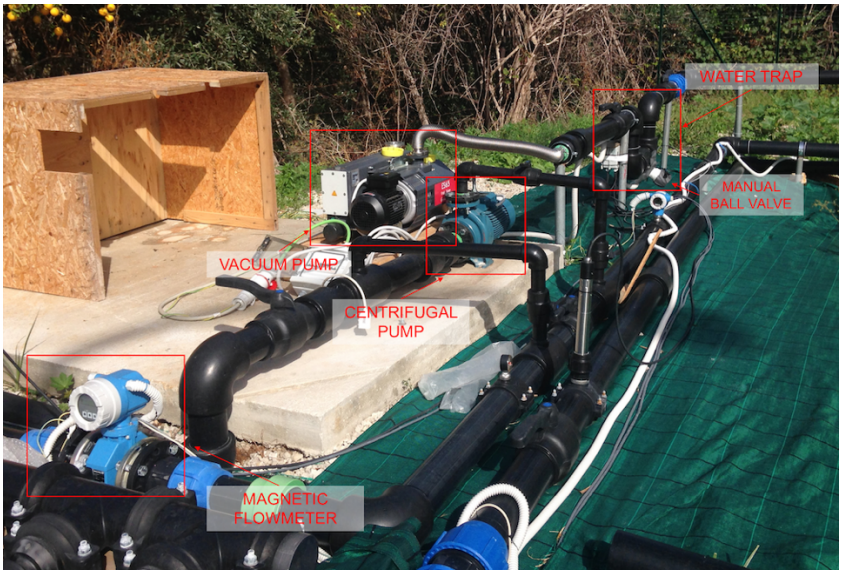

Figure 5.10. Centrifugal pump, vacuum pump, magnetic flowmeter and water trap of the pilot plant.

As already announced, a water trap was placed in the outlet section of the degaser before external environment connection to vacuum pump. This water trap was simply created by a siphon system with a ball valve in the bottom section, as shown in detail in Figure 5.11; whether from degaser line there will be a liquid water, this will be

drained into external environment. Simultaneously, when vacuum pump is started, since it does not have an electronic speed control and maintains the free surface inside in the highest degaser section, ball valve directly allows to partialize vacuum level with the external environment. In addition, in the ball valve an external fine-mesh filter was mounted to prevent dirtying inside vacuum pump.

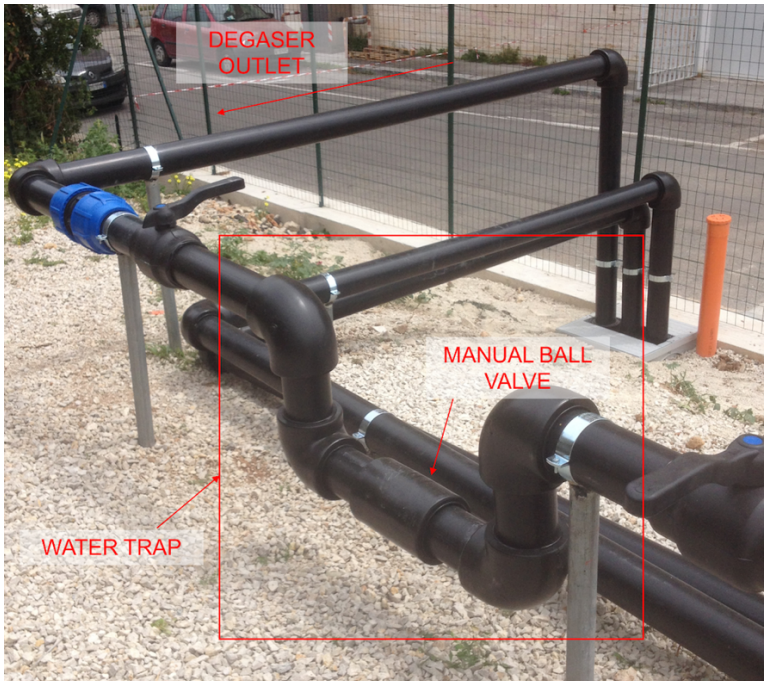

Figure 5.11. Water trap details of the pilot plant.

The measuring instrumentation is constituted by pH/temperature sensors/transmitters (*WTW Sensolyt 700 IQ*), oxygen sensors/transmitters (*WTW FDO 700 IQ*), turbidity sensor/transmitter (*WTW Visoturb 700 IQ*), and digital pressure gauge (*EH Cerabar S PMC 71*) for both inlet/outlet PBR Unit section. An additional digital pressure gauge is installed at the top of Air-Lift, and a CO_2 sensor/transmitter (*Mettler Toledo ISM INPRO 5000i*), is installed near PBR inlet section. The inlet/outlet flow rate of the growth medium was measured by magnetic flowmeters (*EH Promag 10L*). All data were acquired by a data logger positioned and developed

in the laboratory for analysis and preparation of microalgae inocula, as shown in Figure 5.12; this laboratory is described in detail in the next section 5.3.4.

Figure 5.12. Data logger of the pilot plant inside the laboratory.

In this laboratory, a gas input system for the airlift is also present, provided with two liquids filters and by the use of a gas flow meter (AALBORG DFM27), as shown in Figure 5.13, it is possible to control input flow rate to the gas sparger.

Figure 5.13. Gas flow meter inside the laboratory.

After having completed the set-up of the pilot plant with all necessary equipment (April – June 2016), a preliminary hydrodynamics tests and an experimental campaign over a period of four months (July – December 2016) has been performed in this PBR pilot plant. The main results achieved will be described in details in the next section 5.4.

5.3.4 New Laboratory for Analysis and Inocula Production

During pilot area recovery for the plant, an entire new laboratory was created to (i) produce all necessary microalgae inocula, (ii) to control/support the external pilot plant and (iii) to carry out all related research activities. Figure 5.14 shows internal lab with the main equipment acquired during this research project: HPLC (Agilent 1220 Infinity LC), spectrophotometer UV-Vis (Agilent Cary 60 UV-Vis), fluorescence spectrophotometer (Agilent Eclipse), precision balance (KERN ABJ-NM 80), optical and digital microscope (Optika B-800), FTIR (Agilent Cary 630 FTIR) and a Hydraulic Press (Pike CrushIR).

Figure 5.14. Internal lab view with the main equipment: HPLC (Agilent 1220 Infinity LC), spectrophotometer UV-Vis (Agilent Cary 60 UV-Vis), fluorescence spectrophotometer (Agilent Eclipse), precision balance (KERN ABJ-NM 80), optical and digital microscope (Optika B-800), FTIR (Agilent Cary 630 FTIR) and a Hydraulic Press (Pike CrushIR).

In order to obtain necessary microalgae inocula for the pilot plant, six lab-scale photobioreactors were also acquired and three microalgae species were grown: *Nannochloropsis gaditana*, *Chlorella vulgaris* and *Phaeodactylum tricornutum*. As shown in Figure 5.15, microalgae growth starts from small volumes (flasks), and then gradually moved to larger volumes by *10%* of volume step. A culture media with distilled water and an f/2 culture medium [95] was prepared to growth microalgae culture, as the *Phaeodactylum tricornutum*. Furthermore, for the other two microalgae species a commercial powdered fertilizer was chosen (Pavoni&C Spray Feed 20-20-20) with concentrations from *0.5 g/L* to *2.5 g/L*.

(a)

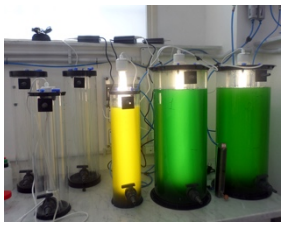

(b)

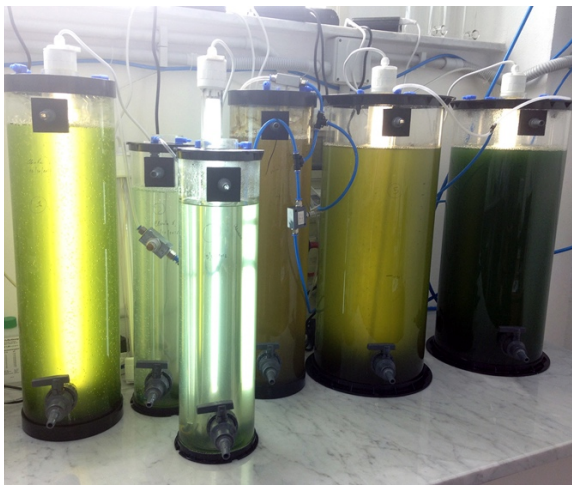

(c)

Figure 5.15. Microalgae inocula preparation: (a) flask vector with small volume of microalgae species; (b) and (c) microalgae species loading from flask vector to lab-scale photobioreactors at different growth time.

In order to obtain microalgae growth rate, two main methods are used: (i) absorbance measuring by UV-Vis spectrophotometer and (ii) dry weight analysis.

This latter method was obtained by centrifugation (ALC 4218) for 20 minutes of known microalgae quantities (in triplicate) and drying in oven at 98 °C for 24 hours to remove remaining water.

Regards first method, this is much faster than the second; this UV-Vis spectrophotometer has a fiber-optic probe to directly obtain the absorbance values without cuvettes or sipper. Taking into account the Beer-Lamber Law that defines the absorbance by the transmitted radiation, it is possible to obtain biomass concentration since it is directly proportional to the absorbance. Therefore, by performing a dry weight measurements series on successive days and then a linear or polynomial regression of data obtained, it's possible to obtain the coefficients required to calculate biomass concentration as a function of absorbance gained from the instrument. It is worth noting that at higher biomass concentrations there are deviations from linearity, and then, during experimental measurements, absorbance should not exceed values of 1 Au (Absorbance units); these values can be easily obtained by dilutions of the solution analyzed.

All experimental data obtained in lab are reported and discussed in the following section 5.4.1.

5.4 PBR Pilot Plant: Operation and results

As already introduced, once having completed the set-up of the pilot plant with all necessary equipment (April – June 2016), a preliminary hydrodynamics tests and an experimental campaign over a period of four months (July – December 2016) has been performed. Two main research activities were conducted: the first concerns microalgae growth and analysis in laboratory and the second concerns the pilot plant experimental tests.

5.4.1 Laboratory experimental results

In this first phase, laboratory experimental activities concerned absorbance measurements of microalgae species cultivated in the lab-scale photobioreactor were

carried out. Absorbance, i.e. optical density OD, was measured at 500 nm using the fiber-optic probe of UV-Vis spectrophotometer in BD Falcon tubes (triplicate format for each analysis). Figure 5.16 shows the results obtained during one month of cultivation with one main nutrient loading; after about eighteen days of exponential growth, microalgae cultivation tends to remain stable, and then there will be a decrease phase if additional nutrients are not provided. Finally, these medium cultures can be used as inoculum for the Pilot Plant, where it will require about 50 litres (10% in volume) of medium culture.

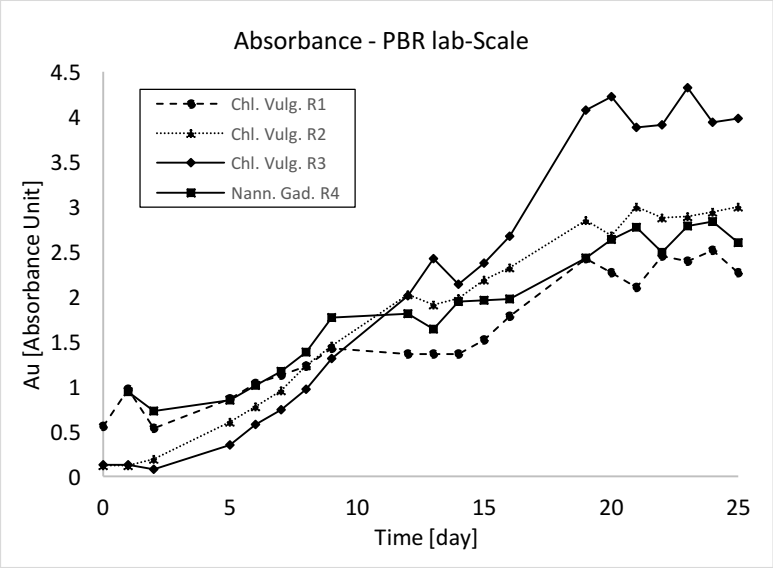

Figure 5.16. Absorbance measurements of two microalgae species *Nannochloropsis gaditana* and *Chlorella vulgaris* cultivated in the lab-scale photobioreactor.

5.4.2 Preliminary pilot plant tests

Prior to loading microalgae inoculum in the pilot plant, preliminary hydrodynamics tests were performed.

As already discussed in the previous section, a vacuum pump was inserted for gas stripping from degaser section; Figure 5.17 shows the experimental results by

activating (Air-Lift head evacuated) and deactivating (atmospheric pressure) the vacuum pump. Water liquid Level (WL), i.e. free surface, was set with graduation marks in the highest section of degaser (Figure 5.7-b).

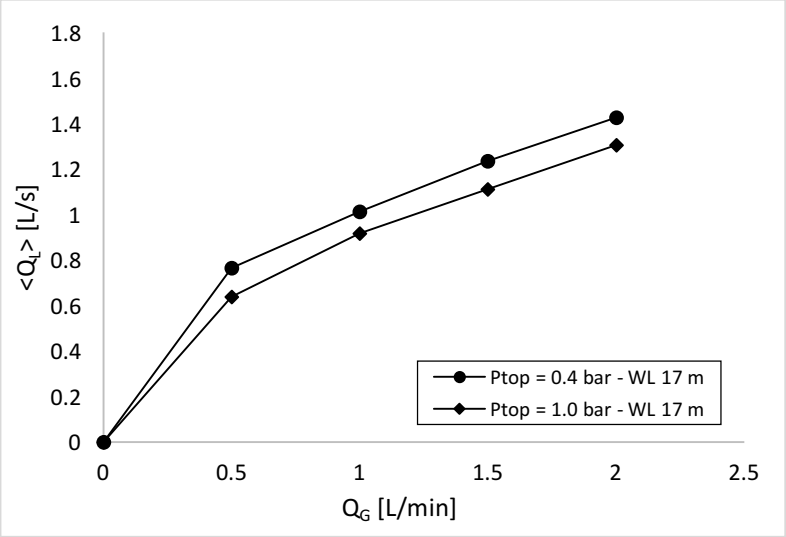

Figure 5.17. Pilot Plant experimental results by activating (Air-Lift head evacuated) and deactivating (atmospheric pressure) vacuum pump, with a water level (WL) of 17 meters.

As can be seen, vacuum pump enhances the liquid circulation performance from a minimum of 8% up to a maximum of 17% with the same inlet gas flow rate. It is worth noting that, in this comparison, higher inlet gas flow rate values were not considered since it was noticed high bubbles entrainment in the downcomer-bottom section by activating vacuum pump.

In order to obtain a comparison between pilot plant experimental tests and numerical results obtained with Matlab code (discussed in section 2.6), Figure 5.18 and Figure 5.19 show this comparison. Figure 5.18-a-b show results with two different water level; numerical results show to be very promising for liquid flow rate prediction with percentage deviations between -25% and -3%, i.e. increasing the inlet gas flow rate.

Figure 5.19 shows instead results obtained by activating vacuum pump; numerical results are comparable with the experimental ones, and with percentage deviations between -15% and -3% by increasing the inlet gas flow rate.

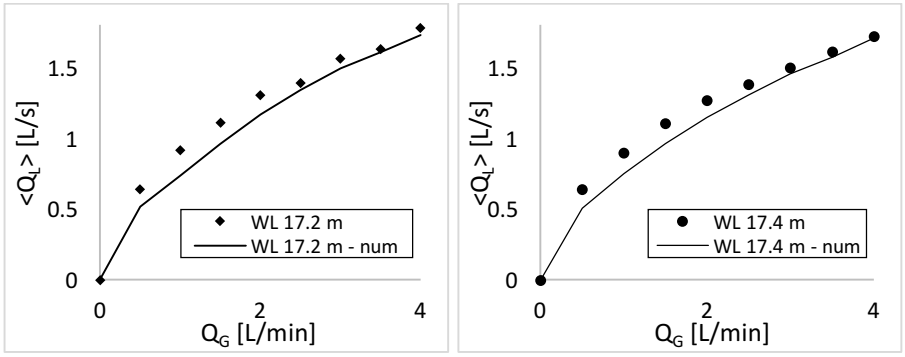

(a) (b)

Figure 5.18. Comparison between Pilot Plant experimental- and numerical results, with a water level (WL) of (a) 17.2 meters and (b) 17.4 meters.

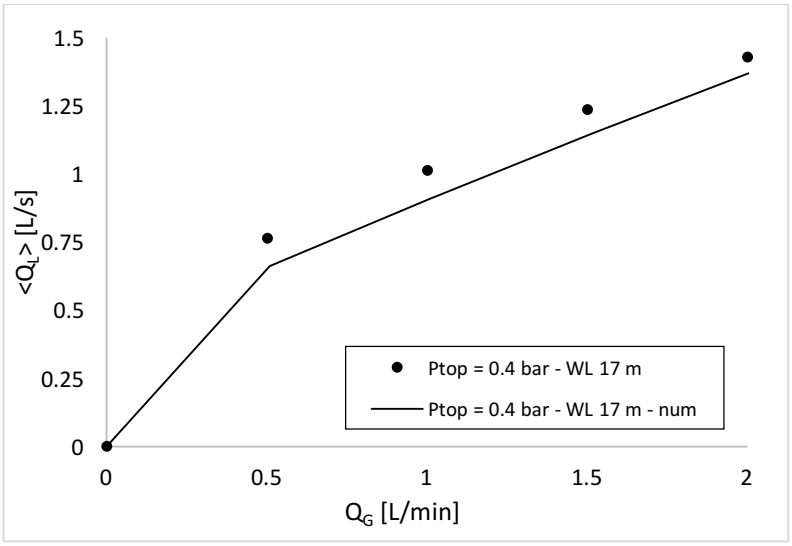

Figure 5.19. Comparison between Pilot Plant experimental- and numerical results by activating (Air-Lift head evacuated) vacuum pump, with a water level (WL) of 17 meters.

In order to obtain a relation for microalgae growth as a function of irradiance, a quantum flux meter (Apogee PAR SQ-110-L-10) was placed in photobioreaction area, directly exposed to sunlight.

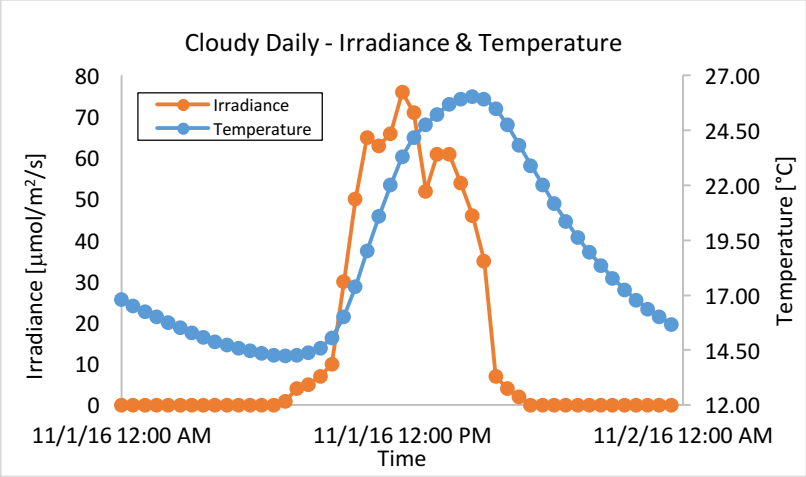

Figure 5.20. Daily variation of irradiance and temperature inside the PBR Pilot Plant (one cloudy day).

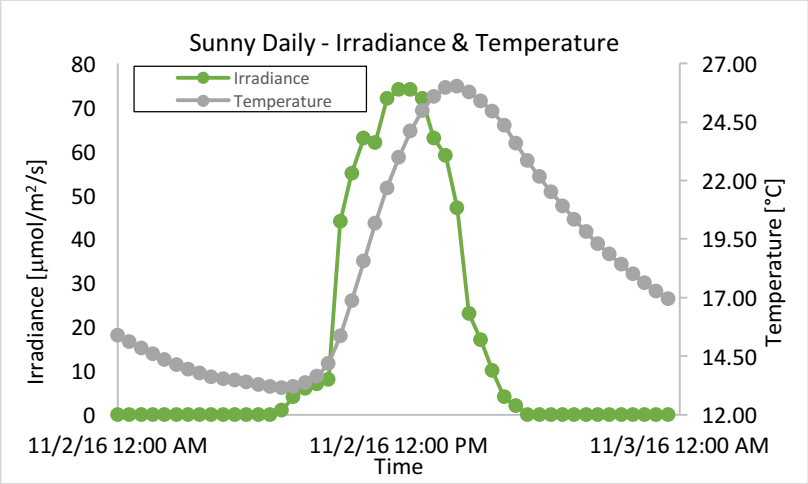

Figure 5.21. Daily variation of irradiance and temperature inside the PBR Pilot Plant (one sunny day).

Figure 5.20 and Figure 5.21 show daily variation of irradiance on a cloudy- and sunny day, respectively. In addition, temperatures inside the photobioreactor are shown in the graphs. As it can be seen, in both cloudy- and sunny day, irradiance trend remains almost similar, with some peak variation to mid-day.

Temperature, instead, shows its maximum value slightly moved forward from irradiance peak; this trend is to attribute to thermal inertia and convective motions inside the photobioreactor, and is not subjected to sudden variation.

6 MICROALGAE POST-TREATMENT: FIRST GASIFICATION STEP IN SUPERCRITICAL WATER REACTOR*

Abstract

In the processes of wet biomass conversion, as microalgae biomass, gasification in supercritical water is a new treatment can be inserted in the processes of conventional gasification. Without the need to dry the wet biomass and much shorter residence times than conventional processes, gasification in supercritical water is considered to be a promising technology for a complete and efficient conversion of wet biomass into gaseous products. Therefore, in order to study this innovative conversion process, it started with a simple gasification of glucose solution.

The supercritical water gasification (SCWG) of glucose as a model compound for H_2 production is studied in term of process development at 25 MPa and 650 °C. Gasification has been investigated using a laboratory scale continuous plant comprising a continuous down flow reactor with a volume of 200 cm^3, a heat recovery section and pre-heat of the biomass to simulate more closely an industrial design. Feed streams (pure water and glucose solution) are introduced at the top of the vessel and products are extracted from the bottom. The reactor is equipped with various inlet points that allow to modify the inlet position of reacting streams in order to study the effect of stream mixing on reaction performance. Moreover, in order to obtain a description of the fluid flow inside the reactor, computational fluid dynamics (CFD) simulations were carried out. The simulations were conducted by the ANSYS CFX

* Part of this chapter has been published in revised form as:

- G. Caputo, P. R. Blasquez, F. Scargiali, G. Marotta, A. Brucato, *Experimental and fluid dynamic study of continuous supercritical water gasification of glucose*, J. of Supercritical Fluids 107, (2016) 450–461.
- G. Caputo, M. Dispenza, P. Rubio, F. Scargiali, G. Marotta, A. Brucato, *Supercritical water gasification of microalgae and their constituents in a continuous reactor*, J. of Supercritical Fluids 118, (2016) 163–170.

code which uses a finite volume method. Simulation allowed not only to understand the complex fluid dynamics that describe the system, but also to optimize the reactor configuration in order to attain good process performance.

Experimental results coupled with CFD analysis, allowed to find that the reactor has the top section that behaves like a mixed reactor and the bottom section that behaves like a plug flow reactor. The two jet streams (water and glucose solution) entering the reactor cause back mixing in the top-side of the reactor, so contributing to rapid initiation of reaction and down-flow of species through the chamber. Using the best reactor configuration in term of mixing and temperature distribution allowed to maximize the gasification efficiency and H_2 yield up to 72% and 74% by mole, respectively.

After these first experimental tests with glucose compound, supercritical water gasification of *nannochloropsis gaditana* microalgae was studied in term of process development at 24 MPa and 660 °C. *Nannochloropsis Gaditana* was successfully gasified up to 92.7wt% as gasification efficiency and 77.7wt% as carbon efficiency. The product gas is mainly composed of hydrogen (55.4%), methane (13.7%) and CO_2 (23.9%).

6.1 Introduction

Supercritical water gasification (SCWG) is a well-known process suitable for converting high-water-content biomasses. SCWG promises a rapid, direct route to gases like H_2, CO, CO_2 and CH_4 without char formation and without the variety of products that have to be recovered from the aqueous phase [96]. Since the pioneering work of Modell and co-workers [97], research on SCWG has produced a diversified set of experimental data covering a large variety of experimental conditions. Experiments revealed that gasification is not simple, but has to overcome its special problems and particularly char formation at high biomass concentrations, salts and solid continuous removal from the reactor, pumping of high concentration slurries at high pressure, plugging of reactor and heat exchangers, energy and economic balance.

In SCWG, due to the high temperature and pressure, reactor setup needs special consideration. A large variety of reactors have been studied at laboratory scale including batch autoclaves and continuous tubular reactors with or without catalysts. Also quartz capillary batch reactors and fluidized bed micro reactors have been proposed [98]. Reactors described in scientific literature usually have small or very small size (ID of few mm). Two pilot scale installations are known to be under operation [99], but little information on their behaviour is available in the open literature. Large scale industrial installations do not exist yet.

Experimental data obtained with small reactors suffer from luck of information on temperature and flow profiles inside the reactors, that are usually considered constant. Although it is proven that complete gasification of glucose and other substances can be reached working at 600 °C, the gas yield and composition were found to depend on the condition of the reactor wall in term of surface/volume ratio, wall temperature, metal composition, and on temperature and flow distribution inside the reactor [98]. Thus, research is still needed in order to understand inefficiency causes and improve reactor design.

In this work the gasification of glucose, as a model compound, is studied in a continuous down-flow reactor having an internal diameter of 2.5 cm, aspect ratio (length to diameter ration) of 17 and volume of 200 cm^3.

Although size is still small for industrial scale-up purposes, it allows investigating the effects of flow and thermal fields on gasification reactions.

The aim of this paper is thus to improve the understanding of thermal and fluid-dynamic condition inside a tubular down-flow reactor in order to gain insight in the relationship between reactor configuration and gasification efficiency.

The down flow reactor has been specifically designed for the scope of this work. The reactor vessel has a longitudinal axis vertically oriented so that gravitational force favours solids deposition on the bottom of the vessel. Feed streams are introduced at the top of the vessel and products are extracted from the bottom. As compared to strongly elongated tubular reactors this reactor has the advantage of being less susceptible to plugging. Also, the lower surface to volume ration allows to reduce heat losses. It is equipped with various inlet points, that allow to modify the inlet position of the reacting streams, and with temperature sensors along reactor wall.

CFD simulations of various water and glucose solution feed-stream positions were carried out and compared with experimental data. CFD-simulated glucose residence time distributions (RTD) were employed to interpret experimental results.

6.2 Experimental apparatus

In the present section, details are provided on the materials, experimental apparatus and analytical procedures employed to characterize reactor performance.

6.2.1 Experimental set-up and procedure

SCWG experiments were carried out using the custom-built continuous apparatus depicted in Figure 6.1. The major components of the apparatus were the down-flow reactor, two feed preheaters, a chiller, feed pumps, and a backpressure valve. A detailed drawing of the down-flow reactor is reported in Figure 6.2. It was made of Inconel 625 with an inside diameter of 25 mm and a length of 400 mm, giving it an inner volume of 200 cm^3. The reactor was built by SEPAREX s.a.s, France.

Reactor heating was provided by large electric band heaters wrapped around reactor outer wall for ¾ of its axial length of the vessel.

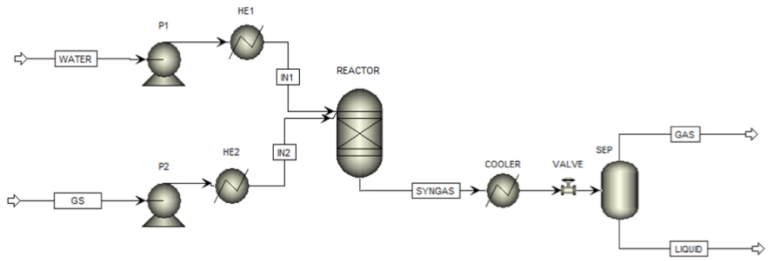

Figure 6.1. Scheme of the experimental plant utilized in the present study.

During gasification, temperature was recorded in various points. The main reference temperature is the reactor wall temperature (T_w) measured at half length of the vessel with a Type-K thermocouple inserted in the middle of the wall thickness. This temperature was controlled by means of a PID controller connected to the band heaters. A second thermocouple was inserted inside the upper portion of the vessel. This sensor measured the average temperature (T_1) of the top section, where mixing between the two streams occurred.

Two other thermocouples were placed on the outer wall of the reactor on the top and bottom zones not covered by band heaters (T_2, T_3). Finally, a thermocouple was put in contact with the outlet product stream that leaves the reactor from the bottom (T_5).

The reactor was fed from the top side with two streams: a glucose solution (GS) with a flow rate of 2.5-5 mL/min and a stream of pure water (W) with a flow rate of 5-10 mL/min depending on the experiments. These flow rates allowed working with residence times ranging from 64 s to 128 s. Gasification performance dependence on the relative position of the two streams was investigated, as illustrated in Figure 6.3.

In the configurations 1 and 3, pre-heating of the water stream up to 670 °C was obtained by pumping water through an Inconel coil inserted in a slot on the reactor wall and wrapped by the band heaters. In the case of configuration 2, water preheating

up to 600 °C was obtained by using a separate ceramic radiant heater. Glucose solution was preheated at 100 °C in all experiments using a ceramic radiant heater.

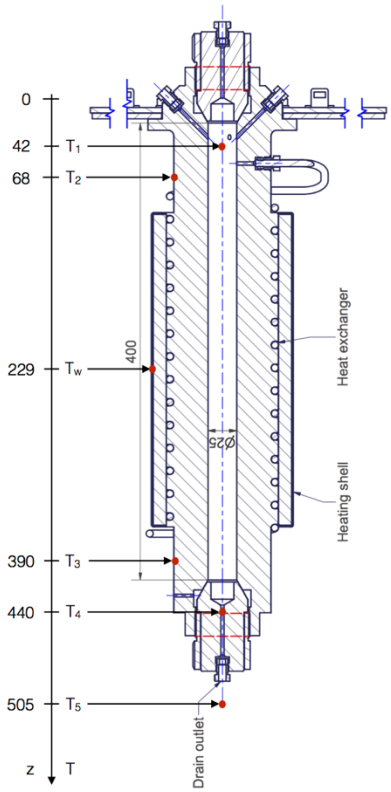

Figure 6.2. Drawing of the gasification reactor with black arrows indicating temperature probes.

Prior to each gasification experiment, distilled water was introduced to the reactor system using a high-pressure digital metering pump (KNAUER AZURA P 2.1S). The reactor was stabilized for at least one hour before the glucose solution was introduced into the reactor using a high-pressure membrane pump (MILTON ROY, France).

Reactor outlet was quickly cooled down to room temperature by means of a cooling bath. The system was pressurized to 25 MPa by adjusting the backpressure regulator (TESCOM). After cooling and expansion of the products to atmospheric pressure, the output stream of the reactor was passed through a glass liquid/gas

separator. The gas flow leaving the separator was continuously metered by means of a mass flow meter prior to entering a GC sampling valve for gas composition analysis. Each experiment was repeated three times and average values with minimum and maximum deviations were reported.

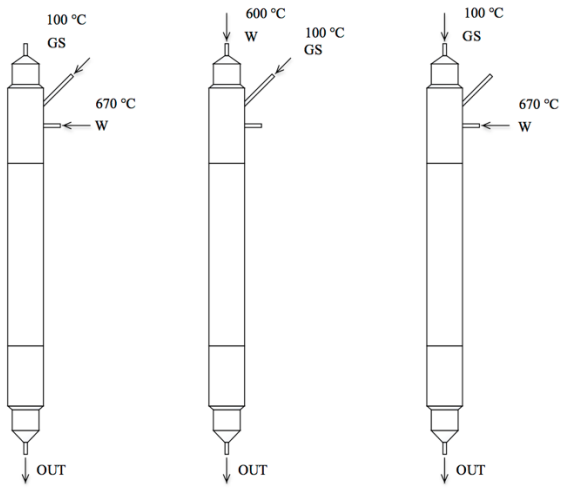

Figure 6.3. Schematic representation of the three configurations adopted for the glucose gasification. From the left: configuration 1, 2 and 3. In configuration 1 and 2 the inlet lines are at 45°, in configuration 3 they are at 90°.

6.2.2 Materials and methods

D-(+)-Glucose (powder type) was purchased from CARLO ERBA Reagents and used as received. The glucose solution employed in all experiments was prepared, by dissolving 54 g of glucose per liter of deionized water.

The composition of the gas produced was determined using a gas chromatograph (GC) to quantify all gaseous products including H_2, CO_2, CO, CH_4, C_2H_6 and C_2H_4. The GC was a model 7890 B, manufactured by Agilent Technologies with two different detectors: a thermal conductivity detector (TCD) and a flame ionization detector (FID). The GC was equipped with a silica capillary analytical column (SUPELCO, Carboxen-1010 PLOT). The column had an outer diameter 0.53 mm, 30

m long and molecular sieve 7Å. The temperature of the columns was maintained at 250 °C and the temperatures of the TCD and FID were kept at 230°C. Argon (99.999%) was used as carrier gas. H_2, CO_2, CO, CH_4, C_2-C_3 hydrocarbons, were detected and concentrations were calculated against gas standards.

The carbon content in the liquid product was analyzed using a total organic carbon analyzer (TOC). The TOC analyzer was a model TOC-L CSN 638-91109-48, manufactured by Shimadzu Corporation (Kyoto, Japan). The performance metrics used for the definitions of the product yields in this study are described below. The Gasification efficiency (GE), measures the conversion of the feedstock to product gases and can be described as the ratio between the sum of the masses of product gases and that of the feedstock. Mathematically it can be written as:

$$GE, \% = \frac{Gas\ Mass\ Flow\ Rate\ Out}{Glucose\ Mass\ Flow\ Rate\ In} \cdot 100 \quad (6.1)$$

The carbon efficiency (CE) can be defined as the mass percentage of carbon converted from the initial biomass towards gases products.

$$CE, \% = \frac{moles\ of\ carbon\ in\ the\ gas\ product}{moles\ of\ carbon\ in\ the\ feed} \cdot 100 \quad (6.2)$$

H_2 yield (%) can be defined as the mass percentage of hydrogen converted from the initial biomass towards gas molecular hydrogen.

$$H_2\ Yield, \% = \frac{moles\ of\ hydrogen\ in\ the\ gas\ product}{moles\ of\ hydrogen\ in\ the\ feed} \cdot 100 \quad (6.3)$$

6.2.3 Aspen Plus® simulation

The gasification process was simulated by commercial software Aspen Plus. Glucose was used as the biomass in the simulation. The thermodynamic method selected was the predictive Soave-Redlich-Kwong (PSRK) EoS as it is considered to be the best method to characterize the properties of the supercritical fluids involved in the process [100].

The fluid streams and biomass were modelled using conventional components, whose thermo-physical data are stored in Aspen Plus databanks. Therefore, no data input was required for these components. The components include glucose ($C_6H_{12}O_6$),

hydrogen (H_2), water (H_2O), carbon monoxide (CO), carbon dioxide (CO_2), and methane (CH_4) [101].

The simulated process scheme is shown in Figure 6.1 (where the relevant Aspen Plus print out is actually reported) and is obviously fully coherent with the experimental set up.

The objective of this simulation was that of obtaining preliminary data to be compared with experimental results.

The input to the plant was made up of two streams, a stream of glucose solution (GS 2.5 ml/min) and a stream of pure water (W 5 ml/min). The simulation was performed with 54 g/l glucose content. Both fluxes were at standard conditions, 25 °C and 0.1 MPa.

After being pumped at 25 MPa, both streams were heated by means of two heat exchangers. The block HE1 heats the WATER stream up to 600 °C. The block HE2 heats the glucose solution stream up to 100 °C. The SCWG reactor was modelled as a reactor (REACTOR) based on the minimization of Gibbs free energy. Based on a user-defined list, the REACTOR block calculates the chemical species minimizing the Gibbs free energy for the given thermodynamic conditions [102]. The reaction occurred at 650 °C and 25 MPa. The resulting stream leaving the reactor is SYNGAS. It is first cooled in the COOLER heat exchanger and then depressurized by the VALVE down to atmospheric pressure.

The last process unit is a separator (SEP) that separates the gas and liquid streams at 25 °C and 0.1 MPa.

The specifications of the individual process units for the simulation are shown in Table 6.1.

Table 6.1 Specifications of the units used in the simulation of process.

Unit	Equipment	Temperature (°C)	Pressure (MPa)
P1	Pump	25	25
P2	Pump	25	25
HE1	Heat exchanger	600	25
HE2	Heat exchanger	100	25
REACTOR	Gibbs reactor	650	25
COOLER	Heat exchanger	25	25

VALVE	Back pressure valve	25	0.1
SEP	G-L separator	25	0.1

The results of the simulation are shown in Table 6.2**.** In this table the percentage obtained for each component can be seen.

Table 6.2 Molar gas composition of simulated gasification of glucose at 650 °C and 25 MPa.

Compound	% Simulated
H_2	65.00
CH_4	0.65
CO	3.17
CO_2	31.18

6.3 Experimental Results

The main design features of the apparatus used in this study are:

1. Pre-heating of the pure water stream that enters from the top of the reactor at the same value of the wall temperature of 670 °C and where it mixes with the glucose solution. This configuration should provide fast glucose heating up so reducing hot water reactions that produce char and tar.

2. Availability of various ports on the top of the reactors that allowed to modify the relative positions of water and glucose streams.

3. Experiments were successfully performed in continuous mode over day without incurring into blockages due to solid products.

Temperature and its distribution inside the reactor is of paramount importance for a successful gasification. Temperature shows a significant effect on biomass gasification in SCW, particularly when catalysts are not present, as in the present case. Various authors reported that above 600 °C glucose is nearly completely gasified, whereas below 600 °C a yellow liquid effluent containing various organics (oil-like tar and char) is formed [103]. High temperature also increases hydrogen concentration due to the water-gas shift reaction of CO. Moreover, heating rate is an important parameter in SCW gasification. High heating rates in the reactor top section of are

necessary for biomass to completely gasify. Indeed, slow heating leads to the formation of phenolic intermediates that are difficult to be gasified [104].

Temperature distribution inside the reactor is the result of the way of mixing of the two feed streams. Table 6.3 compares results from gasification in the three different investigated configurations (see Figure 6.3) for a WATER stream of 10 g/min and a glucose solution stream of 5 g/min (residence time = 64 s).

Table 6.3 Performance metrics obtained from gasification of a 54 g/l glucose solution in the feed stream. Pressure 25 MPa, wall temperature 670 °C. Other parameters as reported in the text.

Residence time 64 s						
	Conf. 1		Conf. 2		Conf. 3	
Performance metrics	**Experimental data**	**Deviation (%)**	**Experimental data**	**Deviation (%)**	**Experimental data**	**Deviation (%)**
GE (%)	56.0	± 3.0	53.0	± 4.0	72.0	± 1.5
CE (%)	50.50	± 2.0	39.0	± 3.0	57.0	± 1.0
H_2 YIELD (%)	50.30	± 9.5	70.37	± 0.3	74.0	± 1.5
TOC (mg/l)	1213	± 4.0	1787.4	± 3.0	1039.8	± 5.0

Configuration 3 with glucose solution fed from the top and pure water at right angle gives the best result in terms of GE and H_2-yield. The poor value of GE obtained with conf. 1 and 2 can be explained assuming that locally poor mixing between streams produces favourable condition for carbon formation (tar and char) and other residues in liquid phase. This hypothesis is confirmed by the lower value of carbon efficiency, high value in the TOC analysis with conf. 1 and conf. 2, with respect to CE of 57.00 % with conf. 3.

In a second series of experiments, the effect of residence time was also investigated. By doubling to 128 s the residence time we noticed an increase of GE in all configurations. Particularly, with conf. 3 the GE increased to 83%.

Gas composition was also affected by inlet streams configurations as shown in Table 6.4.

Table 6.4 Compositions of gas product from gasification of a 54 g/l glucose solution in the feed stream. Pressure 25 MPa, wall temperature 650 °C.

Residence time 64 s						
	Conf. 1		Conf. 2		Conf. 3	
Compound (% molar	**Experimental data**	**Deviation (%)**	**Experimental data**	**Deviation (%)**	**Experimental data**	**Deviation (%)**
H_2	50.47	± 3.7	64.95	± 1.2	57.49	± 0.5
CH_4	7.59	± 0.6	5.76	± 5.6	6.55	± 0.8
CO_2	19.04	± 0.1	26.37	± 5.3	28.21	± 1.1
CO	21.46	± 8.8	1.88	± 9.8	5.95	± 4.4
C_2H_4	0.28	± 7.2	0.0	± 0.0	0.22	± 4.7
C_2H_6	1.15	± 2.5	1.0	± 8.6	1.59	± 2.4

Hydrogen concentration is quite stable among the various configurations, apart from the case of conf. 1 that produces the highest concentration of CO (21.46%) in accordance with H_2 yield data reported in Table 6.4.

Composition data are not in good agreement with equilibrium composition simulated by Aspen plus. Simulations predict much higher CO_2 concentrations and very low CH_4 concentration (<1%) compared to a value of about 6-7% obtained experimentally. Similar results were obtained by Guo et al. [103]. Authors attributed the discrepancy to the free-radical mechanism leading to CH_4 formation, which is not predictable by equilibrium calculations.

Comparing GE values with those reported in literature, a lower gasification efficiency was observed in the present work. For example, Guo et al. [103] reported a gasification efficiency higher than 100% for sawdust at 650 °C in a reactor with 6 mm i.d. Antal et al. [105] reported that glucose can be gasified completely at 600°C and 28 s residence time [105].

Other authors reported gasification efficiencies closer to those here obtained. For example, Jin et al [106] using a 30 mm fluidized bed reactor obtained a GE of about 50% with a solution concentration of 10% of glucose and 600 °C.

Results comparison is clearly made difficult by the great differences of reactor size, inlet configuration, and volume-to-surface ratio adopted in the various studies

and the present work. Particularly, it seems that higher gasification efficiencies are obtained when the reactor is made of long small-bore tubes, as in this case mixing and temperature gradient effects are minimized.

In order to gain insight in the reactor performance and its dependence on the mixing mode between streams, and also to help understanding the discrepancies between the results reported by various authors, a detailed Computational Fluid Dynamics (CFD) analysis of the reactor here employed was carried out.

6.4 CFD Simulation

6.4.1 Model equations and solutions procedure

In order to obtain information about reactor fluid dynamics, CFD simulations were carried out by means of the CFX 15.0 commercial code. Numerical results compared with experimental data may be useful to understand reactor performances and to optimize the operating parameters.

The IAPWS-IF97 database [74] available in the CFX code was used to describe water properties change over the range of temperatures and pressures investigated.

Taking into account the large difference between temperatures of the two incoming streams, respectively 100 °C for the glucose solution and 670 °C for pure water (this last coinciding with reactor wall temperature T_w) very high fluid density gradients exist inside the reactor, that lead to significant buoyancy effects on fluid flow ([107] and [108]). This implies that natural convection effects may be significant [75]. Grashof number (Gr) is commonly employed to evaluate the magnitude of buoyancy [109]. Gr is a non-dimensional number, germane to Re in forced convection, defined as the ratio between buoyancy and viscous forces:

$$\mathrm{Gr} = \frac{g\Delta\rho\delta^3}{\upsilon^2\rho} \tag{6.4}$$

where υ and δ are kinematic viscosity and characteristic length, respectively. This latter is frequently chosen as the vertical distance where buoyancy occurs [110]. In the present study, the reactor axial length in the active zone (268 mm) was chosen as the characteristic length, which led to values of Gr number ranging from $5.6 \cdot 10^{10}$ to

$6.3 \cdot 10^{10}$. These values are significantly larger than the reference value of $4 \cdot 10^{8}$ that marks turbulent flow conditions when natural convection is prevailing [110].

6.4.2 Transport equations

Actually, the early simulation runs were performed under steady-state assumptions. However, in such simulations the "residual terms" (the numbers that indicate the distance from the "true" solution) never became negligible, but rather kept oscillating over fairly large values. This behaviour is typical of systems in which a transition from creeping flow towards turbulence is taking place.

To overcome this difficulty, unsteady 3-D simulations were performed for all investigated cases. These confirmed that in the simulated conditions the flow field gives rise to sustained oscillations. In order to simulate the turbulent flow, the unsteady Navier-Stokes equations were modified by introducing average and fluctuating quantities to produce the Reynolds Averaged Navier-Stokes (RANS) equations. To mathematically close the equations system, the *k-ε* turbulence model, developed by Launder and Spalding [69], has been used in various works on supercritical water reactors ([111], [112] and [113]) obtaining satisfactory predicted results when compared to experiment.

Thus, for a compressible turbulent flow the Reynolds-averaged mass, momentum, energy conservation and scalar transport equations are expressed hereinafter. If the *standard k-ε turbulence model* is used for turbulence and the Newton's indicial notations is adopted, these can be written as:

$$\frac{\partial \rho}{\partial t} + \frac{\partial \rho u_j}{\partial x_j} = 0 \tag{6.5}$$

$$\frac{\partial \rho u_i}{\partial t} + \frac{\partial \rho u_j u_i}{\partial x_j} = -\frac{\partial P}{\partial x_i} + \frac{\partial}{\partial x_j}\left[(\mu + \mu_t)\left(\frac{\partial u_i}{\partial x_j} + \frac{\partial u_j}{\partial x_i}\right)\right] + \rho g_i \tag{6.6}$$

$$\frac{\partial \rho h}{\partial t} + \frac{\partial \rho u_j h}{\partial x_j} = \frac{\partial}{\partial x_j}\left(\lambda \frac{\partial T}{\partial x_j}\right) + \frac{\partial}{\partial x_j}\left(\frac{\mu_t}{\sigma_\tau}\right)\frac{\partial h}{\partial x_j} \tag{6.7}$$

$$\frac{\partial (\rho \varphi)}{\partial t} + \frac{\partial \left(\rho \varphi u_j\right)}{\partial x_j} = \frac{\partial}{\partial x_i}\left(\rho D_\varphi + \frac{\mu_t}{Sc_t}\right)\frac{\partial \varphi}{\partial x_j} \tag{6.8}$$

The term μ_t is turbulent viscosity obtained from the Prandtl-Kolmogorov equation:

$$\mu_t = C_\mu \rho \frac{\varepsilon^2}{k} \tag{6.9}$$

where C_μ is a constant equal to 0.09. The differential transport equations for the turbulence kinetic energy k and turbulence dissipation rate ε are expressed as:

$$\frac{\partial}{\partial t}(\rho k) + \frac{\partial}{\partial x_i}(\rho u_i k) = \frac{\partial}{\partial x_j}\left[\left(\mu + \frac{\mu_t}{\sigma_k}\right)\frac{\partial k}{\partial x_j}\right] + P + G_b - \rho\varepsilon \tag{6.10}$$

$$\frac{\partial}{\partial t}(\rho \varepsilon) + \frac{\partial}{\partial x_i}(\rho u_i \varepsilon) = \frac{\partial}{\partial x_j}\left[\left(\mu + \frac{\mu_t}{\sigma_k}\right)\frac{\partial \varepsilon}{\partial x_j}\right] + C_{1\varepsilon}\frac{\varepsilon}{k}\rho P - C_{2\varepsilon}\rho\frac{\varepsilon^2}{k} \tag{6.11}$$

In equations (6.10) and (6.11) the term P provides the shear production and, it is defined by:

$$P = (\mu + \mu_t)\frac{\partial u_i}{\partial x_j}\left(\frac{\partial u_i}{\partial x_j} + \frac{\partial u_j}{\partial x_i}\right) \tag{6.12}$$

whereas the term G_b is the production of turbulent kinetic energy due to buoyancy. Terms σ_k and σ_ε are the relevant turbulent Prandtl numbers for k and ε equation. The values of the parameters used in all simulations are the standard k-ε model values: $C_{1\varepsilon}$= 1.44, $C_{2\varepsilon}$= 1.92, σ_k =1.0, and σ_ε=1.3. It is worth noting that, the contribution of buoyancy effects to the balance of Reynolds stress k is taken into account in the turbulent kinetic energy equation only, since it is proved that the contribution of buoyancy dissipation is negligible when compared to buoyancy production [75]. The expression of the buoyancy production term G_b, present in equation (6.13), is:

$$G_b = -\frac{\mu_t}{\rho\sigma_k} g_i \frac{\partial \rho}{\partial x_i} \tag{6.13}$$

The *scalable wall function* [74] formulation implemented in the CFX code was used in order to model the viscous-conductive sublayer [75] in the proximity of the walls.

6.4.3 Solution domain and boundary conditions

The 3-d fluid domain was created by means of the ANSYS Designer Modeller. The domain was then meshed by means of the ICEM code using only hexahedral cells.

In Figure 6.4 the entire meshed domain and a cross central section of the mesh are shown. As it is possible to appreciate in Figure 6.4-b, the *o-grid function*, available in the ICEM code, was used to increase hexahedral cells quality in the proximity of domain curved zones.

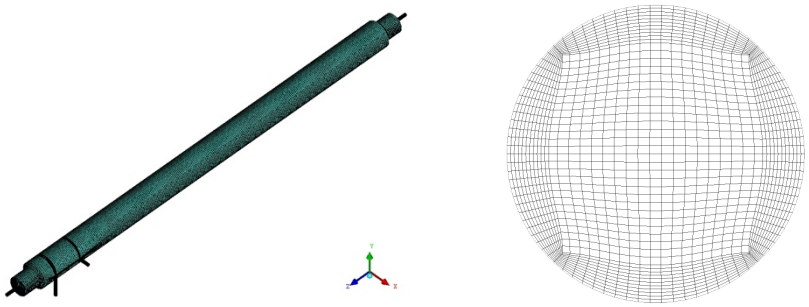

(a) (b)

Figure 6.4. (a) Mesh domain and (b) cross central section of the computational multi-block hexahedral mesh.

6.4.4 Convergence criteria

Transient simulations of the continuous phase were conducted for all analysed cases. The High-Resolution scheme was selected for spatial discretization of the advective terms and the second order backward Euler was selected as the transient scheme. Convergence control of max 10 coefficient loops for each time-step was used with a residual target of $1 \cdot 10^{-6}$. The simulation was firstly conducted with the inlet of hot water only. This method allows to quickly obtain a converged solution for the next step where a second inlet, with different physical properties, is introduced. Suitable values for the time-step ranging from $5 \cdot 10^{-4}$ *s* to $1 \cdot 10^{-3}$ *s* were chosen as a good

compromise between the need to obtain accurate results (on the basis of Courant-Friedrichs-Lewy, CFL condition) and computational efficiency.

6.4.5 Simulation strategy

Satisfactory completion of each simulation run was based on several criteria: (i) sufficient reduction of mass residuals; (ii) an accurate balance between the flow rates entering and leaving the reactor and (iii) either practically constant or regularly oscillating local values of all flow quantities. "Pseudo-steady state" conditions were considered to have been attained when all the above criteria were met.

The operating pressure P_{ref} inside the supercritical reactor was set to 25 MPa as in experiments. Inlet conditions with constant mass flow rate and temperature were imposed at the inlets of the two entering feeds, while at the reactor outlet constant pressure P_{ref} (25 MPa) was imposed. No-slip boundary conditions were imposed at reactor walls. In order to simulate the external heating configuration of the reactor, an imposed constant temperature of 670°C was set in the reactor "central-heated" section while adiabatic conditions were imposed in the top and bottom reactor walls.

6.4.6 Grid refinement and validation

In order to obtain grid-independent results while maintaining acceptable computational effort, a preliminary sensitivity analysis was carried out. Four different computational grids of (A) 45 x 10^3, (B) 100 x 10^3, (C) 250 x 10^3 and (D) 650 x 10^3 cells for configuration 1 were set up. To test grid independency temperature axial distributions obtained with the various grids were compared with each other. As it can be seen in Figure 6.5, the fine (D) and medium (C) grids give rise to very similar profiles of axial temperature. The profile obtained with the coarsest grid (A) is clearly different from that of the finer grids, while the intermediate (B) grid gives rise to results much closer to those obtained with the finer grids (C) and (D), yet with still visible differences especially in the top-central transition zone of the reactor. As the differences between the numerical results for the medium and fine grid are small and

considering the computational time for all examined cases, the 250 x 10^3 elements mesh (C) was chosen for all the simulations carried out in this work.

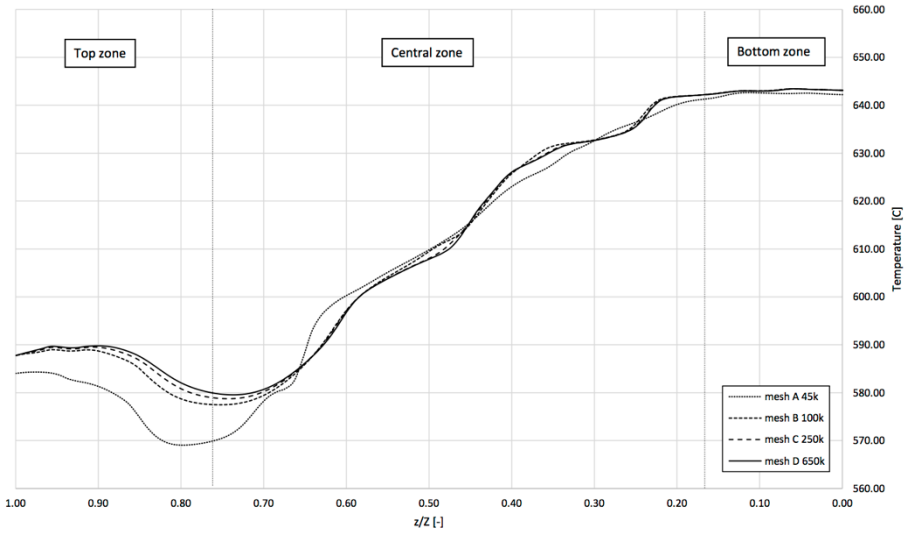

Figure 6.5. Grid independency – Axial temperature profile for configuration 1.

The numerical results for configuration 1 were preliminary validated by comparing the calculated temperatures inside the reactor with the experimental values read by the thermocouples installed in the reactor. Results are shown in Figure 6.6 where it can be seen that CFD simulations are in good agreement with experiment, apart from a moderate temperature overestimation in the top reactor section, likely due to heat losses not accounted for in the simulation. In Figure 6.6 the experimental value T_5, recorded quite away from the reactor (see Figure 6.2) and thus outside the computational domain, is also reported for the sake of completeness.

6.4.7 Residence Time Distribution (RTD) simulations

A useful tool for looking at reactor fluid dynamics is the residence times distribution (RTD) of fluid parcels, expressed by the so-called *E(t)* curve.

This was obtained by carrying out transient simulations with fully developed flow field in which an almost instantaneous pulse of a passive tracer φ was injected in the glucose solution inlet.

By recording the tracer concentration dynamics at the reactor outlet the *E(t)* curve is simply obtained by the following equation [114]:

$$E(t) = \frac{C_{out}(t)}{\int_0^t C_{out}(t)\, dt} \tag{6.14}$$

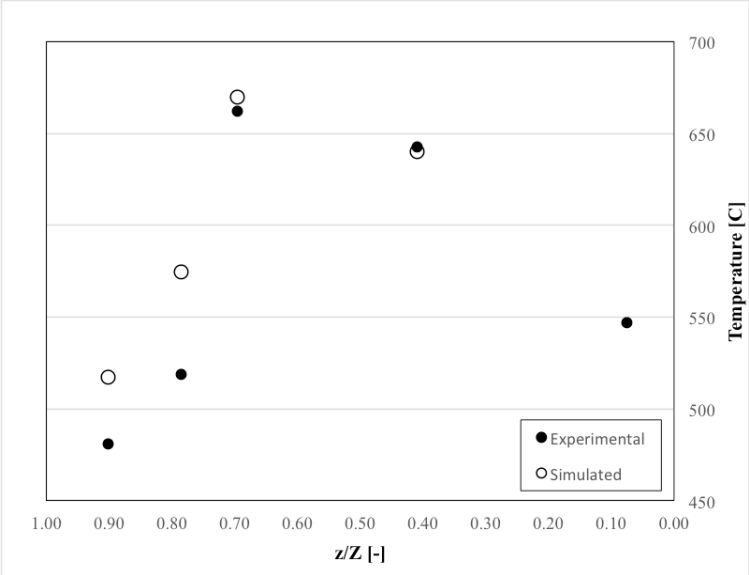

Figure 6.6. Measured and simulated temperatures for configuration 1 in correspondence of temperature probes.

6.5 CFD Results

6.5.1 Temperature fields

Temperature contour plots on an axial vertical plane inside the SCWR are reported in Figure 6.7 for the three cases analysed. As it can be seen, while the lower section of the reactor shows a homogeneous temperature distribution close to the operating temperature of 640°C, the first half of the reactor shows a variable temperature distribution, which is quite significantly affected by the reactor inlet

configuration. In particular, in configuration 1 (Figure 6.7-a) and 2 (Figure 6.7-b) in which the cold inlet (glucose solution) is at 45°, the inlet side of the reactor (right side in the two figures) is much colder than the central core. As a matter of fact, the cold feed tends to move down the reactor due to its higher density so resulting in a delayed mixing between the two feeds. Different results are obtained with configuration 3 (Figure 6.7-c), where the cold feed is injected from the upper inlet of the reactor. In this configuration, not only the cold feed goes through a longer path inside the reactor, but it also gives rise to an earlier mixing, as can be appreciated in Figure 6.7-c by noticing that the "greener" (i.e. colder) vessel portion observable in Figure 6.7-b is much less pronounced in Figure 6.7-c.

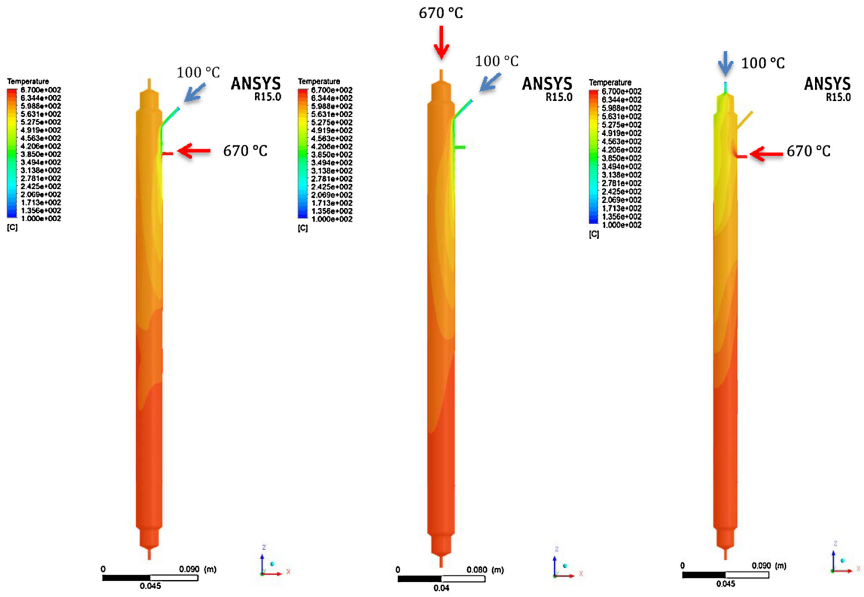

Figure 6.7. Temperature contour plot in a vertical axial plane of the SCR: a) Configuration 1, b) Configuration 2; c) Configuration 3.

Temperature profiles along the SCR vertical axis are reported in Figure 6.8 for configurations 1, 2 and 3. As it can be seen, apart from the upper portion (about 1/4 of total height) of the reactor the axial temperature is almost the same for the three

cases analysed, reaching the final temperature of about 650 °C in the lower half of the reactor. As regards the upper portion of the reactor, of course the temperature differences between configurations 1, 2 and 3 along reactor axis are particularly evident due to the fact that we are not looking at the average temperature in the various sections but at the local temperature at reactor axis.

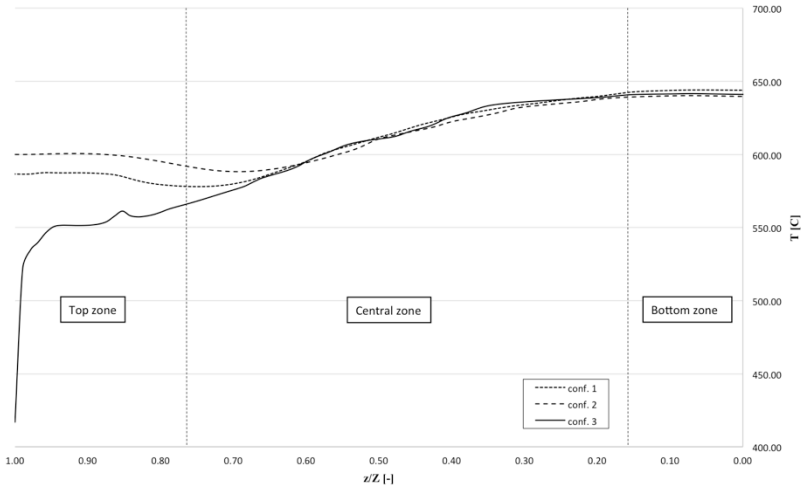

Figure 6.8. Temperature profile along the SCR vertical axis for configurations 1, 2 and 3.

6.5.2 Velocity fields

In Figure 6.9 velocity vector plots in the upper portion on a vertical axial plane of the SCR are shown for configurations 1, 2 and 3. It is confirmed that with configurations 1 (Figure 6.9-a) and 2 (Figure 6.9-b) the cold feed entering from the 45° inlet tends to move downward the reactor along the wall due to its much larger density. A natural clockwise convective ring can also be observed. It is worth noting here that this is the stream carrying the main reactant, and that the result of natural convection s that of delaying mixing with the hot stream.

The situation is totally different with configuration 3 (Figure 6.9-c), where the horizontal hot feed turns upwards almost immediately after reactor entrance then moves upwards to meet the cold feed entering from the top inlet. Interestingly this

configuration gives rise to an anticlockwise convective ring, which seems to better promote mixing between the two incoming feeds.

The Grashof number calculated inside the central zone of mixing is comprised between $1.5 \cdot 10^{11}$ and $1.7 \cdot 10^{11}$, values showing that the flow regime is clearly turbulent as already stated in the previous considerations about flow regime.

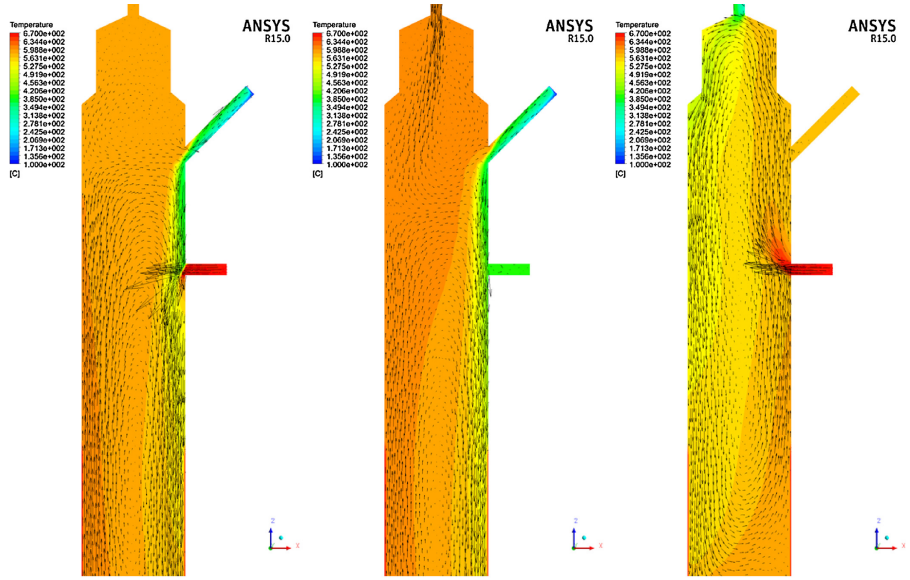

Figure 6.9. Temperature profile along the SCR vertical axis for configurations 1 (a), 2 (b) and 3 (c).

In Figure 6.10 vector plots on the x-y plane at different z positions are shown for configuration 3. Vector plots are over imposed on temperature contours on the left side (Figure 6.10 – a, c, e, g, i) and on axial velocity contours on the right side (Figure 6.10 - b, d, f, h, l). Negative velocity w values indicate a downwards direction in the reactor.

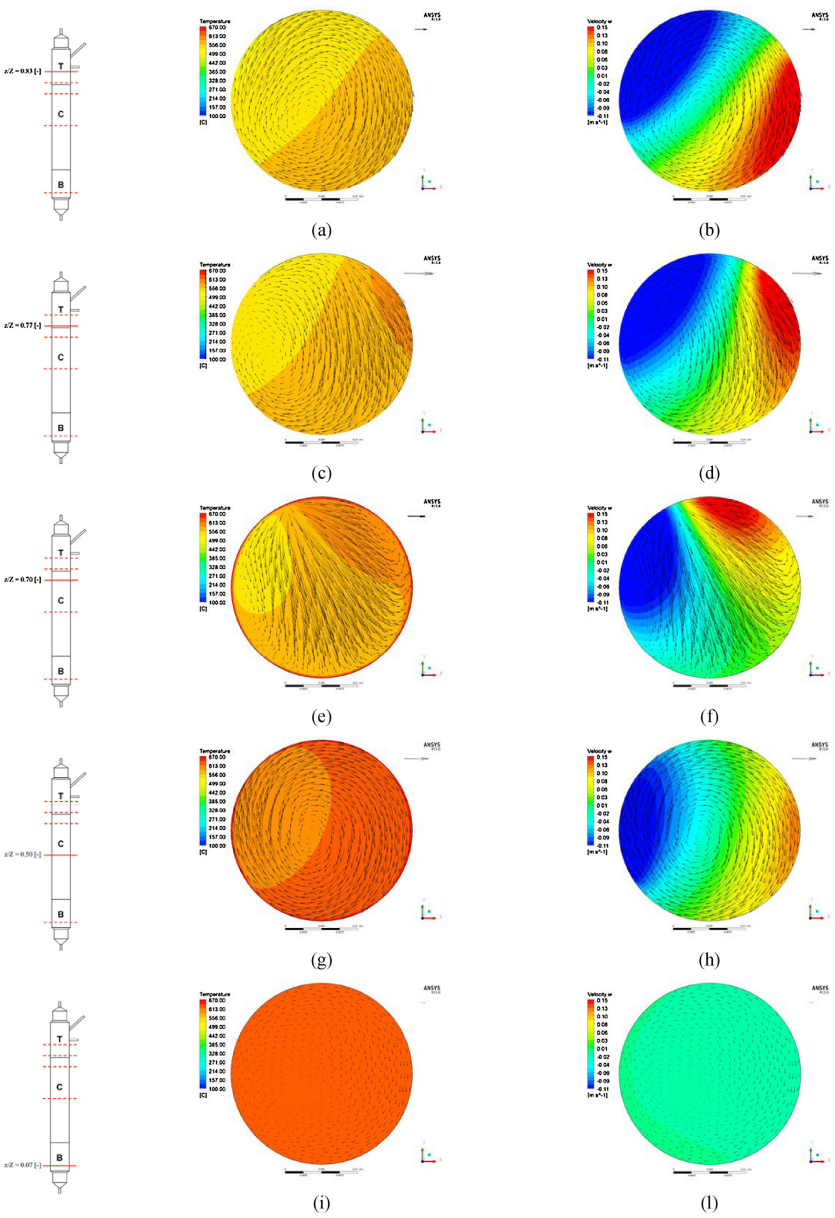

Figure 6.10. Vector plots on the x-y plane of the configuration 3 at different z position on to temperature contour (a, c, e, g, i) and velocity w contours (b, d, f, h, l). Negative velocity values indicate a downwards direction in the reactor. Reference vector for all x-y planes is 0.13 $m \cdot s^{-1}$, except in the bottom section (i – l) with dimension of 0.01 $m \cdot s^{-1}$.

The reference vector reported in the upper right corner represents a velocity of 0.13 $m \cdot s^{-1}$ for all figures but Figure 6.10-i and Figure 6.10-l, where the reference vector value was decreased to 0.01 m/s in an attempt to make the vectors visible despite the very small values of x-y plane velocities.

As it can be observed, apart from confirming the strong recirculation induced by buoyancy forces already observed in Figure 6.10-c, a clockwise swirling motion occurs that displaces the flow structures over the x-y planes while moving upwards (see for instance in sequence Figure 6.10-f, d and b). Due to planar symmetry system with respect to Figure 6.9 plane, the direction of the swirling motion should be interpreted as being the result of a random result of initial computational details, and as such it might have as well been directed anti-clockwise. In any case, after being started it is reinforced and maintained by the forces acting on the system. At the height corresponding to Figure 6.10-e and Figure 6.10-f the major vertical recirculation ring closes, giving rise to stronger velocity components on the x-y planes. In the bottom portion of the vessel temperature is almost uniform and the flow field is very regular with almost-constant downward-directed w velocities and almost nil u and v velocities.

6.5.3 Residence Time Distribution (RTD) results

The *E(t)* curves obtained by applying equation (14) to the tracer concentration dynamics are reported in Figure 6.11 for the three configurations analysed. As it is possible to notice, all the three configurations show a mixing pattern that may be modelled by a combination of a CSTR plus a PFR reactor or, as an alternative, a PFR with axial dispersion (Scargiali et al., 2004 [115] and [116]). In particular, in configurations 1 and 2 the contribution of the CSTR over the PFR in the CSTR+PFR model is more important than in configuration 3 where a larger time lag is appreciable in the *E(t)* curve which is slightly shifted towards the right side of the graph.

These considerations are also confirmed by the values obtained for the average residence time τ:

$$\tau = \int_0^\infty tE(t)dt \tag{6.15}$$

and the standard deviation:

$$\sigma = \sqrt{\int_0^\infty (t-\tau)^2 E(t)dt} \tag{6.16}$$

calculated for the three configurations analysed and reported in Table 6.5, where, as it is possible to notice, configuration 3 shows the highest τ and the lowest standard deviation.

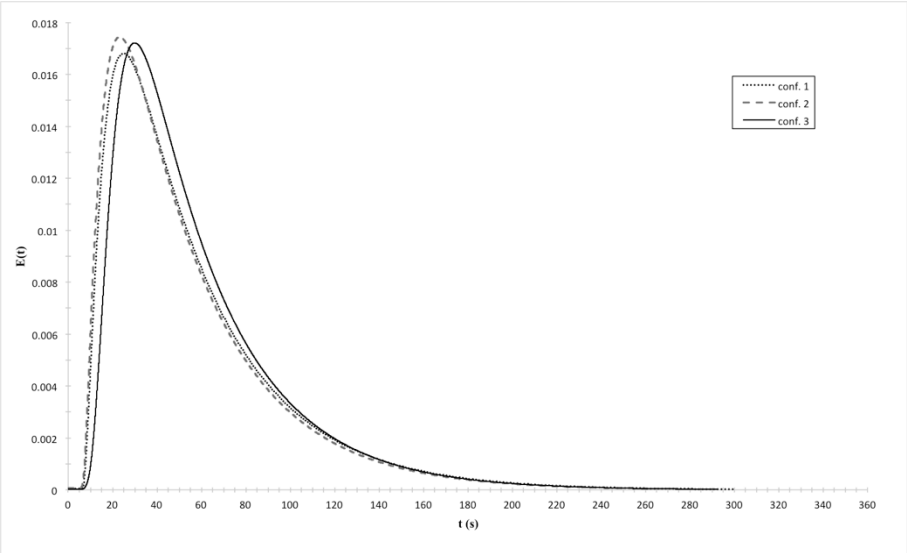

Figure 6.11. Residence time distribution RTD (E(t) curve) versus time for the three configurations analyzed.

6.6 Discussion

RTD analysis showed that the down flow reactor can be modeled as a combination of an ideal CSTR plus a PFR reactor where a mixing pattern plays a

fundamental role. As shown in Table 6.5, the calculated residence time is higher in conf. 3 with respect to conf. 1 and 2.

By analyzing the RTD curves obtained by CFD simulations, configuration 3 performs the best mixing pattern in the upper portion of the reactor, while the lower portion behaves as a PFR reactor.

Table 6.5 Average residence time, eqn. (6.15), and standard deviation, eqn. (6.16), of conf. 1, 2 and 3.

Configuration	τ (s)	σ
1	56.22	40.10
2	54.27	39.63
3	59.02	38.19

The cold feed is suddenly mixed with the lateral hot feed and, even if the average temperatures in the upper part of the reactor are lower than in the other two configurations, the cold feed goes through a longer path inside the reactor and gives rise to an earlier mixing.

These conditions are favorable for glucose conversion, giving rise to the highest GE, CE efficiency and H_2-yield among the three configurations, as reported in Table 6.3. However, as shown in Figure 6.8 average axial temperatures are relatively low (<600 °C for half of the reactor length) with respect to wall temperature of 670 °C and at the exit of the reactor reaches about 650 °C. Moreover, it must be taken in account that simulated temperatures shown in Figure 6.7 are higher than actual temperatures due to heat losses (see Figure 6.6). As a consequence, GE and H_2- yield do not reach 100%. Indeed, it is known from experiments reported in literature and from simulations that GE and H_2 yield strongly increases with temperature. Particularly, H_2 formation is enhanced by the water-gas shift reaction rate (toward the formation of H_2 and CO_2 from CO) that requires temperature above 650°C. This temperature distribution inside the reactor is likely to be responsible for the lower performance of the present reactor with respect to the small-bore tubular reactors often employed at lab scale. On the other hand, small bore reactors are more prone to blockage due to solid products accumulation, and therefore a lesser operability with respect to larger bore reactors may be anticipated.

The temperature drawback in larger bore SCWRs is clearly due to both the smaller heat exchange surface and smaller heat exchange coefficients exhibited by these in comparison with smaller bore reactors. A way of circumventing this drawback, while still retaining the greater operability of larger bore reactors, might be that of preheating the pure water stream at temperatures above that of the reactor, in order to rely on mixing only (and not on wall heat exchange) for attaining the desired reaction temperature. These aspects are clearly of great importance in the realm of SCWG development and scale-up.

6.7 *Nannochloropsis gaditana* experimental gasification results

After previous experimental tests with glucose compound, supercritical water gasification of *nannochloropsis gaditana* microalgae was studied.

Microalgae *Nannochloropsis Gaditana* was purchased in powder form Algaspring BV. The composition of the algae as provided by the supplier and elemental analysis by us is reported in Table 6.6.

Microalgae gasification was performed at a reactor wall temperature of 663 °C, pressure of 24 MPa and residence time of 128 s. The dry algae powder was suspended in water at weight of 3 or 5 wt% and pumped at flow rate of 2.5 mL/min. Water was pumped into the reactor at a flow rate of 5 mL/min causing the effective concentration entering the reactor to be 1 and 1.6 wt% respectively.

Table 6.6 Nannochloropsis gaditana chemical composition (wt%) elemental composition and lower heating value. [a]Obtained by elemental analysis. [b]According to the analysis furnished by the vendor, ashes are composed by K, Ca, P, Fe, Mg, Na, Zn and S.

dry weight	95
proteins	38
lipids	32
carbohydrates	12
Ash[a]	14
molar composition[b]	$C_9H_{16}NO_4$
lower heating value (MJ/kg)	-19.39

The composition of the product gas was determined using a gas chromatograph to quantify all the gaseous species including H_2, CO_2, CO, CH_4, C_2H_4 and C_2H_6. The GC was an Agilent 7890 B equipped with thermal conductivity detector, sampling valve and a silica capillary column (SUPELCO, Carboxen-1010 PLOT). Argon (99.999%) was used as carrier gas.

The carbon content in the liquid product was analyzed using a Shimadzu total organic compounds analyzer (TOC-L CSN). The performance metrics used for the definitions of the product yields in this study are Gasification Efficiency (GE), that measures the conversion of the feedstock to product gases and can be described as the ratio between the sum of the masses of product gases and that of the feedstock. The carbon efficiency (CE) is defined as the mass percentage of carbon converted from the initial biomass towards gases products. H_2 yield (%) is defined as the mass percentage of hydrogen converted from the initial biomass towards gas molecular hydrogen. The energy recovery (ER) is defined as the ratio between the lower heating value of the gas produced and that of the algal biomass fed in the reactor.

Table 6.7 Performance data obtained from gasification of *nannochloropsis gaditana* microalgae. Pressure 24 MPa, wall temperature 663°C, residence time 128 s.

Microalgae concentration, wt %	3	3*	3	5
K_2CO_3 Catalyst, wt %	0	0	0.6	1
GE, %	81.9	73.6	92.7	31.1
CE, (%)	77.0	63.9	77.6	23.8
H_2 yield, (%)	50.9	53.7	90.8	33.3
Energy Recovery (%)	93.6	83.0	102.2	34.0
TOC (mg/L)	434.1	391.5	544.7	121.8
lost carbon, %	9.5	20.0	0.02	71.3
GAS COMPOSITION, %mol				
H_2	41.9	45.7	55.4	57.4
N_2	0.4	4.3	0.0	4.2
CO	1.8	0.7	0.2	0.00
CO_2	25.2	22.1	23.9	20.51
CH_4	19.9	18.2	13.7	12.09
C_2H_4	2.7	2.2	1.3	1.12
C_2H_6	8.1	6.8	5.4	4.73

Results are summarized in Table 6.7. Experiments at microalgae slurry concentration of 3 wt% give satisfactory values of gasification efficiency (92.7%) and carbon efficiency (77.6%).

The product gas is mainly composed of hydrogen (55.4%), methane (13.7%) and CO_2 (23.9%). GE values reported in Table 6.7 has been calculated as the ratio between mass of gas obtained and the mass of algae fed to the reactor minus the ash content of algae. Indeed, because ash is composed of metals that cannot be gasified, the performance of the process must be evaluated considering only the organic part of the biomass (i.e. protein, lipids and carbohydrates). If one took in account the ash mass in the feed, the GE would drop from 81.9 to 70%.

6.8 Conclusions

This work highlights the differences of conversion performance of a down flow reactor with three different positions of the inlet ports of the reacting streams.

The adopted plant scheme allowed to perform gasification in a continuous mode over day without blockage due to solid products.

Experimental results coupled with CFD analysis, allowed to find that temperature is not uniform inside the reactor and the wall temperature, that should allow complete conversion of glucose, is never reached in any section of the reactor. Using the best reactor configuration in terms of mixing and temperature distributions and with the lower residence time (64 sec) allowed to improve the gasification efficiency and H_2 yield up to 72% and 74% by mole, respectively. Relatively low temperature inside the reactor is suggested to be responsible for the lower performance of the present reactor with respect to small bore tubular reactors often used for lab scale investigations. These are however bound to incur in reduced reactor operability, due to easier blockage by solid reaction by products. An aspect of paramount importance for process viability. Pure water stream preheating at temperatures high enough to reach the desired reaction temperature by simple mixing with the cold organics-containing stream, might be a way to improve larger bore reactors performance, still retaining their better operability features.

Regarding the gasification of microalgae *Nannochloropsis gaditana*, it can be concluded that gasification of microalgae is feasible in a continuous mode with very high gasification efficiency results, up to 92.7wt% as gasification efficiency and 77.7wt% as carbon efficiency, where gas product is mainly composed of hydrogen (55.4%), methane (13.7%) and CO_2 (23.9%). These results can be of help in evaluating the feasibility of gasification as a possible post-treatment microalgae process after its production, or rather, under defatted microalgae conditions after extraction of the oil.

CONCLUSIONS

The purpose of this work was a comprehensive study of microalgae production using an innovative technology, and one possible post-treatment of the same microalgae, both through modeling and experimental activities, where the research activities were concluded with the construction and first experimental tests of a Pilot Plant for microalgae cultivation.

In this PhD work, the concluding observations achieved during these research activities can be summarized in the following points:

i. *Development of a mathematical model for microalgae cultivation with an innovative PBR Pilot Plant*. All optimal operation parameters for a microalgae species growth, in particular the *Phaeodactylum tricornutum* species, were obtained. Subsequently, the main plant units, i.e. Air-Lift Unit, PBR Unit and Make-Up & Biomass Removal Unit were modeled and interconnected with each other on MATLAB environment. Finally, a GUI interface was also developed to enhance the user experience. Then, main results obtained were: considering the initial input conditions, injected gas flow at riser bottom section is mainly composed of carbon dioxide (84% mol), vapour water (15.9 mol%) and it presents a possible oxygen traces. In output riser section, oxygen molar fraction is increased due to flow rate inside the riser column which allows liquid phase degassing, and resulting in dissolved oxygen stripping. Liquid oxygen concentration is about 4.47 g/L, below limit concentration (equal to 9 g/L), and there is not occur oxygen accumulation beyond the limits of photo-oxidation phenomena. Volumetric productivity is equal to 2.28 g/L day, and it results to be a fairly high value although it is a closed system. Temperature parameters are almost similar even if it is noted a slight liquid cooling at output riser section; this temperature decrease is due to sensible heat exchange between liquid- and gaseous phase. Regarding irradiance models, Beer-Lambert model and Cornet model not show a significant difference between them; in fact, the difference between volumetric productivity is about 5%. Instead, Acién Fernández model returns a volumetric productivity of less than 20% compared to Beer-Lambert

model. Subsequently, Full model allows to take into account fluid dynamics aspects and light-dark cycles frequency; as it can see, these values are slightly higher compared to Acién Fernández model, with a maximum of 25%.

ii. *Experimental investigation of a lab-scale Air-Lift Unit and CFD numerical analysis.* In order to verify performance of an external loop evacuated-head Air-Lift, experimental activities were carried out with a lab-scale model using a 20-liters and 4 meters high system by varying the air flow rate as well as separator pressure. Power law functions which express gas hold-up as function of superficial gas flow rate in riser section, and power law functions which express liquid flow rate as function of inlet gas flow rate, were developed in order to obtain a useful correlation. Then, computational fluid dynamics simulations were also developed to predict liquid circulation rates within the system. Finally, these numerical results were compared with experimental data and a good agreement was found.

iii. *A novel modeling of radiation transfer effect on microalgae cultivation.* In order to properly model the radiation field inside photobioreactors, the *local volumetric rate of photon absorption* LVRPA in a cross section of a horizontal-pipe photobioreactor has been investigated, where a simplified mathematical model based on a Monte Carlo approach was developed. Results show that optical properties affect the LVRPA inside the cross-section while the scattering phase function may be neglected in terms of computational complexity. These results are particular evident at low biomass concentration while become negligible when biomass concentration larger than 1 g/L. Moreover, in order to experimentally study light intensity effects on microalgae productivity, a thin-slab quasi-isoactinic photobioreactor was realized in laboratory-scale.

iv. *Design, construction and first testing of the PBR Pilot Plant.* A 500-liter pilot plant was built, where this is presently being operated in batch mode under solar irradiation and external climatic conditions. The relevant Air-Lift deployed is about 20 meters high and has an internal diameter of 8 centimetres. The main pilot plant performances were carried out with the evacuated Air-Lift head and without evacuation, i.e. to atmospheric pressure. The vacuum pump enhances the

liquid circulation performance from a minimum of 8% up to a maximum of 17% with the same inlet gas flow rate. It is noting that higher inlet gas flow rate values were not considered since it was noticed high bubbles entrainment in the downcomer-bottom section by activating vacuum pump. Finally, the previous mathematical model for the entire pilot plant was used and good results were achieved in the experimental results-mathematical model comparison, with percentage deviations between -8% and + 1.5%.

v. *Experimental investigation of microalgae gasification in supercritical water and CFD numerical analysis*. In order to study this innovative process, it started with a simple gasification of glucose solution. Gasification has been investigated using a laboratory scale continuous plant comprising a continuous down flow reactor with a volume of 200 cm^3, a heat recovery section and pre-heat of the biomass to simulate more closely an industrial design. Moreover, in order to obtain a description of the fluid flow inside the reactor, computational fluid dynamics (CFD) simulations were carried out. Experimental results coupled with CFD analysis, allowed to find that the reactor has the top section that behaves like a mixed reactor and the bottom section that behaves like a plug flow reactor. The two jet streams (water and glucose solution) entering the reactor cause back mixing in the top-side of the reactor, so contributing to rapid initiation of reaction and down-flow of species through the chamber. Using the best reactor configuration in term of mixing and temperature distribution allowed to maximize the gasification efficiency and H_2 yield up to 72% and 74% by mole, respectively. After these first experimental tests with glucose compound, supercritical water gasification of *nannochloropsis gaditana* microalgae was studied in term of process development at 24 MPa and 660 °C. *Nannochloropsis Gaditana* was successfully gasified up to 92.7wt% as gasification efficiency and 77.7wt% as carbon efficiency. The product gas is mainly composed of hydrogen (55.4%), methane (13.7%) and CO_2 (23.9%).

Targets set at beginning of doctorate, in line with the R&D strategies of the project BIO4BIO, are superbly achieved within three years of research activities. In

particular, it is worth noting that a suitable Pilot Plant was set up to carry out research activities for many years ahead.

Eventually, it is hoped that this PBR Pilot Plant is just the beginning for the development and diffusion of microalgae production on an industrial scale.

APPENDICES

A. Arduino code for quasi-isoactinic photobioreactor (Hathor Project)

```
/*
Palermo (Sicily)
02/05/2016

Hathor Project
by Gaspare Marotta & Francesco Gugliuzza
for microalgae cultivation in a quasi-isoactinic PhotoBioReactor.

*/

// include the library code:
#include <LiquidCrystal.h>

#define REDPIN 3  //number of the interface pin
#define GREENPIN 10
#define BLUEPIN 11

// initialize the library with the numbers of the interface pins
LiquidCrystal lcd(8, 9, 4, 5, 6, 7);

int redValue = 0;
int greenValue = 0;
int blueValue = 0;

unsigned char redPwm = 0;
unsigned char greenPwm = 0;
unsigned char bluePwm = 0;

float frequencyValue = 0.0;
unsigned long lastMillis = 0;
boolean ledStatus = true;

enum modes {
  RED,
  GREEN,
  BLUE,
  FREQUENCY
} selectedMode = RED;

bool needPwmUpdate = true;
```

```
bool needLCDUpdate = true;

void setup() {
  // set up the LCD's number of columns and rows:
  lcd.begin(16, 2);

  pinMode(REDPIN, OUTPUT);
  pinMode(GREENPIN, OUTPUT);
  pinMode(BLUEPIN, OUTPUT);

  // Timer0 is already used for millis() - we'll just interrupt somewhere
  // in the middle and call the "Compare A" function below
  OCR0A = 0xAF;
  TIMSK0 |= _BV(OCIE0A);
}

void updateLCD() {
  lcd.clear(); //to clear the LCD display

  if(selectedMode == RED)
  {
    lcd.setCursor(0, 0);
  }
  else if(selectedMode == GREEN)
  {
    lcd.setCursor(4, 0);
  }
  else if(selectedMode == BLUE)
  {
    lcd.setCursor(8, 0);
  }
  else
  {
    lcd.setCursor(12, 0);
  }

  lcd.print('V');

  lcd.setCursor(0, 1);
  lcd.print('R');
  lcd.print(redValue);
  lcd.setCursor(4, 1);
  lcd.print('G');
  lcd.print(greenValue);
  lcd.setCursor(8, 1);
  lcd.print('B');
  lcd.print(blueValue);
```

```
  lcd.setCursor(12, 1);
  lcd.print('F'); //Frequency
  lcd.print(frequencyValue);

  needLCDUpdate = false;
}

void updatePwm() {
  redPwm = (float) redValue * 255 / 100;
  greenPwm = (float) greenValue * 255 / 100;
  bluePwm = (float) blueValue * 255 / 100;

/*
  analogWrite(REDPIN, redPwm);
  analogWrite(GREENPIN, greenPwm);
  analogWrite(BLUEPIN, bluePwm);
*/

  needPwmUpdate = false;
}

void updateKey() {
  int adc_key_in = analogRead(0);

  if (adc_key_in < 50)   return;
  if (adc_key_in < 195) {
    // UP
    if(selectedMode == RED)
      redValue = min(redValue+1, 100);
    else if(selectedMode == GREEN)
      greenValue = min(greenValue+1, 100);
    else if(selectedMode == BLUE)
      blueValue = min(blueValue+1, 100);
    else
      frequencyValue = min(frequencyValue+0.5, 100);

    needLCDUpdate = true;
    needPwmUpdate = true;

    return;
  }
  if (adc_key_in < 380) {
    // DOWN
    if(selectedMode == RED)
      redValue = max(redValue-1, 0);
    else if(selectedMode == GREEN)
      greenValue = max(greenValue-1, 0);
```

```
    else if(selectedMode == BLUE)
      blueValue = max(blueValue-1, 0);
    else
      frequencyValue = max(frequencyValue-0.5, 0.0);

    needLCDUpdate = true;
    needPwmUpdate = true;

    return;
   }
   if (adc_key_in < 555)  return;
   if (adc_key_in < 790) {
    // SELECT
    if(selectedMode == RED)
      selectedMode = GREEN;
    else if(selectedMode == GREEN)
      selectedMode = BLUE;
    else if(selectedMode == BLUE)
      selectedMode = FREQUENCY;
    else
      selectedMode = RED;

    needLCDUpdate = true;

    return;
   }
}

// Interrupt is called once a millisecond
SIGNAL(TIMER0_COMPA_vect) {
  unsigned long currentMillis = millis();

  if(frequencyValue < 0.1)
    ledStatus = true;
  else if((currentMillis - lastMillis) >= (500 / frequencyValue)) {
    ledStatus = !ledStatus;
    lastMillis = currentMillis;
  }

  if(ledStatus) {
    analogWrite(REDPIN, redPwm);
    analogWrite(GREENPIN, greenPwm);
    analogWrite(BLUEPIN, bluePwm);
  } else {
    analogWrite(REDPIN, 0);
    analogWrite(GREENPIN, 0);
    analogWrite(BLUEPIN, 0);
```

```
  }

  /*
  sweeper1.Update(currentMillis);

  if(digitalRead(2) == HIGH)
  {
     sweeper2.Update(currentMillis);
     led1.Update(currentMillis);
  }

  led2.Update(currentMillis);
  led3.Update(currentMillis);
  */
}

void loop() {
  updateKey();
  if(needLCDUpdate)
    updateLCD();
  if(needPwmUpdate)
    updatePwm();

  delay(100); //milli-seconds
}
```

REFERENCES

[1] B. Wang, C.Q. Lan, M. Horsman, Closed photobioreactors for production of microalgal biomasses, Biotechnol. Adv. 30 (2012) 904–912. doi:10.1016/j.biotechadv.2012.01.019.

[2] M. Morweiser, O. Kruse, B. Hankamer, C. Posten, Developments and perspectives of photobioreactors for biofuel production, Appl. Microbiol. Biotechnol. 87 (2010) 1291–1301. doi:10.1007/s00253-010-2697-x.

[3] P. Thangavel, G. Sridevi, Environmental Sustainability, Springer India, New Delhi, 2015. doi:10.1007/978-81-322-2056-5.

[4] A. Richmond, Q. Hu, Handbook of Microalgal Culture: Applied Phycology and Biotechnology: Second Edition, 2013. doi:10.1002/9781118567166.

[5] E.W. Becker, Microalgae: Biotechnology and microbiology, (1994).

[6] G. Palma, A. Bertucco, Sforza, E., Produzione di microalghe in fotobioreattori: influenza della luce e sfruttamento della biomassa esausta, Università degli Studi di Padova, 2012.

[7] M. Caiazzo, C. Rigano, A. Bordi, Studio delle caratteristiche di crescita di microalghe in impianti indoor ed outdoor per la produzione di biomassa algale pregiata, Università degli Studi di Napoli "Federico II"., 2007. http://www.fedoa.unina.it/1323/1/CAIAZZO-ACQUACOLTURA_XVII_CICLO.pdf.

[8] P.G. Kroth-Pancic, A.R. Grossman, Stable nuclear transformation of the diatom Phaeodactylum tricornutum, Mol. Gen. Genet. 252 (1996) 572–579.

[9] U.S. Doe, U. DOE, National algal biofuels technology roadmap, US Dep. Energy. (2010) 140. doi:Public Law No. 106-554.

[10] A. Mazzitelli, S. Consonni, F. Viganò, Produzione di Energia ed Elettricità da Alghe, (2010) 1–113.

[11] Y. Chisti, Biodiesel from microalgae., Biotechnol. Adv. 25 (2007) 294–306. doi:10.1016/j.biotechadv.2007.02.001.

[12] M. Menegus, A. Bertucco, A. Botto, Progettazione di un fotobioreattore per la coltivazione su scala industriale di microalghe utilizzabili per fini energetici, (2011) 1–82.

[13] B. Agrarie, M.R. Tredici, Le microalghe : Mercato e tecnologie, (1990).

[14] L. Brennan, P. Owende, Biofuels from microalgae-A review of technologies for production, processing, and extractions of biofuels and co-products, Renew. Sustain. Energy Rev. 14 (2010) 557–577. doi:10.1016/j.rser.2009.10.009.

[15] J. Ferrell, V. Sarisky-Reed, U.S. Doe, U. DOE, National Algal Biofuels Technology Roadmap, U.S. Dep. Energy. (2010) 140. doi:Public Law No. 106-554.

[16] E. Sforza, M. Enzo, A. Bertucco, Design of microalgal biomass production in a continuous photobioreactor: An integrated experimental and modeling approach, Chem. Eng. Res. Des. 92 (2014) 1153–1162. doi:10.1016/j.cherd.2013.08.017.

[17] C. Federico, Produzione Di Olio Combustibile Da Microalghe: Analisi Delle Tecnologie Di Processo E Dell'Impatto Sulle Risorse Idriche, (2012).

[18] R. Keeling, Scripps CO2 Program, (2016). http://scrippsco2.ucsd.edu/.

[19] Acta Plantarum, (2016). www.actaplantarum.org.

[20] CO2 Club, 2016. (n.d.). www.co2club.it/Sectionse32a.html.

[21] E. Jacob-Lopes, C.H.G. Scoparo, L.M.C.F. Lacerda, T.T. Franco, Effect of light cycles (night/day) on CO2 fixation and biomass production by microalgae in photobioreactors, Chem. Eng. Process. Process Intensif. 48 (2009) 306–310. doi:10.1016/j.cep.2008.04.007.

[22] F.. G. Acién Fernández, D.O. Hall, E. Cañizares Guerrero, K. Krishna Rao, E. Molina Grima, Outdoor production of Phaeodactylum tricornutum biomass in a helical reactor, J. Biotechnol. 103 (2003) 137–152. doi:10.1016/S0168-1656(03)00101-9.

[23] Phaeodactylum Tricornutum species, (2015). http://bioinformatics.psb.ugent.be/genomes/view/Phaeodactylum-tricornutum.

[24] A. De Martino, Diatomea species, (n.d.). http://www.alestuariodelplata.com.ar/diatomeas.html.

[25] Nature: P.T. microalgae species, (n.d.). http://www.nature.com/srep/2014/140204/srep03958/full/srep03958.html.

[26] F.X.M. A.P. Carvalho, S.O. Silva, J.M. Baptista, Light requirements in microalgal photobioreactors: an overview of biophotonic aspects, Appl. Microbiol. Biotechnol. 89 (2011) 1275–1288.

[27] Photosystem, 2016. (n.d.). https://en.wikipedia.org/wiki/Photosystem.

[28] Light phase of photosynthesis, (2015).

[29] F. García-Camacho, Sánchez-Mirón, J.C.M. Molina-Grima , AF. Camacho-Rubio, A mechanistic model of photosynthesis in microalgae including dynamics, J. Theor. Biol. 304 (2012) 1–15.

[30] E. Molina, F. Fernández, Scale-up of tubular photobioreactors, J. Appl. …. 12 (2000) 355–368. doi:10.1023/A:1008110819338.

[31] A.M. Kunjapur, R.B. Eldridge, Photobioreactor design for commercial biofuel production from microalgae, Ind. Eng. Chem. Res. 49 (2010) 3516–3526. doi:10.1021/ie901459u.

[32] D. Zhang, P. Dechatiwongse, K. Hellgardt, Modelling light transmission, cyanobacterial growth kinetics and fluid dynamics in a laboratory scale multiphase photo-bioreactor for biological hydrogen production, Algal Res. 8

(2015) 99–107. doi:10.1016/j.algal.2015.01.006.

[33] F. Ippolito, A. Brucato, A. Busciglio, Modellazione fluidodinamica di un sistema fotobioreattore-unità di sollevamento a gas destinato alla produzione di microalghe, Palermo University, 2013.

[34] M.J. Griffiths, S.T.L. Harrison, Lipid productivity as a key characteristic for choosing algal species for biodiesel production, J. Appl. Phycol. 21 (2009) 493–507. doi:10.1007/s10811-008-9392-7.

[35] F.G. Acién Fernández, J.M. Fernández Sevilla, E. Molina Grima, Photobioreactors for the production of microalgae, Rev. Environ. Sci. Biotechnol. 12 (2013) 131–151. doi:10.1007/s11157-012-9307-6.

[36] I. Khozin-Goldberg, Z. Cohen, The effect of phosphate starvation on the lipid and fatty acid composition of the fresh water eustigmatophyte Monodus subterraneus, Phytochemistry. 67 (2006) 696–701. doi:10.1016/j.phytochem.2006.01.010.

[37] Y. Chisti, Biodiesel from microalgae beats bioethanol, Trends Biotechnol. 26 (2008) 126–131. doi:10.1016/j.tibtech.2007.12.002.

[38] D. Bilanovic, A. Andargatchew, T. Kroeger, G. Shelef, Freshwater and marine microalgae sequestering of CO2 at different C and N concentrations – Response surface methodology analysis, Energy Convers. Manag. 50 (2009) 262–267. doi:10.1016/j.enconman.2008.09.024.

[39] E. Molina, J. Fernández, F.G. Acién, Y. Chisti, Tubular photobioreactor design for algal cultures, J. Biotechnol. 92 (2001) 113–131. doi:10.1016/S0168-1656(01)00353-4.

[40] F.X.M. H.M. Amaro, A.C. Guedes, Advances and perspectives in using microalgae to produce biodiesel, Appl. Energy. 88 (2011) 3402–3410.

[41] A.M. Silva Benavides, G. Torzillo, J. Kopecký, J. Masojídek, Productivity and biochemical composition of Phaeodactylum tricornutum (Bacillariophyceae) cultures grown outdoors in tubular photobioreactors and open ponds, Biomass and Bioenergy. 54 (2013) 115–122. doi:10.1016/j.biombioe.2013.03.016.

[42] A. Pandey, D.J. Lee, Y. Chisti, Biofuels from Algae, 2014.

[43] E. Molina, T.A. Costache, Fernandez, F.G., M.M. Morales, J.M.F. Sevilla, I. Stamatin, Comprehensive model of microalgae photosynthesis rate as a function of culture conditions in photobioreactors, Appl. Microbiol. Biotechnol. 97 (2013) 7627–7633.

[44] E. Bitaubé Pérez, I. Caro Pina, L. Pérez Rodríguez, Kinetic model for growth of Phaeodactylum tricornutum in intensive culture photobioreactor, Biochem. Eng. J. 40 (2008) 520–525. doi:10.1016/j.bej.2008.02.007.

[45] A. Singh, P.S. Nigam, J.D. Murphy, Mechanism and challenges in commercialisation of algal biofuels, Bioresour. Technol. 102 (2011) 26–34. doi:10.1016/j.biortech.2010.06.057.

[46] E. Molina Grima, F.G.A. Fernández, F. García Camacho, Y. Chisti, Photobioreactors: light regime, mass transfer, and scaleup, J. Biotechnol. 70 (1999) 231–247. doi:10.1016/S0168-1656(99)00078-4.

[47] R.N. Singh, S. Sharma, Development of suitable photobioreactor for algae production – A review, Renew. Sustain. Energy Rev. 16 (2012) 2347–2353. doi:10.1016/j.rser.2012.01.026.

[48] C.U. Ugwu, H. Aoyagi, H. Uchiyama, Photobioreactors for mass cultivation of algae, Bioresour. Technol. 99 (2008) 4021–4028. doi:10.1016/j.biortech.2007.01.046.

[49] E.M. Grima, F.G. Camacho, J.A.S. Pérez, J.M.F. Sevilla, F.G.A. Fernández, A.C. Gómez, A mathematical model of microalgal growth in light-limited chemostat culture, J. Chem. Technol. Biotechnol. 61 (1994) 167–173. doi:10.1002/jctb.280610212.

[50] J.F. Cornet, C.G. Dussap, P. Cluzel, G. Dubertret, A structured model for simulation of cultures of the cyanobacteriumSpirulina platensis in photobioreactors: II. Identification of kinetic parameters under light and mineral limitations, Biotechnol. Bioeng. 40 (1992) 826–834. doi:10.1002/bit.260400710.

[51] F.G. Acién Fernández, F. García Camacho, J.A. Sánchez Pérez, J.M. Fernández Sevilla, E. Molina Grima, F.G. Acie, J.A. Sa, E.M. Grima, F.G. Acién Fernández, F. García Camacho, J.A. Sánchez Pérez, J.M. Fernández Sevilla, E. Molina Grima, F.G. Acie, J.A. Sa, E.M. Grima, A Model for Light Distribution and Average Solar Irradiance Inside Outdoor Tubular Photobioreactors for the Microalgal Mass Culture, Biotechnol. Bioeng. 55 (1997) 701–714. doi:10.1002/(SICI)1097-0290(19970905)55.

[52] B.A. Shannak, Frictional pressure drop of gas liquid two-phase flow in pipes, Nucl. Eng. Des. 238 (2008) 3277–3284. doi:10.1016/j.nucengdes.2008.08.015.

[53] Y. Chisti, M. Moo-Young, Improve the performance of airlift reactors, Chem. Eng. Prog. 89 (1993) 38–45.

[54] R.K. SINNOTT, CHEMICAL ENGINEERING. Volume 6, 2013. doi:10.1017/CBO9781107415324.004.

[55] W.L. McCabe, J.C. Smith, P. Harriott, Unit operations of chemical engineering, 1993. http://scilab.in/files/textbooks/PrashantDave/McCabe.pdf.

[56] T. Huld, D. Ewan D., Institute for Environment and Sustainability, (2014). http://re.jrc.ec.europa.eu/pvgis/apps4/pvest.php.

[57] A. Richmond, Handbook of microalgal culture: biotechnology and applied phycology/edited by Amos Richmond., Orton.Catie.Ac.Cr. (2004) 472. doi:10.1002/9780470995280.

[58] E. Molina-Grima, F. Gabriel Acien Fernandez, F. García-Camacho, Y. Chisti, F.G. Aci??n Fern??ndez, F. Garc??a Camacho, Y. Chisti, E. Molina Grima,

F.G.A. Fernández, F. García Camacho, Y. Chisti, Photobioreactors: light regime, mass transfer, and scaleup, J. Biotechnol. 70 (1999) 231–247. doi:10.1016/S0079-6352(99)80118-0.

[59] F.G. Acién Fernández, J.M. Fernández Sevilla, J. a. Sánchez Pérez, E. Molina Grima, Y. Chisti, F.G. Aci??n Fern??ndez, J.M. Fern??ndez Sevilla, J.A. S??nchez P??rez, E. Molina Grima, Y. Chisti, Airlift-driven external-loop tubular photobioreactors for outdoor production of microalgae: Assessment of design and performance, Chem. Eng. Sci. 56 (2001) 2721–2732. doi:10.1016/S0009-2509(00)00521-2.

[60] J.C.C. Merchuk, M. Gluz, Bioreactors, air-lift reactors, Encycl. Bioprocess Technol. (1999) 320–394. doi:10.1002/0471250589.ebt029.

[61] Y. Rujiruttanakul, P. Pavasant, Influence of configuration on the performance of external loop airlift contactors, Chem. Eng. Res. Des. 89 (2011) 2254–2261. doi:http://dx.doi.org/10.1016/j.cherd.2011.02.017.

[62] A. a Kulkarni, J.B. Joshi, Bubble Formation and Bubble Rise Velocity in Gas - Liquid Systems : A Review, Ind. Eng. Chem. Res. 44 (2005) 5873–5931. doi:10.1021/ie049131p.

[63] R.A. Bello, C.W. Robinson, M. Moo-Young, Gas holdup and overall volumetric oxygen transfer coefficient in airlift contactors., Biotechnol. Bioeng. 27 (1985) 369–81. doi:10.1002/bit.260270323.

[64] M.Y. Chisti, B. Halard, M. Moo-Young, Liquid circulation in airlift reactors, Chem. Eng. Sci. 43 (1988) 451–457. doi:10.1016/0009-2509(88)87005-2.

[65] J.H. Hills, The operation of a bubble column at high throughputs: I. Gas holdup measurements, Chem. Eng. J. 12 (1976) 89–99. doi:10.1016/0300-9467(76)87002-5.

[66] B.J.C. Merchuk, Airlift Bioreactors : Review of Recent Advances, Can. J. Chem. Eng. 81 (2003) 324–337. doi:10.1002/cjce.5450810301.

[67] A.D. Gosman, C. Lekakou, S. Politis, R.I. Issa, M.K. Looney, Multidimensional modeling of turbulent two-phase flows in stirred vessels, AICHE J. 38 (1992) 1946–1956.

[68] R. Clift, J.R. Grace, M.E. Weber, Bubbles, Drops, and Particles, 1978. http://books.google.it/books/about/Bubbles_Drops_and_Particles.html?id=n8gRAQAAIAAJ&pgis=1 (accessed March 19, 2015).

[69] W. Szablewski, B. E. Launder and D. B. Spalding, Mathematical Models of Turbulence. 169 S. m. Abb. London/New York 1972. Academic Press. Preis geb. $ 7.50, ZAMM - Zeitschrift Für Angew. Math. Und Mech. 53 (1973) 424–424. doi:10.1002/zamm.19730530619.

[70] F. Scargiali, A. Busciglio, A. Cipollina, F. Grisafi, G. Micale, A. Tamburini, G. Vella, A. Brucato, Modelling and Simulation of Gas–liquid Hydrodynamics in a Rectangular Air-lift Reactor, Int. J. Chem. React. Eng. 11 (2013). doi:10.1515/ijcre-2012-0040.

[71] E. Delnoij, J. Westerweel, N.G. Deen, J. a. M. Kuipers, W.P.M. van Swaaij, Ensemble correlation PIV applied to bubble plumes rising in a bubble column, Chem. Eng. Sci. 54 (1999) 5159–5171. doi:10.1016/S0009-2509(99)00233-X.

[72] A. Sokolichin, G. Eigenberger, Applicability of the standard k } turbulence model to the dynamic simulation of bubble columns : Part I . Detailed numerical simulations, 54 (1999) 2273–2284.

[73] J.B. Joshi, Computational flow modelling and design of bubble column reactors, Chem. Eng. Sci. 56 (2001) 5893–5933. doi:10.1016/S0009-2509(01)00273-1.

[74] ANSYS Inc., ANSYS, ANSYS CFX-Solver Theory Guide, 2013.

[75] G. Comini, G. Croce, E. Nobile, Fondamenti di termofluidodinamica computazionale, SGE, 2014.

[76] ANSYS Inc., ANSYS, ANSYS CFX-Solver Modeling Guide, Knowl. Creat. Diffus. Util. 15317 (2013) 724–746. f:/Eigene Dokumente/My EndNote Library.Data/PDF/0004154979/cfx_mod.pdf.

[77] A.K. Pegallapati, Y. Arudchelvam, N. Nirmalakhandan, Energy-efficient photobioreactor configuration for algal biomass production, Bioresour. Technol. 126 (2012) 266–273. doi:10.1016/j.biortech.2012.08.090.

[78] S. Xue, Q. Zhang, X. Wu, C. Yan, W. Cong, A novel photobioreactor structure using optical fibers as inner light source to fulfill flashing light effects of microalgae, Bioresour. Technol. 138 (2013) 141–147. doi:10.1016/j.biortech.2013.03.156.

[79] M. Janssen, Cultivation of microalgae : effect of light / dark cycles on biomass yield, Unpubl. Master's Thesis Wageningen Univ. Wageningen Netherlands. 1191 (2002) 184. doi:10.1016/S0168-1656(99)00084-X.

[80] R. Pandey, A. Sahu, K.K. Vasumathi, M. Premalatha, Studies on light intensity distribution inside an open pond photo-bioreactor, Bioprocess Biosyst. Eng. 38 (2015) 1547–1557. doi:10.1007/s00449-015-1398-3.

[81] B. Kong, R.D. Vigil, Simulation of photosynthetically active radiation distribution in algal photobioreactors using a multidimensional spectral radiation model, Bioresour. Technol. 158 (2014) 141–148. doi:10.1016/j.biortech.2014.01.052.

[82] A. Souliès, J. Legrand, H. Marec, J. Pruvost, C. Castelain, T. Burghelea, J.F. Cornet, Investigation and modeling of the effects of light spectrum and incident angle on the growth of Chlorella vulgaris in photobioreactors, Biotechnol. Prog. 0 (2016) 1–16. doi:10.1002/btpr.2244.

[83] J. Pruvost, F. Le Borgne, A. Artu, J. Legrand, Development of a thin-film solar photobioreactor with high biomass volumetric productivity (AlgoFilm©) based on process intensification principles, Algal Res. 21 (2017). doi:10.1016/j.algal.2016.10.012.

[84] R. Kandilian, J. Pruvost, J. Legrand, L. Pilon, Influence of light absorption rate by Nannochloropsis oculata on triglyceride production during nitrogen starvation, Bioresour. Technol. 163 (2014). doi:10.1016/j.biortech.2014.04.045.

[85] J. Colina, F. Machuca-Martínez, G. Li Puma, Radiation Absorption and Optimization of Solar Photocatalytic Reactors for Environmental Applications, 44 (2010) 5112–5120.

[86] F. Machuca-Martínez, J. Colina-Marquez, M. Mueses, Determination of quantum yield in a heterogeneous photocatalytic system using a fitting-parameters model, 11 (2008).

[87] A. Brucato, M. Carlo, Estimating Radiant Fields in Flat Heterogeneous Photoreactors by the Six-Flux Model, AIChE J. 52 (2006). doi:10.1002/aic.

[88] D.C. Hammersley, J. M., Handscomb, Monte Carlo Methods, Chapman and Hall Ltd, London, 1983.

[89] A. Brucato, F. Grisafi, L. Rizzuti, A. Sclafani, G. Vella, Quasi-isoactinic reactor for photocatalytic kinetics studies, Ind. Eng. Chem. Res. 46 (2007) 7684–7690. doi:10.1021/ie0703991.

[90] A. Busciglio, O.M. Alfano, F. Scargiali, A. Brucato, A probabilistic approach to radiant field modeling in dense particulate systems, Chem. Eng. Sci. 142 (2016) 79–88. doi:10.1016/j.ces.2015.11.025.

[91] J. Pruvost, J.F. Cornet, F. Le Borgne, V. Goetz, J. Legrand, Theoretical investigation of microalgae culture in the light changing conditions of solar photobioreactor production and comparison with cyanobacteria, Algal Res. 10 (2015). doi:10.1016/j.algal.2015.04.005.

[92] E. Lee, J. Pruvost, X. He, R. Munipalli, L. Pilon, Design tool and guidelines for outdoor photobioreactors, Chem. Eng. Sci. 106 (2014) 18–29. doi:10.1016/j.ces.2013.11.014.

[93] R. Kandilian, J. Pruvost, A. Artu, C. Lemasson, J. Legrand, L. Pilon, Comparison of experimentally and theoretically determined radiation characteristics of photosynthetic microorganisms, J. Quant. Spectrosc. Radiat. Transf. 175 (2016) 30–45. doi:10.1016/j.jqsrt.2016.01.031.

[94] R. Kandilian, A. Soulies, J. Pruvost, B. Rousseau, J. Legrand, L. Pilon, Simple method for measuring the spectral absorption cross-section of microalgae, Chem. Eng. Sci. 146 (2016). doi:10.1016/j.ces.2016.02.039.

[95] R.R.L. Guillard, Culture of Phytoplankton for Feeding Marine Invertebrates, in: W.L. Smith, M.H. Chanley (Eds.), Cult. Mar. Invertebr. Anim. Proc. --- 1st Conf. Cult. Mar. Invertebr. Anim. Greenport, Springer US, Boston, MA, 1975: pp. 29–60. doi:10.1007/978-1-4615-8714-9_3.

[96] G. Brunner, Hydrothermal and Supercritical Water Processes, Elsevier, 2014. http://store.elsevier.com/Hydrothermal-and-Supercritical-Water-Processes/Gerd-Brunner/isbn-9780444594136/ (accessed July 27, 2015).

[97] M. Modell, Gasification and Liquefaction of Forest Products in Supercritical Water, in: Fundam. Thermochem. Biomass Convers., Springer Netherlands, 1985: pp. 95–119. doi:http://dx.doi.org/10.1007/978-94-009-4932-4_6.

[98] Y. Matsumura, T. Minowa, B. Potic, S. Kersten, W. Prins, W. Vanswaaij, B. Vandebeld, D. Elliott, G. Neuenschwander, A. Kruse, Biomass gasification in near- and super-critical water: Status and prospects, Biomass and Bioenergy. 29 (2005) 269–292. doi:10.1016/j.biombioe.2005.04.006.

[99] A. Kruse, Hydrothermal biomass gasification, J. Supercrit. Fluids. 47 (2009) 391–399. doi:10.1016/j.supflu.2008.10.009.

[100] S. Galera, F.J. Gutiérrez Ortiz, Techno-economic assessment of hydrogen and power production from supercritical water reforming of glycerol, Fuel. 144 (2015) 307–316. doi:10.1016/j.fuel.2014.12.033.

[101] M.S.H.K. Tushar, A. Dutta, C. (Charles) Xu, Simulation and kinetic modeling of supercritical water gasification of biomass, Int. J. Hydrogen Energy. 40 (2015) 4481–4493. doi:10.1016/j.ijhydene.2015.02.033.

[102] L. Fiori, M. Valbusa, D. Castello, Supercritical water gasification of biomass for H2 production: process design., Bioresour. Technol. 121 (2012) 139–47. doi:10.1016/j.biortech.2012.06.116.

[103] L. Guo, Y. Lu, X. Zhang, C. Ji, Y. Guan, A. Pei, Hydrogen production by biomass gasification in supercritical water: A systematic experimental and analytical study, Catal. Today. 129 (2007) 275–286. doi:10.1016/j.cattod.2007.05.027.

[104] S. Karagöz, T. Bhaskar, A. Muto, Y. Sakata, M.A. Uddin, Low-Temperature Hydrothermal Treatment of Biomass: Effect of Reaction Parameters on Products and Boiling Point Distributions, Energy & Fuels. 18 (2004) 234–241. doi:10.1021/ef030133g.

[105] D. Yu, M. Aihara, M.J. Antal, Hydrogen production by steam reforming glucose in supercritical water, Energy and Fuels. 7 (1993) 574–577. http://www.scopus.com/inward/record.url?eid=2-s2.0-0027660317&partnerID=tZOtx3y1.

[106] H. Jin, Y. Lu, L. Guo, C. Cao, X. Zhang, Hydrogen production by partial oxidative gasification of biomass and its model compounds in supercritical water, Int. J. Hydrogen Energy. 35 (2010) 3001–3010. doi:10.1016/j.ijhydene.2009.06.059.

[107] K. Yamagata, K. Nishikawa, S. Hasegawa, S. Fujii, T., Yoshida, Forced convective heat transfer to supercritical water flowing in tubes, Int. J. Heat Mass Trans. 15. (1972) 2575–2593.

[108] M. Bazargan, D. Fraser, V. Chatoorgan, Effect of Buoyancy on Heat Transfer in Supercritical Water Flow in a Horizontal Round Tube, J. Heat Transfer. 127 (2005) 897. doi:10.1115/1.1929787.

[109] M. Van Der Kraan, M.M.W. Peeters, M. V. Fernandez Cid, G.F. Woerlee, W.J.T. Veugelers, G.J. Witkamp, The influence of variable physical

properties and buoyancy on heat exchanger design for near- and supercritical conditions, J. Supercrit. Fluids. 34 (2005) 99–105. doi:10.1016/j.supflu.2004.10.007.

[110] R. Smith, H. Inomata, Introduction to Supercritical Fluids: A spreadsheet-based Approach, Elsevier, 2013.

[111] Y.S. Cheng, S.W. Kim, Computation of turbulent flows using an extended k–ε turbulence closure model, NASA. (1987) CR-179204. http://ntrs.nasa.gov/archive/nasa/casi.ntrs.nasa.gov/19880002587.pdf (accessed June 16, 2015).

[112] X. Cheng, B. Kuang, Y.H. Yang, Numerical analysis of heat transfer in supercritical water cooled flow channels, Nucl. Eng. Des. 237 (2007) 240–252. doi:10.1016/j.nucengdes.2006.06.011.

[113] F. Roelofs, CFD Analyses of Heat Transfer to Supercritical Water Flowing Vertically Upward in a Tube Underthe contract of the Netherlands Ministry of Economic Affairs, Distribution. (2004) 1–28.

[114] O. Levenspiel, Chemical Reaction Engineering, 1998. http://eu.wiley.com/WileyCDA/WileyTitle/productCd-047125424X.html (accessed July 9, 2015).

[115] F. Scargiali, F. Grisafi, J. Cermakova, V. Machon, A. Brucato, Particle flow modeling in slurry-fed stirred vessels, Chem. Eng. Technol. 27 (2004) 249–256. doi:10.1002/ceat.200402008.

[116] F. Scargiali, F. Grisafi, J. Cermakova, V. Machon, a. Brucato, Residence time distribution of solid particles in a continuous, high-aspect-ratio multiple-impeller stirred vessel, Chem. Eng. Sci. 59 (2004) 3601–3618. doi:10.1016/j.ces.2004.05.021.